BULGARIAN CHEMICAL COMMUNICATIONS

2026 Volume 58 / Number 3

Papers presented at the 12th International Conference on New Trends in Chemistry, 10-12 April 2026, Barcelona, Spain

Journal of the Chemical Institutes
of the Bulgarian Academy of Sciences
and of the Union of Chemists in Bulgaria

Bulgarian Chemical Communications, Volume 58, Issue 3 (pp. 241-246) 2026 *DOI: 10.34049/bcc.58.3.D001*

Production of desalination membranes from recycled PVDF polymers

A. Katırcı[1]*, F. U. Nigiz[2]

[1]*Çanakkale Onsekiz Mart University, School of Graduate Studies, Çanakkale, 17100, Türkiye*
[2]*Çanakkale Onsekiz Mart University, Department of Chemical Engineering, Çanakkale, 17100, Türkiye*

Accepted: July 28, 2026

Water is of critical importance to industry. Numerous technologies have been developed regarding water use in industrial applications. In this study an innovative membrane distillation method is investigated for the separation of brackish water that can be used in process and cooling water applications. The primary focus of this study is the use of a membrane recovered from waste polymers in a membrane distillation system. This approach will prevent waste from entering the environment by facilitating its revaluation, while also contributing to the national economy by promoting recycling as an alternative to the use of new products. To this end, polyvinylidene fluoride (PVDF), a commercial membrane material, was recycled from waste and reused. The recovered PVDF was converted into a porous membrane structure using the electrospinning method. The membrane surface was modified using poly(vinyl alcohol) (PVA) *via* the dip-coating method. Characterization of the produced membranes included FTIR, DSC, and mechanical strength analyses. Salt separation efficiencies exceeding 99% were achieved in membrane performance evaluations.

Keywords: Desalination, Membrane distillation, PVDF, Recycling

INTRODUCTION

Industrial water use is a critical area of study and research that is growing day by day alongside technological and industrial advancements, yet due to environmental concerns, it is essential to ensure that water is reused as much as possible. In industrial processes, water is used as process water and cooling water. In particular, facilities with high water consumption (such as thermal power plants) are located near natural water sources and treat saltwater for use in their systems. Desalination, literally meaning “removal of salt,” can be described as a technological process of obtaining fresh drinking water from brackish or saltwater. Thanks to desalination technology, seawater resources are utilized to produce drinking water, providing a solution to water scarcity in the face of a growing population. It also supports the sustainability of agriculture and industry. There are two primary technological approaches for removing salt from water: thermal and membrane-based methods.

Membrane distillation is a desalination method used to convert saltwater into potable water. In this system which primarily uses hydrophobic and porous membranes, the separation gradient is driven by both temperature and partial pressure differences. As water vapor generated by heat in the feed section passes through the hydrophobic membrane, salt and contaminants are separated. Membrane distillation is a method that operates at low temperatures, requires no pretreatment, and utilizes waste heat as a heat source. From this perspective, it offers significant economic and environmental advantages [1].

Vacuum membrane distillation (VMD) is one of the membrane distillation techniques. It is used in desalination processes to separate salt and other dissolved substances from seawater. This distillation technique is based on the principle of conducting the evaporation process under vacuum. Applying a vacuum to create low pressure lowers the boiling point, allowing the system to operate at lower temperatures. As a result, less energy is consumed compared to other distillation techniques, since the energy required to reach high temperatures is minimized. In the VMD process, the saltwater is heated and fed to one side of the membrane under vacuum. The heated water evaporates and passes through the semi-permeable membrane, while the salt and impurities remain behind. The vapor is cooled in the vacuum environment and condenses, resulting in the production of pure, salt-free water. High salt removal is achieved [2]. The most important component of this system is the membrane used.

There are several key characteristics that determine the performance of membranes used in desalination processes. A high water flux is critical for reducing process time and lowering energy costs. Low fouling tendency contributes to reduced maintenance requirements and extended service life for the membrane. Additionally, low energy requirements enable high efficiency to be achieved

* To whom all correspondence should be sent:
E-mail: *katirciaysenur@gmail.com*

© 2026 Bulgarian Academy of Sciences, Union of Chemists in Bulgaria

with minimal energy input. Mechanical durability ensures physical integrity of the membrane over an extended period, while high salt rejection capacity allows for the maximum extraction of pure water from saline water. Thermal stability supports the membrane's ability to operate at high temperatures without structural degradation. Furthermore, high porosity facilitates the passage of water vapor while limiting the passage of dissolved substances [1].

Recycling reduces dependence on raw materials required for new polymer production. The methods used to dispose of membranes—landfilling and incineration—are not environmentally sound. For these reasons, new methods for disposing of these membranes are needed. It has been demonstrated that recycled polymers reduce both operational costs and carbon emissions. Processes that continue without the need to constantly replace membranes by using recycled polymer membranes are highly beneficial to the operation in terms of cost. Moreover, since the polymers do not need to be replaced continuously, there is no waste problem, and because no energy is consumed, they are environmentally friendly. Furthermore, the pollution problem caused by the membranes used is eliminated, and thanks to recycled polymer membranes, there is no longer a need for pollution removal processes.

The literature contains numerous significant studies on the use of membrane distillation systems to produce pure water from seawater. The majority of these studies have been conducted using polyvinylidene fluoride (PVDF). PVDF is an important polymer that is non-reactive, thermally stable, and mechanically strong, with good processability and chemical resistance to various materials such as acids, bases, organic solvents, and oils [3, 4]. It is a microfiltration polymer and is commercially available. However, particularly in water treatment processes, its hydrophobic nature makes it prone to membrane fouling; to address this and enhance its hydrophilicity, various modifications can be applied. PVDF membranes are widely used in various fields such as microfiltration, ultrafiltration, membrane bioreactors, membrane distillation, gas separation, and stripping [5-7].

In recent years, it has been observed that PVDF is recyclable, just like polyethylene terephthalate, polystyrene, and polyamide, and that it retains its properties after recycling. PVDF was included in this project specifically because it serves as the primary material for microfiltration membranes and because of the concept that these membranes can be recycled and reused after use. New studies on recycled PVDF have begun to emerge in the literatüre [8]. Therefore, within the scope of this project, the aim is to produce purified water *via* membrane distillation using recycled PVDF produced by the electrospinning method.

EXPERIMENTAL

A DMF-acetone solution containing PVDF (20% by weight) and PVP (10% by weight relative to PVDF) was prepared and stirred at 50 °C. The homogeneous solution was drawn into a syringe and loaded into an electrospinning system. The solution was collected onto a plate at a voltage of 17 kV, a flow rate of 0.05 mL/min, and a distance of 150 mm. Subsequently, the produced PVDF membranes were modified using a dip-coating technique. The membranes were immersed in a 10% (w/w) aqueous polyvinyl alcohol (PVA) solution for a specific duration, followed by a drying process to ensure the formation of a thin, homogeneous PVA layer on the nanofiber surfaces. This modification step was used to optimize the membrane's desalination performance. The samples were coded according to the number of coating cycles; each cycle contributed approximately 2 μm to the total coating thickness. Scheme 1 illustrates the electrospinning and PVA coating method used in membrane production.

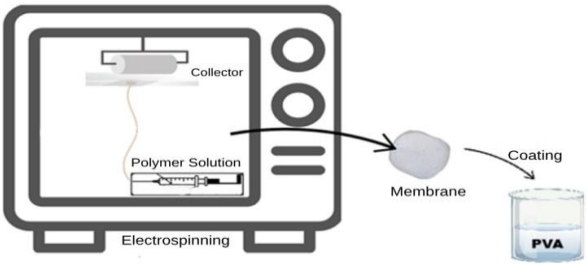

Scheme 1. Schematic representation of the electrospinning and PVA coating methods in membrane production

FTIR spectra were recorded on a Shimadzu Tracer spectrometer (IRTracer-100, Shimadzu Corporation, Kyoto, Japan). A differential scanning calorimeter (DSC-60 Plus, Shimadzu Corporation, Kyoto, Japan) was used for DSC analysis. In compliance with the ASTM D882 standard, the tensile strength and elongation at break values were measured during the mechanical testing phase using the ANKARIN universal testing machine. The agar diffusion method was used to conduct antimicrobial tests [9]. The test microorganisms were *Staphylococcus aureus* (+) and *Escherichia coli* (-), which were seeded separately on liquid media and maintained at 37°C for one day.

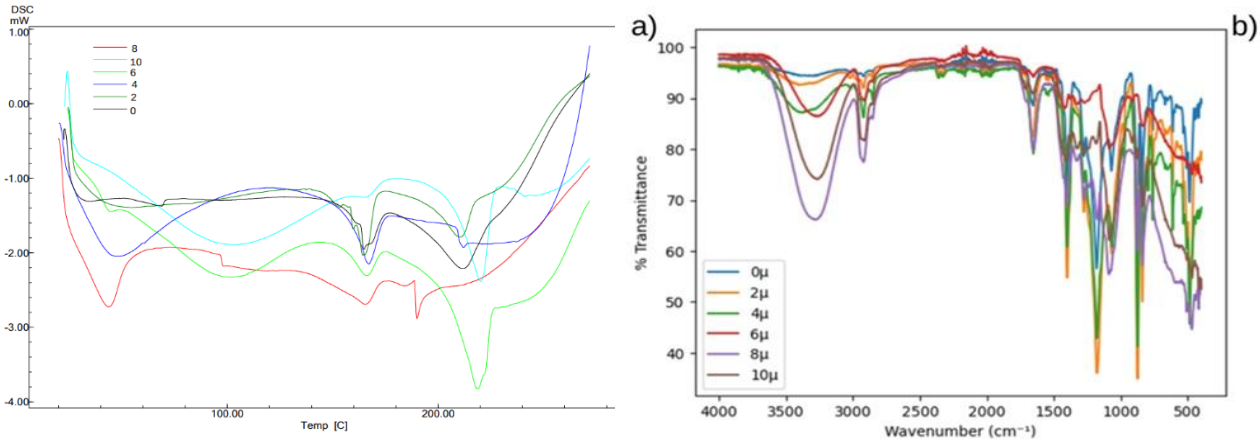

Figure 1. FTIR spectra (a) and DSC analysis (b) of recycled PVDF-PVA coating membranes

After reducing it to 0.5 McFarland turbidity, a sterile brush was used to evenly disperse it across the agar surface. Film samples were placed on Petri dishes and stored at 37°C for one day. In the end, the diameter of the formed zones was measured.

RESULTS AND DISCUSSION

Characterization tests

As part of the characterization tests, FTIR, DSC, mechanical analysis, and contact angle tests were performed. The disk diffusion method was used for antimicrobial analysis.

- *FTIR.* The FTIR spectra are shown in Figure 1a. The FTIR analysis confirmed that the PVA modification has been successfully integrated into the PVDF membrane surface. The broad peaks observed around 3300 cm^{-1} in all spectra confirm the presence of hydroxyl (-OH) groups in the PVA structure [10, 11]. The fact that the peak's intensity is highest in the 8 µm- and 10 µm-samples indicates that the most dense coating occurred in these samples. On the other hand, the decrease in the intensity of the -OH peak in the 2 µm and 0 µm samples indicates a reduction in coating thickness.
- *DSC.* The DSC analysis results are presented in Figure 1b. The broad endothermic peaks observed between 50 and 100°C indicate the removal of moisture from the structure. Additionally, the peaks between 40 and 70 °C can be associated with the glass transition temperature of PVA [11]. The fact that these peaks are more pronounced at higher coating thicknesses (8–10 µm) indicates an increase in PVA content. The sharp melting peaks around 170°C and 220°C represent the melting temperature (T_m) of PVA's crystalline regions [11]. The weaker presence of this effect at 2 µm and 0 µm indicates a low coating amount and a low PVA content. In the 6 µ sample, a deep endothermic peak (~220 °C) indicates a regular structure and optimal PVA distribution. Since the classic melting peak of PVDF is not very clear, the PVA coating may have masked the crystallization of PVDF.
- *Mechanical analysis.* The results of the mechanical analysis are presented in Table 1. Among the tested samples, the 6µ-sample exhibited superior mechanical strength with a peak tensile stress of approximately 31 MPa, indicating an optimal balance between the recycled PVDF matrix and the modification process. Although the 10µ-sample exhibited the highest flexibility with an elongation value exceeding 0.40, its lower tensile capacity indicates a structure that is more ductile but less resistant to pressure. A consistent decrease in both mechanical strength and flexibility was observed from 4µm down to 0µm.

Table 1. Results of the mechanical analysis

Membrane	Stress (MPa)	Strain
10µ	12.29	0.41
8µ	21.19	0.22
6µ	31.15	0.31
4µ	9.59	0.28
2µ	8.13	0.25
0µ	5.89	0.18

Contact angle analysis

The contact angle results are presented in Figure 2. As the PVA coating thickness increased, the contact angle showed a significant decrease from 76° to 44°, indicating a significant increase in surface hydrophilicity. This is attributed to the increased presence of PVA-derived hydroxyl (–OH) functional groups, which support hydrogen bonding with water molecules. A more pronounced decrease beyond 6 µm indicates the formation of a more homogeneous and continuous coating layer. These findings confirm that PVA modification effectively improves the wettability of PVDF membranes.

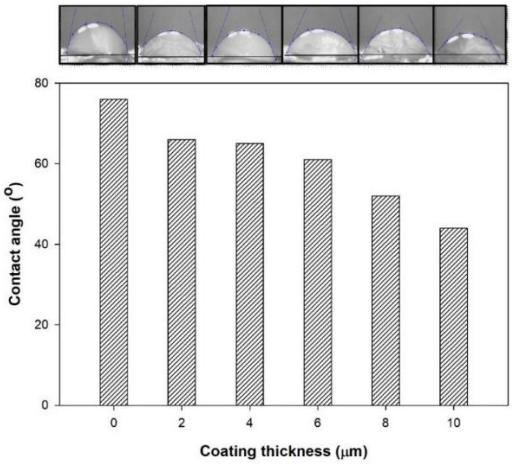

Figure 2. Contact angle results for recycled PVDF-PVA-coated membranes

Antımıcrobıal analysıs

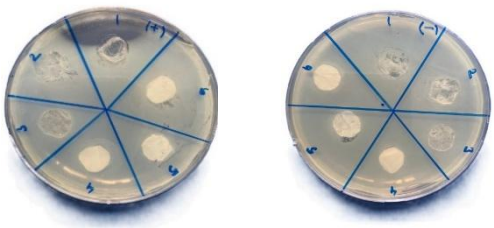

Figure 3. Antimicrobial analysis results for recycled PVDF-PVA coating membranes

The results of the antimicrobial tests conducted by the disk diffusion method are presented in Figure 3. No distinct zone of inhibition is seen around the samples. In this case, there is no strong antibacterial activity. Since PVA is not an antimicrobial substance by nature, this result is expected [12]. Consequently, the modification of PVA has not imparted antibacterial properties to the PVDF membranes.

Desalination tests

The graph in Figure 4a shows that the flux value gradually decreases as the coating thickness increases from 0 μm to 10 μm. The flux, which was approximately 11.6 kg/m²h at the start (~0 μm), has decreased to approximately 6.4 kg/m²h at a thickness of 10 μm. As the coating layer thickens, the mass transfer resistance that water molecules must overcome, increases. This is directly proportional to Fick's law; the increase in resistance reduces the effect of the driving force, thereby lowering permeability. It is observed that salt retention efficiency dramatically increases as coating thickness increases. While the rejection rate was below 30% in the uncoated (0 μm) state, even a 2 μm coating alone raised this rate to over 70%. At thicknesses of 8 μm and 10 μm, the system has nearly reached a 100% (full efficiency) rejection rate. The coating layer seals defects and large pores in the membrane, allowing the dissolution-diffusion mechanism to become dominant. This permits only water molecules to pass through while blocking salt ions. The critical range in the graph is between 4 μm and 6 μm. This is because beyond 8 μm, the salt rejection rate has already reached saturation (very close to 100%), yet the flux continues to decrease. Therefore, it can be concluded that this thickness is the most suitable.

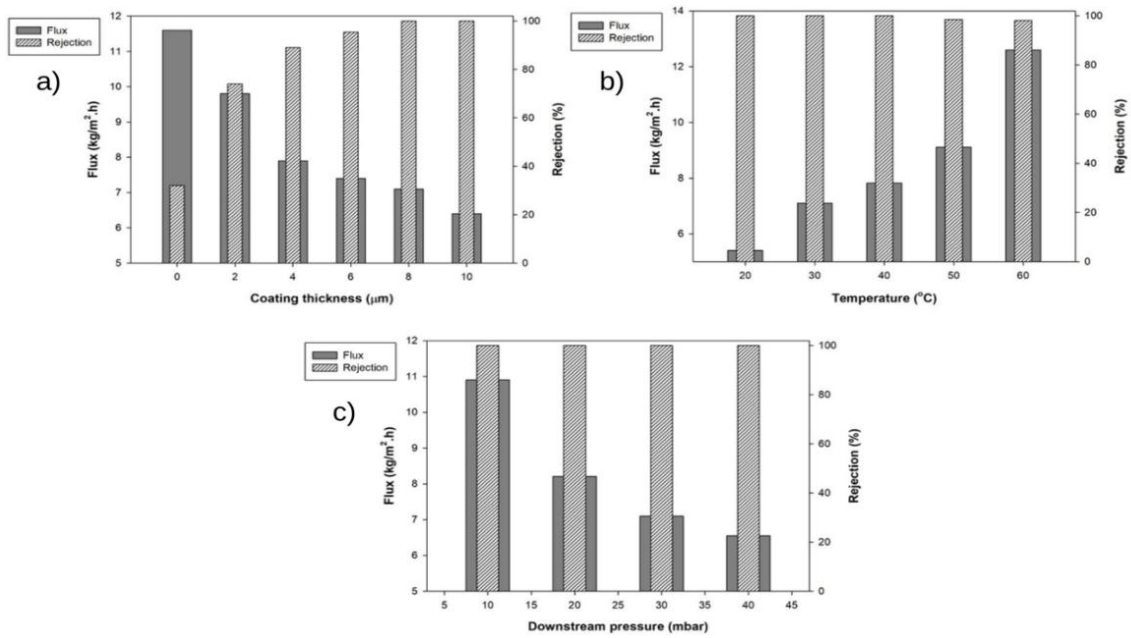

Figure 4. Effect of operating parameters on VMD performance: coating thickness *vs*. permeate flux and salt rejection (a), feed temperature *vs*. permeate flux and salt rejection (b) and downstream pressure *vs*. permeate flux and salt rejection (c).

The effect of temperature is one of the most dynamic parameters in membrane processes, both from a thermodynamic and kinetic perspective. When the temperature rose from 20°C to 60°C, the flux value increased from 5.4 to 12.6 kg/m²h, representing an increase of over 130% (Figure 4b). This is an expected phenomenon and has two main causes: as water temperature increases, its viscosity decreases. The thermal motion of the polymer chains in the membrane increases with temperature. This creates temporary free volumes within the polymer, thereby increasing the diffusion rate of water. This relationship is typically explained by the Arrhenius equation: an arithmetic increase in temperature leads to a logarithmic/exponential increase in flux.

As temperature increases, the kinetic energy of water molecules increases directly. This affects the transport within the membrane as follows:

- An increase in temperature enhances the thermal vibrations of water molecules, causing them to "bounce" more rapidly through the voids in the membrane's polymeric matrix.
- According to the Stokes-Einstein equation, the diffusion coefficient is directly proportional to temperature and inversely proportional to viscosity. Thus, as temperature rises, the diffusion coefficient increases, which is the primary cause of the flow increase.

The rise in temperature triggers the primary driving force—namely, the vapor pressure difference. According to Antoine's equation, as the temperature on the feed side increases, the vapor pressure of the liquid exponentially increases. The partial pressure difference between the feed side (hot) and the product side (vacuum) of the membrane sharply increases. The flow rate is directly proportional to this pressure difference.

Figure 4b shows that salt rejection performance remains remarkably stable at 99.99% up to 40°C, but drops slightly to 98.1% at 50°C and 60°C. The structural integrity of the membrane is very well preserved in the 20–40°C range. The membrane successfully prevented the passage of salt ions despite the increase in flux. At 50–60°C, the slight decrease in salt rejection is due to the accelerated diffusion of salt ions. Like water molecules, the kinetic energy of salt ions also increases. Additionally, excessive relaxation of polymer chains at high temperatures may create microscopic pathways through which salt ions can pass to widen.

In the graph in Figure 4c, we see that the flux value decreases as the feed pressure increases from 10 mbar to 40 mbar (from 10.90 to 6.55 kg/m²·h). In pervaporation, the driving force is the difference in partial vapor pressure on either side of the membrane. The lower the pressure on the feed side, the stronger is the force drawing water molecules to the other side. When the feed pressure increases from 10 to 40 mbar, the vacuum force decreases. This increases the water vapor concentration on the product side of the membrane, thereby weakening the driving force. As a result, the flux decreases.

The most striking performance metric regarding pressure is that salt rejection remains constant at 99.99%, regardless of the vacuum pressure. This is due to the fact that salt is non-volatile. In pervaporation and membrane distillation, as water passes through the membrane and crosses to the other side in the vapor phase, salt ions remain in the liquid phase and cannot evaporate. As long as changes in vacuum pressure do not disrupt the pore structure of the membrane's selective layer, salt permeation theoretically remains close to zero. The highest flow rate was achieved at 10 mbar. This is the most efficient point from an industrial perspective because the highest product yield per unit time was obtained at this pressure. The lowest flow rate was achieved at 40 mbar. While this can reduce the energy consumption of the vacuum pump, it significantly lowers production capacity.

The graph in Figure 5 shows that the flux value starts at approximately 7.1 kg/m²·h in the first experiment and decreases at a slight downward slope to approximately 6.7 kg/m²·h by the end of the 10th experiment. This decrease of approximately 5–6% is considered quite acceptable in the membrane literature. Salt ions accumulating on the membrane surface over time may slightly impede water passage. Under continuous pressure or vacuum, the polymer chains may adopt a tighter packing arrangement, which could slightly reduce the flux. If the feed water contains trace amounts of organic matter, these may slightly block the pores/free volumes in the active region.

The most impressive aspect here is that the salt rejection curve remains at the 100% (or 99.99%) line. The fact that selectivity remained completely intact over 10 cycles demonstrates that the active layer adheres very well to the substrate and does not experience mechanical issues such as peeling, cracking, or swelling during operation. This stability is also a strong indication that the membrane can return to its original performance after cleaning cycles.

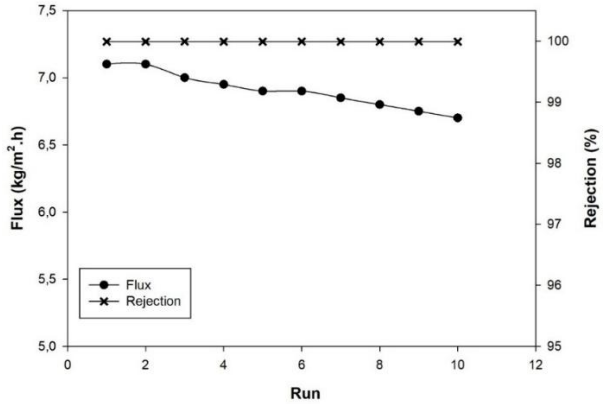

Figure 5. Evaluation of the membrane's reusability performance based on flux and rejection efficiency

CONCLUSIONS

This study has demonstrated that PVDF polymer recycled from waste membranes can be converted into high-performance desalination membranes by the electrospinning technique. Characterization studies confirmed that the PVA coating was successfully integrated into the membrane surface and that as the coating thickness increased, the surface acquired a more hydrophilic structure (with the contact angle decreasing from 76° to 44°). In desalination tests, it was observed that an increase in temperature raised the flux value by over 130% in accordance with the Arrhenius equation, while vacuum pressure directly affected the filtration rate by triggering the driving force. In particular, achieving a salt rejection rate of 99.99% at a coating thickness of 8 µm and above demonstrates the commercial potential of the domestically produced membrane. The fact that selectivity was maintained and flux loss remained at an acceptable level of 6% throughout 10 cycles of stability testing supports the membrane's long-term usability in industrial processes. In conclusion, this project has contributed to both the prevention of environmental pollution through the recovery of waste polymers and the development of a sustainable desalination technology with high economic value.

Abbreviations:
DSC: Differential scanning calorimeter
FTIR: Fourier transform infrared spectroscopy
VMD: Vacuum membrane distillation
PVA: Polyvinyl alcohol
PVDF: Polyvinylidene fluoride

Declaration of competing interest: *The authors affirm the absence of any known competing financial interests or personal relationships that may have influenced the work presented in this paper.*

Author contribution statement: *Ayşenur Katırcı: investigation, writing - original draft, carried out the experiment. Filiz Uğur Nigiz: investigation, visualization, conceptualization, methodology, writing - original draft, methodology, data curation, validation, writing - review & editing.*

Acknowledgements: *This study was supported by Çanakkale Onsekiz Mart University Scientific Research Projects Coordination Unit. (Project No: FBA-2025-4996).*

Funding: *This research project was funded by Çanakkale Onsekiz Mart University Scientific Research Projects Coordination Unit with Project Code of FBA-2025-4996.*

Data availability: *The datasets used and/or analyzed during the current study are available from the corresponding author on reasonable request.*

Ethics approval and consent to participate: *Not applicable.*

Consent for publication: *Consent for publication is not required, as this work does not include previously published data or involve any third party.*

REFERENCES

1. J. Ravi, M. H. D. Othman, T. Matsuura, M. Ro'il Bilad, T. H. El-badawy, F. Aziz, A. F. Ismail, M. A. Rahman, J. Jaafar, *Desalination*, **490**, 114530 (2020).
2. C.-K. Chiam, R. Sarbatly, *Chem. Eng. Process.*, **74**, 27 (2013).
3. P. Saxena, P. Shukla, *Adv. Compos. Hybrid Mater.*, **4**, 8 (2021).
4. F. Liu, N. A. Hashim, Y. Liu, M. M. Abed, I. K. Li, *J. Membr. Sci.*, **375**, 1 (2011).
5. S. F. Anis, R. Hashaikeh, N. Hilal, *J. Water Process. Eng.*, **32**, 100941 (2019).
6. J. A. Kharraz, A. K. An, *J. Membr. Sci.*, **595**, 117596 (2020).
7. C. Liu, L. Wu, C. Zhang, W. Chen, S. Luo, *Appl. Surf. Sci.*, **457**, 695 (2018).
8. A. G. Veiga, G. D. A. Frederico, L. D. N. Batista, M. L. M. Rocco, M. F. Costa, *Mater. Today Commun.*, **25**, 101269 (2020).
9. E. Eliuz, *Eurasian J. For. Sci.*, **8**, 295 (2020).
10. D. M. Mamand, B. Y. Ahmed, D. S. Muhammad, W. O. Karim, S. B. Aziz, B. A. Al-Asbahi, A. A. A. Ahmed, J. Hassan, *J. Sci. Adv. Mater. Devices*, **10**, 100955 (2025).
11. B. S. Chee, The development of novel PVA hydrogel for biomedical and drug delivery applications, PhD Thesis/Report (2021).
12. H. L. Abd El-Mohdy, S. Ghanem, *J. Polym. Res.*, **16**, 1 (2009).

Bulgarian Chemical Communications, Volume 58, Issue 3 (pp. 247-253) 2026 *DOI: 10.34049/bcc.58.3.D002*

Freeze drying of manila clam: drying kinetics and mathematical modelling

Y. Cagliyan, Z. O. Ozyalcin, A. S. Kipcak*

Faculty of Chemistry and Metallurgy, Department of Chemical Engineering, Yildiz Technical University, Istanbul, Turkiye

Accepted: July 28, 2026

This study investigates the freeze-drying kinetics and mathematical modeling of Manila clam (*Ruditapes philippinarum*), a highly valued seafood species. While freeze-drying is a preservation method that maintains the physical and chemical integrity of food by removing water through sublimation, its high operational costs due to long processing times necessitate the use of pretreatments. The objective of this research was to examine the impact of various pretreatment parameters, including ultrasonication, blanching, and saltwater immersion, on drying rates and moisture diffusivity to optimize the dehydration process. Samples were subjected to ten different pretreatment conditions: ultrasonication (1 and 5 min), blanching (1 and 5 min), blanching in 10% and 20% saltwater (1 min), and immersion in saltwater (5 and 10 min at 10% and 20% concentrations). The drying data were fitted against 13 mathematical models to determine the most accurate predictive framework for each method. The experimental results revealed that the drying processes were completed within 240 to 480 min, all samples exhibiting a dominant falling rate period. Effective moisture diffusivity (D_{eff}) values were found to range between 3.47 and 6.89 × 10^{-10} m^2/s. Notably, blanching emerged as the most effective pretreatment for minimizing drying time and achieving the highest D_{eff} values. In the saltwater immersion groups, D_{eff} increased proportionally with both salt concentration and immersion time. Statistical analysis indicated that Verma and Aghbashlo *et al*. models were the most fitting to all samples.

Keywords: Blanching; lyophilization; modelling; seafood; shell

INTRODUCTION

Drying is simply based on the removal of water from the product and is the most common method used to preserve food products for a long time. While traditional drying methods often struggle to achieve high quality end products, modern methods include techniques developed to improve the quality of the end product and reduce the energy consumed [1]. In the freeze-drying process, water in the product is first frozen and subsequently removed by sublimation under reduced pressure. This low-temperature dehydration method enables long-term storage while preserving the original physical, chemical, and biological properties of the product. Freeze-drying is widely used as an effective preservation technique for high-moisture foods such as fruits, vegetables, and meat products, minimizing quality deterioration and nutrient losses [2]. Although it is an effective method for product preservation, freeze drying is a costly method due to long drying times. Pre-treatments are frequently used to reduce drying times and consequently the energy consumed. Drying pre-treatments are processes carried out before the product enters the dryer to reduce the dryer load, drying time or temperature and to maintain quality parameters [3]. Among these, the most commonly used are ultrasonic and blanching pretreatments. Ultrasonic pretreatment can be used to change the tissue micro-structure of foods to reduce water content or accelerate the drying process. Blanching pretreatment can be called thermal pre-drying. Blanching reduces microorganism load by inactivating common enzymes that negatively affect product quality [4-6].

Seafood, with its high-quality protein content, constitutes a large food category with increasing consumption rates alongside traditional meat products. According to Food and Agriculture Organization (FAO) statistics, approximately 20 million tons of mollusks were consumed as food in 2020 [7]. The Manila clam (*Tapes philippinarum*), a commercially important bivalve species belonging to the family *Veneridae*, is widely distributed in the Adriatic Sea, Mediterranean Sea, Black Sea, North Sea, and Caspian Sea. Due to its high nutritional value and sensory quality, it is widely consumed and considered a valuable seafood product [8].

Freeze-drying is a method widely used for many meat and agricultural products. As the popularity and consumption of seafood increase, the variety of freeze-dried seafood products is also growing. Whilst there are studies on commonly consumed products such as sea cucumber [9], squid [10], shrimps [11, 12], mussels [10, 13], and salmon [14], research into the freeze-drying of Manila clams remains limited. This study aims to examine the

* To whom all correspondence should be sent:
E-mail: *skipcak@yildiz.edu.tr*

© 2026 Bulgarian Academy of Sciences, Union of Chemists in Bulgaria

drying kinetics of freeze-dried Manila clams using various pretreatments. To enhance drying performance, clams underwent ten different pretreatment parameters, including ultrasonication for 1 and 5 min, blanching for 1 and 5 min, blanching in 10% and 20% saltwater for 1 min, 10% and 20% saltwater immersions for 5 min, and 10 min. The collected data were analyzed by comparing them with control samples. Furthermore, the compatibility of the data with 13 mathematical models was tested, and the models exhibiting the highest compatibility were determined.

MATERIALS AND METHODS:

The Manila clams used in this study originated from the Aegean Sea and were purchased frozen from a local market in Istanbul, Turkiye, in May 2022. They were stored in a Flavel FLV 1090 (Flavel, Turkiye) deep freezer at -20 C until the start of the experiments. Clams were cleaned by removing the shells and weighed at an average weight of 7.0 ± 0.5 g using a Radwag AS 220.R2 digital balance with an accuracy of 0.0001 g (Radwag, Radom, Poland) at each drying step. Then, the moisture content determination before drying treatments was carried out at 105°C for 3 h using a KH-45 hot air-drying oven (Kenton, Guangzhou, China). Ultrasonic pretreatment was completed with the Isolab water bath with 1°C sensitivity and 120 W ultrasonic power (Isolab, Germany). Freeze drying was carried out in a Labart LFD-10N model freeze dryer (ART Laborteknik, Istanbul, Turkiye).

Drying experiments

Frozen clams were weighed at 7.0 ± 0.5 g for 11 sets of experiments. Experimental sets included control, ultrasonication for 1 min (1 min US) and 5 min (5 min US); blanching for 1 min (1 min BWB) and 5 min (5 min BWB); blanching for 1 min with 10% saltwater (1 min BWB w/10%) and 1 min with 20% saltwater (1 min BWB w/20%); 5 min immersion in 10% saltwater (5 min SI w/10%) and 20% saltwater (5 min SI w/20%); 10 min immersion in 10% saltwater (10 min SI w/10%) and 20% saltwater (10 min SI w/20%). During freeze drying, the vacuum of the dryer was turned off every 60 minutes and the samples were weighed in less than 2 minutes and the results were recorded. Then, the products were placed back in the dryer and the vacuum was turned on. Samples were dried to 5% moisture content and packed under vacuum.

Mathematical modelling

Moisture content (M) and moisture ratio (MR) were calculated using equations (1, 2) [15]:

$$M = {m_w}/{m_d} \quad (1)$$

where M, m_w, and m_d are the moisture content (kg water / kg dry matter), water content (g) and dry matter content (g), respectively.

$$MR = \frac{M_t - M_e}{M_i - M_e} \quad (2)$$

where M_t is the moisture content at a specific time, M_e is the moisture content at equilibrium, and M_i is the moisture content of the material initially. Mathematical models were tested for compatibility with clam MR and time data. The 13 published mathematical models examined for compatibility are listed in Table 1. In these models, a, b, and c are drying exponent coefficients defined for each equation separately; k, k_1, and k_2 are drying coefficients defined for each equation separately, and t stands for time in min.

Table 1. Drying models and equations

Model	Equation	Ref.
Aghbashlo *et al.*	$MR = \exp(-k_1 t / (1 + k_2 t))$	[16]
Alibas	$MR = a.\exp((-kt^n) + bt) + g$	[17]
Henderson & Pabis	$MR = a.\exp(-kt)$	[18]
Jena & Das	$MR = a.\exp(-kt + b\sqrt{t}) + c$	[19]
Lewis	$MR = \exp(-kt)$	[20]
Logarithmic	$MR = a.\exp(-kt) + c$	[21]
Midilli *et al.*	$MR = a.\exp(-kt^n) + bt$	[22]
Page	$MR = \exp(-kt^n)$	[23]
Parabolic	$MR = a + bt + c\,t^2$	[24]
Verma *et al.*	$MR = a.\exp(-kt) + (1 - a).\exp(-gt)$	[25]
Wang & Singh	$MR = \exp(-(t/b)^a)$	[26]
Modified page	$MR = a.\exp(-(kt^n))$	[27]
Two-term	$MR = a.\exp(k_0 t) + b.\exp(k_1 t)$	[28]

To find the best suitable model coefficient of determination (R^2), root-mean-square error (RMSE), and reduced chi-squared (χ^2) statistic are used. Required parameters for given models are estimated using the non-linear regression method with Statistica (Statistica, 2016). Equations for these methods are given below in equations (3-5) [29]:

$$R^2 = 1 - \frac{\sum_{i=1}^{n}\left(MR_{exp,i} - MR_{pre,i}\right)^2}{\sum_{i=1}^{n}\left(MR_{exp,i} - \left(\frac{1}{n}\right)MR_{exp,i}\right)^2} \quad (3)$$

$$RMSE = \left(\frac{1}{n}\sum_{i=1}^{n}\left(MR_{exp,i} - MR_{pre,i}\right)^2\right)^{1/2} \quad (4)$$

$$\chi^2 = \frac{\sum_{i=1}^{n}\left(MR_{exp,i} - MR_{pre,i}\right)^2}{n - z} \quad (5)$$

where MR_{exp} is the experimental moisture ratio values, MR_{pre} is the predicted moisture ratio values, n is the total number of the experiments, and z is the number of the constants in the given model. In the

selection of best fitted model, R^2 values are expected to be closer to 1. On the other hand, RMSE and χ^2 values are expected to be closer to 0 [29].

Effective moisture diffusivity determination

Moisture removal during food drying is generally governed by diffusion mechanisms, particularly during the falling-rate period. Several mathematical approaches have been applied to express Fick's second law for this stage of drying, as presented in equation (6) [29, 30];

$$\frac{\partial M}{\partial t} = \nabla\left[D_{eff}(\nabla M)\right] \quad (6)$$

Fick's second law for unsteady-state diffusion is commonly used to determine the moisture ratio. By assuming that moisture migration occurs only through diffusion, the effective diffusion coefficient remains constant, and volume shrinkage is negligible, the analytical solution for unsteady diffusion can be expressed as equation (7):

$$MR = \frac{8}{\pi^2}\sum_{n=1}^{\infty}\frac{1}{(2n+1)^2}e^{\left(-\frac{(2n+1)^2\pi^2 D_{eff}t}{4L^2}\right)} \quad (7)$$

In those equations D_{eff} represents effective moisture diffusivity (m^2/s), t represents time (s), L represents the half-thickness of samples (m) and n represents a positive integer. This complex equation can be simplified for longer drying periods without much affecting the results, thus accuracy and this equation can be given as shown in equation (8):

$$MR = \frac{8}{\pi^2}e^{\left(-\frac{\pi^2 D_{eff}t}{4L^2}\right)} \quad (8)$$

When equation (8) is rearranged by taking the logarithm, then it can be expressed as a linear function. This linear function is given as shown in equation (9):

$$ln(MR) = ln\left(\frac{8}{\pi^2}\right) - \left(-\frac{\pi^2 D_{eff}t}{4L^2}\right) \quad (9)$$

From the slope of ln(MR) *versus* t, D_{eff} can easily be calculated.

RESULTS AND DISCUSSION

The initial moisture content of the clam samples varied noticeably with the applied pre-treatment, indicating that these processes already influence water distribution before freeze-drying. As shown in Table 2, which lists the moisture content and drying times for all samples, the control sample exhibited an initial moisture content of 84.42% (5.4180 kg water/kg dry matter). Among the treatments, US application slightly increased the initial moisture content, reaching 85.53% for 1 min US and 86.27% for 5 min US. This increase may be attributed to structural disruption caused by cavitation, which enhances water retention within the tissue matrix.

In contrast, BWB significantly reduced the initial moisture content. The values decreased to 75.49% (3.0794 kg/kg dry matter) for 1 min BWB and further to 69.92% (2.3242 kg/kg dry matter) for 5 min BWB. This reduction is likely due to protein denaturation and cell structure collapse, facilitating water loss during the pretreatment stage. When salt was incorporated into blanching (10% and 20%), the initial moisture content remained lower than the control but slightly higher than plain BWB, suggesting that osmotic effects partially limited water loss. SI treatments showed intermediate behavior. Initial moisture contents ranged from 76.69% to 82.94%, depending on salt concentration and immersion time. Higher salt concentrations and longer immersion times generally resulted in lower moisture contents, indicating osmotic dehydration effects.

Table 2. Moisture content and drying time of the clam samples

Sample	Initial moisture		Drying time	Final moisture
	% (wet basis)	kg water/ kg dry matter	min	kg water/ kg dry matter
Control	84.42	5.4180	420	0.2926
1 min US	85.53	5.9114	480	0.2816
5 min US	86.27	6.2821	480	0.4155
1 min BWB	75.49	3.0794	300	0.1291
5 min BWB	69.92	2.3242	240	0.1526
1 min BWB w/10%	74.53	2.9264	240	0.2134
1 min BWB w/20%	72.93	2.6943	240	0.1936
5 min SI w/10%	82.94	4.8625	480	0.2253
5 min SI w/20%	80.91	4.2375	300	0.2108
10 min SI w/10%	82.30	4.6492	360	0.1604
10 min SI w/20%	76.69	3.2895	300	0.1603

Regarding drying time, pre-treatments had a pronounced impact on the efficiency of the freeze-drying process. The control sample required 420 minutes to reach the target moisture level. Ultrasonic treatments resulted in the longest drying times (480 min for both 1 min and 5 min US), despite their relatively high initial moisture contents. This suggests that although ultrasonication disrupts tissue

structure, it may also lead to water being more strongly retained within the matrix, thereby slowing down sublimation during freeze-drying. In contrast, blanching treatments significantly reduced drying time. The 1 min BWB sample required 300 minutes, while 5 min BWB further decreased the drying time to 240 minutes, representing the shortest duration among all samples. This improvement can be attributed to thermal damage to cellular structures, which enhances moisture diffusivity and facilitates ice sublimation. Blanching combined with salt (BWB with 10% and 20%) maintained similarly short drying times (240 min), indicating that the addition of salt does not hinder the drying rate and may even support moisture removal through osmotic effects prior to freeze-drying.

SI treatments showed variable effects on drying time depending on process conditions. While 5 min SI with 10% salt resulted in a prolonged drying time (480 min), increasing salt concentration or immersion time reduced the drying duration (300–360 minutes). In particular, 10 min SI treatments demonstrated improved drying efficiency compared to shorter immersion, likely due to enhanced osmotic dehydration and partial removal of free water before drying. All these changes in moisture content observed during drying are also displayed in the graphs showing the change in moisture content over time (Figure 1) and the change in drying rate as a function of moisture content (Figure 2).

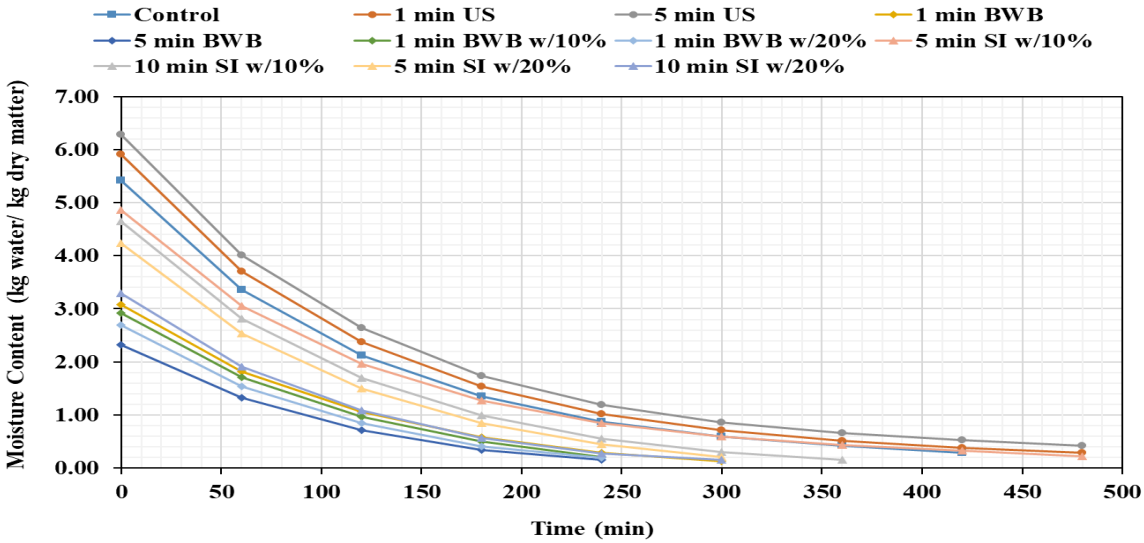

Figure 1. Change in moisture content with time

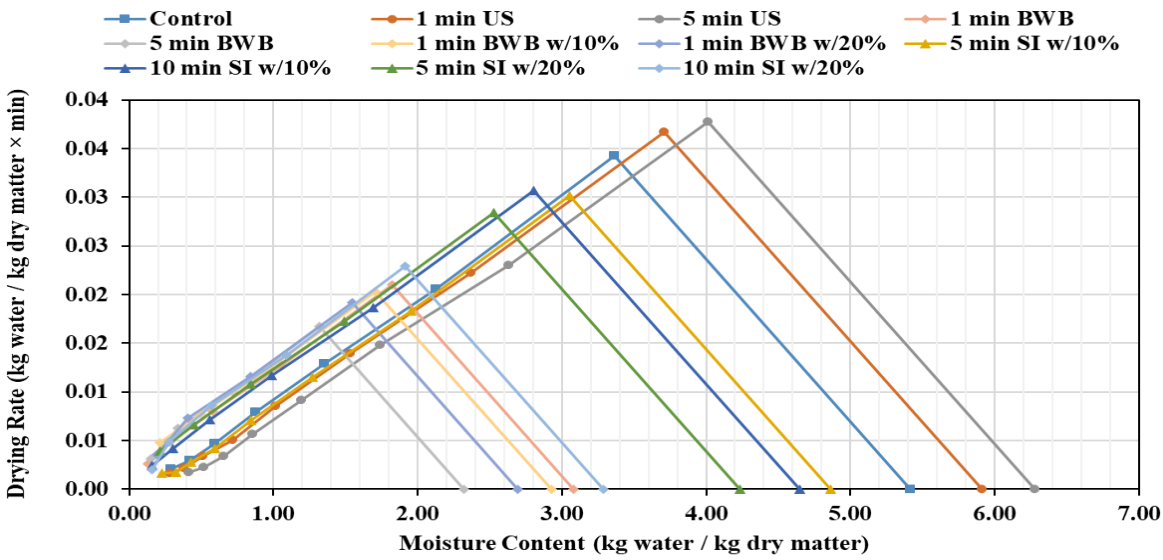

Figure 2. Change in drying rate with moisture content

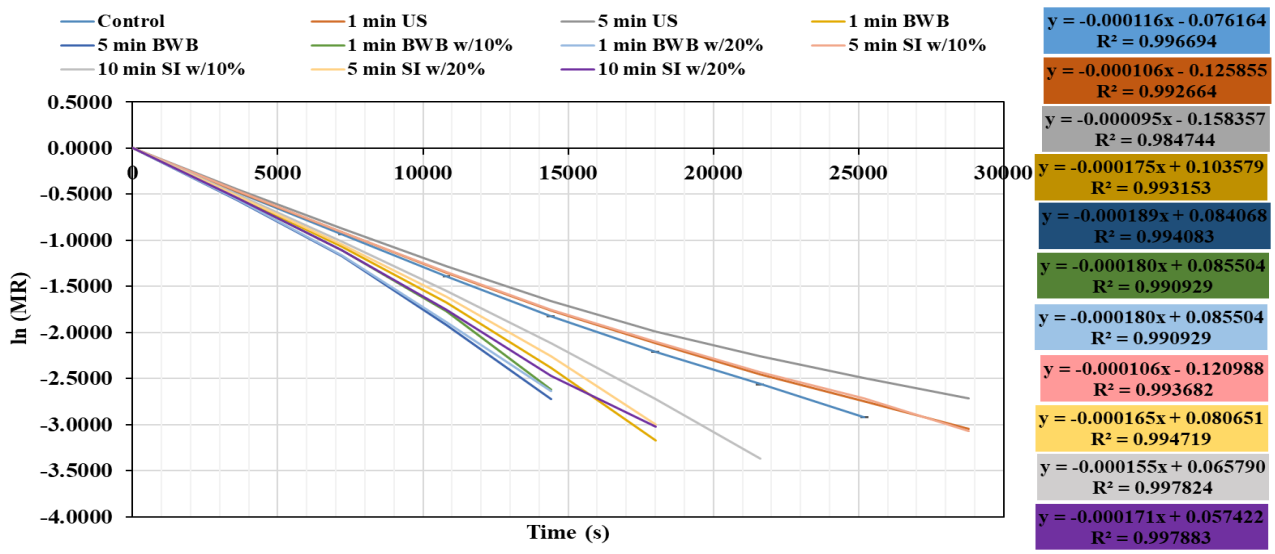

Figure 3. ln(MR) change over drying time

Regarding the final moisture content after freeze-drying, all pretreated samples exhibited lower or comparable values relative to the control (0.2926 kg water/kg dry matter), except for the 5 min US sample, which showed a higher final moisture (0.4155 kg/kg dry matter). This suggests that prolonged ultrasonication may hinder effective moisture removal, possibly due to structural compaction or reabsorption effects. Blanching treatments resulted in the lowest final moisture contents, particularly 1 min BWB (0.1291 kg/kg dry matter), indicating enhanced drying efficiency. Similarly, salt-assisted treatments, especially longer immersion times (e.g., 10 min SI), also achieved low final moisture levels (~0.1603–0.1604 kg/kg dry matter), demonstrating the effectiveness of osmotic dehydration in facilitating freeze-drying.

Effective moisture diffusivities

The graph of ln(MR) *versus* drying time, plotted using MR data calculated based on Fick's second law, is shown in Figure 3. The D_{eff} values of the samples were calculated from the slope of this graph, in accordance with equation 9. D_{eff} values clearly demonstrate the influence of pre-treatments on mass transfer during freeze-drying. The control sample exhibited the lowest D_{eff} value (3.47×10^{-10} m^2/s), indicating limited internal moisture movement in untreated clam tissues. All pre-treatment methods increased D_{eff} to varying extents, confirming their role in enhancing moisture transport. US treatment resulted in a moderate increase in D_{eff}, reaching 3.87×10^{-10} m^2/s for 1 min and 4.23×10^{-10} m^2/s for 5 min. This improvement can be attributed to cavitation-induced microchannel formation, which facilitates moisture diffusion. However, the relatively small increase compared to other treatments suggests that ultrasound alone provides limited structural modification. BWB showed the most significant enhancement in effective diffusivity. D_{eff} values increased to 6.38×10^{-10} m^2/s (1 min) and 6.89×10^{-10} m^2/s (5 min), representing a nearly twofold increase compared to the control. This substantial improvement is likely due to protein denaturation and cell membrane disruption, which reduce internal resistance to moisture movement. The addition of salt during blanching (10% and 20%) maintained similarly high D_{eff} values (6.57×10^{-10} and 6.68×10^{-10} m^2/s), indicating that osmotic effects complement thermal damage and further promote water mobility. SI treatments exhibited time and concentration-dependent behavior. While 5 min SI with 10% salt showed only a slight increase (3.87×10^{-10} m^2/s), extending the immersion time to 10 min significantly improved D_{eff} (5.65×10^{-10} m^2/s). Similarly, higher salt concentration (20%) resulted in greater diffusivity values (6.02×10^{-10} and 6.24×10^{-10} m^2/s for 5 and 10 min, respectively). These results indicate that osmotic dehydration plays a key role in enhancing moisture diffusion, particularly at higher concentrations and longer treatment times.

Mathematical modeling results

Drying values obtained during freeze drying for all samples were modeled according to commonly used drying mathematical models. Table 3 presents the coefficients and constants for the four models—Aghbashlo *et al.*, Page, Verma, and Two-term—which demonstrated the highest fit for all samples. Upon examination of the table, it is observed that the Verma and Aghbashlo *et al.* model exhibits the highest fit among all models, respectively.

In previous studies involving shrimp [11] and squid [30] freeze-dried following similar pre-treatments, the Verma and Aghbashlo *et al*. models were also found to be among the models showing

high fit. This suggests that the Verma and Aghbashlo *et al*. models can be used to provide consistent predictions for the freeze-drying of seafood following ultrasonication, blanching, or saltwater immersion pre-treatments.

CONCLUSION

This study focused on investigating the effects of different pre-treatments on the freeze-drying kinetics of Manila clams and evaluated the suitability of several mathematical models for describing the drying behavior. The results showed that pre-treatment application significantly influenced the initial moisture content, drying time, final moisture content, and effective moisture diffusivity of the clam samples. Compared with the untreated control, blanching-based treatments were the most effective in improving drying performance. In particular, 5 min blanching resulted in the shortest drying time, while blanching with saltwater also maintained high drying efficiency. These improvements were associated with structural changes caused by thermal treatment, which reduced internal resistance to moisture movement and facilitated sublimation during freeze-drying. Ultrasonic pre-treatment increased the effective moisture diffusivity to some extent; however, it also resulted in longer drying times compared with the control. This indicated that although ultrasonication may modify tissue structure through cavitation effects. Saltwater immersion showed concentration- and time-dependent effects. Longer immersion times and higher salt concentrations generally improved drying efficiency, suggesting that osmotic dehydration contributed to water removal before freeze-drying and enhanced moisture diffusion. The control sample exhibited the lowest diffusivity value, whereas blanching and salt-assisted treatments produced considerably higher values. Among the mathematical models tested, Verma and Aghbashlo *et al.* models provided the best fit for the experimental drying data. Overall, the findings demonstrated that appropriate pre-treatment selection can substantially improve the freeze-drying efficiency of Manila clams by reducing drying time, lowering final moisture content, and enhancing effective moisture diffusivity.

Table 2. Mathematical model parameters and coefficients

Model	Parameter	Control	1 min US	5 min US	1 min BWB	5 min BWB	1 min BWB w/10%	1 min BWB w/20%	5 min SI w/10%	5 min SI w/20%	10 min SI w/10%	10 min SI w/20%
Aghbashlo et al.	k_1	0.008181	0.008119	0.007940	0.008283	0.008808	0.008402	0.008746	0.008099	0.008158	0.008207	0.008663
	k_2	0.000379	0.000520	0.000724	-0.00066	-0.000926	-0.000862	-0.000866	0.000530	-0.000316	-0.000520	-0.000574
	R^2	0.999955	0.999907	0.999732	0.999907	**0.999933**	0.999834	**0.999941**	0.999913	0.999967	0.999911	**0.999887**
	χ^2	0.000006	0.000011	0.000030	0.000015	0.000013	0.000031	0.000011	0.000010	0.000005	0.000014	0.000019
	RMSE	0.002061	0.002909	0.004857	0.003206	0.002772	0.004291	0.002578	0.002809	0.001854	0.003097	0.003538
Page	k	0.010122	0.010984	0.012051								
	n	0.944712	0.922128	0.892688								
	R^2	0.999820	0.999573	0.999005								
	χ^2	0.000023	0.000050	0.000113								
	RMSE	0.004135	0.006245	0.009364								
Verma	a	0.061517	0.081900	0.062816	-0.35365	-1.141420	-0.040304	-1.230980	0.112937	-0.113017	-0.048372	-1.870660
	k	0.001935	0.001922	0.000591	0.003871	0.004990	-0.002064	0.005100	0.002484	0.003345	0.000340	0.005980
	g	0.008409	0.008404	0.008008	0.007306	0.006910	0.008392	0.006860	0.008569	0.007781	0.008080	0.006990
	R^2	**0.999989**	**0.999989**	**0.999981**	**0.999975**	0.999927	**0.999997**	0.999898	**0.999975**	**0.999990**	**0.999992**	0.999815
	χ^2	0.000002	0.000002	0.000003	0.000006	0.000021	0.000001	0.000029	0.000003	0.000002	0.000002	0.000041
	RMSE	0.001006	0.001003	0.001311	0.001668	0.002897	0.000614	0.003386	0.001506	0.001034	0.000919	0.004528
Two-term	a				-136.369	-43.91150	-11.88150	-21.37190	0.113942	225.02400	-202.5990	-31.70450
	k_0				0.013000	0.015100	0.005500	0.006000	0.002499	0.011000	0.012000	0.006500
	b				137.3680	44.91080	12.88070	22.37240	0.886244	-224.0240	203.5980	32.70540
	k_1				0.013000	0.015000	0.005800	0.006100	0.008577	0.011000	0.012000	0.006600
	R^2				0.999713	0.999746	0.999965	0.999902	**0.999975**	0.999925	0.999788	0.999818
	χ^2				0.000095	0.000145	0.000020	0.000056	0.000004	0.000018	0.000069	0.000061
	RMSE				0.005634	0.005391	0.001977	0.003335	0.001505	0.002804	0.004795	0.004494

REFERENCES

1. A. Dagdeviren, B. Acar, A. Alhammadi, K. Roshanaei, T. Coskun, O. Inanc, M. Ozkaymak, *Politek. Derg.*, **26**, 487 (2023).
2. D. Nowak, E. Jakubczyk, *Foods*, **9**, 1488 (2020).
3. D. Dziki, *Processes*, **8**, 1661 (2020).
4. Pandiselvam, A. Y. Aydar, N. Kutlu, R. Aslam, P. Sahni, S. Mitharwal, A. Kothakota, *Ultrason. Sonochem.*, **92**, 106261 (2023).
5. Z. O. O. Genc, A. S. Kipcak, *Aquat. Sci. Eng.*, **38**, 137 (2023).
6. J. C. Ribeiro, J. P. Marques, T. R. Fernandes, M. E. Pintado, S. M. Carvalho, L. M. Cunha, *LWT*, **191**, 115646 (2024).
7. FAO, The State of World Fisheries and Aquaculture Sustainability in Action, Rome (2020).
8. S. Vincenzetti, A. Felici, G. Ciarrocchi, S. Pucciarelli, M. Ricciutelli, A. Ariani, P. Polidori, *Food Chem*, **219**, 223 (2017).
9. S. Mamatov, M. Zhang, A. Jia, X. Liu, C. Liu, *Int. J. Innov. Technol. Explor. Eng.*, **8**, 475 (2019).
10. Z. O. Ozyalcin, E. Gules, D. Uygunoz, F. Bozkurt, O. Sagdic, I. Doymaz, A. S. Kipcak, *Turk. J. Fish. Aquat. Sci.*, **25**, 2 (2024).
11. Z. O. Ozyalcin, A. S. Kipcak, *Bulg. Chem. Commun.*, **57**, 252 (2025).
12. J. G. Ling, X. T. Xuan, N. Yu, Y. Cui, H. T. Shang, X. J. Liao, D. H. Liu, *J. Food Sci.*, **85**, 1167 (2020).
13. N. Alp, Z. O. Ozyalcin and A. S. Kipcak, *Ege J. Fish. Aquat. Sci.*, **42**, 48 (2025).
14. E. Midik, Z. O. Ozyalcin, A. S. Kipcak, *J. Chem. Technol.*, **33**, 136 (2025).
15. Z. O. Ozyalcin, A. S. Kipcak, *Bulg. Chem. Commun.*, **55**, 234 (2023).
16. M. Aghbashlo, M. H. Kianmehr, S. Khani, M. Ghasemi, *Int. Agrophys.*, **23**, 313 (2021).
17. I. Alibas, *J. Biol. Environ. Sci*., **6**, 161 (2012).
18. S. M. Henderson and S. Pabis, *J. Agric. Eng. Res*., **6**, 169 (1961).
19. S. Jena, H. Das, *J. Food Eng.*, **79**, 92 (2007).
20. W. K. Lewis, *J. Ind. Eng. Chem.*, **13**, 427 (1921).
21. I. T. Togrul, D. Pehlivan, *J. Food Eng.*, **58**, 23 (2003).
22. A. Midilli, H. Kucuk, Z. Yapar, *Drying Technol.*, **20**, 1503 (2002).
23. G. E. Page, Factors Influencing the Maximum Rates of Air Drying of Shelled Corn in Thin Layer, M.Sc. Thesis, Purdue University, Lafayette, IN, USA (1949).
24. I. Doymaz, *Food Bioprod. Process.*, **88**, 124 (2010).
25. L. R. Verma, R. A. Bucklin, J. B. Endan, F. T. Wratten, *Trans. ASAE*, **28**, 296 (1985).
26. C. Y. Wang, R. P. Singh, A Single Layer Drying Equation for Rough Rice, ASAE Press, St. Joseph, MI, USA, 1978.
27. D. D. Overhults, G. M. White, M. E. Hamilton, I. J. Ross, *Trans. ASAE*, **16**, 195 (1973).
28. S. M. Henderson, *Trans. ASAE*, **17**, 1167 (1974).
29. Z. O. Ozyalcin, A. S. Kipcak, Z. Tugrul, *J. Aquat. Food Prod. Technol.*, **32**, 384 (2023).
30. Z. O. Ozyalcin, A. S. Kipcak, *Bulg. Chem. Commun.*, **57** (3), 213 (2025).

Bulgarian Chemical Communications, Volume 58, Issue 3 (pp. 254-260) 2026 *DOI: 10.34049/bcc.58.3.D003*

Rehydration characteristics of freeze-dried mussel, shrimp and squid

O. Ercan, Z. O. Ozyalcin, A. S. Kipcak*

Faculty of Chemistry and Metallurgy, Department of Chemical Engineering, Yildiz Technical University, Istanbul, Turkiye

Accepted: July 28, 2026

Seafood is a vital nutrient source, but its high perishability necessitates efficient preservation methods like drying. While traditional drying often impairs quality, freeze-drying preserves the pore structure by removing ice through sublimation, facilitating rapid reabsorption of water. This study aimed to investigate the rehydration behaviour of freeze-dried shrimp, squid and mussels, both with and without ultrasonic (US) pretreatment. In the experiments, pink shrimps, blue mussels, and European squid were freeze-dried under identical conditions (control and 5-min US pre-treated), and their rehydration behaviour was monitored at 25, 40 and 60°C. Using the data obtained, effective moisture diffusion (D_{eff}) was calculated, compatibility with Peleg and Two-term exponential mathematical models was assessed, and colour changes were recorded throughout the experiments. The results demonstrated that rehydration occurred rapidly in the initial stages, with mussels and shrimps reaching maximum rates within 10-min, while squids peaked at 20-min. Across all samples, increasing the rehydration temperature led to a decrease in the final rehydration ratio. Mathematical modeling revealed that the Peleg model provided the most accurate fit for all samples across various temperatures, yielding the highest R^2 and lowest RMSE and χ^2 values. Calculated D_{eff} values ranged from 1.21×10^{-9} to 5.59×10^{-9} m^2/s. Color analysis indicated that US pretreatment generally resulted in higher lightness values for rehydrated squids and shrimps.

Keywords: lyophilization; modelling; seafood; swelling; ultrasonication

INTRODUCTION

Drying is one of the oldest and most widely used preservation methods applied to maintain and improve the quality and shelf life of food products. The process is based on simultaneous heat and mass transfer and requires energy to remove water from the food matrix by converting liquid water into vapor. Since seafood products are highly perishable and may undergo rapid quality deterioration after harvesting, drying is an important processing method for extending their usability and stability. However, the quality of dried foods is strongly affected by the drying method and processing conditions, since moisture removal may cause structural, physical, and visual changes in the product [1, 2]. Among different drying techniques, freeze-drying is regarded as a high-quality drying method because the material is first frozen and then water is removed by sublimation under low pressure. This process generally causes limited structural damage and helps preserve the original shape and structure of the material [3, 4]. Freeze-drying consists of freezing, primary drying by sublimation, and secondary drying by desorption, and the freezing temperature and ice morphology can influence mass transfer during the process [1]. Because ice crystals leave pores after sublimation, freeze-drying typically creates a porous microstructure with interconnected networks. This porous structure can support water absorption and transport during rehydration, which may result in shorter rehydration times and higher rehydration capacities compared with products dried by other methods [4].

Rehydration is a critical quality-related step for dried foods because freeze-dried products are commonly rehydrated before consumption or use in food formulations. During rehydration, water absorption, wetting of the dry matrix, penetration of water into pores, and solute leaching can occur simultaneously [3, 5]. The rehydration ability of a dried product is closely related to the structural changes occurring during drying, since microstructural damage can affect the ability of the product to regain water [4]. In freeze-dried materials, water can rapidly fill the pores of the dried structure during the initial stage of rehydration through capillary effects, followed by a slower increase until equilibrium is reached [3].

Freeze-drying and rehydration have been investigated in several food systems. Lopez-Quiroga *et al*. (2020) studied the drying and rehydration kinetics of freeze-dried tomatoes and highlighted the role of porous microstructure in water absorption [4]. Zotarelli *et al*. (2022) compared mango powders produced by cast-tape drying, freeze-drying, and spray drying, and reported that drying method influenced wetting time, solubility, color, rheology, and microstructure of reconstituted products [5]. Qiu *et al*. (2022) investigated freeze-dried and hot-air

* To whom all correspondence should be sent:
E-mail: *skipcak@yildiz.edu.tr*

© 2026 Bulgarian Academy of Sciences, Union of Chemists in Bulgaria

dried shiitake mushrooms from the perspective of pores and cell wall fibrous material and showed that freeze-drying affected rehydration characteristics through structural changes caused by ice crystal formation [6]. Fauster *et al*. (2020) reported that pretreatment affected shrinkage, rehydration capacity, and texture of freeze-dried plant materials [1]. In seafood, drying studies have been reported for molluscs, crustaceans, and fish, including sea cucumber, shrimps, mussels, octopus, calamari, and salmon [2, 7-12]. But only a few of these studies have examined rehydration behavior. The aim of this study was to investigate the rehydration behavior of freeze-dried shrimp, squid, and mussel samples produced with and without 5-min ultrasonic pretreatment. The freeze-dried samples were rehydrated in deionized water at 25, 40, and 60 °C. Effective diffusivity values were calculated to evaluate water movement during rehydration, and color parameters were analyzed before and after rehydration to determine the visual quality changes caused by the process. The study was designed to compare the effects of sample type, ultrasonic pretreatment, and rehydration temperature on the rehydration performance and color characteristics of freeze-dried seafood products.

MATERIALS AND METHODS:

Drying experiments

Shrimp, squid, and mussel were purchased from a fish market in Istanbul, Turkiye, in October 2021 and kept in a 1050T model refrigerator (Arcelik, Eskisehir, Turkiye) at 4 °C until the experiments. Samples were weighed using a Radwag AS 220.R2 digital balance with an accuracy of 0.0001 g (Radwag, Radom, Poland) and divided into two groups: control group and ultrasonic (US) pretreatment group. For the US pretreatment, the samples were placed individually into beakers containing deionized water at a 1:10 (w:v) ratio and subjected to pretreatment for 5 min using an Isolab water bath with 1°C sensitivity and 120 W ultrasonic power (Isolab, Germany). After pretreatment, excess water on the sample surfaces was gently dried. Immediately the samples were placed into a Labart LFD-10N freeze dryer (ART Laborteknik, Istanbul, Turkiye) and dried until the final moisture content fell below 5%. Following freeze-drying, the samples were subjected to color analysis using a PCE-CSM 1 colorimeter (PCE Instruments UK Ltd., Southampton, Hampshire, United Kingdom). The dried samples were stored in a desiccator until rehydration experiments.

Rehydration experiments

Rehydration procedures were carried out without stirring on an MI0102003 magnetic stirrer (Four E's, Beltsville, USA) with a heating function, in beakers containing deionized water supplied by Liston A1104 (Liston, LLC, Russia) at a ratio of 1:100 (w:v) at 25, 40, and 60 °C. The samples were divided into 1.5 g batches; accordingly, six parallel systems were set up for each of the shrimp, squid and mussel samples, comprising a control and a US-pretreated group. Temperature monitoring was carried out before and during the experiments. Shrimps and mussels were weighed at 10-min intervals, and squid at 20-min intervals, until the weights stabilized. During the weighing process, the samples were carefully removed from the water, excess water was gently drained off, and the weights were recorded.

Rehydration curves

The rehydration process can be expressed as the reabsorption of the lost water by a substance that has lost the water in its structure as a result of drying. This process occurs as a result of mass transfer. Rehydration content and rehydration rate are important properties in the rehydration process of dried substance. Equation (1) is used to calculate the rehydration content R_c (g/g dry weight).

$$R_c = \frac{w_r - w_d}{w_d} \quad (1)$$

where w_r is weight of the rehydrated sample at time t, and w_d is the weight of the original dried sample [13]. Equation 2 is used to calculate the rehydration rate RR. It is calculated based on the change in rehydration content in the sample per unit time.

$$RR = \frac{R_{c(\Delta t+t)} - R_{c(t)}}{\Delta t} \quad (2)$$

where $R_{c(t)}$ is the rehydration content at any time (g/g dry weight) and $R_{c(t+\Delta t)}$ represents the dry content-based rehydration content at a time "t + Δt" [13].

Effective diffusivity coefficient

Rehydration kinetics occur by the diffusion of water from the sample surface towards its center. It can be assumed that the rehydration kinetics take place by uniform diffusion at a fixed matrix size and a fixed diffusivity value. For this reason, the concentration gradient of water is among the factors affecting mass transfer by pure diffusion [14].

For drying agricultural products in a falling rate period, Fick's second law of diffusion equation, represented as a mass-diffusion equation the equation (3) expresses the Fick's second law of unsteady state diffusion [15].

$$\frac{\partial M}{\partial t} = \nabla\left[D_{eff}(\nabla M)\right] \quad (3)$$

Fick's second law is used to propose mathematical models for the rehydration process [15]. Equation (3) can be used to determine the moisture ratio in equation (4).

$$MR = \frac{8}{\pi^2}\sum_{n=0}^{\infty}\frac{1}{(2n+1)^2}\exp\left(-\frac{(2n+1)^2\pi^2 D_{eff}}{4L^2}t\right) \quad (4)$$

where D_{eff} is the effective moisture diffusivity (m^2/s), L is the half of the sample's thickness (m) and t drying time (s), n is positive integer. For long drying periods, the above equation can be simplified to equation (5):

$$MR = \frac{8}{\pi^2}\exp\left(-\frac{\pi^2 D_{eff}}{4L^2}t\right) \quad (5)$$

When this equation is linearized by taking the natural logarithm, equation 6 is obtained:

$$\ln(MR) = \frac{8}{\pi^2} - \left(-\frac{\pi^2 D_{eff}}{4L^2}t\right) \quad (6)$$

Equation (6) represents a straight line, and the value of D_{eff} can be found by the slope of the t-dependent graph of ln(MR).

Evaluation of the mathematical modeling

The equations (7) and (8) of Peleg and Two-term mathematical models were applied to the rehydration data of shrimp, squid and mussels with computer program Statistica 8.0 (StatSoft, Tulsa, USA). The Levenberg-Marquardt algorithm was used as the nonlinear regression procedure while assuming the parameters of the models [15, 16]. Equations (9), (10), and (11) were used to calculate root mean square error (RMSE), coefficient of determination (R^2) and reduced chi-square (χ^2) values calculated by nonlinear regression [13, 14].

Peleg model: $$RR = M_0 + \frac{t}{k_1 + k_2 \times t} \quad (7)$$

Two-term model: $$RR = a \times e^{-k_0 \times t} + b \times e^{-k_1 \times t} \quad (8)$$

M_0 is the initial moisture content k_1, k_2 are Peleg constants, a, b, k_0, k_1 are coefficients, and t is time.

$$R^2 = 1 - \sum_{i=1}^{N}\frac{\left(RR_{exp,i} - RR_{pre,i}\right)^2}{\sum_{i=1}^{N}\left(\frac{RR_{exp,i}}{\frac{\sum_{i=1}^{N} RR_{exp,i}}{N}} - RR_{pre,i}\right)^2} \quad (9)$$

$$\chi^2 = \frac{\sum_{i=1}^{N}(RR_{exp,i} - RR_{pre,i})^2}{N-n} \quad (10)$$

$$RMSE = \sqrt{\frac{\left(\sum_{i=1}^{N}(RR_{pre,i} - RR_{exp,i})^2\right)}{N}} \quad (11)$$

where RR_{pre} is the rate of predicted rehydration, and RR_{exp} is the rate of experimental rehydration, N is the number of data and n is the number of models' constants. The most appropriate model was selected based on its highest R^2 and the lowest χ^2 and RMSE [17, 18].

Color analysis

Color is the most significant factor when it comes to determining product quality and consumer choice. Hunter color analysis is a method that shows the product's lightness value as +L* (100 = white), redness value as +a*, green value as -a*, yellowness value as +b*, and blueness value as -b* [17, 19]. Color parameters were measured using a hand-held colorimeter (PCE-CSM 1; PCE Instruments UK Ltd., Southampton Hampshire, UK) prior to and after rehydration. At least five measurements were made for each sample and the values were averaged +as shown in Table 3. Total color changes (ΔE) were calculated from equation (12), L_0, a_0, and b_0 are the color parameters of the dry sample [19].

$$\Delta E = \sqrt{((L_0 - L)^2 + (a_0 - a)^2 + (b_0 - b)^2)} \quad (12)$$

RESULTS AND DISCUSSION

Rehydration curves

The rehydration rates and rehydration rate curves for shrimp, squid and mussels are shown in Figures 1–3, respectively. As can be seen in Figure 1, the rehydration rates of the shrimp increased rapidly during the first 30 min, then slowed over time and eventually stabilized at levels that could be considered constant rates. It was observed that this behavior developed more rapidly as the rehydration temperature increased; samples at 60 °C rapidly reached their equilibrium weights, whilst those at 25 °C continued to absorb water. The highest rehydration rate was observed in the control sample at 25 °C, whilst the lowest rate was observed in the control sample at 60 °C. It was observed that the rehydration rates in the shrimp samples tended to be higher than those in the US-pre-treated samples at the same temperatures. The highest rates for the shrimp samples at control 25 °C, US 25 °C, control 40 °C, US 40 °C, control 60 °C, and US 60 °C were obtained at 10 min as 0.3032, 0.2705, 0.2302, 0.2546, 0.1846, and 0.2123 g/g × min; and the final rehydration ratios were obtained as 4.3308, 3.5474, 2.7161, 3.0756, 2.1373, and 2.5016 g/g at the 70th min.

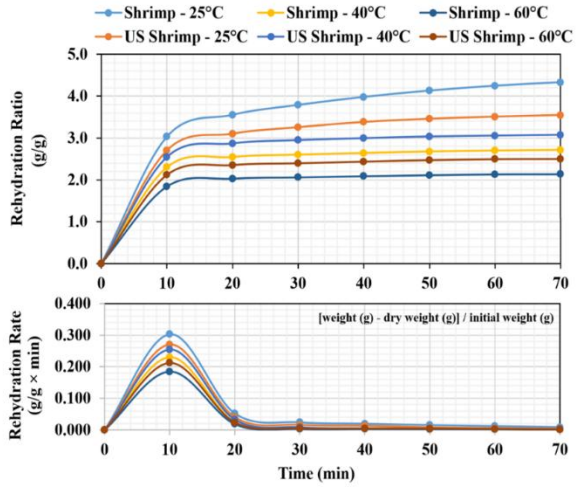

Figure 1. Rehydration ratio (g/g) and rehydration rate (g/g ×min) graphs of shrimp samples

The rehydration rates of the squid samples increased rapidly during the first 20 min and then slowed down over time; however, water uptake continued for a long time compared to the other samples. The highest rehydration rate was observed in the control sample at 25 °C, whilst the lowest rate was observed in the control sample at 60 °C. It was observed that the rehydration rates in squid samples tended to be higher than those in US-pretreated samples at the same temperatures. For the shrimp samples, the highest rates at 25 °C (control), 25 °C (US), 40 °C (control), 40 °C (US), 60 °C (control) and 60 °C (US) were obtained at the 10th min as 0.0858, 0.0741, 0.0619, 0.0664, 0.0484, and 0.0556 g/g × min, respectively; and the final rehydration rates were 5.1586, 4.9373, 4.2029, 4.6321, 3.4767, and 3.8141 g/g at the 260th min.

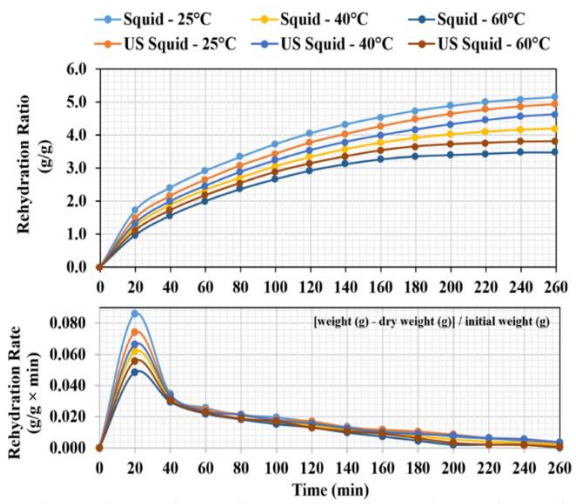

Figure 2. Rehydration ratio (g/g) and rehydration rate (g/g ×min) graphs of squid samples

The mussel samples exhibited a similar profile to the shrimp samples, rehydration rates increased rapidly during the first 20 min, then slowed over time and eventually stabilized at levels that could be considered constant rates.

Whilst the samples at 60 °C rapidly reached their equilibrium weights, those at 25 °C continued to absorb water. At all temperatures, the US samples achieved higher rehydration rates than the mussel samples. For the mussel samples, the highest rates at 10 minutes were 0.1928, 0.2096, 0.1708, 0.1795, 0.1551, and 0.1639 g/g ×min; the final rehydration ratios were 2.1519, 2.2874, 1.9659, 2.0407, 1.7483, and1.8906 g/g at 50th min for the control 25 °C, US 25 °C, control 40 °C, US 40 °C, control 60 °C, and US 60 °C samples, respectively.

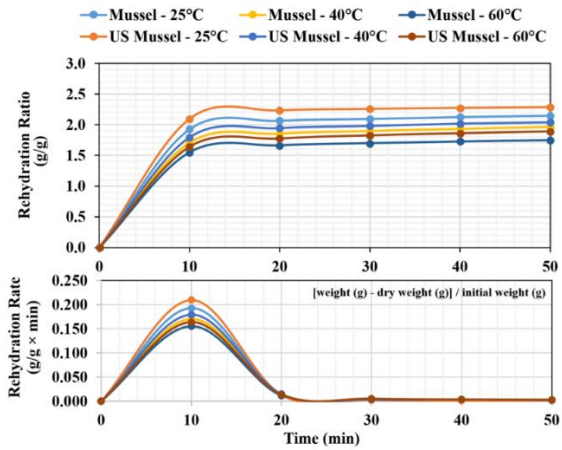

Figure 3. Rehydration ratio (g/g) and rehydration rate (g/g ×min) graphs of mussel samples

Effective diffusivity coefficient results

The D_{eff} values calculated using the slopes of the ln(MR)-t graph are given in Table 1. As can be seen from the table, D_{eff} values are in the range of approximately 3.56 – 5.59 × 10^{-9} m^2/s, 1.21 – 1.27 × 10^{-9} m^2/s, and 5.86 – 7.38 × 10^{-9} m^2/s for shrimp, squid, and mussel, respectively. In general, mussel samples showed the highest D_{eff} values, especially at 25°C, indicating faster water diffusion into the dried matrix compared with shrimp and squid. Shrimp exhibited intermediate D_{eff} values, while squid had the lowest values at all rehydration temperatures, suggesting a slower rehydration process, probably due to a denser or less porous tissue structure after freeze drying.

Table 1. D_{eff} values of the samples (×10^{-9})

Treatment	Temp. (°C)	Sample		
		Shrimp	Squid	Mussel
Control	25	3.56	1.27	6.28
US	25	4.16	1.24	7.38
Control	40	4.53	1.23	5.89
US	40	4.66	1.23	6.26
Control	60	5.59	1.21	6.24
US	60	5.47	1.22	5.86

Temperature affected the D_{eff} values in different ways depending on the type of sample; in general, moisture mobility increased as the rehydration temperature increase. US pretreatment did not show a uniform effect on all samples. In shrimp and mussels, US slightly increased D_{eff} at 25°C and 40°C, but a slight decrease was observed at 60°C. In squid, the differences between control and US-treated samples were very small, indicating a negligible effect of pretreatment.

Mathematical modeling results

Mathematical model constants are listed in Table 2. The appropriate models were chosen based on minimum value of root mean square error (RMSE) and chi-square (χ^2) and maximum value of coefficient of determination (R^2) for all different rehydration temperature. Both Peleg and Two-term models showed high compatibility with the rehydration data.

Table 2. Mathematical model constants

			Peleg						Two-term						
Sample		Temp (°C)	R^2	RMSE	χ^2	a	k_1	k_2	R^2	RMSE	χ^2	a	k_0	b	k_1
Shrimp	Control	25	0.99452	0.06851	0.00597	-0.003	304.249	3.6742	**0.99935**	0.19726	0.05448	-0.2245	0.0104	0.22646	7.3E-05
		40	0.99456	0.00977	0.00012	-0.0067	111.45	2.0448	**0.99951**	0.06848	0.00657	-0.3896	0.01593	0.38893	-0.0002
		60	**0.99901**	0.00931	4.6E-05	-0.0009	81.3472	1.81321	0.99678	0.04619	0.00427	-0.416	0.02115	0.42057	-0.0004
	US	25	0.99452	0.01839	0.00043	-0.003	304.249	3.6742	**0.99935**	0.05	0.0035	-0.2245	0.0104	0.22646	7.3E-05
		40	0.99456	0.00949	0.00012	-0.0067	111.45	2.0448	**0.99951**	0.0197	0.00054	-0.3896	0.01593	0.38893	-0.0002
		60	**0.99901**	0.01034	0.00017	-0.0009	81.3472	1.81321	0.99678	0.05831	0.0068	-0.416	0.02115	0.42057	-0.0004
Squid	Control	25	**0.99452**	0.09346	0.01048	-0.003	304.249	3.6742	**0.99452**	0.99935	0.49782	0.31863	-0.2245	0.0104	0.22646
		40	**0.99456**	0.0752	0.00679	-0.0067	111.45	2.0448	**0.99456**	0.99951	0.45202	0.2627	-0.3896	0.01593	0.38893
		60	**0.99901**	0.06578	0.00551	-0.0009	81.3472	1.81321	**0.99901**	0.99678	0.36924	0.19087	-0.416	0.02115	0.42057
	US	25	0.99452	0.0898	0.00968	-0.003	304.249	3.6742	**0.99935**	0.4945	0.31439	-0.2245	0.0104	0.22646	7.3E-05
		40	0.99456	0.07299	0.00639	-0.0067	111.45	2.0448	**0.99951**	0.47066	0.28481	-0.3896	0.01593	0.38893	-0.0002
		60	**0.99901**	0.06092	0.00472	-0.0009	81.3472	1.81321	0.99678	0.37857	0.20065	-0.416	0.02115	0.42057	-0.0004
Mussel	Control	25	0.99452	0.01021	0.00014	-0.003	304.249	3.6742	**0.99935**	0.03963	0.00236	-0.2245	0.0104	0.22646	7.3E-05
		40	0.99456	0.01251	0.00021	-0.0067	111.45	2.0448	**0.99951**	0.04527	0.00307	-0.3896	0.01593	0.38893	-0.0002
		60	**0.99901**	0.00931	0.00012	-0.0009	81.3472	1.81321	0.99678	0.03392	0.00173	-0.416	0.02115	0.42057	-0.0004
	US	25	0.99452	0.00539	3.9E-05	-0.003	304.249	3.6742	**0.99935**	0.03635	0.00198	-0.2245	0.0104	0.22646	7.3E-05
		40	0.99456	0.01607	0.00034	-0.0067	111.45	2.0448	**0.99951**	0.04045	0.00245	-0.3896	0.01593	0.38893	-0.0002
		60	**0.99901**	0.00999	0.00013	-0.0009	81.3472	1.81321	0.99678	0.04434	0.00295	-0.416	0.02115	0.42057	-0.0004

Table 3. Color parameters of the samples

		Shrimp			Squid			Mussels		
Temp.	Color Parameter	FD	Control	US	FD	Control	US	FD	Control	US
25 °C	L	93.98	61.16	70.84	85.11	68.29	72.80	75.30	72.14	65.27
	a	0.42	2.81	2.77	1.67	0.21	1.86	10.82	8.58	22.07
	b	8.89	7.53	9.84	10.50	5.50	9.57	29.39	26.25	51.73
	ΔE	-	32.94	23.28	-	18.78	13.7	-	15.89	16.51
40 °C	L	-	67.55	73.14	-	71.07	73.02	-	73.64	68.94
	a	-	2.24	1.39	-	0.14	0.71	-	4.48	10.91
	b	-	10.96	11.23	-	7.66	9.91	-	25.26	34.99
	ΔE	-	26.58	21.00	-	15.67	13.53	-	18.71	9.40

60 °C	L	-	70.59	77.57	-	75.17	78.34	-	73.73	68.34
	a	-	2.09	1.06	-	0.11	0.67	-	7.85	12.75
	b	-	11.09	11.28	-	10.49	11.12	-	26.27	33.74
	ΔE	-	23.56	16.60	-	11.48	8.35	-	16.00	9.79

The Peleg model gave consistently high R^2 values, between 0.99452 - 0.99901, with relatively low RMSE and χ^2 values. This indicates that the Peleg model successfully described the rehydration behavior of shrimp, squid, and mussel samples under different temperatures and treatments. The Two-term model also showed very high R^2 values, generally ranging from 0.99452 - 0.99951. In several cases, especially for shrimp and mussel, the Two-term model produced slightly higher R^2 values than the Peleg model. However, for squid, the RMSE and χ^2 values of the Two-term model were relatively higher, particularly in the control samples, indicating a weaker fit compared with the Peleg model for squid rehydration.

Color analysis results

The color parameters given in Table 3 showed that rehydration led to visible color changes in all samples. For shrimp, the dried sample had a high L* value of 93.98, indicating a very light appearance. After rehydration, L* decreased markedly in all treatments, showing darkening of the samples. However, increasing the rehydration temperature improved lightness, especially in the US samples. The ΔE values decreased from 32.94 to 23.56 in control samples and from 23.28 to 16.60 in US samples as temperature increased from 25 to 60°C. US reduced total color difference at all temperatures, suggesting a positive effect on color preservation. For squid, the overall color change was lower than in shrimp. The L* values increased with temperature in both control and US samples, indicating better recovery of brightness during rehydration at higher temperatures. The ΔE values decreased from 18.78 to 11.48 in control samples and from 13.70 to 8.35 in US samples. This shows that squid color was better preserved at 60°C, and ultrasonication further reduced the total color difference. Squid also had the lowest ΔE values among the three seafood samples, suggesting the most stable color after rehydration.

For mussel, the color response was different from shrimp and squid because of its naturally higher a* and b* values. Rehydration caused changes mainly in redness and yellowness. In control samples, ΔE values remained relatively high and did not decrease regularly with temperature. However, US-treated mussels showed much lower ΔE values at 40 and 60°C, especially 9.40 and 9.79, compared with the control samples. This suggests that US was effective in reducing color changes in mussel, particularly at higher rehydration temperatures.

CONCLUSION

This study evaluated the rehydration behavior, effective moisture diffusivity, mathematical modeling compatibility, and color changes of freeze-dried shrimp, squid, and mussel samples produced with and without ultrasonic pretreatment. The results showed that seafood type, rehydration temperature, and ultrasonic pretreatment influenced the rehydration performance and visual quality of the samples. In all the samples, water uptake occurred rapidly during the initial stage of rehydration and then gradually slowed until reaching equilibrium. This behavior confirmed the typical rehydration pattern of freeze-dried products, where water first penetrates rapidly into the porous structure and then continues more slowly as the matrix approaches saturation.

Among the tested seafood products, squid showed the highest final rehydration ratios but the lowest effective diffusivity values, indicating that although squid absorbed a higher amount of water overall, water movement into its structure occurred more slowly. Mussel samples exhibited the highest effective diffusivity values, suggesting faster water diffusion into the dried matrix, while shrimp showed intermediate behavior. Rehydration temperature affected the samples differently; higher temperatures generally accelerated the approach to equilibrium, while lower temperatures often resulted in higher final rehydration ratios. Ultrasonic pretreatment did not produce a uniform effect on rehydration kinetics. It slightly improved effective diffusivity in shrimp and mussel at 25 and 40 °C, whereas its effect on squid was limited.

The mathematical modeling results showed that both the Peleg and Two-term models successfully described the rehydration behavior of freeze-dried seafood samples. The Peleg model provided consistently high compatibility for all samples, while the Two-term model also showed strong fitting performance, particularly for shrimp and mussel. Therefore, both models can be considered suitable for predicting the rehydration kinetics of freeze-dried seafood products under different temperature and pretreatment conditions. Color analysis

demonstrated that rehydration caused visible color changes in all samples. However, higher rehydration temperatures and ultrasonic pretreatment generally reduced total color difference, especially in squid and mussel samples. The results suggest that ultrasonic pretreatment and suitable rehydration temperatures may improve color preservation and, in some cases, enhance water diffusion, contributing to the optimization of rehydrated freeze-dried seafood quality.

REFERENCES

1. T. Fauster, M. Giancaterino, P. Pittia, H. Jaeger, *LWT Food Sci. Technol.*, **121**, 108937 (2020).
2. Z. O. Ozyalcin and A. S. Kipcak, *Bulg. Chem. Commun.*, **55**, 234 (2023).
3. Y. Liang, F. Teng, M. He, L. Jiang, J. Yu, X. Wang, Y. Li, Z. Wang, *Food Struct.*, **28**, 100169 (2021).
4. E. Lopez-Quiroga, V. Prosapio, P. J. Fryer, I. T. Norton, S. Bakalis, *J. Food Process Eng.*, **43**, e13192 (2020).
5. M. F. Zotarelli, A. Durigon, V. M. da Silva, M. D. Hubinger, J. B. Laurindo, *Drying Technol.*, **40**, 175 (2022).
6. Y. Qiu, J. Bi, X. Jin, X. Wu, L. Hu, L. Chen, *Food Chem.*, **383**, 132360 (2022).
7. S. Mamatov, M. Zhang, A. Jia, X. Liu, C. Liu, *Int. J. Innov. Technol. Explor. Eng.*, **8**, 475 (2019).
8. Z. O. Ozyalcin, E. Gules, D. Uygunoz, F. Bozkurt, O. Sagdic, I. Doymaz and A. S. Kipcak, *Turk. J. Fish. Aquat. Sci.*, **25**, 2 (2024).
9. Z. O. Ozyalcin, A. S. Kipcak, *Bulg. Chem. Commun.*, **57**, 252 (2025).
10. J. G. Ling, X. T. Xuan, N. Yu, Y. Cui, H. T. Shang, X. J. Liao, D. H. Liu, *J. Food Sci.*, **85**, 1167 (2020).
11. N. Alp, Z. O. Ozyalcin, A. S. Kipcak, *Ege J. Fish. Aquat. Sci.*, **42**, 48 (2025).
12. E. Midik, Z. O. Ozyalcin, A. S. Kipcak, *J. Chem. Technol.*, **33**, 136 (2025).
13. A. S. Kipcak, O. Ismail, I. Doymaz, S. Piskin, *J. Chem.*, **2014**, 1 (2014).
14. A. Benseddik, A. Azzi, M. N. Zidoune, R. Khanniche, C. Besombes, *J. Saudi Soc. Agric. Sci.*, **18**, 401 (2019).
15. I. Doymaz, A. S. Kipcak, S. Piskin, *Czech J. Food Sci.*, **33**, 83 (2015).
16. Z. O. Ozyalcin, A. S. Kipcak, *Sigma J. Eng. Nat. Sci.*, **41**, 858 (2023).
17. Z. O. Ozyalcin, A. S. Kipcak, *Sigma J. Eng. Nat. Sci.*, **41**, 1077 (2023).
18. A. S. Kipcak, I. Doymaz, E. M. Derun, *Chem. Ind. Chem. Eng. Q.*, **25**, 1 (2019).
19. A. S. Kipcak, Z. O. Ozyalcin, *J. Aquat. Food Prod. Technol.*, **31**, 187 (2022).

Bulgarian Chemical Communications, Volume 58, Issue 3 (pp. 261-268) 2026 *DOI: 10.34049/bcc.58.3.D004*

Degradation mechanisms of selected aminopolycarboxylic acid molecules by DFT method

B. Eren[1]*, A. H. Dökmeci[2]

[1] *Tekirdag Namik Kemal University, Rectorate, Tekirdag, Turkiye*
[2] *Tekirdag Namik Kemal University, Faculty of Health Sciences, Emergency and Disaster Management, Tekirdag, Turkiye*

Accepted: July 28, 2026

In this study, pentetic acid or diethylenetriamine pentaacetic acid (DTPA), ethylenediamine tetraacetic acid (EDTA) and hydroxyethylenediamine tetraacetic acid (HEDTA) were investigated, selected from the group of aminopolycarboxylic acids (APCA), which are chemical compounds in which one or more nitrogen atoms are bonded to two or more carboxyl groups *via* carbon atoms and used in various chemical, medical, and environmental applications. The toxicological properties of these compounds are important for both human health and environment. Aminopolycarboxylic acids, such as EDTA and DTPA, are compounds that can persist in the environment and are difficult to biodegrade. Therefore, the risk of EDTA becoming a "persistent organic pollutant," is being discussed. Environmental degradation generally occurs through sunlight, and this process is slow which increases the risk of accumulation in wastewater and natural environment. The ability of these acids to bind metal ions can reduce the bioavailability of some metals in aquatic environments and lead to imbalances in ecosystems. This and similar factors have led to the investigation of the degradation pathways of these molecules in nature.

The aim of this study is to theoretically elucidate the fate of both the main molecule and its hydroxylated fragments in nature as they enter the natural cycle as a result of mixing with wastewater. Geometric optimizations of the fragments were performed using the DFT/B3LYP/6-31G(d) basis set of quantum mechanical density functional theory (DFT) to theoretically determine all possible reaction pathways of the selected molecules with the OH radical.

Keywords: DFT, aminopolycarboxylic acids (APCA), DTPA, EDTA, HEPTA

INTRODUCTION

An aminopolycarboxylic acid (APCA) is a chemical compound containing one or more nitrogen atoms bonded to two or more carboxyl groups *via* carbon atoms. Aminopolycarboxylates, that have lost their acidic protons, form strong complexes with metal ions. This property makes APCAs useful complexing agents in a wide variety of chemical, medical and environmental applications [1]. APCAs are synthetic chelators because they contain multiple carboxylate and amine groups and can form strong, stable complexes with metal ions. The most used of these compounds are: pentetic acid or diethylenetriamine pentaacetic acid (DTPA), ethylenediamine tetraacetic acid (EDTA) and hydroxyethylenediamine tetraacetic acid (HEDTA) [2, 3].

DTPA consists of a diethylenetriamine structure with five carboxymethyl groups. The DTPA molecule can be seen as an extended version of EDTA and is used similarly.

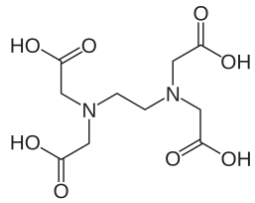

EDTA

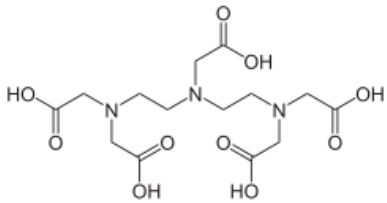

DTPA

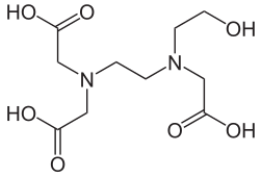

HEDTA

Figure 1. Two-dimensional representations of DTPA, EDTA, and HEDTA molecules

* To whom all correspondence should be sent:
E-mail: *beren@nku.edu.tr*

© 2026 Bulgarian Academy of Sciences, Union of Chemists in Bulgaria

It is a white solid with limited solubility in water. In the textile industry, EDTA is used to bind metal ions in aqueous solution, preventing dyed products from changing color. In the pulp and paper industry, EDTA inhibits the ability of metal ions, particularly Mn^{2+}, to catalyze the disproportionation of hydrogen peroxide used in chlorine-free bleaching. While it is used as a preservative or stabilizer in some foods to prevent catalytic oxidative discoloration catalyzed by metal ions, in the cosmetics industry, EDTA salts are used in shampoos, cleaners, and other personal care products to improve their stability in air [4-6]. Sodium calcium edetate, an EDTA derivative, is used to bind metal ions in chelation therapy for conditions such as mercury and lead poisoning. It is also used to remove excess iron from the body. This therapy is used to treat complications of repeated blood transfusions, as well as in the treatment of thalassemia [7].

EDTA is used so widely that questions are being raised about whether it is a persistent organic pollutant. While EDTA has many positive functions in industrial, pharmaceutical, and other fields, its longevity can cause serious problems for the environment. EDTA degrades slowly, mostly abiotically in the presence of sunlight [8]. EDTA and its derivatives are widely used in wastewater treatment, particularly for binding and removal of heavy metal ions, and as stabilizers in the food and cosmetics industries [9, 10]. DTPA stands out as a radionuclide carrier in nuclear medicine and as an industrial cleaning agent, while HEDTA is preferred in agricultural micronutrient fertilizers and detergent formulations [11]. The widespread use of these compounds leads to their accumulation as persistent organic pollutants in environmental settings and the emergence of potential ecotoxicological risks [12]. Owing to their high chemical stability and difficult biological degradation, APCAs such as EDTA and DTPA are detected in wastewater, surface, and groundwater [13, 14]. EDTA is among the substances recommended for monitoring under the European Union Water Framework Directive and attracts attention due to its environmental persistence [15]. The fate of these compounds in the environment is closely related to the toxicological profiles not only of the parent molecules but also of their degradation products. For example, nitrilotriacetic acid (NTA), formed during the environmental degradation of EDTA, is classified as a probable human carcinogen (group 2B) by the International Agency for Cancer Research (IARC) [16].

To understand the environmental fate and toxicological effects of APCAs, it is necessary to examine the degradation mechanisms of these molecules in detail. Degradation processes occurring under environmental conditions (light, pH, microbial activity) are generally slow and lead to the formation of intermediate products rather than complete mineralization [17]. Therefore, the persistence and potential risks of APCAs in the environment are investigated not only by experimental studies but also by computational chemistry methods. Density functional theory (DFT) stands out as a powerful tool in understanding chemical reactions and degradation mechanisms at the molecular level. DFT-based studies play an important role in elucidating the structural properties of APCA metal complexes, bond breaking energies, and possible intermediate formation pathways [18]. Recent DFT studies have shown that the key step in the biodegradation of chelators such as EDTA and S, S-EDDS is the breaking of the C–N bond, and the energy barrier required for this step determines the environmental persistence of the compound [19]. Similarly, the environmental degradation mechanisms of derivatives such as DTPA and HEDTA, and the toxicological profiles of their intermediates are better understood thanks to calculations made with DFT.

The molecules to be examined are organic compounds. Recent studies show that organic pollutants are present in water at very low concentrations. Therefore, purifying drinking water from organic pollutants is very important. Sunlight on Earth helps to naturally purify lakes, rivers, and other water systems. Large organic molecules are broken down into smaller molecules by sunlight [20, 21]. Organic compounds undergo photolysis by reacting with OH radicals, and this is the most dominant decomposition reaction in the atmosphere. Biomolecules, which are hydroxyl scavengers at various rates, are specific detectors for hydroxyl radicals due to their hydroxylation capabilities. Any hydroxyl radical attack on an aromatic compound result in the formation of a hydroxylated product, and these newly formed products can be far more harmful than the original products at the beginning of the process. Therefore, monitoring these products is very important. The OH radical acts as an electrophile in its reaction with any organic molecule and therefore readily binds to unsaturated bonds, while the O radical is a nucleophile and therefore does not interact with these bonds. When an aliphatic side chain is attached to an aromatic molecule, the OH radical prefers the aromatic ring to bind to [21-29].

The main objective of this study is to track the initial products released into the environment, as

well as the new products that may be more dangerous as a result of a degradation reaction, and to explain the degradation reaction. Because the decomposition reactions of organic pollutants can produce products that are even more harmful than the main pollutants themselves, knowledge of intermediate products is crucial for air and water treatment. The reactions that cause organic pollutants to disappear in the atmosphere are those involving OH, NO_3 radicals, O_3, and Cl atoms. Among these radicals, the most active are those involving OH radicals. Knowing the half-lives of these substances in the troposphere is the most important factor in providing information about whether they will be transported to the stratosphere [30-32].

MATERIALS AND METHODS

In order to theoretically determine all possible reaction pathways for the molecules under study, geometric optimizations were performed using the DFT/B3LYP/6-31G(d) basis set of the quantum mechanical density functional theory (DFT), an electronic structure method. Energy values for all fragments were calculated using the Gauss View 6 molecular representation program and the Gaussian16 program for trajectory calculations, and geometric optimizations [33]. The fragmentation reaction energy is affected by the water molecules in the aqueous medium. In addition, the geometric stress in the solutions is triggered by H_2O. In other words, the presence of a dielectric medium such as H_2O causes the geometry associated with the solute to relax and has a stabilizing effect by reducing the energy of this mechanism [21]. Therefore, in this study, the CPCM in the COSMO (conductor-like shielding solvation model) solvent model in the Gaussian 16 package was used to explain the solvent effect of the H_2O molecule +. OH reaction [33].

Gaussian 16 is a comprehensive program that includes molecular mechanics, quasi-empirical and ab initio methods. It offers a wide range of theory and fundamental set options for all three methods. The program enables the calculation of atomic and molecular energies, geometric optimizations, and the calculation of vibration frequencies, force constants, and dipole moments. Gauss View 6 is a graphical interface designed for creating input files and visualizing outputs for Gaussian package programs. Gauss View 6 allows us to rotate, move, and arrange molecules as desired by visualizing them. It also easily prepares input files even for complex calculations. It allows us to graphically examine the results calculated by the Gaussian 16 program. These results may include optimized molecular structures, molecular orbitals, electrostatic potential surfaces, atomic charges, IR, Raman, and NMR spectra, and normal mode animations based on vibration frequencies [33].

Since the reactions of molecules with the OH radical are important for both water treatment and atmospheric chemistry, calculations were performed in both gas phase and water phase using the COSMO (conductor-like screening solvation model) model, using CPCM. The Mulliken charges of molecules, the electronegative atoms in the molecule and the arrangement of the atoms surrounding them, stable double bonds, weak bonds at the ends of the molecule, calculated energies, bond lengths, and bond angles between atoms were examined, and these data helped select all the fragments that would determine the degradation mechanism. By examining the molecules for their reactions with OH radicals in air or water, the degradation reaction of each molecule was documented, starting with the lower-energy fragments, and their fate in nature was determined.

RESULTS AND DISCUSSION

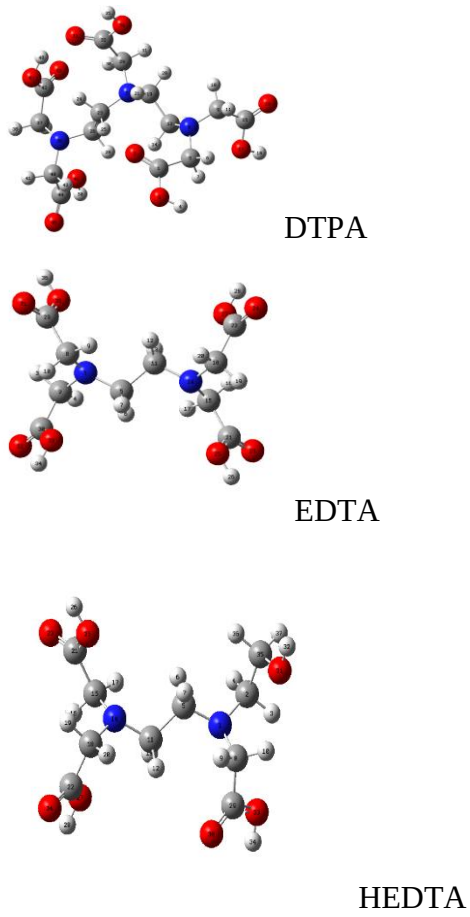

Figure 2. Geometric structure of DTPA, EDTA, and HEDTA molecules optimized by the DFT method (C atom is shown in gray, O atom in red, N atom in blue, and H atom in white)

Figures 1 and 2 show the two-dimensional and the optimized geometric structures of the three molecules studied. Double bonds in molecules are stable structures. If they are to be separated from the molecule, they initially do not want to separate. Single bonds at the ends of the molecule indicate atoms that can be removed from the compound. When writing the fragmentation path, the first thing to consider is whether there is a closed loop or double bond in the molecule, and what kind of arrangement exists around electronegative atoms. Table 1 shows the bond lengths, bond angles, and Mulliken charges of electronegative atoms in the DTPA molecule.

Table 1. Bond lengths, bond angles, and Mulliken charges of electronegative atoms in the DTPA molecule

Bond Lengths	(A^0)	Bond Angles	(^{0})	Mulliken Charges	
$C_{15}O_{17}$	1.35797	$C_9C_{15}O_{17}$	113.42037	O_2	-0.429521
C_9C_{15}	**1.53616**	**$N_8C_9C_{15}$**	**119.28590**	**O_3**	**-0.563245**
N_8C_9	1.44302	$N_8C_5C_1$	112.81975	C_5	-0.257605
C_5N_8	1.44279	$C_5C_1O_3$	113.98490	N_8	-0.356586
C_5C_1	**1.53410**	**$C_5N_8C_{12}$**	**116.33977**	C_9	-0.250553
O_3C_1	1.36111	$N_8C_{12}C_{19}$	111.70246	C_{12}	-0.133821
$C_{12}N_8$	1.46684	$C_{12}C_{19}N_{22}$	110.38509	O_{16}	-0.450194
$C_{12}C_{19}$	**1.53677**	$C_{19}N_{22}C_{23}$	114.81808	**O_{17}**	**-0.562539**
$N_{22}C_{19}$	1.46522	$N_{22}C_{23}C_{26}$	112.17940	C_{19}	-0.138476
$C_{29}N_{22}$	1.46245	$C_{23}C_{26}N_{35}$	111.32709	N_{22}	-0.393991
$N_{22}C_{23}$	1.47242	**$C_{26}N_{36}C_{40}$**	**117.01964**	C_{23}	-0.170861
$C_{23}C_{26}$	**1.54726**	**$N_{36}C_{40}C_{44}$**	**119.41875**	C_{26}	-0.153528
$C_{26}N_{36}$	1.47102	$N_{36}C_{37}C_{43}$	110.06062	C_{29}	-0.228362
$N_{36}C_{37}$	1.46362	$N_{22}C_{29}C_{32}$	114.12929	O_{33}	-0.485948
$N_{36}C_{40}$	1.44105	$C_{29}C_{32}O_{34}$	112.38119	**O_{34}**	**-0.547331**
$C_{40}C_{44}$	**1.53665**	$C_{40}C_{44}O_{49}$	113.45427	N_{36}	-0.374885
$C_{44}O_{49}$	1.35604	$C_{37}C_{43}O_{47}$	112.69966	C_{37}	-0.169482
$C_{37}C_{43}$	**1.52521**	$C_{37}N_{36}C_{40}$	114.77181	C_{40}	-0.244046
$C_{43}O_{47}$	1.34136	**$C_{19}N_{22}C_{29}$**	**115.70621**	C_{40}	-0.244046
		$C_5N_8C_9$	**116.20264**	O_{45}	-0.466818
		$C_9N_8C_{12}$	**115.42464**	O_{46}	-0.457541
				O_{47}	**-0.566968**
				O_{49}	**-0.555565**

When examining the Mulliken charges in Table 1, the most electronegative atoms are dark colored

These are shown with the following values: O_{47} -0.566968, O_3 -0.563245, O_{17} -0.562539, O_{49} -0.555565. Following these are O_{33}, O_{45}, O_{46}, O_{16}, O_2, N_{22}, and N_8. If we were to try to predict the decay path by only looking at these electronegative atoms, decay would be expected to occur at this stage.

Looking at the bond lengths in Table 1, the longest bond lengths are highlighted in dark color. These are, in order, the C-C bond lengths of $C_{23}C_{26}$, $C_{12}C_{19}$, $C_{40}C_{44}$, C_9C_{15}, C_5C_1. Following these are the C-N bond lengths of $N_{22}C_{23}$, $C_{26}N_{36}$, $C_{12}N_8$, $N_{22}C_{19}$, $C_{29}N_{22}$, ... If we try to predict the decay path by only looking at the bond lengths between these pairs of atoms, decay would be expected to occur in that order.

Again, when examining the bond angles in Table 1, the widest bond angles are highlighted in dark color. These are the bond angles between the C-N-C atoms $N_{36}C_{40}C_{44}$, $N_8C_9C_{15}$, $C_{26}N_{36}C_{40}$, $C_5N_8C_9$, $C_{19}N_{22}C_{29}$, and $C_9N_8C_{12}$, respectively. If we try to predict the decay path by only looking at the bond angles between these three atoms, decay would be expected to occur at this stage.

While one might expect the fission process to begin with atoms that have the longest bond lengths, atoms with the widest bond angles, or atoms surrounding the most electronegative atom, making the choice isn't that simple.

Table 2 presents the energy, enthalpy, and Gibbs free energy values for the three molecules studied, in both the gas and water phases, respectively, in atomic mass units. The values for the fragments are only for the gas phase. The reason for giving the energy values in atomic mass units (AU) is that the digits after the decimal point are very close to each other when converted to SI units.

Energy values are a determining factor for the decomposition pathway, as the pathway is written starting from the lowest energy value. The energy values in this table show that, without any external influence, molecules and their fragments spontaneously react with negative energy values and return to nature in the gaseous phase.

Table 2. ΔE, ΔH, ΔG (Au) values of DTPA, EDTA and HEDTA molecules and their fragments in the degradation pathways, respectively.

(AU)	DTPA	D1	D11	D2	D14
ΔE	-1463.395214	-1388.152850	-1312.906205	-1274.847813	-1237.659647
ΔH	-1463.394270	-1388.151906	-1312.905261	-1274.846869	-1237.658703
ΔG	-1463.489906	-1388.247331	-1312.999051	-1274.936787	-1237.750728
	D3	D15	D31	D32	EDTA
	-1235.576589	-1162.423835	-1160.326589	-1047.020875	-1095.762452
	-1235.575645	-1162.422891	-1160.325645	-1047.019931	-1095.761508
	-1235.660255	-1162.512971	-1160.409956	-1047.101265	-1095.841083
	D12	HEDTA	D4	H1	D5
	-1087.178138	-1021.991923	-1007.742701	-947.129545	-952.422596
	-1087.177193	-1021.990979	-1007.741756	-947.128601	-952.421652
	-1087.265588	-1022.067206	-1007.819769	-947.203927	-952.496679
	D6	D7	D8	D9	D10
	-913.137940	-873.860150	-798.614399	-685.312181	-646.033802
	-913.136996	-873.859206	-798.613455	-685.311237	-646.032858
	-913.208954	-873.926720	-798.679580	-685.371004	-646.089233
	D13	DTPA (water)	EDTA (water)	HEDTA (water)	
	-520.674327	-1463.429359	-1095.798667	-1022.023250	
	-520.673383	-1463.428415	-1095.797722	-1022.022306	
	-520.731514	-1463.528972	-1095.875473	-1022.098166	

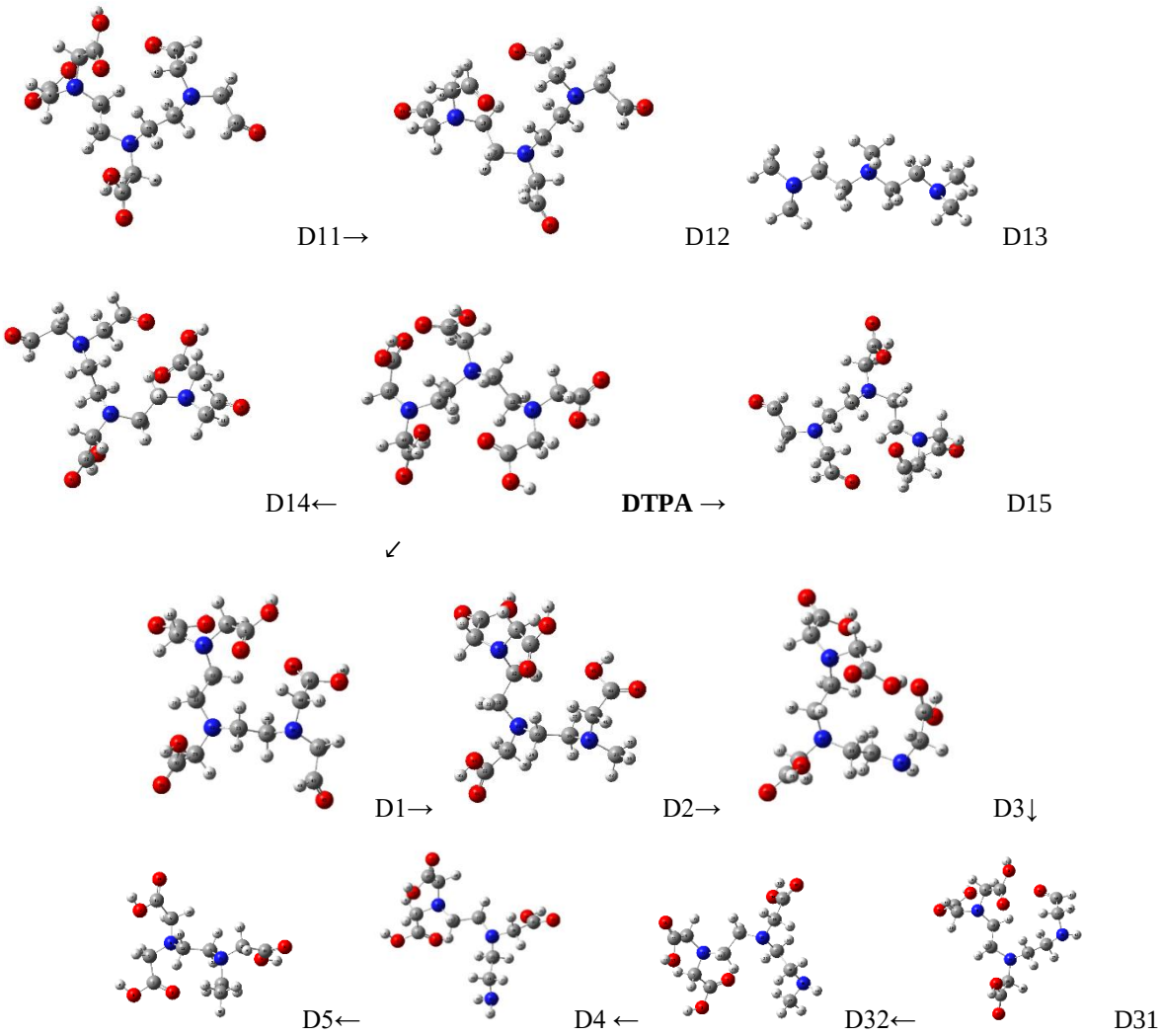

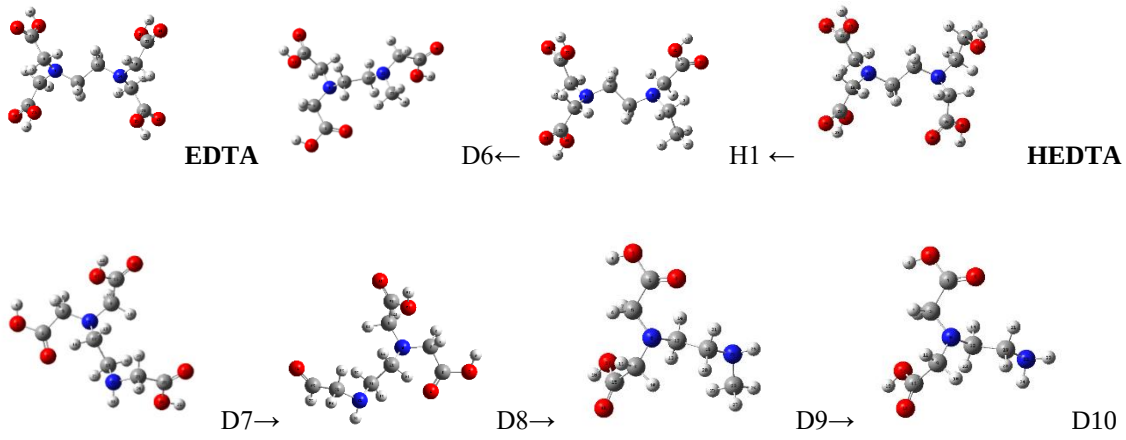

Figure 3. Designed degradation pathways for DTPA, EDTA, and HEDTA molecules

By examining all values in Figure 2 and Tables 1 and 2, that is, by looking at the bond lengths, bond angles, and Mulliken charges between electronegative atoms within the molecules and the atoms around them and supporting this with energy values, the degradation pathway shown in Figure 3 was determined.

Table 3. Half-life for the molecules studied [43-45]

Period	EDTA	DTPA	HEDTA
Photodegradation (λ > 290 nm, pH 7) half-life	20–30 days	10–15 days	18–25 days
Aerobic biological half-life (20 °C, activated sludge)	<10 %/60 days	<5 %/60 days	12 %/60 days
Soil	10–30 L/ kg (very mobile)	15–40	20–35
Wastewater treatment plant outlet average concentration.	35–120 µg/ L	5–25 µg/ L	2–10 µg/ L

CONCLUSION

In the literature, EDTA and its derivatives are safely used in chelation therapies (e.g., in the treatment of lead and mercury poisoning) for human health. However, it is known that high doses or prolonged exposure can negatively affect kidney function and lead to the excretion of important minerals from the body. When used as a stabilizer in food and cosmetic products, according to international toxicology reports, it is considered safe only within the specified limits [34]. In terms of human and animal toxicity, $CaNa_2$-EDTA and $CaNa_3$-DTPA are FDA-approved chelators in lead/plutonium poisoning [35]. Parenteral administration of EDTA can cause significant decreases (15-40%) in serum calcium and zinc levels, and cases of hypercalcaemic tetany have been reported [36]. In terms of renal and electrolyte imbalance, repeated EDTA infusions reduced glomerular filtration rate by 25% in rats [37]. Repeated administration of EDTA has been shown to reduce renal function, while urinary Ca^{2+} excretion increases fivefold after intravenous administration of DTPA [38]. In terms of in vitro genotoxicity, EDTA was found not to be genotoxic in the micronucleus test, but the Fe-EDTA complex increased reactive oxygen species (ROS) production by 180% [39].

In terms of regulation and limit values, the EU Water Framework Directive EQS-recommendation for EDTA is an average of 2.2 µg/L, the USEPA maximum secondary contaminant level (SMCL) for EDTA in drinking water is 0.25 mg/L, Cosmetics Europe's total release limit for EDTA is 2%, and the FAO/WHO JECFA acceptable daily intake (ADI) for EDTA in food is 2.5 mg/kg body weight [46-49]. When selected molecules are released onto the market, whether for therapeutic use or simply for disposal at the end of their shelf life, these organic compounds enter the natural cycle due to a lack of awareness in our country. Whether medical, commercial, or general waste, these organic compounds and their fragments enter the natural cycle. The half-lives of the molecules studied are presented in Table 3. They constitute a significant group of air and water pollutants. To remove these residues which persist in the environment for days from air and water, it is necessary to elucidate their degradation mechanisms.

Experimental kinetic data regarding the gas-phase and water-phase reactions of selected molecules with OH radicals are available in the literature. However, the reaction mechanisms of these substances have not been fully determined. In this study, the reactions of selected molecules with

OH radicals were investigated, and their degradation mechanisms were calculated using the DFT method. First, the gas-phase reactions were finalized, and their energy values in aqueous environments were also examined under the influence of water, due to their potential to cause pollution in wastewater. The mechanism of the reactions of the compounds with OH radicals in the atmosphere and in water was fully elucidated, and the reaction products were also fully identified. The findings were also evaluated from an environmental and toxicological perspective. Thus, the aim was to provide a more holistic view of the environmental fate and potential risks of these compounds.

Acknowledgement: *(Project No: NKUBAP.00.GA. 23.506) The current study was produced using a workstation obtained from the NKUBAP.00.GA. 23.506 project titled "Theoretical investigation of the degradation mechanisms of selected pharmaceutical product active ingredients" within the scope of the TNKU BAP project. It was produced using Gaussian16 & Gauss View 6 & TCP Linda Programs, (2009) TRUBA program.*

REFERENCES

1. G. Anderegg, F. Arnaud-Neu, R. Delgado, J. Felcman, K. Popov, *Pure Appl. Chem.,* **77** (8), 1445 (2005).
2. S.J. Flora, V. Pachauri, *Int. J. Environ. Res. Public Health,* **7**(7), 2745 (2010).
3. M. Bucheli-Witschel, T. Egli, *FEMS Microbiology Reviews*, **25**(1), 69 (2001).
4. J. Buckingham, J. B. Bucking, in: Dictionary of organic compounds. Chapman & Hall, Chapman & Hall/CRC, 6th edn. 1996
5. T. Furia, Gıdalarda EDTA - Teknik bir inceleme, *Gıda Teknolojisi*. **18** (12), 1874 (1964).
6. R.S. Lanigan, T. A. Yamarik, *International Journal of Toxicology. 21 Suppl.* **2** (5), 95 (2002).
7. R. DeBusk, et al. Ethylenediaminetetraacetic acid (EDTA). University of Maryland Medical Center. Archived from the original on 2007-05-04, (2002).
8. M. Bucheli-Witschel, T. Egli, *FEMS Microbiology Reviews,* **25** (1), 69 (2001).
9. R.S. Lanigan, T.A. Yamarik, *International Journal of Toxicology*, **21**(2), 95 (2002).
10. Agency for Toxic Substances and Disease Registry (ATSDR). (2019). Toxicological profile for EDTA. U.S. Department of Health and Human Services. https://www.atsdr.cdc.gov/toxprofiles/tp.asp?id=1112&tid=236
11. J.T. Li, A.J.M. Baker, Z.H. Ye, H.B. Wang, W.S. Shu, *Critical Reviews in Environmental Science and Technology*, **42**(20), 2113 (2012).
12. L.B. Barber, S.H. Keefe, G.K. Brown, E.T. Furlong, J.L. Gray, D.W. Kolpin, M.T. Meyer, M.W. Sandstrom, S.D. Zaugg, *Environmental Science & Technology*, **47**(5), 2177 (2013).
13. B. Nowack, *Environmental Science & Technology*, **36**(19), 2009 (2002).
14. M. Behbehani, E. Manoli, *Water Research*, **24**(2), 163 (1990).
15. European Commission. (2024). Watch List under the Water Framework Directive. https://environment.ec.europa.eu/topics/water/water-framework-directive/water-framework-directive-watch-list_en
16. International Agency for Research on Cancer (IARC). (1999). IARC Monographs on the Evaluation of Carcinogenic Risks to Humans: Nitrilotriacetic acid and its salts (vol. 73). https://monographs.iarc.fr/wp-content/uploads/2018/06/mono73-27.pdf
17. M. Bucheli-Witschel, T. Egli, *FEMS Microbiology Reviews*, **25**(1), 69 (2001).
18. L. Chen, T. Liu, C. Ma, *The Journal of Physical Chemistry A,* **114**(1), 443 (2010).
19. C. Ding, M. Xia, F. Wang, W. Lei, *Spectrochimica Acta Part A: Molecular and Biomolecular Spectroscopy*, **281** (2022).
20. D.F. Ollis, H.,Al-Ekabi, Photocatalytic Purification and Treatment of Water and Air (Eds.). Elsevier Sci. Publishers, Amsterdam, 1993, p. SI 1.
21. B. Eren, Y. Yalcin Gurkan, *J. Serb. Chem. Soc.,* **82**(3), 277 (2017).
22. M. Anbar, P. Neta, *Int. J Appl. Radiat. Isot.,* **18,** 493 (1967).
23. V.G. Buxton, L.C. Greenstock, P.W. Helman, *Journal of Physical and Chemical Reference Data,* **17**, 513 (1988).
24. B. Halliwell, M. Grootveld, J.M.C. Gutteridge, *Methods Biochem. Anal.,* **33**, 59 (1998).
25. S.M. Aschmann, E.C. Tuazon, R. Atkinson, *J. Phys. Chem. A*, **109**, 2282 (2005).
26. Aschmann, S.M., Tuazon, E.C., Long, W.D., and Atkinson, R. *J. Phys. Chem. A,* **114**, 3523 (2010).
27. S.M. Aschmann, R. Atkinson, *J. Phys. Chem. A,* **110** (2006).
28. R. Atkinson, S.M. Aschmann, M.A. Goodman, A.M. Winer, *Int. J. Chem. Kinet*., **20**, 273 (1988).
29. R. Atkinson, J. Arey, *Chem. Rev*., **103**, 4605 (2003).
30. B. Eren, Y. Yalcin Gurkan, *Bulgarian Chemical Communications*, **53**, 456 (2021).
31. B. Eren, Y. Yalcin Gurkan, *Bulgarian Chemical Communications*, **54**, 224 (2022).
32. B. Eren, Y. Yalcin Gurkan, Innovative Research in Engineering, Duvar Publishing, İzmir Turkey,4,49 (2023a).
33. B. Eren, Y. Yalcin Gurkan, *(IJANSER) International Journal of Advanced Natural Sciences and Engineering Research*, **7**, 31 (2023b).
34. Gaussian16 & Gauss View 6 & TCP Linda Programs, TRUBA (2009).
35. B. Nowack, *Environmental Science & Technology,* **36**(19), 4009 (2002).
36. S.J.S. Flora, V. Pachauri, G. Saxena, *International Journal of Environmental Research and Public Health,* **9**(12), 4748 (2012).

37. R. S. Lanigan, T. A. Yamarik, *International Journal of Toxicology,* **21**(2), 95 (2002).
38. V. B. Braide, *General Pharmacology,* **15**(1), 37 (1984).
39. S. Fukuda, H. Iida, Toxicological study on the safety of DTPA as a drug (I). *Hoken Butsuri,* **18**, 37(1983).
40. K. Heindorff, O. Aurich, A. Michaelis, R. Rieger, *Mutation Research/Genetic Toxicology,* **115**(2), 149 (1983).
41. T.L. Batchelder, H.C. Alexander, W.M. McCarty, *Bulletin of Environmental Contamination and Toxicology,* **24**(4),543 (1980).
42. D.B. Huebert, J.M. Shay, L. *Archives of Environmental Contamination and Toxicology,* **22**(3), 313 (1992).
43. R. Frank, H. Rau, *Ecotoxicology and Environmental Safety,* **19**(1), 55 (1990).
44. M. Bucheli-Witschel, T. Egli, *FEMS Microbiology Reviews,* ***25***(1), 69 (2001).
45. T. P. Knepper, *TrAC Trends in Analytical Chemistry,* **22**(10), 708 (2003).
46. R. Loos, et al. Analytical methods for substances in the Watch List under the Water Framework Directive. *Science of The Total Environment,* ***912***, 168703 (2024). https://doi.org/10.1016/j.scitotenv.2023.168703
47. European Parliament. Surface water and groundwater pollutants. Texts adopted, 24 April 2024. https://www.europarl.europa.eu/doceo/document/TA-9-2024-0358_EN.html
48. USEPA. National Secondary Drinking Water Regulations (2023). https://www.epa.gov/dwstandardsregulations/secondary-drinking-water-standards-guidance-nuisance-chemicals
49. Cosmetics Europe. Cosmetic Ingredient Database. https://cosmeticseurope.eu/cosmetic-ingredient-database (2024).
50. FAO/WHO JECFA. (2002). Evaluation of certain food additives and contaminants: EDTA. WHO Food Additives Series 44. https://inchem.org/documents/jecfa/jecmono/v44jec09.htm

Bulgarian Chemical Communications, Volume 58, Issue 3 (pp. 269-275) 2026 *DOI: 10.34049/bcc.58.3.D005*

Utilization of sugar beet pulp as an agricultural by-product in vegan leather production

*A. Menekse, B. K. Isik, N. Tugrul**

Yıldız Technical University, Faculty of Chemistry and Metallurgy, Department of Chemical Engineering, Davutpaşa Campus, 34220 Esenler, Istanbul, Türkiye.

Accepted: July 28, 2026

The ecological degradation from traditional chrome-tanning and synthetic leathers necessitates biodegradable alternatives within polymer science and sustainable development frameworks. This study focuses on the valorization of sugar beet pulp (SBP), an abundant Turkish agro-industrial by-product, as a lignocellulosic matrix component for high-performance vegan leathers. SBP fibers were integrated into a starch/sodium alginate polymeric network and transformed into flexible vegan leathers *via* solution-casting. The fabricated leathers were characterized using Fourier transform infrared spectroscopy (FT-IR), tensile strength, water vapor transmission rate (WVTR), and water solubility analyses. Findings demonstrated that plasticizer selection and formulation parameters decisively influence matrix morphology, structural integrity, and barrier properties. FT-IR confirmed characteristic hydroxyl and polysaccharide-derived functional groups, proving molecular compatibility and stable cross-linking. The sorbitol-modified SBP4-So sample exhibited superior mechanical performance with a tensile strength of 22.26 MPa and a Young's modulus of 1374.22 MPa, making it competitive with traditional leather. Regarding barrier properties, the SBP4-AG sample optimized breathability and moisture management, yielding a minimized WVP of 1.15 g/m²·h. Furthermore, a minimum water solubility of 31% (SBP6-G) proved structural stability in aqueous environments. In conclusion, sugar beet pulp can be effectively engineered as a mechanically durable, eco-friendly, functional, and competitive leather alternative, offering a scalable innovation model aligned with circular economy principles.

Keywords: Vegan leather; sugar beet pulp; bio-material; biodegradable; sustainable

INTRODUCTION

The global leather industry is currently navigating a period of significant transformation driven by escalating environmental and ethical concerns. Traditional animal-based leather production is inherently resource-intensive, requiring vast grazing lands and contributing to high greenhouse gas emissions [1]. Moreover, the conventional tanning process relies heavily on chromium salts and consumes an average of 50 million m^3 of water annually in regions like Türkiye, posing severe risks to aquatic ecosystems and human health when inadequately treated [2]. As an alternative, synthetic leathers based on petroleum-derived polymers such as polyvinyl chloride (PVC) and polyurethane (PU) have gained market share due to lower cost and scalability. However, these materials increase dependence on non-renewable fossil fuels and raise sustainability issues, as their low biodegradability leads to long-term environmental persistence and microplastic pollution [3]. These drawbacks have catalyzed a global demand for biodegradable "vegan leather" alternatives within polymer science and sustainable frameworks that mimic the aesthetic and functional properties of animal leather without the associated environmental footprint [4-8]. Recent innovations have introduced diverse plant-based alternatives, including mycelium-based Mylo™, cactus-derived Desserto®, and pineapple leaf-based Piñatex [9-12]. Despite their potential, many require complex growth cycles or synthetic coatings to achieve durability, leaving a critical need for leather alternatives derived from abundant, low-cost agricultural by-products with minimal chemical modification. Türkiye, as a major producer of sugar beets, generates approximately 1.5 million tons of sugar beet pulp (SBP) annually [13]. Currently utilized primarily as low-value animal feed, SBP is a lignocellulosic biomass rich in cellulose (~25%), hemicellulose (~30%), and pectin (~22%) [14], making it a highly promising matrix for various biocomposite applications [15]. Its high pectin content is particularly advantageous, as it can form cross-linked gel structures that serve as a natural binder, potentially reducing the need for synthetic additives [16].

The objective of this study is to investigate the direct utilization of SBP powder as a primary matrix for the synthesis of sustainable, biodegradable, and high-performance vegan leathers. By employing a solvent-casting method with natural binders like starch and sodium alginate, and eco-friendly

* To whom all correspondence should be sent:
E-mail: *ntugrul@yildiz.edu.tr*

© 2026 Bulgarian Academy of Sciences, Union of Chemists in Bulgaria

plasticizers such as glycerol and sorbitol, this research evaluates the mechanical and chemical characteristics of SBP-based vegan leathers. This approach addresses waste management challenges in the sugar industry while proposing a low-energy production model that consumes significantly less water and energy compared to traditional leather manufacturing.

EXPERIMENTAL

Materials

The primary raw material, sugar beet pulp (SBP), was obtained as a byproduct from the Alpullu Sugar Factory (Lüleburgaz, Türkiye) in February 2025. Natural additives used to enhance the structural properties included starch (ZAG Kimya), sodium alginate (Alfasol). Plasticization was achieved using glycerol (Sigma-Aldrich, PEG600), sorbitol (ZAG Kimya). Distilled water was utilized as the solvent phase for all formulations.

Preparation and standardization of SBP powder

To prepare the SBP for vegan leathers production, the wet pulp was first weighed into 200 g portions and dried in an oven (Ecocell) at 60°C for 48 h. The moisture content of the dried pulp was determined to be 14.6% based on the weight difference. Subsequently, the dried biomass was mechanically ground and sieved to achieve a uniform particle size of 250 µm. The resulting SBP powders were stored in a desiccator at room temperature (22±0.5°C) to maintain their stability and prevent moisture absorption.

Production of SBP-based vegan leathers

SBP-based vegan leathers were synthesized using a standardized solvent casting technique, with formulations optimized on a dry weight basis. SBP served as the primary structural matrix, ranging from 15.4% to 42.9% of the total dry weight. To ensure structural integrity and leather-forming characteristics, natural binders (starch and sodium alginate) were incorporated according to the ratios specified in Table 1, each constituting between 12.5% and 30.8% of the formulation's dry mass.

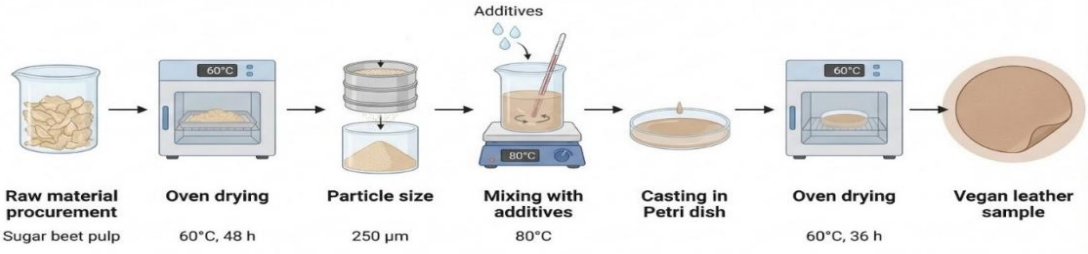

Figure 1. Schematic representation of the fabrication process of SBP-based vegan leather

Table 1. Detailed formulations and component ratios of the SBP-based vegan leather

Sample	SBP (g)	Starch (g)	Sodium alginate (g)	Glycerol (mL)	Sorbitol (g)	Additive* (wt%)	Plasticizer* (wt%)
SBP6-G	6	2	2	6	-	34.2	43.1
SBP4-G1	4	4	4	6	-	20.5	38.7
SBP4-SG	4	4	2	6	-	22.8	43.1
SBP4-AG	4	2	4	6	-	22.8	43.1
SBP6-SoG	6	2	2	3	3	35.7	40.4
SBP4-G2	4	2	2	6	-	25.7	48.6
SBP4-G3	4	2	2	8	-	22.1	55.7
SBP4-So	4	2	2	-	3	36.4	27.3
SBP2-G	2	2	2	6	-	14.7	55.8
SBP2-SG	2	4	2	6	-	12.8	48.6
SBP2-AG	2	2	4	6	-	12.8	48.6

*All weight percentages (wt%) for additives and plasticizers are calculated relative to the total solid weight of the formulation (total solids = starch + sodium alginate + SBP + plasticizer weight (glycerol + sorbitol)). Glycerol density was taken as 1.26 g/mL.

The fabrication process began with preparing a homogeneous hydrogel, where a predetermined amount of sodium alginate was dissolved in 250 mL of distilled water under constant stirring (500–900 rpm) at 80°C for 10–15 min. Starch and plasticizers, comprising 18.8% to 46.2% of the dry weight, were then integrated into the hydrogel matrix. Finally, the pre-treated SBP powder was added, and the mixture was homogenized at 80°C and 900 rpm for 30 min. The resulting viscous dopes were cast into 145 x 21 mm Petri dishes, allowed to degas, and thermally cured in a convection oven at 60°C for 36 h to yield the finalized SBP-based vegan leather (Fig. 1). Sample codes are designated by SBP content in grams (prefix SBP2/4/6), binder dominance (suffixes -SG for starch-dominant and -AG for alginate-dominant), and plasticizer type (-G for liquid glycerol, -So for solid sorbitol, and -SoG for their blend).

Characterization of produced SBP-based vegan leathers

- *Fourier transform infrared (FT-IR) spectroscopy.* The chemical structure of the SBP-based vegan leather was analyzed by ATR-FTIR (Perkin Elmer, Spectrum 100) in the range of 4000 to 650 cm^{-1} at a resolution of 4 cm^{-1} [17, 18].
- *Water vapor transmission rate (WVTR).* The WVTR of SBP-based vegan leathers was measured gravimetrically according to the ISO 14268 standard [19, 20]. Prior to testing, samples were dried at 105°C to a constant mass. Test tubes containing 15 g of anhydrous silica gel were then sealed with the vegan leather samples and secured with parafilm. The assembly weights were monitored at 24, 48, and 120 h over a five day period, and WVTR was calculated using Eqn. 1:

$$\mathrm{WVTR} = \frac{\Delta W/\Delta t}{A} \quad (1)$$

where $\Delta W/\Delta t$ is the amount of water vapor gain per unit time (g/h) and A is the exposed area of the vegan leather (m^2).

- *Water solubility.* To evaluate moisture stability, the water solubility of vegan leathers was determined [21]. Samples (2×2 cm) were dried at 105°C for 1.5 h to a constant initial dry weight (W_0), then immersed in 40 mL of distilled water for 30 min. After filtering with Sartorius 391 filter paper and draining for 40 min, the specimens were dried at 105°C for 24 h to determine their final dry weight (W_t). The water solubility percentage (WS%) was calculated according to Eqn. 2:

$$\mathrm{WS}\ (\%) = \frac{W_0 - W_t}{W_0} \times 100 \quad (2)$$

- *Thickness.* The thickness of the SBP-based vegan leathers was measured using a digital micrometer (0.1 mm precision). In accordance with the ISO 2589 standard, measurements were taken at three different points to determine the average value [22].
- *Mechanical characterization.* The mechanical properties of SBP-based vegan leathers were characterized using an Instron 5982 electromechanical universal testing machine at 22±0.5°C with a crosshead speed of 100 mm/min, following the ISO 3376 standard [23-25]. Maximum tensile force, percentage elongation, and tensile modulus were recorded. The Young's modulus (E) was evaluated from the stress-strain curves according to Eqn. 3:

$$\mathrm{E} = \frac{\sigma}{\varepsilon} = \frac{F/A}{\Delta L/L_0} \quad (3)$$

where σ is the stress (MPa), ε is the strain, F is the force (N), A is the cross-sectional area (mm^2), ΔL is the extension (mm), and L_0 is the initial gauge length (mm).

RESULTS AND DISCUSSION:

FT-IR spectroscopy

FT-IR spectroscopy was employed to elucidate the functional groups and intermolecular interactions within the SBP-based vegan leathers (Fig. 2).

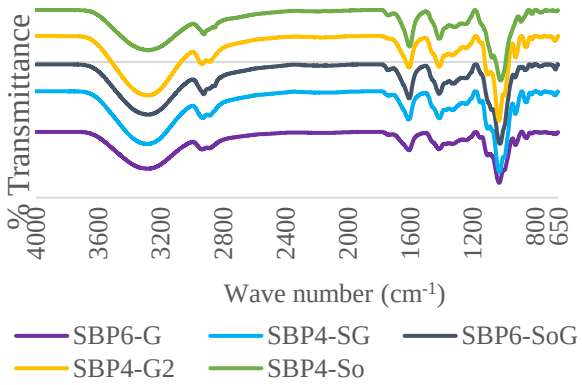

Figure 2. FT-IR spectra of SBP6-G, SBP4-SG, SBP6-SoG, SBP4-G2 and SBP4-So

The broad, intense bands at 3300–3500 cm^{-1} correspond to -OH stretching vibrations. Since SBP, starch, glycerol, and sorbitol are rich in hydroxyl moieties, peak intensities reflect moisture or plasticizer concentrations; for instance, the higher intensity in SBP6-SoG compared to SBP6-G indicates higher glycerol content [26]. The 2900–3000 cm^{-1} region represents aliphatic C-H stretching from SBP cellulose/hemicellulose, starch glucose units, and glycerol methylene ($-CH_2-$) groups, with intensity variations between SBP4-G2 and SBP4-So

directly correlating with glycerol concentration [27, 28]. The C=O stretching region (1600–1700 cm^{-1}) features carbonyl peaks from sodium alginate carboxylate ($-COO^-$) groups; where asymmetric stretching at 1600–1650 cm^{-1} and symmetric stretching near 1400 cm^{-1} confirm the alginate binder's presence [29]. The 1000–1200 cm^{-1} interval covers C-O stretching from carbohydrates (starch, SBP) and sorbitol, where peaks at 1050–1100 cm^{-1} match starch glycosidic linkages [30] and the peak around 1150 cm^{-1} stemming from SBP cellulose. Finally, sodium alginate displays a unique peak near 900–950 cm^{-1} related to its uronic acid units [31].

Barrier properties and hydrolytic stability

The water vapor transmission rate (WVTR) and water solubility (WS) of SBP-based vegan leathers are detailed in Fig. 3 and Table 2, showing significant dependence on SBP concentration, bio-material binder type, and plasticizer parameters.

Formulations with higher SBP content, such as SBP6-G (34.2%) and SBP6-SoG (35.7%), exhibited moderately increased permeability due to diffusion-facilitating micro-voids, yet achieved the lowest water solubility (31% for SBP6-G) [32]. This structural stability is attributed to the high cellulose and lignin content in SBP, which acts as a vapor hydrophobic reinforcement within the carbohydrate matrix to hinder water penetration. Exceptional barrier profiles were noted in SBP4-AG (1 $g/m^2 \cdot 120$ h) and SBP2-SG (3 $g/m^2 \cdot 120$ h). The balanced starch/sodium alginate network in SBP4-AG enhanced path tortuosity, restricting moisture transmission; however, sodium alginate-rich sets (AG series) inherently displayed higher dissolution tendencies up to 89% in the absence of additional cross-linking [28, 29].

Plasticizer type and dosage decisively influenced both moisture transport and matrix degradation. Glycerol-doped formulations (e.g., SBP4 series G1 to G3) exhibited higher WVTR and WS values because increasing glycerol content from 38.7% to 55.7% expanded the free volume and enhanced surface moisture solubility [33, 34].

Conversely, the sorbitol-plasticized SBP4-So sample demonstrated superior hydrolytic resistance and a more compact architecture; despite its low plasticizer ratio (27.3%), it maintained a balanced solubility of 47% and low permeability through a tortuous path created by sorbitol's higher crystallinity. Benchmarked against traditional shoe-upper leather, which exhibits high breathability (4.6 $mg/cm^2 \cdot h$) due to a porous fibrillar structure, the engineered SBP vegan leathers present a barrier-centric profile [25].

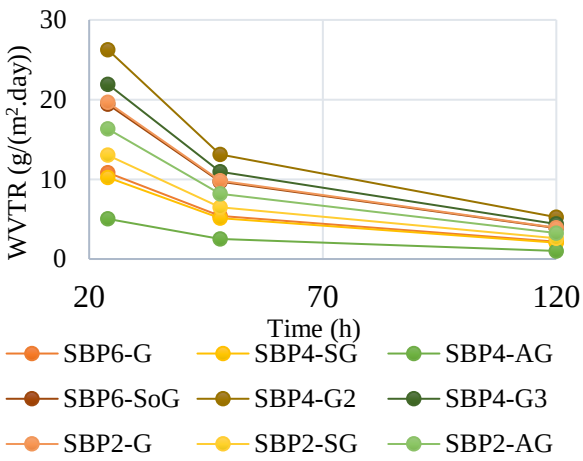

Figure 3. Time-dependent WVTR trends over a 120-h period

Table 2. Influence of SBP content and plasticizer characteristics on water solubility and WVTR of SBP-based vegan leathers

Sample	WS (%)	WVTR ($g/m^2 \cdot day$)	Plasticizer type
SBP6-G	31	10.83	Glycerol
SBP6-SoG	45	13.02	Glycerol + sorbitol
SBP4-So	47	10.23	Sorbitol
SBP4-G1	41	19.41	Glycerol
SBP4-G2	37	5.03	Glycerol
SBP4-G3	51	16.32	Glycerol
SBP4-SG	45	26.26	Glycerol (starch-rich)
SBP4-AG	58	21.93	Glycerol (alginate-rich)
SBP2-G	56	19.65	Glycerol
SBP2-SG	77	5.03	Glycerol (starch-rich)
SBP2-AG	89	-	Glycerol (alginate-rich)

Their daily WVTR values (15–50 g/m^2·day) closely align with dense, polymeric-coated commercial alternatives like Appleskin (0.4 mg/cm^2·h), Desserto (0.5 mg/cm^2·h), and Vegea (0.7 mg/cm^2·h), staying highly competitive with traditional PU/PVC synthetics. While bio-based alternatives frequently encounter moisture-sensitivity challenges, the optimized stability of SBP6-G (31% WS) and SBP4-G2 (37% WS) demonstrates that adjusting binder-filler and plasticizer configurations successfully regulates water resistance. As emphasized by Haneef *et al.* [35], plant-based composites offer superior functional comfort through regulated moisture transfer compared to purely synthetic materials, validating these durable SBP formulations for advanced footwear and upholstery applications.

Mechanical characterization and tensile performance

The mechanical properties of SBP-based vegan leathers were systematically evaluated to elucidate the effects of filler-binder interactions and plasticizer types (Table 3).

Table 3. Thickness (mm), tensile strength (MPa), elongation (%) and Young modulus (MPa) of produced SBP-based vegan leathers

Sample	Thickness (mm)	Tensile strength (MPa)	Elongation at break (%)	Young's modulus (MPa)
SBP6-G	1.2	6.00	53.81	7.19
SBP4-SG	0.7	4.49	15.40	66.58
SBP6-SoG	1.1	5.95	23.43	29.29
SBP4-G2	0.8	3.32	41.89	6.38
SBP4-So	0.5	22.26	2.34	1374.22

The mechanical profile is predominantly governed by SBP loading and the molecular characteristics of the plasticizing agent. Formulations with elevated SBP content, such as SBP6-G and SBP6-SoG, exhibited moderate tensile strength. While SBP fibers function as structural reinforcement, an excessive filler to binder ratio disrupts the polymer matrix's continuity, promoting stress concentration points and limiting tensile strength relative to optimized intermediate formulations [36].

Fig. 4 illustrates the macrostructural appearance and flexibility of the fabricated vegan leathers. A profound divergence in mechanical performance is observed based on the specific plasticizer utilized.

Figure 4. Macrostructural appearance of the fabricated A) SBP4-SG and B) SBP6-SoG

Glycerol-plasticized SBP4-G2 demonstrated a ductile profile with low rigidity, whereas SBP4-So outperformed all variations, achieving peak tensile strength of 22.26 MPa and Young's modulus of 1374.22 MPa. This substantial enhancement is linked to the higher crystallinity and distinct molecular configuration of sorbitol. While smaller polyols like glycerol increase free volume and chain mobility, sorbitol's larger structure and higher hydroxyl density facilitate a denser hydrogen-bonded network, resulting in a more compact and rigid architecture [37]. In alignment with polymer theory, an inverse correlation was recorded between elongation at break and Young's modulus (Fig. 5). Formulations with high glycerol content (e.g., SBP4-SG and SBP4-G2) exhibited superior ductility due to reduced intermolecular forces and enhanced chain slippage ("lubrication effect") [38]. Conversely, SBP4-So transitioned toward a high-strength, semi-brittle state. These findings confirm that the mechanical profile can be tailored for diverse industrial needs by strategically selecting the plasticizer and SBP loading.

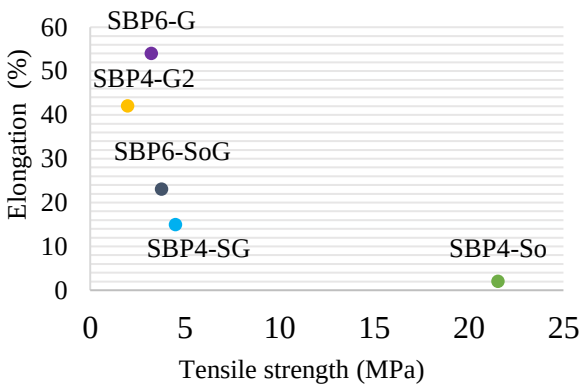

Figure 5. Relationship between tensile strength and elongation at break of SBP-based vegan leathers

The technical performance of SBP4-So exhibits highly competitive characteristics when benchmarked against commercial leather and contemporary alternatives reported by Meyer *et al.* [39]. The thickness of the synthesized specimens (0.5–1.2 mm) directly aligns with commercial bio-based alternatives like Appleskin (1.14 mm), Desserto (0.88 mm), and Vegea (1.06 mm). In terms of mechanical strength, traditional shoe leather

maintains the highest value at 39.5 N/mm^2; however, alternatives like Appleskin (14.0 N/mm^2), Vegea (9.4 N/mm^2), and Muskin (0.2 N/mm^2) fall substantially below the value achieved in this study. Notably, the tensile strength of SBP4-So successfully meets the industrial requirement for shoe uppers (>15 N/mm^2). While Desserto (20.8 N/mm^2) and SnapPap (24.9 N/mm^2) present similar profiles, the superior load-bearing capacity of sorbitol-based SBP vegan leathers positions them as technically viable, sustainable candidates for high-durability applications.

CONCLUSION

This study demonstrates the potential of SBP as a sustainable reinforcing agent in starch and sodium alginate-based vegan leathers. FT-IR analysis confirmed robust hydrogen bonding interactions between the bio-material binders and lignocellulosic SBP fibers, proving it acts as an effective reinforcing filler. The thickness of the synthesized specimens directly aligns with commercial standards, while water solubility analyses revealed that the cellulosic nature of SBP combined with the crystalline structure of sorbitol enhanced hydrolytic resistance. Plasticizer type and filler ratio were critical to mechanical performance; the sorbitol-plasticized SBP4-So formulation exhibited the most outstanding profile, with tensile strength and Young's Modulus values that exceed the industrial limit for shoe-upper production and surpass commercial competitors. Regarding barrier properties, SBP4-AG and SBP2-SG displayed exceptional character with low transmission rates. While differing from the high breathability of traditional leather, these WVTR values align closely with commercial alternatives. In conclusion, the optimized SBP-based vegan leathers integrate low environmental impact with high mechanical strength, offering a technically viable and sustainable alternative to traditional synthetic PU/PVC materials in the textile, footwear, and upholstery sectors.

REFERENCES

1. C. R. China, M. M. Maguta, S. S. Nyandoro, A. Hilonga, S. V. Kanth, K. N. Njau, *Chemosphere*, **254**, 126847 (2020).
2. A. Kaya, B. Demir, C. Yilmaz, *J. Clean. Prod.*, **215**, 123 (2023).
3. K. Niinimäki, Sustainable fashion in a circular economy, Routledge, London, 2017, p. 1.
4. X. Liu, X. Zhang, X. Wang, O. Yue, H. Jiang, *Trends Biotechnol.*, **43**, 1104 (2025).
5. G. Venturelli, L. Guida, M. G. T. Fasani, S. Mantero, P. Petrini, M. Levi, *Appl. Mater. Today*, **44**, 102776 (2025).
6. J. Crouse, S. Sellers, K. Wawrousek, R. M. Sabino, *ACS Omega*, **10**, 12002 (2025).
7. Ethicwater, Comprehensive guide on single-use plastics, Ethicwater Reports, London, 2024, p. 1.
8. S. Golomeova Longurova, S. Risteski, S. Zhezhova, S. Jordeva, V. Dimitrijeva-Kuzmanoska, *Koža Obuća*, **74**, 7 (2025).
9. Bolt Threads, What is Mylo™, Technical Brief, Emeryville, 2024, p. 1.
10. Desserto, Sustainable cactus-based biomaterial, Product Whitepaper, Guadalajara, 2024, p. 1.
11. C. R. M. Sanchez, J. A. Torres, L. M. Gomez, *J. Nat. Fibers*, **18**, 641 (2021).
12. S. S. Muthu, M. Ramchandani, Vegan alternatives for leather, Springer, Singapore, 2024, p. 1.
13. TÜİK, Turkish sugar industry waste statistics, Turkish Statistical Institute, Ankara, 2023, p. 1.
14. J. F. Thibault, *Food Hydrocolloids*, **15**, 1 (2001).
15. B. Gökdemir, K. Sever, M. Atagür, İ. Şen, *J. Eng. Sci. Des.*, **13**, 791 (2025).
16. M. K. ResearchGate, Ferulic acid crosslinking in pectin networks, *Polym. Briefs*, **4**, 15 (2019).
17. H. N. Phan, S. Okubayashi, *Cellulose*, **32**, 4939 (2025).
18. P. Narayanan, S. K. Janardhanan, *Collagen Leather*, **6**, 1 (2024).
19. B. W. J. Ko, S. H. Park, Y. J. Kim, *Polym. Test.*, **76**, 101 (2019).
20. ISO 14268, Leather-Physical and mechanical tests-Determination of water vapour permeability, International Organization for Standardization, Geneva, 2023, p. 1.
21. S. Farris, L. Piergiovanni, J. M. Krochta, *Food Hydrocolloids*, **30**, 383 (2013).
22. ISO 2589, Leather-Physical and mechanical tests-Determination of thickness, International Organization for Standardization, Geneva, 2016, p. 1.
23. ASTM D882-18, Standard test method for tensile properties of thin plastic sheeting, ASTM International, West Conshohocken, 2018, p. 1.
24. ISO 527-3, Plastics—Determination of tensile properties—Part 3, International Organization for Standardization, Geneva, 2018, p. 1.
25. ISO 3376, Leather-Physical and mechanical tests-Determination of tensile strength and percentage elongation, International Organization for Standardization, Geneva, 2020, p. 1.
26. M. Kacuráková, R. H. Wilson, *J. Appl. Polym. Sci.*, **82**, 1 (2001).
27. R. M. Silverstein, Spectrometric identification of organic compounds, Wiley, New York, 2014, p. 1.
28. L. Pereira, A. M. Silva, G. T. Sousa, *Carbohydr. Polym.*, **93**, 402 (2013).
29. G. T. Grant, E. R. Morris, D. A. Rees, *Nature*, **215**, 756 (1967).
30. K. Bledzki, A. Jaszkiewicz, *Compos. Sci. Technol.*, **70**, 1687 (2010).

31. H. H. Tønnesen, J. Karlsen, *Drug Dev. Ind. Pharm.*, **28**, 621 (2002).
32. D. Gorecka, M. Krzywdzinska, A. Szwengiel, *Carbohydr. Polym.*, **291**, 119502 (2022).
33. S. Chen, B. Zhang, J. Wang, *Polym. Test.*, **89**, 106621 (2020).
34. Syarifuddin, N. Haliza, N. Izzah, M. M. Tahir, A. Dirpan, *Foods*, **14**, 1219 (2025).
35. M. Haneef, H. Bertrand, D. S. Cloutier, *Sci. Rep.*, **7**, 46647 (2017).
36. C. Yılmaz, B. Sever, A. E. Öztürk, *Waste Biomass Valorization*, **13**, 1123 (2022).
37. S. Demir, M. Atagür, İ. Şen, *Sustain. Mater. Technol.*, **35**, 105678 (2023).
38. E. Öztürk, K. Sever, B. Gökdemir, *J. Clean. Prod.*, **312**, 127689 (2021).
39. M. Meyer, S. Dietrich, H. Schulz, A. Mondschein, *Coatings*, **11**, 226 (2021).

Bulgarian Chemical Communications, Volume 58, Issue 3 (pp. 276-280) 2026 *DOI: 10.34049/bcc.58.3.D006*

Forensic identification of pen ink pigments using dual-wavelength Raman spectroscopy combined with chemometrics

D. S. İşlek*, E. Kiriş, A. Şen Yılmaz, E. Köse

Istanbul University-Cerrahpasa Institute of Forensic Sciences and Legal Medicine, Department of Science, Istanbul, Türkiye

Accepted: July 28, 2026

In forensic document examination, ink analysis plays a crucial role in investigating forgery crimes. Raman spectroscopy is frequently preferred in ink analysis due to the absence of a sample preparation step, its non-destructive nature, and its rapid analysis process. In this study, pigment blue (PB 15:1, 15:3, 15:4, and PB 15:4 Mallak), which is commonly used as a colorant in ballpoint pen inks, methyl violet (MV), and crystal violet (CV) pigments, which are commonly used as colorants in ballpoint pen inks, were analyzed using confocal Raman spectroscopy at wavelengths of 532 nm and 785 nm. After applying data preprocessing to the obtained spectra, the spectral data were analyzed using principal component analysis (PCA). Upon examining the study results, it was determined that the spectral data were separated into two distinct clusters (triarylmethanes and phthalocyanines) that did not overlap. In conclusion, the use of two-wavelength Raman spectroscopy in conjunction with PCA provides a fast, reliable, and statistically validated non-destructive approach for the characterization and classification of pigments commonly used in inks.

Keywords: Pigment analysis, Raman spectroscopy, Forensic chemistry, Principal component analysis (PCA)

INTRODUCTION

Document examination in forensic science plays a critical role in solving forgery cases. In these examinations, ink analysis is one of the most fundamental methods used to detect forgery. Traditionally, the chemical profiling of inks has been performed using separation techniques such as thin-layer chromatography (TLC), gas chromatography-mass spectrometry (GC-MS), and high-performance liquid chromatography (HPLC) [1, 2]. However, chromatographic methods cannot fully meet the non-destructive analysis requirements of the judicial system today, as they require physical sample collection and compromise the integrity of the document.

For this reason, in recent years, experts have preferred fast and non-destructive spectroscopic techniques that do not require a sample preparation stage in forensic document examinations. In this context, Raman spectroscopy has become one of the most preferred analytical techniques in ink analysis due to its ability to characterize the chemical structure of inks on documents with high precision [3-5]. Raman spectroscopy has been used for the analysis and differentiation of a wide variety of ink formulations, including gel pens and stamp inks [6, 7]. Furthermore, the superiority of Raman spectroscopy over other methods in elucidating ink aging processes, the photodegradation of dyes over time, and degradation dynamics on paper has been reported in numerous studies [8-10].

The identification and classification of inks is possible through the accurate identification of the dyes and pigments present in their formulations. In particular, triarylmethane dyes and phthalocyanine pigments, which are frequently found in the composition of blue and black ballpoint pen inks, constitute one of the main focuses of ink analysis [11-13]. In the literature, studies have been conducted on the vibrational characterization of triarylmethane-derived dyes (e.g., crystal violet), their analysis *via* surface-enhanced Raman scattering (SERS), and their degradation mechanisms under light exposure [14, 15]. Similarly, phthalocyanine-based pigment blue 15 (PB15) derivatives have been analyzed both as a dye pigment and as an ink component [16]. These studies are based on the complex chemical and structural variations inherent in these pigments. crystal violet and methyl violet, which stand out in ink formulations, are closely related triarylmethane dyes sharing a common molecular skeleton and possessing a carbocation structure with resonance stabilization. In both pigments, there is a central, positively charged carbon atom bonded to three phenyl rings, at least two of which contain nitrogen groups, and the main structural differences between

* To whom all correspondence should be sent:
E-mail *dsislek@iuc.edu.tr*

© 2026 Bulgarian Academy of Sciences, Union of Chemists in Bulgaria

the molecules stem from the number of methyl groups attached to the nitrogen atoms [17, 18]. The PB 15 pigments has a large, flat, and symmetrical macrocyclic ring. It consists of four isoindole units linked to each other *via* nitrogen atoms. A 16-membered inner ring containing a chelated copper ion is formed at its center. PB 15:1 (alpha form) has an unstable alpha crystal structure. PB 15:3 (beta form) has a stable beta crystal structure. It is a pure, unchlorinated copper phthalocyanine. PB 15:4 (beta form + derivatives) shares the same pure, unchlorinated beta-copper phthalocyanine chemical core as PB 15:3. However, it is physically/chemically modified with specific derivatives (such as sulfonated or aminomethyl-substituted phthalocyanines) to prevent agglomeration [19-21]. The chemical structures of the pigments are shown in Figure 1.

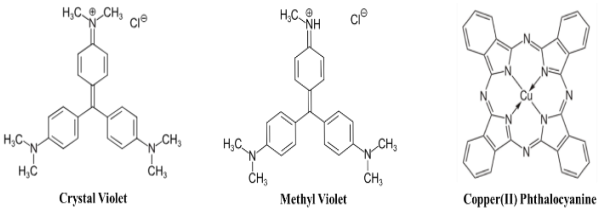

Figure 1. Chemical structures of the pigments

Upon reviewing studies on pigment analysis in the literature, it has been observed that due to the structural complexity of spectral data obtained via Raman spectroscopy and matrix effects, multivariate data analysis techniques must be used in conjunction with these analyses. The integration of chemometric methods, such as principal component analysis (PCA), with spectroscopic data enables the statistical clustering of chemical variations in inks and the creation of discrimination models [22, 23].

In this study, phthalocyanine pigment derivatives commonly encountered in ink structures during forensic document examination (PB 15:1, 15:3, 15:4, and PB 15:4 Mallak) and the pigments MV and CV, using wavelengths of 532 nm and 785 nm. The obtained data were examined using principal component analysis (PCA), revealing that the ink spectra could be classified into two main clusters: triarylmethane and phthalocyanine. In conclusion, the combination of two-wavelength Raman spectroscopy with chemometric approaches (PCA) was found to be a fast, reliable, and non-destructive analytical method for the characterization and classification of ink pigments in the investigation of forgery crimes.

EXPERIMENTAL

Chemicals and sample preparation

In this study, methyl violet (MV), crystal violet (CV), and phthalocyanine group derivatives (PB 15:1, 15:3, 15:4, PB 15:4 Mallak) which are commonly used as colorants in inks—were analyzed. Phenoxyethanol (TCI, Japan) was used as the solvent during the transfer of pigments onto paper. A 1 mg sample of each pigment was weighed and dissolved in 2 mL of phenoxyethanol to form a solution. The prepared solutions were dispensed onto a standard paper surface using a glass pipette and left to dry to allow the solvent to evaporate, thereby preparing the samples for spectroscopic analysis.

Raman spectroscopy analysis

Spectral analyses were performed using a confocal Raman spectrometer with two different wavelengths. The system utilized a 532 nm (green) diode laser with a power of 50 mW and a 1800 lines/mm grating, along with a 785 nm (red) air-cooled diode laser source with a power of 300 mW and a 1200 lines/mm grating. During measurements, parameters such as exposure time, laser power, and accumulation were optimized to maximize spectral quality.

A 785 nm laser source was used in the analysis of phthalocyanine group pigment blue (PB 15:1, 15:3, 15:4) derivatives, which are frequently encountered in gel pen formulations. The characteristic spectra of this group were successfully obtained in static mode at a central wavelength of 1100 cm^{-1}, with an exposure time of 25 seconds and a laser power of 0.0001%.

In contrast, during the analysis of triarylmethane based MV and CV pigments, severe fluorescence interference was observed at the 785 nm wavelength due to their specific chromophore structures, and spectral data could not be obtained. To overcome this issue, a laser source with a wavelength of 532 nm was used in the system. By re-optimizing the parameters (static mode, center: 1100 cm^{-1}, exposure time: 5 sec, Laser power: 0.5%), the fluorescence effect was successfully suppressed, and the characteristic Raman peaks of these pigments were clearly observed.

Data preprocessing and chemometric analysis

Data preprocessing steps were applied to reduce noise in the raw spectral data obtained from the Raman system and to improve the quality of the analysis. To this end, baseline subtraction was performed, and the data were smoothed using the

Savitzky–Golay algorithm (Window: 9, Polynomial Order: 2).

The chemometric analysis and graphical representations of the spectral data following preprocessing were performed using OriginPro 2025b (OriginLab Corporation, Northampton, MA, USA) software. PCA was applied to reduce the complexity and dimensionality of the multivariate dataset, explain the relationships among variables, and visualize the clustering tendencies of the samples. To prevent the variables included in the analysis from being affected by differences in scale, the PCA model was constructed based on the correlation matrix, and the principal components explaining the highest variance in the system were interpreted.

RESULTS AND DISCUSSION

CV and MV analysis

CV and MV, which belong to the triarylmethane class of dyes, constitute the primary coloring components of blue ballpoint pen inks. The Raman spectra of CV and MV, obtained experimentally, are shown in Figure 2.

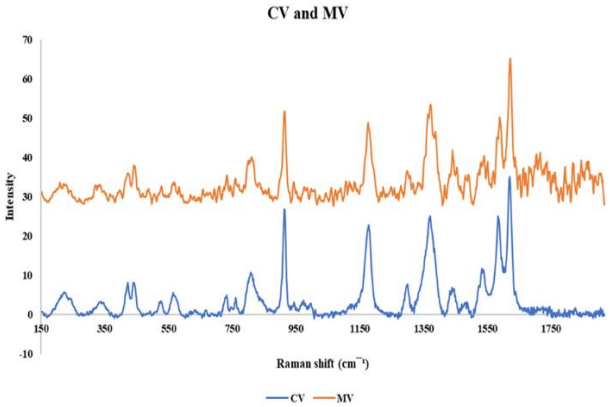

Figure 2. Raman spectra of CV and MV

Upon examination of the spectral data in Figure 2, the ~1619–1621 cm⁻¹ band was identified as the most intense peak for both pigments. This peak corresponds to the C–C central stretching vibrations of the aromatic ring in the triarylmethane structure [11, 12]. The strong peaks observed in the ~1584–1588 cm⁻¹ band represent the C=C stretching and asymmetric stretching vibrations of the aromatic ring [23]. The asymmetric stretching vibrations of the structure linking the central carbon atom to the phenyl rings, or the N-phenyl bond (C-N), appear as a very distinct peak in the ~1370–1371 cm⁻¹ band range [15]. The in-plane bending vibrations of the C–H bonds in the aromatic structure produce a strong peak in the ~1175–1177 cm⁻¹ range, consistent with the literature [13]. The ~912–914 cm⁻¹ band is characterized by the ring skeleton vibrations of the triarylmethane molecule and is one of its characteristic peaks [9]. The peak around ~809 cm⁻¹ reflects C-H out-of-plane bending and yields a signal of moderate intensity; while the signals in the ~422–443 cm⁻¹ range form weak peaks representing deformations of the entire molecular skeleton [15].

PB15 analysis

PB15 pigment derivatives, commonly used as colorants in the formulation of blue gel pen inks, were analyzed by Raman spectroscopy.

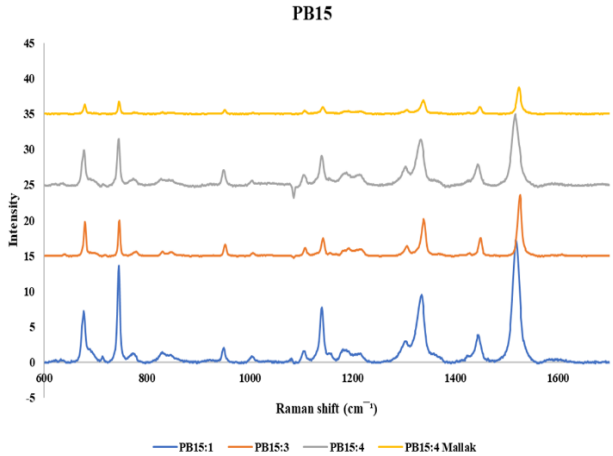

Figure 3. Raman spectra of pigment blue (PB 15:1, 15:3, 15:4) derivatives

Upon examination of the spectral data in Figure 3, characteristic and reproducible spectral profiles were identified due to the highly stable macrocyclic structure of the PB15 derivatives. The high Raman scattering of PB15 ensures that the pigment can be distinguished despite fluorescence or masking effects that may be caused by resins, solvents, and other additives in the ink mixture. In the obtained data, the intense peaks at 1530 cm⁻¹, 1342 cm⁻¹, and 748 cm⁻¹ are considered distinctive peaks indicating the presence of PB15 in the ink formulation [6]. Furthermore, upon examination of the spectral data obtained in the study, the strong signal observed at the ~1530 cm⁻¹ band was found to correspond to the asymmetric stretching of C=N and C=C bonds in the pyrrole rings; the peak at the ~1342 cm⁻¹ band, on the other hand, corresponds to the symmetric stretching of C-N and C-C bonds in the isoindole skeleton. The peak detected in the low-wavenumber region at ~748 cm⁻¹ originates from a vibration representing the overall stretching of the molecule [16]. The characteristic Raman vibrational modes, types, and signal intensities of triarylmethane (CV and MV) and macrocyclic phthalocyanine pigment derivatives (PB 15:1, 15:3, 15:4) are presented in a comparative manner in Table 1.

Table 1. Characteristic Raman vibration modes of CV, MV, and PB15

Raman shifts (cm^{-1})	Vibration type	Triaryl methane group (CV, MV)	Cu(II) phthalo cyanine group (PB 15:1, 15:3, 15:4)
~1619 - 1621	Aromatic ring C-C stretching	S	-
~1584 - 1588	Aromatic ring C=C stretching	S	-
~1528 - 1530	Pyrrole ring C=N and C=C asymmetric stretching	-	S
~1450 - 1453	Isoindole ring stretching	-	M
~1370 - 1371	N-phenyl (C–N) stretching	S	-
~1340 - 1342	Isoindole ring C–N and C–C symmetric stretching	-	S
~1175 - 1177	Aromatic C–H in-plane bending	S	-
~1143 - 1145	C–H in-plane bending	-	M
~912 - 914	Ring skeletal vibration	S	-
~809 - 811	C–H out-of-plane bending	M	-
~746 - 748	Macrocycle breathing and C–H out-of-plane bending	-	S
~680 - 682	Skeletal deformation	-	W
~422 - 443	Skeletal deformation	W	-

S: strong, M: medium, W: weak

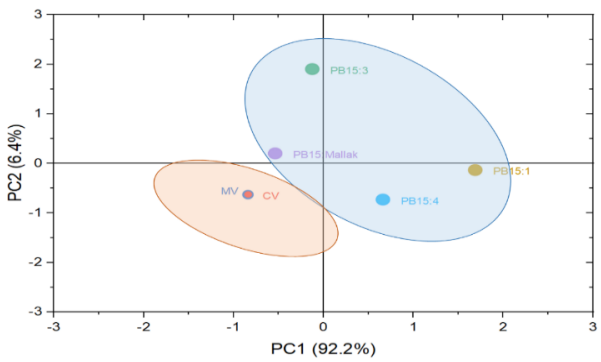

Figure 4. PCA plot of the analyzed pigments (CV, MV, PB 15:1, PB 15:3, and PB 15:4)

PCA analysis

The PCA plot created to statistically model the vibrational differences at the molecular level of the analyzed pigments (CV, MV, PB 15:1, PB 15:3, and PB 15:4) is shown in Figure 4.

When examining the model based on the first two principal components (PC1 and PC2), which account for the vast majority of the system's total variance, the dataset is seen to be modeled quite successfully from a chemometric perspective. The distributions in the graph not only separate the pigment classes with different chemical skeletons but also distinguish derivatives that are structurally very close to one another.

The graph clearly shows that the triarylmethane group (CV and MV) and the phthalocyanine-based macrocyclic pigments (PB 15 series) are clustered in distinct planes. In the grouping of triarylmethane pigments, the C-C and C=C stretching vibrations of the aromatic ring skeleton (1621 cm^{-1} and 1586 cm^{-1}), the N-phenyl C-N asymmetric stretch (1371 cm^{-1}), and the in-plane bending vibrations of the aromatic C-H bonds (1176 cm^{-1}). In contrast, the 1530 cm^{-1} peak, representing the C=N and C=C stretches of the pyrrole ring, the 1342 cm^{-1} peak indicating the C-N/C-C symmetric stretching specific to the isoindole ring, and the 748 cm^{-1} peak corresponding to the molecule's macrocycle vibration were found to emerge as statistical discriminants distinguishing PB15 derivatives from triarylmethanes.

CONCLUSION

In this study, triarilmethanes (crystal violet and methyl violet) and phthalocyanines (pigment blue 15 derivatives), which are the coloring components of blue ballpoint and gel pen inks frequently encountered in forensic document examinations, were characterized and classified using dual-wavelength (532 nm and 785 nm) confocal Raman spectroscopy and chemometric analysis.

The spectroscopic analyses performed demonstrated that severe fluorescence interference caused by different chromophore structures in the ink matrices can be effectively overcome by selecting laser wavelengths appropriate for the target molecule (532 nm for triarylmethanes, 785 nm for phthalocyanines) and optimizing the analysis parameters. Thanks to this approach, characteristic molecular vibrations of both pigment classes were identified.

The obtained spectral data were statistically modeled using PCA. As a result, triarylmethane and phthalocyanine pigments were separated into two main clusters, and the more difficult-to-distinguish crystal polymorphs (PB 15:1, PB 15:3, PB 15:4) were also distinguished within their own groups.

In conclusion, the use of multivariate chemometric analyses such as PCA in confocal Raman spectroscopy offers a fast and reliable approach for

the examination of suspect documents while preserving sample integrity.

Acknowledgement: *This study was supported by Istanbul University-Cerrahpasa Scientific Research Project Unit (BAP) under ID Number 38215.*

REFERENCES

1. V. N. Aginsky, *Journal of the American Society of Questioned Document Examiners*, **9**(1) 19 (2006). https://doi.org/10.69525/jasqde.128
2. J. Andrasko, *Journal of Forensic Sciences*, **46**(1), 21 (2001). https://doi.org/10.1520/JFS14907J
3. A. Braz, M. López-López, C. García-Ruiz, *Forensic Science International*, **232**(1-3), 206 (2013). https://doi.org/10.1016/j.forsciint.2013.07.017
4. H. G. Edwards, Analytical Raman spectroscopy of inks, 2018, https://doi.org/10.1039/9781788013475-00001
5. R. R. Souza, L. M. Duarte, G. B. Ferreira, *Analytical Methods*, **17**(12), 2515 (2025). https://doi.org/10.1039/D4AY01951B
6. W. D. Mazzella, P. Buzzini, *Forensic Science International*, **152**(2-3), 241 (2005). https://doi.org/10.1016/j.forsciint.2004.09.115
7. A. Raza, B. Saha, *Science & Justice*, **53**(3), 332 (2013). https://doi.org/10.1016/j.scijus.2012.11.001
8. M. V. Adamos, W. D. Rickard, W. van Bronswijk, G. Sauzier, *Applied Surface Science*, **705**, 163500 (2025).https://doi.org/10.1016/j.apsusc.2025.163500
9. K. O. Gorshkova, I. I.Tumkin, L. A. Myund, A. S Tverjanovich, A. S. Mereshchenko, M. S. Panov, V. A. Kochemirovsky, *Dyes and Pigments* **131,** 239 (2016). https://doi.org/10.1016/j.dyepig.2016.04.009
10. N. M. Grechukha, K. O. Gorshkova, M. S. Panov, I. I. Tumkin, E. O. Kirillova, V. V. Lukianov, V. A. Kochemirovsky, *Applied Sciences*, **7**(10), 991 (2017). https://doi.org/10.3390/app7100991
11. A. Alyami, K. Barton, L. Lewis, A. Mirabile, D. Iacopino, *Journal of Raman Spectroscopy*, **50**(1), 115-126 (2019). https://doi.org/10.1002/jrs.5512
12. I. Geiman, M. Leona, J. R. Lombardi, *Journal of Forensic Sciences*, **54**(4), 947 (2009). https://doi.org/10.1111/j.1556-4029.2009.01058.x
13. D. Saviello, M. Trabace, A. Alyami, A. Mirabile, P. Baglioni, R. Giorgi, D. Iacopino, *Frontiers in Chemistry*, **7**, 727 (2019). https://doi.org/10.3389/fchem.2019.00727
14. A. Cesaratto, J. R. Lombardi, M. Leona, *Journal of Raman Spectroscopy*, 48(3), 418 (2017). https://doi.org/10.1002/jrs.5056
15. W. Meng, F. Hu, L. Y. Zhang, X. H. Jiang, L. D. Lu, X. Wang, *Journal of Molecular Structure*, **1035**, 326 (2013). https://doi.org/10.1016/j.molstruc.2012.10.066
16. C. Defeyt, D. Strivay, *E-Preservation Science*, **11** (2014). https://hdl.handle.net/2268/191490
17. National Center for Biotechnology Information, PubChem Compound Summary for CID 11057, Crystal Violet. https://pubchem.ncbi.nlm.nih.gov/compound/Crystal-Violet
18. National Center for Biotechnology Information, PubChem Compound Summary for CID 14345209, Methyl Violet 2B(1+). https://pubchem.ncbi.nlm.nih.gov/compound/14345209
19. Baoxu Chemical, Pigment Blue 15:4, BASF K7104 Supplier. https://www.additivesforpolymer.com/portfolio/pigment-blue-154/
20. CymitQuimica, CAS 147-14-8: Pigment Blue 15:3. https://cymitquimica.com/cas/147148/?srsltid=AfmBOoqc6foN9HUQvG4biPGLs2NtglDlJzoJfgWuTtFHITV5EQmjh4Vl
21. iSuoChem, C.I.74160/Phthalocyanine Blue/Phthalo Blue/PB 15:1. https://www.ispigment.com/c-i-74160-phthalocyanine-blue-phthalo-blue-pb-15-1-isuochempigmentforpaints_p574.html
22. C. A. Teixeira, R. J. Poppi, *Microchemical Journal*, **144**, 411 (2019). https://doi.org/10.1016/j.microc.2018.10.002
23. B. Doherty, M. Vagnini, K. Dufourmantelle, A. Sgamellotti, B. Brunetti, C. Miliani, *Spectrochimica Acta Part A: Molecular and Biomolecular Spectroscopy*, **121**, 292 (2014). https://doi.org/10.1016/j.saa.2013.10.069

Bulgarian Chemical Communications, Volume 58, Issue 3 (pp. 281-285) 2026 *DOI: 10.34049/bcc.58.3.D007*

Removal of Disperse Orange 30 dye from simulated wastewater using formaldehyde-stabilized quince leaf powder bioadsorbent

D. Şakar[1]*, H. K. Gürakin[2],

[1*]*Yildiz Technical University, Chemistry Department, 34220, Esenler, Istanbul, Türkiye*
[2]*SETAŞ Kimya Sanayi A.Ş., Organized Industrial Zone, Karaagac Mah. 9th Street No:3 59510 Kapakli, Tekirdağ, Türkiye*

Accepted: July 28, 2026

In this work, quince leaves, which are a natural adsorbent, were used in their pure form with stabilised with formaldhyde. The formaldhyde stabilised quince leaves was prepared and used to determine the optimum conditions for the adsorption of disperse orange 30 (DO-30) from simulated synthetic wastewater. Within this scope, parameters such as bioadsorbent dosage (0.8 g and 1 g), 10, 30, 60, 90, and 120 min as contact time, 25, 30, 40, 50, and 60 °C as adsorbtion temperature, and 50, 100, 150, 200, 250, 300 mg/L as initial dye concentrations were investigated. Based on the experimental data obtained, the adsorption behavior of DO-30 onto formaldhyde stabilised quince leaves was evaluated. Langmuir, Freundlich, and Temkin isotherm models were applied to analyze the adsorption equilibrium of DO-30 dye adsorbed on formaldhyde stabilised quince leaves bioadsorbent, while the pseudo-first-order, pseudo-second-order, and intraparticle diffusion models were used to examine the adsorption kinetics.

Keywords: *Formaldhyde stabilised quince leaves bioadsorbent; disperse orange 30 dye; dye removal yield; adsorption kinetics and isotherms*

INTRODUCTION

In recent years, the use of biologically derived adsorbents has increased in line with environmentally friendly and sustainable approaches. Biosorbents obtained from natural materials have attracted attention due to eco-friendly dye removal from wastewater. Biosorbents are biological materials used to adsorb or absorb contaminants, such as microorganisms, trash formed from biomass, or industrial byproducts. Heavy metals, dyes, and medications are just a few of the pollutants they have been utilized to eliminate. These materials are inexpensive, renewable, biodegradable, and require little processing. Because of their abundance, inherent surface functionality, and efficiency in binding dye molecules, plant-based adsorbents in particular have been thoroughly researched. Biosorbents, owing to their chemical and porous structures, can be used without any modification. Plant waste and biomass-based adsorbents are considered as alternatives to activated carbon due to their low cost, renewability, and lack of environmental impact [1-3]. Literature shows that quince leaves, thanks to their phenolic structures and functional groups, are an effective bioadsorbent for the adsorption of dyes such as safranin [4].

This study's primary goal is to investigate formaldhyde stabilised quince leaves adsorption capabilities for removing Disperse orange 30 dye from artificial wastewater solutions. Adsorption experiments were conducted using formaldhyde stabilised quince leaves under different adsorbent dosages (0.8 g and 1 g), adsorption contact time, adsorption temperature, and initial dye concentrations. The effects of both adsorbent dosage on dye removal were analyzed. Furthermore, the suitability of the system for isotherm and kinetic models was evaluated based on the experimental data obtained, and inferences were made regarding the adsorption mechanism.

EXPERIMENTAL

Cleaned and dried quince leaves were stabilised with formaldyhde to stabilize the green colour of leaves and used as bioadsorbents in the study. Disperse orange 30 dye was supplied by SETAŞ. The used devices were Sigma trademark 3-18K model ultracentrifuge, Shimadzu UV/ VIS 2600 spectrophotometer and Daihan Scientific multi-heat mixer. The UV spectra of DO-30 dye solutions at different concentrations was done and the DO-30 calibration curve equation was obtained as $A=0.0201C+0.9979$ ($R^2=0.9929$) at 450 nm absorbances.

RESULTS AND DISCUSSION

The dried ground quince leave bioadsorbents were used to eliminate the DO-30 dyestuff from artificial wastewater solutions via adsorption process. The parameters such as 10–30-60-90-120

* To whom all correspondence should be sent:
E-mail: *dsakar@yildiz.edu.tr*

© 2026 Bulgarian Academy of Sciences, Union of Chemists in Bulgaria

min adsorption contact time in 100 mg/L DO-30 dye, 25-30-40-50–60 °C adsorption temperatures in 100 mg/L DO-30 dye, 50-100-150-200-250-300 mg/L initial dye concentrations, and 0.8 and 1 g adsorbent dosages were applied.

In contact time studies conducted using 0.8 and 1 grams of adsorbent, it was seen that the adsorption efficiency decreased as the contact time increased. The graph of the relevant parameters is shown in Figure 1.

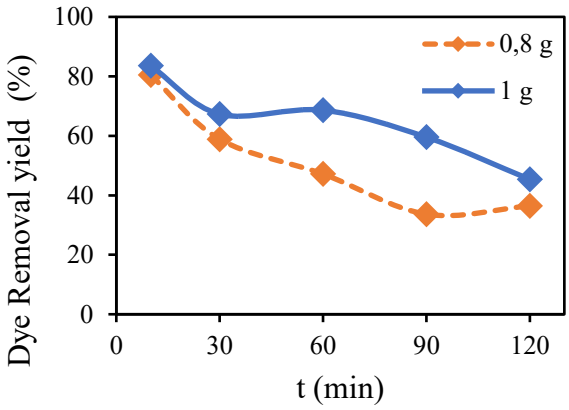

Figure 1. Contact time effect on dye removal yield for 0.8 g and 1 g bioadsorbent

As shown in Figure 1, increasing the adsorbent dose from 0.8 g to 1 g and increasing the contact time significantly reduced the dye removal efficiency from 10 min. to 30 min. This result suggests that the dye in the quince leaf transferred to the water over time because of this, dye in quince leaf stabilised with formaldyhde.

The temperature studies were conducted between 25-60 °C, a decrease in adsorption efficiency was observed with increasing temperature. The temperature study performed with a dosage of 0.8 g of bioadsorbent is shown in Figure 2, and with 1 g - in Figure 3.

Other studies were done with formaldhyde stabilised quince leaves bioadsorbent. Langmuir [5], Freundlich [6], and Temkin [7] isotherm models were applied for 0.8 g and 1g of adsorbents at 10, 30 and 60 min.

In studies conducted in the concentration range of 50-300 mg/L, removal efficiency decreased with increasing concentration. The best removal efficiencies for both adsorbent dosages were obtained at a concentration of 100 mg/L. Concentration studies for 0.8 g of adsorbent are shown in Figure 4 and concentration studies for 1 g of adsorbent are shown in Figure 5.

The highest regression coefficients were determined at the adsorption of 0.8 g and 1g of adsorbents at 30 min for Freundlich isotherm. (Figure 6).

Pseudo-first-order, pseudo-second-order, and intraparticle diffusion models were used to determine the adsorption mechanism for 0.8 g and 1 g adsorbents for 100 mg/L DO-30 dye solution as 50 mL at 10, 30, 60, 90 and 120 min contact time. The highest correlation coefficient were obtained as the pseudo-second-order kinetic model (PSO KM) for 0.8 g and 1 g adsorbents as following in Figure 7.

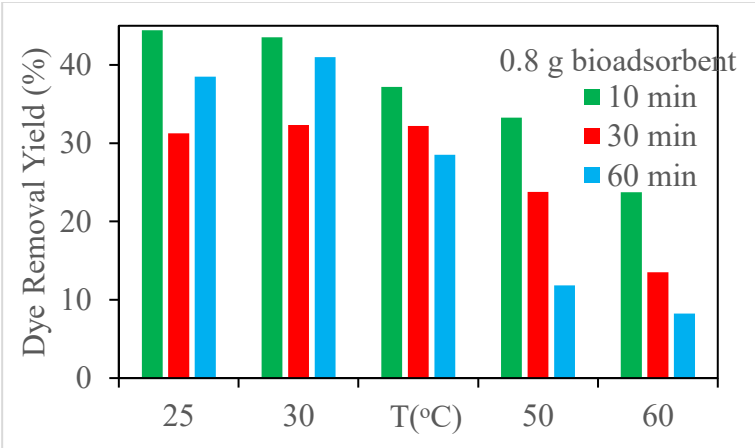

Figure 2. Temperature affect on dye removal yield for 0,8g bioadsorbent at 10 min, 30 min, 60 min

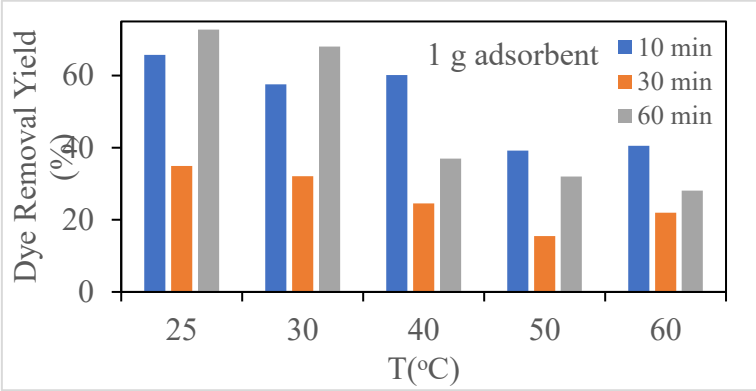

Figure 3. Temperature affect on dye removal yield for 1g adsorbent at 10 min, 30 min, 60 min

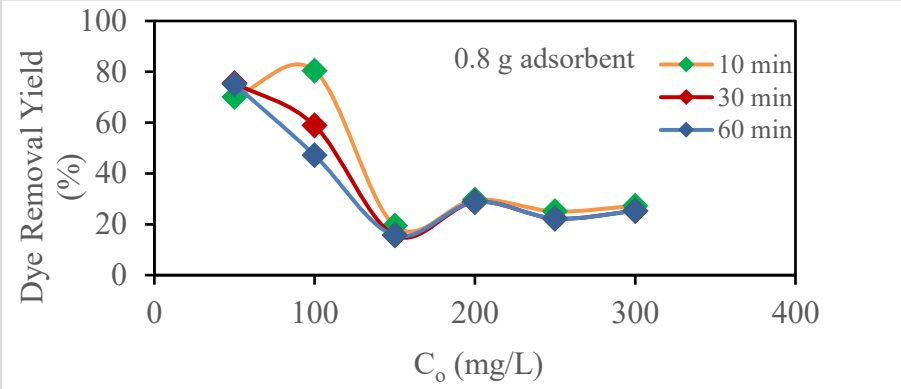

Figure 4. Concentration effect on dye removal yield of 0.8 g adsorbent with different contact time

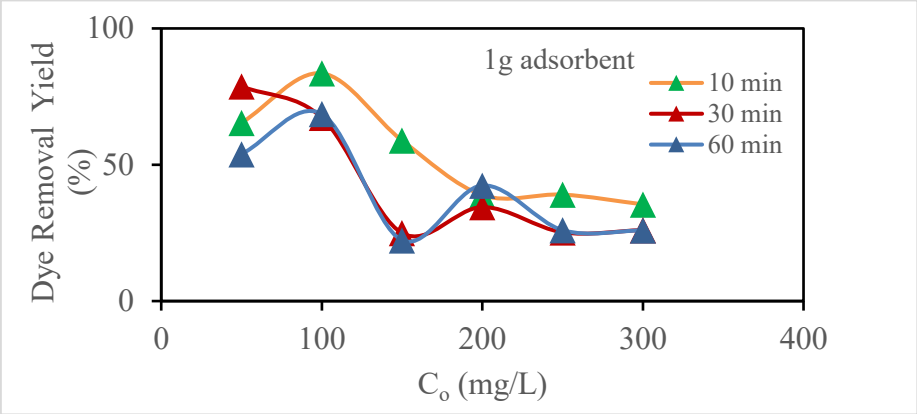

Figure 5. Concentration effect on dye removal yield of 1 g adsorbent with different contact time

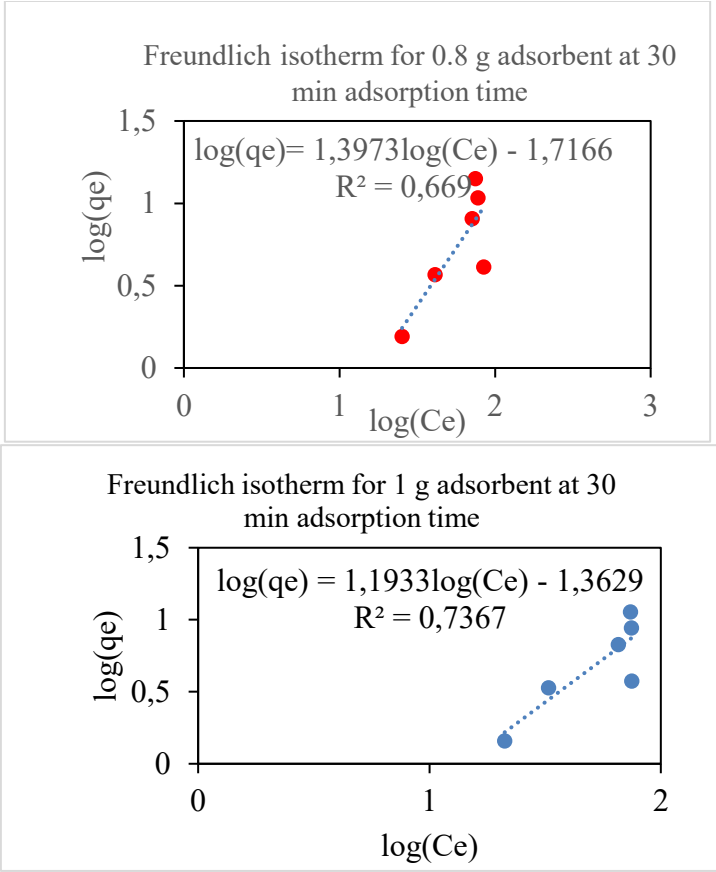

Figure 6. The Freundlich adsorption isotherms for 0.8 g and 1 g adsorbents at 30 min adsorption time

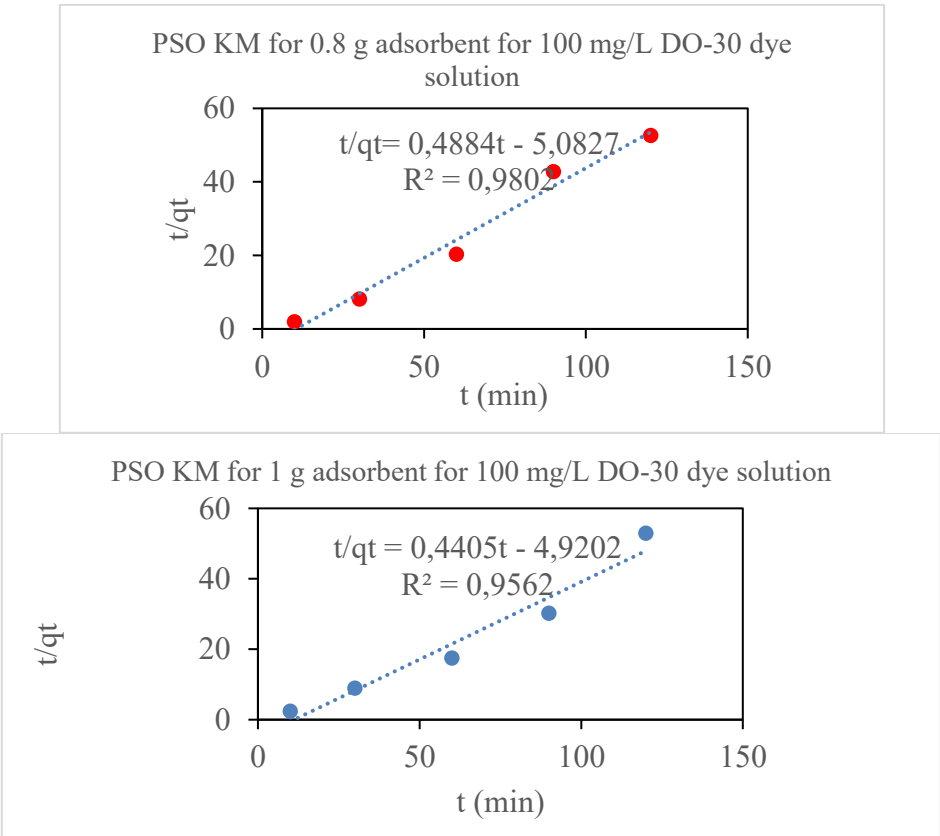

Figure 7. The Pseudo Second Order Kinetic Model for 0.8 g and 1 g adsorbents between 10 and 120 min adsorption time

CONCLUSION

It was found that increasing the contact time (from 10 min to 120 min) and temperature (from 25 to 60 ºC) negatively affected the removal yield of DO-30 dye with quince leaf powder from synthetic wastewater (as 30 %) due to the dye releasing from pure quince leaf.

The results of this study revealed the potential of dried quince leaves with treated with formaldhyde as an environmentally friendly and effective wastewater purification method and contributed to the removal of disperse orange 30 dye. The adsorption kinetics and adsorption models were examined with formaldehyde-stabilized quince leaf powder bioadsorbent. The regression coefficient of the Freundlich isotherm was higher than the Langmuir and Temkin model. The kinetic studies proved that the adsorption of DO-30 dye on formaldehyde-stabilized quince leaf powder bioadsorbent fits the PSO KM with good correlation.

REFERENCES

1. M. Molebatsi, B. Nkoane, N. Keroletswe, S. Chigome, M. T. Kabomo, *Environments*, **12**(9), 302 (2025).
2. O. Sahu, N. Singh, *The Textile Institute Book Series, The Impact and Prospects of Green Chem. Text. Technol*. 367 (2019).
3. T.A. Aragaw, F.M. Bogale, *Front. Environ. Sci*. **9**, 764958 (2021).
4. O. Çaylak, *Journal of Molecular Liquids*, **433**, 127960 (2025).
5. A. Dabrowski *Advances in Colloid and Interface Science*, **93**(1–3), 135 (2001).
6. T. Etemadinia, B. Barikbin, A. Allahresani, *Surf. Interf*., **14** (2019).
7. H.K. Admawi, *Progress in Engineering Science*, **2**(4) 100156 (2025).

Bulgarian Chemical Communications, Volume 58, Issue 3 (pp. 286-290) 2026 *DOI: 10.34049/bcc.58.3.D008*

Preparation and analysis of an herbal extract solution having potential restorative effects against radiation dermatitis

A. B. Demir[1], D. Bahçeci[1], S. Özer[1], Ö. Y. Şahin[1], D. Şakar[2]*

[1]*Private Bahcesehir College, Department of Chemistry, Istanbul, Turkey*
[2]*Yildiz Technical University, Chemistry Department, 34220, Esenler, Istanbul, Turkey*

Accepted: July 28, 2026

Radiodermatitis refers to skin reactions that occur after radiotherapy in cancer patients, such as redness, scaling, and crusting. The medications used to treat radiodermatitis often contain chemical substances. However, cancer patients, who are already exposed to intense chemical treatments, may find the use of such chemically based drugs burden. For the treatment of wounds resulting from radiotherapy, plant-based substances can be considered as alternatives to chemical-containing products. Plantago lanceolata has wound-healing properties and supports cell viability. Cistus possesses antimicrobial effects that help prevent infection and support the healing process. Centella asiatica is known for its wound-healing and moisturizing properties and it helps prevent deeper fissures caused by dryness. Aloe vera hydrates the skin and contributes to wound healing.

In our study, we prepared a plant-based solution in PBS containing *Plantago lanceolata* (allantoin), Cistus (*Cistus creticus; laden*), *Centella asiatica* (gotu kola) and *Aloe vera* to help the skin wounds that develop in patients receiving radiotherapy heal faster. Allantoin supports wound healing and cell vitality. Laden helps prevent infections and supports the healing process. *Centella asiatica* has wound-healing and moisturizing effects, and it also prevents deeper cracks that may form when the wound becomes too dry. Aloe vera moisturizes the skin and helps the wounds heal. For the treatment of the skin wounds that appear in cancer patients undergoing radiotherapy, these plant-based ingredients were combined to obtain the solution. This solution was integrated this solution in cotton pads for ease of use. The solution-infused cotton pads were tested using UV/VIS spectrophotometry, microscopy and zetasizer analysis. The obtained results showed that this solution may have the potential to benefit wounds in patients undergoing radiotherapy.

Keywords: *Plantago lanceolata* (allantoin), Cistus (*Cistus creticus*; laden), *Centella asiatica* (gotu kola), Aloe vera

INTRODUCTION

Cancer is a disease known since ancient times and as time has progressed, various treatment methods have been developed. Radiotherapy, one of the oldest known methods and still used today, is carried out by directing radiation to diseased tissue. The radiation affects not only the diseased tissue but also healthy tissue, leading to a condition called radiodermatitis. Radiodermatitis refers to the morphological and functional changes that occur in non-cancerous skin tissue as a result of therapeutic radiation application [1]. It is recommended that patients keep the irradiated area clean and dry, wash it with lukewarm water and pH-appropriate soaps, avoid perfume and alcohol-based solutions, refrain from environments such as saunas and baths and protect themselves from sunlight [2]. Radiation-induced skin damage, a common complication of radiotherapy, occurs in approximately 90% of patients undergoing treatment and negatively affects their quality of life and treatment processes [3]. The chemical substances in the medications used after radiodermatitis may cause cytotoxic effects. One of the substances used in these drugs, silver sulfadiazine (SSD) has the potential to negatively affect healing by causing toxic effects on keratinocytes and fibroblasts [4]. It also carries the risk of developing contact dermatitis and recurrence in wounds [5]. Patients undergoing radiotherapy use appropriate creams or solutions for radiodermatitis wounds. The fewer chemical substances these wound-covering materials contain, the more beneficial they are for patients. Therefore, herbal-based products can be used. Extracts obtained from the Cistus plant have antioxidant properties. This plant is a rich source of polyphenols, including flavonoids and phenolic acids. Cistus is valuable for its ability to support the immune system. It also has antiviral and antibacterial properties and helps fight infections [6]. *Centella asiatica* extracts are considered natural remedies that alleviate acne, burns, atopic dermatitis, and wounds [7]. Among the main herbal topical agents investigated for the treatment of radiodermatitis are *Aloe vera, Calendula,* and *Centella asiatica* [2]. *Plantago lanceolata* has known pharmacological activities in the literature such as wound healing, irritation relief, moisturizing, removal of necrotic tissue, stimulation

* To whom all correspondence should be sent:
E-mail *dsakar@yildiz.edu.tr*

© 2026 Bulgarian Academy of Sciences, Union of Chemists in Bulgaria

of cell mitosis; as well as supporting epithelial stimulation, analgesic effects, and keratolytic activity. *Plantago lanceolata* has been used for over 70 years for various therapeutic purposes, especially as a wound healing enhancer in cosmetic and pharmaceutical preparations [8]. *Aloe vera,* due to its soothing and moisturizing properties, is used in skin care products and cosmetics such as lotions, creams, gels, and face masks; in pharmaceuticals, *Aloe vera* extracts are used in the production of ointments, creams, and oral medications for burns, wounds, psoriasis, and gastrointestinal disorders [9].

In our study, a solution prepared using a mixture of *Cistus, Centella asiatica, Plantago lanceolata,* and *Aloe vera* plant extracts was integrated into cotton pads. It was aimed that the obtained cotton pads containing plant extracts would help in the healing of radiodermatitis wounds occurring after radiotherapy.

EXPERIMENTAL

Materials

Methanol, ethanol and distilled water were employed to obtain the plant extracts *of Centella asiatica, Plantago lanceolata* and *Cistus*. These substances were combined with the *Aloe vera* gel. To observe the release behavior of the plant extracts in the human body phosphate buffered saline (PBS), a solution that closely resembles human body fluid was used. A balance, a magnetic stirrer, a rotary evaporator (for solvent removal), a Nikon Eclipse E100 device for microscopic examinations, and a Shimadzu UVmini-1240 model UV-VIS spectrophotometer were used to investigate the release of plant extracts. A Brookhaven Instruments Corporation 90 Plus model Zetasizer device was used for zeta potential, electrophoretic mobility and particle size measurements. UV-VIS and Zetasizer measurements were carried out at 37°C, which is body temperature.

Extraction of Centella asiatica plant extract:

10 g of dried *Centella asiatica* plant were taken and 100 mL of a methanol-water mixture (10:90%, v/v) was added. This mixture was left to stand for one day (see Fig. 1). The mixture was then filtered and the solvent in the filtrate was removed using a rotary evaporator. After the evaporation process, the plant extract was obtained [10].

Figure 1. Soaking of *Centella asiatica* plant in a methanol-water mixture.

Extraction of Cistus plant extract

Cistus leaves were ground and 20 g of the ground leaves were taken. They were left for 24 h in a 70% aqueous ethanol solution at a solid-to-solvent ratio of 1:20. The obtained mixture was filtered (see Fig. 2) and the ethanol was removed using a rotary evaporator. After the evaporation process, the plant extract was obtained [11].

Figure 2. Soaking of the Cistus plant in ethanol.

Extraction of Plantago lanceolata plant extract

30 g of dried and ground *Plantago lanceolata* plant was weighed and kept in 100 mL of ethanol for 6 hours. After the mixture was filtered (see Fig. 3) the ethanol was evaporated under vacuum at 40°C using a rotary evaporator. After the evaporation process, the plant extract was obtained [12].

(a) (b)

Figure 3. (a) Soaking of *Plantago lanceolata* plant in ethanol; (b) Solvent–plant extract mixture obtained after filtration.

Extraction of gel from Aloe vera plant

The leaves of the obtained *Aloe vera* plant were thoroughly washed and dried. The gel inside the

leaves was removed with the help of a spatula and transferred into a Petri dish (see Fig. 4).

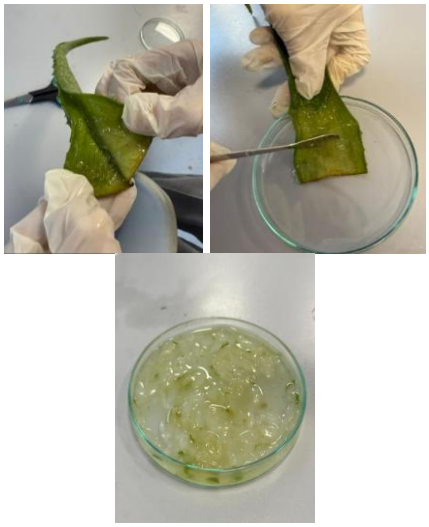

Figure 4. Extraction of gel from the inner part of *Aloe vera* leaves.

Mixing of plant extracts and integration into cotton pads

The extracts of *Centella asiatica, Cistus, Plantago lanceolata*, and *Aloe vera* were each weighed separately so that their mass ratio was 5%. The obtained mixture was blended using a blender. The mixture containing plant extracts was then added onto cotton pads and left to stand at room temperature for 24 h (see Fig. 5).

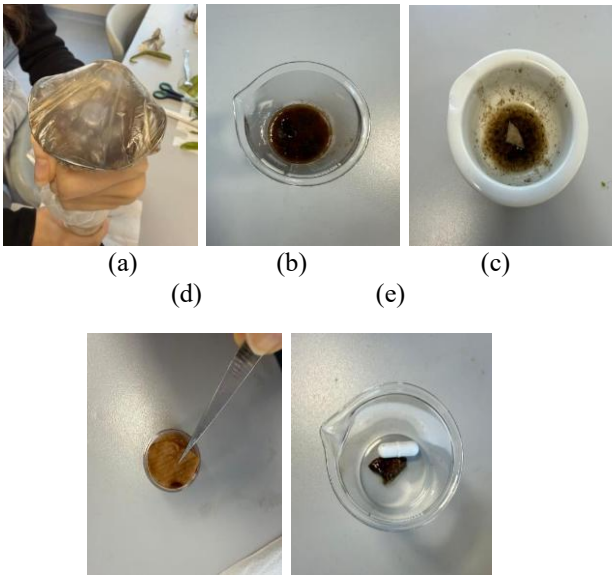

Figure 5. (a) Mixing of plant extracts in a blender; (b) Mixture of plant extracts; (c) Disk cotton integrated with plant extracts; (d) and (e) Appearance of disk cotton coated with the plant extract solution.

Release of cotton pads containing Centella asiatica, Cistus, Plantago lanceolata, and Aloe vera extracts in phosphate-buffered saline (PBS)

First, the cotton pads containing the four different plant extracts were weighed. Then, they were left to degrade in 30 mL of phosphate-buffered saline (PBS) at a constant temperature of 37°C (see Fig. 6). To examine the release of the plant extracts integrated into the cotton pads in the PBS solution, samples were taken from the solution at the 24th, 48th and 72nd h (see Fig. 7). The cotton pads containing plant extracts were removed from the phosphate-buffered saline solution and left to stand at room temperature for one day. The weight of the dried cotton pads containing plant extracts was then measured.

Figure 6. Mixing of disk cotton containing plant extracts in phosphate buffer solution.

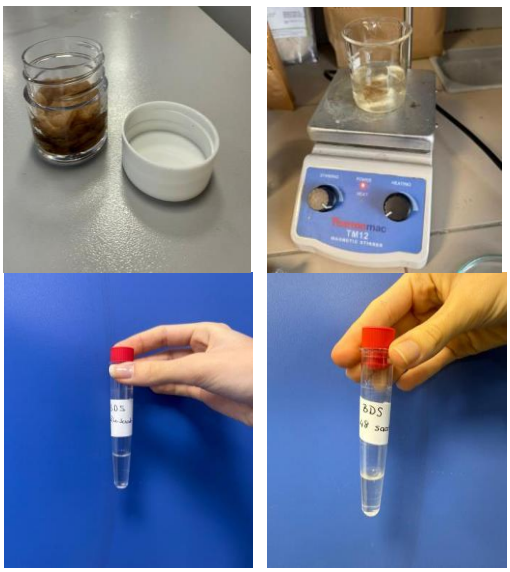

Figure 7. (a) 24th h of dissolution of disk cotton coated with the plant extract mixture in PBS (b) 48th h of dissolution of disk cotton coated with the plant extract mixture in PBS.

To evaluate the degradation-related release of cotton pads containing extracts of *Centella asiatica, Cistus, Plantago lanceolata,* and *Aloe vera* in phosphate-buffered saline (PBS), UV-VIS spectrophotometer measurements were taken from samples collected at the 24th, 48th and72nd hour. The measurements were carried out on samples prepared by diluting the phosphate-buffered saline (PBS) solution, in which degradation occurred, with pure water.

Release of plant extracts integrated into the cotton pad in phosphate buffer solution (PBS)

Centella asiatica, Cistus, Plantago lanceolata, and *Aloe vera* extract-coated cotton discs were incubated in phosphate-buffered saline (PBS), which closely mimics artificial human body fluid, at 37°C. The initial weight of the cotton disc containing the *Centella asiatica, Cistus, Plantago lanceolata,* and *Aloe vera* extract mixture was 11.1 g before immersion in PBS, while its weight decreased to 0.15 g after 72 h of incubation.

The release of the cotton pad containing *Centella asiatica, Cistus, Plantago lanceolata,* and *Aloe vera* extract in phosphate buffer solution (PBS) was analyzed using a UV-VIS spectrophotometer. UV-VIS spectra taken at different wavelengths are given in Figures 8 and 9.

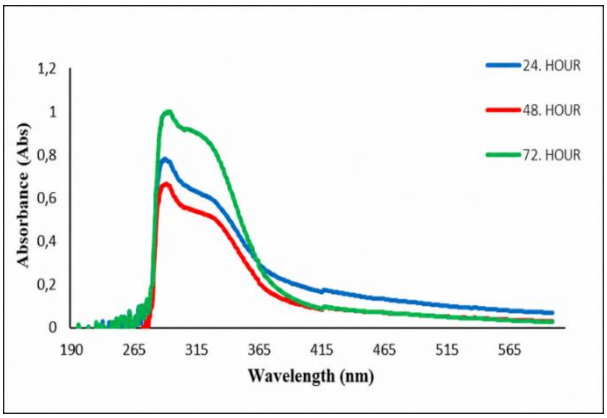

Figure 8. Comparative UV-VIS spectra of the cotton pad integrated with plant extracts, taken at 190–600 nm at the 24th, 48th and 72nd h.

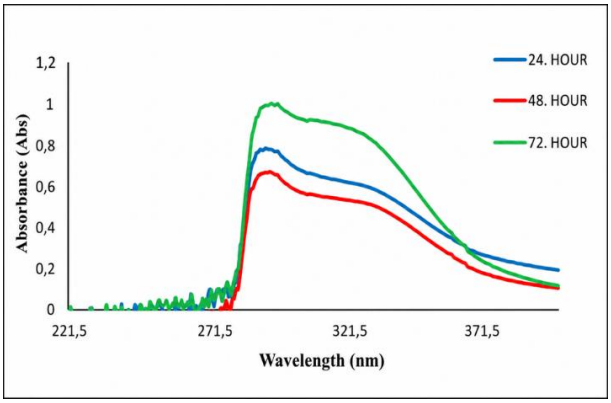

Figure 9. Comparative UV-VIS spectra of the cotton pad integrated with plant extracts, taken at 214–465 nm at the 24th, 48th and 72nd h.

In the data obtained from the comparative UV-VIS spectra, the highest peak value was observed at 297 nm with an absorbance value of 1 at the 72nd h.

Examination of the cotton pad containing plant extracts under the microscope:

The cotton pad integrated with *Centella asiatica, Cistus, Plantago lanceolata,* and *Aloe vera* extracts was examined under the microscope. The magnified images at 40× and 100× under the microscope are given in Figure 10.

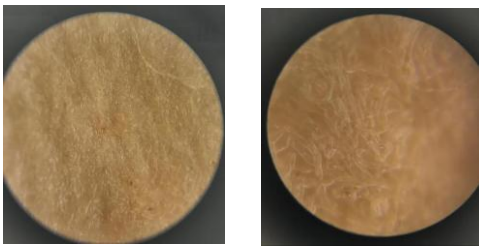

(a) (b)

Figure 10. Photographs of cotton pads coated with plant extracts magnified (a) 40× and (b) 100×.

Investigation of the stability of the cotton pad containing plant extracts in pbs artificial body fluid

- *Effect of the PBS medium on particle size over time.* The behavior of the cotton pad containing plant extracts in phosphate buffer solution (PBS) was examined at the 24th, 48th and 72nd h, and the particle size values are given in Table 1.

Table 1. Particle size of plant extracts in the PBS medium at different times.

Time(h)	Particle size (nm)
24th	19.7
48th	17.6
72nd	20.2
Mean±SD	19.2±1.4

The particle size of the plant extract particles in the PBS medium was approximately 19 nm, indicating that the particles were very small and may easily pass through the skin.

- *Effect of the PBS medium on zeta potential over time:* The behavior of the cotton pad containing plant extracts in phosphate buffer solution (PBS) was examined at the 24th, 48th and 72nd h, and the zeta potential values are given in Table 2.

Table 2. Zeta potential measurement results of plant extracts in the PBS medium at different times.

Time (h)	Zeta potential (mV)
24th	-1.73
48th	-3.20
72nd	-10.03
Mean±SD	-4.9±4.4

The zeta potential values obtained with the release of the plant extracts over time in the PBS medium show that the surface charges of the plant extracts were negative.

RESULTS AND DISCUSSION

With the developing technology for the treatment of cancer disease, different methods have been developed. Despite these developing methods, radiotherapy, which is one of the old methods that has still not been abandoned, causes wound formation in the patient after treatment. The formation of this condition called radiodermatitis, occurs because the radiation applied in radiotherapy damages healthy cells as well as cancerous cells. Patients use different products such as creams, solutions, lotions and gels on the damaged area of their bodies. These products contain chemical substances, and these chemicals are quite dangerous in cancer treatment. In our study, a cotton pad solution integrated with *Centella asiatica, Cistus*, *Plantago lanceolata*, and *Aloe vera* extracts was obtained for patients experiencing radiodermatitis. The cotton pad containing the obtained plant extracts was observed under a microscope at 40x and 100x magnification. In order to examine the release of the cotton pad integrated *with Centella asiatica, Cistus, Plantago lanceolata,* and Aloe vera plant extracts in phosphate buffer solution, which is the closest to human body fluid, samples taken at the 24th, 48th and 72nd hours were analyzed in a UV-VIS spectrophotometer. In addition, the weights of the cotton pad before being placed into the phosphate buffer and at the end of the 72nd h were compared. Furthermore, the particle size and zeta potential of the samples in PBS were measured against time, and the surface charges in this environment were determined.

As a result of the conducted studies, in the observations performed under the microscope on the cotton pad containing plant extracts, the plant extracts were fully integrated into the cotton. When the release in phosphate buffer solution was examined at the 24th, 48th and 72nd h in the UV-VIS spectrophotometer, it was observed that the plant extracts spread in the phosphate buffer over time. In addition, it was revealed that the release reached its peak at the 72nd h. When the weight of the cotton pad containing plant extracts was compared before being placed into the phosphate buffer solution and after the 72nd hour, it was observed that the weight of the cotton pad decreased at the end of the 72nd h. This shows us that the plant extracts spread in the phosphate buffer solution. When the zeta potential and particle size results were examined, it was seen that the particle size of the plant extract in the PBS environment was small enough to pass through the skin barrier and that it was negatively charged.

When all the obtained data were evaluated, it was concluded that the cotton pad containing plant extracts may help heal radiodermatitis wounds that occur after radiotherapy.

CONCLUSION

In conclusion, considering all experiments conducted, it was observed that our solution containing *Centella asiatica, Cistus, Plantago lanceolata,* and *Aloe vera* may have a positive effect on the healing of skin wounds in cancer patients undergoing radiotherapy. In the PBS release study, the release of the proposed solution was found to increase over time and the prepared plant extract particles with an average size of 19 nm were found to have a negative surface charge in solution.

REFERENCES

1. Ö. Kral, S. İlbasmış Tamer, Ü. Gül, F. Tırnaksız, *Türkiye Klinikleri Journal of Dermatology*, **33**(1), 30 (2023).
2. A. Yentek Balkanay, Comparison of the effectiveness of Centella asiatica combination versus mometasone furoate alone in the treatment of breast cancer radiation dermatitis, Master's thesis, Istanbul University, Istanbul (2021).
3. X. Yang, H. Ren, X. Guo, C. Hu, J. Fu, *Aging*, **12**(22), 23379 (2020).
4. I. Khansa, A. R. Schoenbrunner, J. E. Janis, *International Wound Journal*, **16**(4), 852 (2019).
5. B. Elmaz Firoz, J. F. Williams, J. S. Henning, *J. Drugs Dermatol.*, **6**(8), 825 (2007).
6. M. Olszowy-Tomczyk, D. Wianowska, *Agriculture*, **14**(9), 1559 (2024).
7. K. S. Park, Evidence-Based Complementary and Alternative Medicine, doi: 10.1155/2021/5462633 (2021).
8. L. U. Araújo, A. Grabe-Guimarães, V. C. F. Mosqueira, C. M. Carneiro, N. M. Silva-Barcellos, *Acta Cirúrgica Brasileira*, **25**(5), 460 (2010).
9. M. Chelu, A. M. Musuc, M. Popa, J. Calderon Moreno, *Gels*, **9**(9), 708 (2023).
10. O. Bozkaya, In vitro and in vivo investigation of the wound healing effect of polymer fibers containing silver nanoparticles coated with Centalla Asiatica plant extract, PhD dissertation, Hacettepe University, Ankara (2021).
11. M. D. Köse, B. N. Tekin, O. Bayraktar, E. T. Duman, Y. Başpınar, *International Journal of Secondary Metabolite*, **4**(3), 434 (2017).
12. C. Düşgün, Investigation of *in vitro* antioxidant activity in some plants with allantoin metabolism, Master's thesis, Niğde University, Niğde (2015).

Bulgarian Chemical Communications, Volume 58, Issue 3 (pp. 291-296) 2026 DOI: 10.34049/bcc.58.3.D009

Synthesis and characterization of polydopamine-modified MOFs for polymer electrolyte membranes

E. Çolak[1]*, B. Çetin[1], H. C. Kurçin[2], S. K. Aslan[2], D. Ünlü[2], F. U. Nigiz[3]

[1]*Çanakkale Onsekiz Mart University, School of Graduate Studies, 17100, Merkez/Çanakkale, Türkiye*
[2]*Bursa Technical University, Chemical Engineering Department, 16000, Merkez/Bursa, Türkiye*
[3]*Çanakkale Onsekiz Mart University, Chemical Engineering Department, 17100, Merkez/Çanakkale, Türkiye*

Accepted: July 28, 2026

The operational efficiency of batteries, supercapacitors, and fuel cells depends on the delicate balance among ionic conductivity, mechanical robustness, and ion crossover resistance. Proton-conductive membranes are widely used to enhance the performance of these systems. Nafion is a widely used commercial proton-exchange membrane. However, its widespread use is constrained by its high cost and other performance limitations. In this study, novel electrospun sulfonated poly(phenylene sulfone) (sPPSU) composite membranes loaded with metal-organic frameworks were synthesized and characterized. Four types of zirconium-based metal-organic frameworks (MOF-801, MOF-808, MIL-140, and UiO-66) were surface-modified with polydopamine (PDA) and incorporated into an sPPSU matrix. This PDA functionalization improved the dispersion of the MOF particles within the polymer matrix and created additional proton-conducting pathways throughout the membrane structure. The membranes were characterized in terms of morphology using scanning electron microscopy (SEM), electrochemical properties using impedance spectroscopy, and mechanical properties according to the ASTM D882 standard. The experimental results revealed that the UiO-66-P membrane exhibited the highest proton conductivity (16.6 mS/cm). Notably, the ion-exchange capacity of MOF-801-P was 9.75 meq/g, exceeding the 7.35 meq/g of commercial Nafion 212. Additionally, the mechanical strengths of the MIL-140-P and UiO-66-P membranes reached levels comparable to the 22.24 MPa benchmark of Nafion 212. These findings demonstrate that PDA-modified Zr-MOF/sPPSU electrospun membranes are promising candidates for next-generation proton-exchange membrane applications.

Keywords: sulfonated poly(phenylene sulfone), metal-organic framework, proton-exchange membrane, electrospinning, polydopamine, electrochemical energy storage

INTRODUCTION

Proton exchange membranes are considered key elements of advanced electrochemical systems because they allow selective ion transport and act as an important physical barrier between the electrodes. Perfluorinated membranes (e.g., Nafion) are commonly used, but their use is often limited by high manufacturing costs and certain performance limitations under demanding operating conditions. To address these challenges, metal-organic frameworks (MOFs) have emerged as promising functional fillers for advanced membrane applications. Unlike traditional inorganic fillers, MOFs have unique internal nanochannels that allow efficient proton conduction through interconnected pathways and restrict the transport of larger species *via* size-exclusion mechanisms [1]. The high tunability of the pore size and chemical functionality enables the rational design of membranes with optimized ion selectivity and enhanced proton conductivity [2].

Zirconium-based metal-organic frameworks, particularly the MIL-140 family, are emerging materials for electrochemical energy storage applications owing to their high coordination numbers and binding energies, resulting in good chemical stability under corrosive acidic conditions [3]. Zr-based frameworks of the MIL-140 family represent a special class of materials with high hydrolytic stability and densely packed structures. Within this family, MIL-140A is especially characterized by its very restricted triangular apertures, generally smaller than 4 Å, which is a significant advantage for ion-sieving applications. The restricted pore dimensions may favor selective proton transport while hindering the crossover of larger ionic species, which is advantageous for membrane selectivity [4].

Sulfonated poly(phenylene sulfone) (sPPSU) has been employed as a promising matrix for proton-exchange membrane applications owing to its excellent chemical stability and strong mechanical

* To whom all correspondence should be sent:
E-mail: *colakelif12@hotmail.com*

© 2026 Bulgarian Academy of Sciences, Union of Chemists in Bulgaria

properties. The inherent resistance of the polymer to corrosive acidic environments imparts durability during electrochemical cycling, and the tunable sulfonation degree provides a versatile means to control proton transport characteristics. These features position sPPSU as a reliable and cost-effective alternative to conventional perfluorinated membranes for electrochemical energy storage applications. In this study, the surfaces of MOF-801, MOF-808, MIL-140, and UiO-66 architectures were modified with polydopamine to improve their integration and compatibility with the polymer matrix. The modified frameworks were incorporated into sPPSU via electrospinning to prepare composite membranes. Finally, the resulting membranes were systematically characterized in terms of proton conductivity, ion-exchange capacity, and mechanical performance to evaluate their potential for advanced energy-storage systems.

EXPERIMENTAL

MIL 140 preparation

MIL-140 was synthesized by dissolving $ZrCl_4$ and terephthalic acid (H_2BDC) in 30 mL of DMF and transferring the mixture into a PTFE-lined stainless-steel autoclave. The reaction was carried out under hydrothermal conditions at 220 °C for 15 h; this elevated temperature is essential for obtaining the thermodynamically stable MIL-140 phase in pure form [5, 6]. After completion, the product was separated by vacuum filtration, washed with methanol, and dried at 60–80 °C.

MOF-808 preparation

MOF-808 was synthesized by homogeneously mixing $ZrOCl_2 \cdot 8H_2O$ (4.85 g) and H_3BTC (1.05 g) in a DMF/formic acid solvent system (45 mL, 1:1 ratio) and storing the mixture under hydrothermal conditions at 130 °C for 48 hours [7]. After completion, the product was separated by centrifugation and sequentially washed with DMF, deionized water, and acetone. For pore activation, the samples were subjected to thermal treatment at 150 °C for 24 h under vacuum [8].

UiO-66 preparation

UiO-66 was synthesized by dissolving $ZrCl_4$ (2.7 mmol) and HCl as a modulator in 25 mL DMF, followed by the addition of terephthalic acid and 50 mL DMF to obtain a homogeneous suspension. The mixture was maintained at 120 °C for 24 h in a hydrothermal reactor [9]. The resulting precipitate was separated by vacuum filtration, washed three times with DMF, stirred in ethanol for 24 h, and dried at 40 °C [9].

MOF-801 preparation

MOF-801 was synthesized by dissolving $ZrOCl_2 \cdot 8H_2O$ and fumaric acid in a DMF/formic acid solvent system and transferring the mixture to a stainless-steel autoclave. The reaction was carried out under hydrothermal conditions at 130 °C for 6 h [10, 11]. The resulting white precipitate was separated by centrifugation, washed sequentially with DMF and methanol, and thermally activated at 150 °C for 24 h under vacuum [10].

PDA modification

In this study, four different zirconium-based MOFs (MOF-801, MOF-808, MIL-140, and UiO-66) were modified with PDA for the fabrication of electrospun membranes. The polydopamine (PDA) coating process improves the dispersion of MOF particles within the polymer matrix by forming a hydrophilic and highly adhesive layer on their surfaces. It also enhances the ionic conductivity of the system by creating additional proton transport pathways [12]. The literature frequently emphasizes that PDA directly facilitates proton transfer through acid-base pairs formed *via* the hydroxyl (–OH) and amine/imine (–NH_2/–NH–) functional groups in its chemical structure [13].

In the experimental process, 0.200 g of each MOF type was weighed, dispersed in a Tris-HCl buffer solution, and transferred to a dopamine hydrochloride solution. As a result of the coating process, which was carried out at room temperature under magnetic stirring for 24 h, a homogeneous PDA layer was formed on the surface of the MOF particles via spontaneous oxidative polymerization of dopamine [12]. After the reaction was complete, the resulting modified MOF particles were centrifuged, washed with distilled water, dried, and transferred to a solution suitable for electrospinning.

Membrane preparation

In the initial phase, 20 different formulations were tested, and it was determined that the most suitable solution for the electrospinning process was a formulation containing 30% sPPSU, 20–30% acetone, and the remainder as NMP. PDA-modified MOF particles were added at a loading of 3 wt% relative to the mass of sPPSU in the membrane formulation. The solution was stirred for 24 h at 35 °C. Once the appropriate viscosity was achieved, fiber production was performed using an electrospinning device with a voltage of 20 kV, a needle-collector distance of 15 cm, and a flow rate of 0.015 mL/min.

Membrane characterization

Commercial Nafion 212 was used as the reference membrane and characterized under the same experimental conditions for comparison.

Water uptake refers to the increase in membrane mass after water absorption. The membranes were immersed in water for 24 h, and water uptake was calculated from the difference between the wet and dry membrane masses.

$$WU\ (\%) = (\frac{M_{Wet} - M_{Dry}}{M_{Dry}}) \times 100 \quad (1)$$

The empirical porosity of the membranes was determined using 1 cm × 1 cm samples based on their masses before and after water immersion and the densities of water and sPPSU [14].

The membranes were immersed in 1 M H_2SO_4 solution for 24 h before impedance measurements [15, 16]. The proton conductivity (σ) was calculated from the electrical resistance (R) obtained from the impedance measurements using the following equation:

$$\sigma = (\frac{l}{RxS}) \quad (2)$$

where l is the membrane thickness (cm), R is the electrical resistance (Ω), and S is the membrane surface area (cm^2).

The ion exchange capacity (IEC) represents the milliequivalent amount of $–SO_3H$ groups per gram of polymer and is the primary parameter that determines the proton transport performance [10]. The IEC was determined using NaOH back-titration [17].

$$IEC\ (meq/g) = (\frac{C_{NaOH} x V_{NaOH}}{M_d}) \quad (3)$$

Here, C_{NaOH} represents the molarity of the sodium hydroxide (NaOH) solution used in titration, V_{NaOH} represents the volume of NaOH used, and M_d refers to the mass of the dry membrane sample used in the analysis.

For long-term use, the mechanical performance of polymer-based materials, specifically their strength, flexibility, and dimensional stability, must be assessed. Tensile tests were conducted in compliance with the ASTM D882 standard using an ANKARIN universal tensile testing machine. Commercial Nafion 212 was also tested under the same conditions and exhibited a tensile strength of 22.24 MPa. The electrospun reinforcement of sPPSU membranes has been reported to provide higher hydrolytic and mechanical stability than that of cast membranes [14, 18].

RESULTS AND DISCUSSION

Figure 1 shows the SEM images of the synthesized MOF particles. SEM micrographs are critical for understanding the morphology of the synthesized MOFs and their crystal structures, which directly impact their electrochemical performance. The well-defined polyhedral and nanocrystalline geometries of MOF-801 and UiO-66, with homogeneous particle distributions, may favor the formation of effective proton-transport pathways [19].

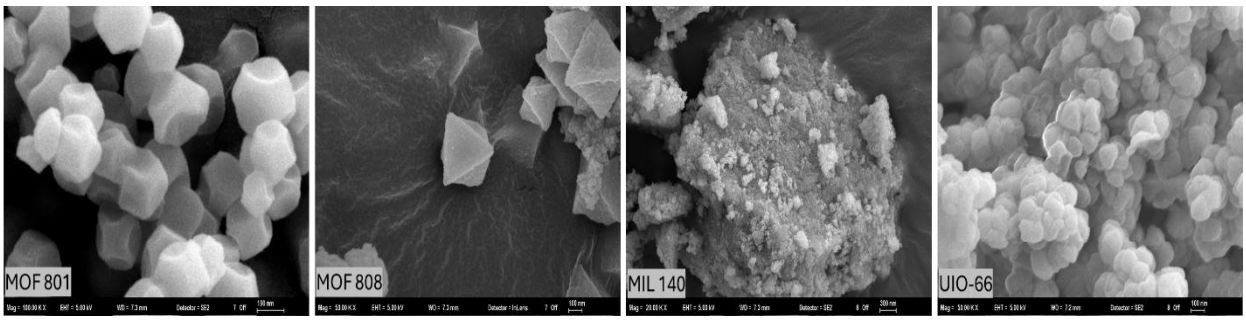

Figure 1. SEM images of synthesized Zr-based MOF particles: (a) MOF-801, (b) MOF-808, (c) MIL-140, and (d) UiO-66.

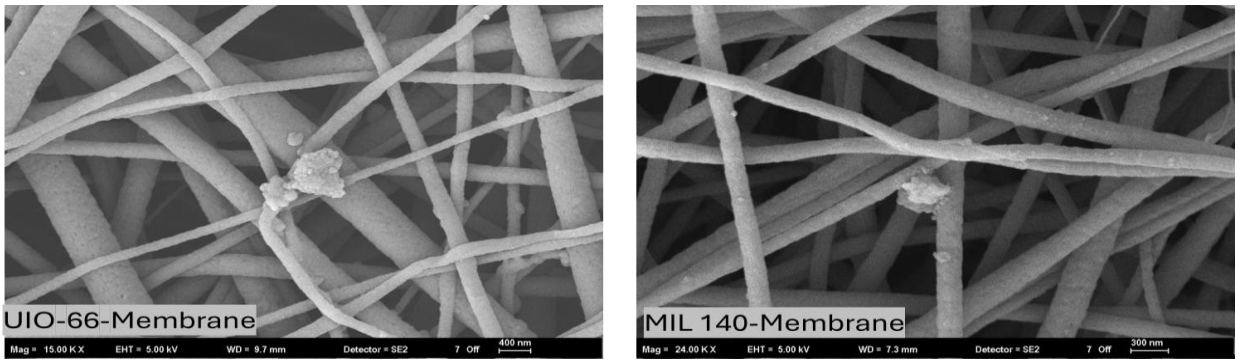

Figure 2. SEM images of electrospun sPPSU composite membranes containing 3 wt% (a) UiO-66-P and (b) MIL-140-P nanofillers.

In contrast, MOF-808 exhibits characteristic large octahedral crystals with sharp surfaces, indicating high crystallinity, and MIL-140 shows a more agglomerated and compact morphology, which may restrict the accessibility of the ion-exchange sites [20]. These morphological differences were directly correlated with the measured ion exchange capacity and proton conductivity.

The SEM images of the UiO-66- and MIL-140-doped membranes at a 3 wt% loading (Figure 2) reveal a highly porous and interconnected nanofiber network structure, indicating successful fiber formation by electrospinning. Continuous and randomly oriented nanofibers provide a high surface area-to-volume ratio, which is critical for optimizing proton conductivity [21]. Although the MOF nanoparticles were incorporated into the polymer matrix, the occasional “bead-on-string” formations suggest some local heterogeneity in the fiber morphology at a 3 wt% MOF loading. The incorporation of MOF particles into the fiber structure may contribute to the IEC and proton transport behavior by providing additional ion-exchange sites and interfacial transport pathways.

The hydrophilic functional groups of PDA may contribute to the water-retention behavior of the composite membranes. At the same time, PDA coating may partially restrict MOF pore accessibility, which could influence membrane porosity and ion transport. In the MOF-808-P membrane, the relatively low proton conductivity may be associated with restricted ion-transport pathways, despite the potential contribution of PDA to interfacial adhesion and water retention. Previous studies have reported that the catechol and amine groups of PDA can form hydrogen-bonding interactions with acidic groups and water molecules in the polymer matrix, which may facilitate the continuity of proton-transport pathways.

These results indicate that porosity and water uptake do not vary proportionally across the investigated membranes. This suggests that hydrophilicity is jointly governed by surface chemistry and physical pore volume [22]. Optimized water retention values facilitate the hydrogen bond networks required for the Grotthuss mechanism, whereas excessive water retention can lead to dimensional instability and negatively impact ion selectivity.

Table 2 presents the electrochemical properties of the MOF-doped membranes. The electrochemical performance of the synthesized MOF-based membranes was evaluated in terms of proton conductivity and ion exchange capacity (IEC).

UiO-66-P exhibited the highest proton conductivity among the investigated composite membranes, at 16.6 mS/cm, followed closely by MOF-801-P (15.6 mS/cm). These values suggest that the pore structure and functionalization of the UiO-66 and MOF-801 frameworks facilitate efficient proton transport, likely via a well-connected hydrogen bonding network.

In contrast, MIL-140-P showed the lowest conductivity (2.9 mS/cm), which may be attributed to its specific crystal packing and the lower density of active proton-conducting sites within its channels. While all investigated composite membranes showed lower proton conductivity than commercial Nafion 212 (26.9 mS/cm), UiO-66-P and MOF-801-P demonstrated promising potential as alternative proton-conducting membrane materials.

MOF-801-P reached the highest IEC value of 9.75 meq/g, exceeding that of Nafion 212 (7.35 meq/g). This indicates a high density of exchangeable proton sites in the MOF-801-P composite membrane. Interestingly, although UiO66-P has a lower IEC (5.26 meq/g) than MOF801-P, it exhibits slightly higher proton conductivity. This suggests that proton transport in UiO-66-P may be facilitated by more effective transport pathways rather than by IEC alone. MIL-140-P showed a different trend, exhibiting a higher IEC (6.04 meq/g) than UiO-66-P and MOF-808-P, while showing the lowest proton conductivity. These

results indicate that a high IEC alone does not necessarily lead to high proton conductivity; membrane morphology and the effectiveness of proton-transport pathways also play important roles.

Table 1. Physical properties of membranes

Membrane	Thickness (µm)	Porosity (%)	Water uptake (%)
MOF-808 - P	65	29.44	32.35
MOF-801 - P	62	63.23	133.33
MIL-140 - P	59	67.36	160.00
UiO-66 - P	83	70.25	183.02

Table 2. Electrochemical properties of the membranes

Membrane	Proton conductivity (mS/cm)	IEC (meq/g)
MOF-801-P	15.6	9.75
MOF-808-P	4.7	4.96
MIL-140-P	2.9	6.04
UiO-66-P	16.6	5.26
Nafion 212	26.9	7.35

Table 3 presents the mechanical characteristics of the fabricated membrane. Overall, the P-series membranes exhibited the most balanced mechanical performance, approaching the reference value of Nafion 212 (22.24 MPa).

Table 3. Mechanical properties of the membranes

Membrane	Stress (MPa)	Strain (-)
MOF-801-P	8.5	0.028
MOF-808-P	13.6	0.050
MIL-140-P	21.86	0.11
UiO-66-P	20.91	0.16

In particular, the mechanical strengths of MIL-140A-P (21.86 MPa) and UiO-66-P (20.91 MPa) were only 2–7% lower than that of Nafion 212, suggesting a beneficial contribution of polydopamine modification to the mechanical performance of the composite membranes.

PDA establishes hydrogen bonds, π–π interactions, and acid-base interactions simultaneously with both the MOF crystal surface and the $–SO_3H$, –C–O–C, and aromatic ring groups in the polymer matrix (sPPSU) via the catechol and amine functional groups on its surface [23]. This multimodal bonding mechanism prevents the agglomeration of MOF particles, homogenizes stress transmission at the fiber-matrix interface, and maintains fiber continuity [23]. The regular and smooth fiber morphology exhibited by the P series in the SEM analysis also confirmed this structural integration. From a technical standpoint, these results suggest that PDA modification improves interfacial compatibility between the inorganic fillers and the polymer phase, which may contribute to more effective stress transfer. This suggests that the commonly reported trade-off between ion-exchange capacity and mechanical strength may be mitigated by the molecular bridging effect of polydopamine [23].

CONCLUSION

In this study, PDA-coated composite membranes were prepared *via* electrospinning and characterized in detail. Four different Zr-based MOFs (MOF-801, MOF-808, MIL-140, and UiO-66) were doped into a sPPSU polymer matrix for electrochemical energy storage applications. SEM analyses indicated good integration of the PDA-modified MOF particles within the polymer matrix while maintaining the continuity of the fibrous morphology.

The porosity and water uptake differed for the different types of MOF, and the highest values were found in the samples UiO-66-P (70.25% porosity, 183.02% water uptake) and MIL-140-P (67.36% porosity, 160.00% water uptake). The results indicated that porosity and water uptake did not vary proportionally across the investigated membranes. Surface chemistry is as important as the physical pore volume in determining hydrophilic properties.

Among all MOF series, UiO-66-P exhibited the highest proton conductivity (16.6 mS/cm). MOF-801-P exhibited an IEC value of 9.75 meq/g, which was higher than that of the commercial reference membrane Nafion 212 (7.35 meq/g). However, MIL-140-P had the lowest proton conductivity in the series (2.9 mS/cm) despite a relatively high IEC value (6.04 meq/g), highlighting that IEC alone is not a sufficient metric for performance. These results indicate that IEC alone is not sufficient to determine proton-conducting performance and that membrane morphology and the effectiveness of proton-transport pathways also play important roles. Mechanical tests revealed that the PDA coating enhanced the fiber matrix fit *via* a multimode bonding mechanism (hydrogen bonding, π–π interaction, and acid-base pairs) at the polymer-MOF interface. MIL-140-P (21.86 MPa) and UiO-66-P (20.91 MPa) exhibited only 2–7% lower mechanical strength than Nafion 212 (22.24 MPa), showing that PDA modification may help mitigate the "conductivity-mechanical strength" trade-off of electrospun membranes.

In general, MOF selection and PDA modification strategies are the decisive factors for membrane performance. Among the investigated membranes, UiO-66-P and MOF-801-P showed the most balanced overall performance in terms of proton conductivity and IEC. The results suggest that Zr-

based MOF/sPPSU electrospun composite membranes can be a functional and cost-effective alternative to Nafion in electrochemical energy storage applications, particularly when combined with PDA surface modification. Future studies should further investigate the individual contributions of MOF structure and PDA modification, as well as the effects of different crosslinking strategies on membrane performance.

Acknowledgement: *This study was supported by the Çanakkale Onsekiz Mart University Scientific Research Projects Coordination Unit (BAP) (Grant Number: FYL-2026-5516) and TÜBİTAK (Grant Number: 214M916)*

REFERENCES

1. D. J. Yoo, S.-H. Hyun, A. R. Kim, G. G. Kumar, K. S. Nahm. *Polym. Int.*, **60**, 85 (2011).
2. F. Yang, H. Huang, X. Wang, F. Li, Y. Gong, C. Zhong, J.-R. Li. *Cryst. Growth Des.*, **15**, 5827 (2015).
3. H. R. Abid, M. R. Azhar, S. Iglauer, Z. H. Rada, A. Al-Yaseri, A. Keshavarz. *Heliyon*, **10**, e23840 (2023).
4. J. Escorihuela, R. Narducci, V. Compañ, F. Costantino. *Adv. Mater. Interfaces*, **6**, 1801146 (2019).
5. M. Schulz, N. Marquardt, M. Schäfer, D. P. Warwas, S. Zailskas, A. Schaate. *Chem. Eur. J.*, **25**, 13598 (2019).
6. J. Jodłowski, G. Kurowski, K. Dymek, M. Oszajca, W. Piskorz, K. Hyjek, A. Wach, A. Pajdak, M. Mazur, D. N. Rainer, D. Wierzbicki, P. Jeleń, M. Sitarz. *Ultrason. Sonochem.*, **95**, 106377 (2023).
7. I. Del Castillo-Velilla, A. Sousaraei, I. Romero-Muñiz, C. Castillo-Blas, A. S. J. Méndez, F. E. Oropeza, V. A. de la Peña O'Shea, J. Cabanillas-González, A. Mavrandonakis, A. E. Platero-Prats. *Nat. Commun.*, **14**, 2506 (2023).
8. S. Bagi, S. Yuan, S. Rojas-Buzo, Y. Shao-Horn, Y. Román-Leshkov. *Green Chem.*, **23**, 9982 (2021).
9. D. Liang, S. Wang, W. Ma, D. Wang, G. Liu, F. Liu, Y. Cui, X. Wang, Z. Yong, Z. Wang. *Electrochim. Acta*, **405**, 139795 (2021).
10. L. Xin, D. Zhang, K. Qu, Y. Lu, Y. Wang, K. Huang, Z. Wang, W. Jin, Z. Xu. *Adv. Funct. Mater.*, **31**, 2104629 (2021).
11. J. Zhang, H.-J. Bai, Q. Ren, H.-B. Luo, X.-M. Ren, Z.-F. Tian, S. Lu. *ACS Appl. Mater. Interfaces*, **10**, 28656 (2018).
12. Y. Lu, S. Lin, H. Cao, Y. Xia, Y. Xia, L. Xin, K. Qu, D. Zhang, Y. Yu, K. Huang, W. Jing, Z. Xu. *JJ. Membr. Sci.*, **671**, 121347 (2023).
13. Z. Rao, M. Lan, Z. Wang, H. Wan, G. Li, J. Zhu, B. Tang, H. Liu. *J. Membr. Sci.*, **644**, 120098 (2022).
14. L. Pasquini, M. Sauvan, R. Narducci, E. Sgreccia, P. Knauth, M. L. Di Vona. *Membranes*, **12**, 1159 (2022).
15. Y. Zhang, J.-D. Kim, K. Miyatake. *J. Appl. Polym. Sci.*, **133**, 44218 (2016).
16. J.-D. Kim, A. Ohira, H. Nakao. *Membranes*, **10**, 31 (2020).
17. C. Hartmann-Thompson, A. Merrington, P. I. Carver, D. L. Keeley, J. L. Rousseau, D. Hucul, K. J. Bruza, L. S. Thomas, S. E. Keinath. *J. Appl. Polym. Sci.*, **110**, 958 (2008).
18. Y. Devrim. *Electrochim. Acta*, **146**, 741 (2014).
19. T. Xu, M. A. Shehzad, X. Wang, B. Wu, L. Ge, T. Xu. *Nano-Micro Lett.*, **12**, 51 (2020).
20. X. Chen, G. Li. *Inorg. Chem. Front.*, **7**, 3765 (2020).
21. S. Koushkbaghi, H. Arjmand Kermani, S. Jamshidifard, H. Faramarzi, M. Khosravi, P. Ghaderi-Shekhi Abadi, F. Sharifian Jazi, M. Irani. *RSC Adv.*, **13**, 12731 (2023).
22. J. Liu, W. Yan, Y. Ma, X. Li, J. Zhong, X. Zheng, Z. Liu. *ACS Appl. Mater. Interfaces*, **16**, 34240 (2024).
23. X. Cui, H. Wang, C. Zhao, Q. Wei, H. Shi. *J. Energy Storage*, **112**, 115597 (2025).

Bulgarian Chemical Communications, Volume 58, Issue 3 (pp. 297-302) 2026 *DOI: 10.34049/bcc.58.3.D010*

Natural pigments-doped polymer films synthesis by solution casting method and characterization

D. Uygunoz, I. Sengor, E. M. Derun*

Faculty of Chemistry and Metallurgy, Department of Chemical Engineering, Yıldız Technical University, Istanbul, Türkiye

Accepted: July 28, 2026

Recently, research and development activities in both public and private sectors have gained significant momentum due to the use of polymeric and polymer composite films in various fields, including packaging, optics, electronics, coatings, and solar cells. However, the increasing consumption of synthetic polymers makes a rise in plastic waste, causing adverse environmental impacts. To eliminate these effects, the use of biodegradable polymers has become increasingly important. In this study, polyvinyl alcohol (PVA) was selected as a biodegradable polymer matrix, and dye-doped polymer films were fabricated by doping natural pigments- lutein and β-carotene- at concentrations ranging from 3% to 5%. The produced films were characterized using differential scanning calorimetry (DSC), Fourier transform infrared spectroscopy (FTIR), tensile testing, scanning electron microscopy (SEM), and X-ray diffractometry (XRD). Tensile test results revealed that β-carotene enhanced the tensile strength of pure PVA films, whereas lutein combination resulted in a reduction in mechanical strength. DSC analysis indicated that the addition of both β-carotene and lutein increased the melting temperature of the PVA matrix. Polyvinyl alcohol, has been proven to be one of the polymers suitable for packaging materials and many other sectors in terms of production conditions, usability and biodegradability. The produced pure and dye-added films can be preferred as packaging materials due to their smooth surface and good durability.

Keywords: Polyvinyl alcohol; Biodegradable polymers; Natural pigments; Polymeric films; Packaging materials

INTRODUCTION:

Due to reasons such as the ever-increasing population, consumption habits and economy, non-biodegradable polymers are preferred and their consumption is increasing in many sectors. At this point, polymers that are completely biodegradable, do not harm the nature and do not create waste should be preferred and new studies should be carried out to solve the problems.

Polymers are long-chain, high molecular weight-compounds formed by the bonding of many equal or different atom groups with more or less regular chemical bonds and it have important application areas [1]. Polymeric structured films can consist of natural and artificial (synthetic) polymers. Layered polymeric structures up to 0.2-0.3 mm thickness are called plastic films or polymeric structured films. There is more than one method of producing films. Each method has its own parameters. The properties of the films to be produced should be determined according to their usage areas and the production method should be selected accordingly. For example, if consumed in the food industry, polymer structured films; carbon dioxide, oxygen etc. They are required to exhibit strong barrier properties against gases and have the ability to come into contact with food. Methods such as extrusion, blow molding, coating, rotational molding, solution casting, double bubble processing, compression molding (pressure thermoforming) and vacuum thermoforming are applied to produce polymer structured films according to the desired properties [2]. Solution casting method is widely preferred due to its advantages such as being more economical than other methods in terms of cost and not requiring pressure. It is generally a process in which a liquid polymer is poured into an open mold or onto a surface and solidified by drying. It can be produced in different shapes such as round, square, tube and rod [3]. As a result, while the material takes the shape of the mold, a polymerization reaction takes place in the mold [4].

There are studies on polymer structured films in the literature. In one study, sustainable packaging materials were developed using biodegradable polymers, namely polylactide (PLA) and polyhydroxybutyrate (PHB), combined with natural colorants such as β-carotene, chlorophyll, curcumin, and lutein, which are widely utilized in the food industry. The incorporation of these pigments enabled the materials to exhibit pronounced color

* To whom all correspondence should be sent:
E-mail: *moroydor@yildiz.edu.tr*

© 2026 Bulgarian Academy of Sciences, Union of Chemists in Bulgaria

variations in response to different environmental conditions, thereby imparting smart packaging functionality by providing visual indications of product status and material lifespan [5]. In another investigation, the performance of starch-based biodegradable films was enhanced through polymer blending. Composite films were fabricated by incorporating different proportions of PVA (10%, 30%, 50%, 70%, and 90% relative to the starch content) into the starch matrix using the solvent-casting technique. The resulting films were comprehensively evaluated for their mechanical properties, barrier performance, water solubility, water contact angle, and biodegradation behavior. The findings demonstrated that starch–PVA composite films possess considerable potential as eco-friendly alternatives for food packaging applications [6]. In another study, hydrogel films based on polyvinyl alcohol (PVA) and tannic acid (TA) at various ratios were synthesized and the structure of the synthesized films was examined with characterization techniques such as FTIR, TGA, DSC, SEM, XRD and DTG. Synthesis of hydrogel films was achieved by first mixing TA and PVA and then pouring the solution into petri dishes and keeping it at 50 °C overnight. In the synthesis of PVA/TA hydrogel films, the films were kept in saturated salt solution for 6 hours to increase durability. As a result of the experiment, it was concluded that the mechanical strength of the films kept in saturated salt solution was better and adding TA to PVA-based films improved the thermal and hardness properties compared to pure PVA polymer [7]. In a separate study, low-cost laser cut-off filters were developed using poly(vinyl alcohol) (PVA)-based composite films containing carmine dye. Both pristine PVA films and carmine dye-incorporated PVA composite films were fabricated via a conventional solution-casting method. For the preparation of pure PVA films, approximately 22.5 g of PVA was dissolved in 1 L of distilled water under continuous magnetic stirring at 50 °C and 700 rpm for 24 h. Composite films were subsequently prepared by incorporating different concentrations of carmine dye into the PVA matrix, with dye contents ranging from 0.11 wt% to 27.27 wt%, following the same casting procedure. Characterization of the films cut into suitable dimensions demonstrated that the carmine dye/PVA composite films exhibited promising performance as laser cut-off filters, indicating their potential applicability in low-cost optical filtering systems. [8]. In this study, polymeric films were produced by mixing different amounts of glycerol, NaCaS (Sodium caseinate) and polyethylene materials in the extruder under certain conditions. Then, the mechanical, thermal, contact angle, water vapor permeability, etc. properties of the produced films were determined, and characterization tests were carried out using SEM and FTIR analyses.

PVA is a polymer with high water retention and moisture retention capacity due to its high hydrophilic properties. Additionally, they are used in many industrial products thanks to their high adhesion and excellent film forming properties [10-12]. Lutein is a natural carotenoid pigment and is found in green leafy vegetables, yellow fruits and eggs. Lutein production generally involves two steps: plant extraction and refining. Plant extraction is carried out by extracting marigold flowers. Afterwards, the lutein extract is refined and made ready for use in various industries [13-15]. Beta-carotene is a type of carotenoid pigment and is an organic, strongly colored red-orange pigment found abundantly in mushrooms, plants and fruits. β-Carotene is a popular ingredient, especially used in nutritional supplements and cosmetic products. It is also popular as an ingredient used in food supplements and colorants [16-18].

In this study, 3 wt% pure PVA films, 3 wt% β-carotene-doped PVA films, and 3 wt% lutein-doped PVA films were produced using the solution casting method. The novelty of this study is the comprehensive evaluation of how lutein and β-carotene specifically affect the thermal, mechanical, chemical, and morphological properties of PVA films. To address the lack in the literature, the films were characterized using XRD, FTIR, SEM, DSC, and tensile testing. This study aims to assess the influence of these natural pigments on PVA films, highlighting their potential as sustainable and functional materials for the packaging industry and other industrial applications.

EXPERIMENTAL

Materıals

Polyvinyl alcohol (PVA) with a molecular weight of 89,000-98,000 was purchased from Interlab Laboratory Products Industry and Trade Inc. and stored at room temperature. Lutein and β-carotene were obtained from Ruber Biotechnology and Chemical Industry Tic. Ltd. and stored at -20 °C. Deionized water, used as the solvent, was produced using a Lauda-GFL pure water system (Gesellschaft für Labortechnik mbH).

Synthesis of pure PVA film

A 3 wt% PVA solution was prepared by accurately weighing the required amount of PVA

using a precision balance (Pioneer, OHAUS). The polymer was dissolved in deionized water in 50 mL beakers and continuously stirred at 500 rpm for 4 h at 85 °C until a clear homogeneous solution was obtained. Subsequently, the solution was cast into Petri dishes and dried in an oven at 40 °C for 48 h to produce PVA films.

Synthesis of dye-doped PVA films

Initially, a 3 wt% PVA solution was prepared by dissolving the polymer in 40 mL of deionized water under continuous stirring at 500 rpm for 4 h at 85 °C. In a separate step, β-carotene (3 wt%) was dispersed in 10 mL of deionized water and stirred at 500 rpm for 4 h at room temperature. The β-carotene dispersion was subsequently incorporated into the PVA solution and mixed for an additional 1 h at 500 rpm. To improve the homogeneity of the final formulation, the mixture was centrifuged at 4000 rpm for 15 min. The resulting solution was then cast into Petri dishes and dried at 40 °C for 48 h to obtain β-carotene-loaded PVA films. Following the same experimental protocol, including identical processing conditions and equipment, lutein-doped PVA films containing 3 wt% lutein were also fabricated. Figures 1a and 1b show the 3 wt% lutein-doped PVA and 3 wt% β-carotene-doped PVA films after the drying process, respectively.

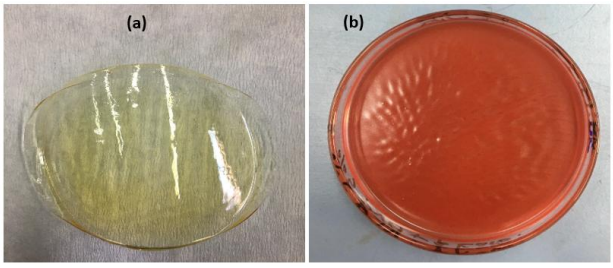

Figure 1. a) Lutein-doped PVA film; b) β-Carotene-doped PVA film

Characterization of pure and dye-doped PVA films

SEM analysis was employed to examine the surface morphology of the samples using a Zeiss EVO® LS 10 microscope at a magnification of 5000×. Crystalline characteristics were investigated by X-ray diffraction (XRD) using a PANalytical X'Pert Pro diffractometer, operating with Cu-Kα radiation (45 kV, 40 mA). XRD measurements were performed by collecting diffraction patterns within a 2θ range of 5°–90° at a scanning rate of 2° min^{-1}. The chemical structures of the films were analyzed using FTIR on a Perkin Elmer Spectrum instrument equipped with an attenuated total reflectance (ATR) accessory, over the wavenumber range of 4000–400 cm^{-1}. Thermal properties were investigated by differential scanning calorimetry (DSC) using a NETZSCH DSC 3500 calorimeter, where samples were heated from 30 ° C to 210 °C at a constant rate of 30 K min^{-1}. Mechanical properties were assessed through tensile testing at ambient temperature using an Instron 5982 universal electromechanical testing machine. Films were prepared in dimensions of 15 mm × 40 mm and tested at a crosshead speed of 10 mm min^{-1}. The elongation at break and Young's modulus of the films were subsequently determined from the obtained stress-strain data.

RESULTS AND DISCUSSION

SEM analysis was performed to investigate the surface morphology and microstructure of pure and dye-doped PVA films. The effect of dye incorporation on the surface properties of the films was evaluated using SEM images. Figure 2 shows SEM images of 3 wt% (a) pure, (b) β-carotene-doped, and (c) lutein-doped PVA films at 5000× magnification. The SEM images of all 3 wt% pure and dye-doped films revealed flat, smooth, and non-porous surfaces, indicating that the incorporation of the natural dyes did not significantly alter the surface morphology of the PVA films.

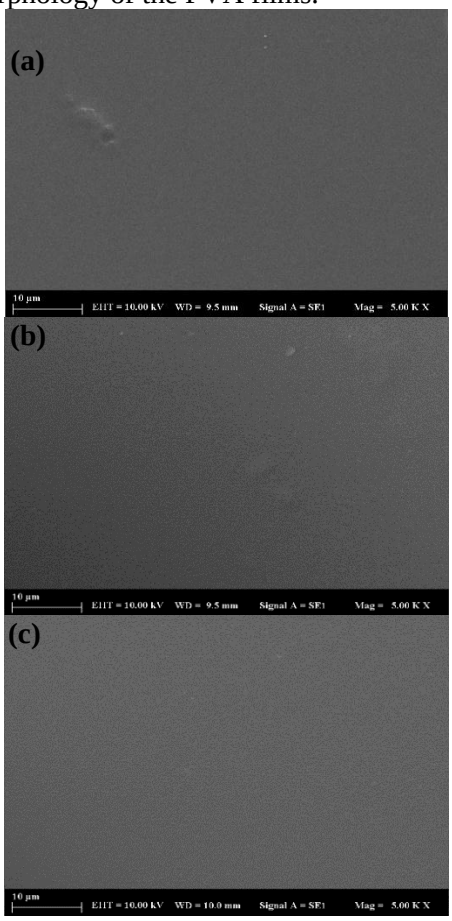

Figure 2. SEM images of 3 wt% a) pure b) β-carotene c) lutein doped PVA films at 5000X magnification.

Bonds and functional groups of the dye-doped polymeric films were characterized by FTIR analysis (Fig. 3). In the pure 3 wt% PVA polymeric film, the main peaks at 3260 cm^{-1}- 2940 cm^{-1} are associated with the stretching of the oxygen-containing functional group OH and CH. The peaks at 1657 cm^{-1} and 1562 cm^{-1} are C=O carbonyl group stretching and C=C stretching, respectively. Additionally, there are C-C stresses at wave frequencies of 1416.37 – 1328.58 cm^{-1}. The functional groups of PVA $(C_2H_4O)x$ films detected are in line with the literature data [19]. When chemical bonds of 3 wt% β-carotene-doped PVA film are examined, the main peaks at 3257.894 cm^{-1}-2909.505 cm^{-1} in the FTIR spectrum are attributed to OH and CH stretching, respectively. The 1655 cm^{-1} peak belongs to the C=O carbonyl group stretching, and the 1419.97 cm^{-1} - 1328.42 cm^{-1} peak belongs to the C-C stretching peaks. In the 3 wt% lutein-doped PVA films, the peaks in the bands 3266.727 cm^{-1}-2937.814 cm^{-1} in the FTIR spectra are referred to OH and CH stretching, respectively. The frequency of 1659.188 cm^{-1} belongs to C=O carbonyl group stretching and 1416.453 cm^{-1}-1327.985 cm^{-1} peaks belong to the C-C functional group. There are no C=C stretch peaks in dye-doped PVA films. In lutein- and β-carotene-loaded PVA samples, a slight broadening and small shifts in the O–H band may indicate weak hydrogen bonds or interactions formed by the loaded carotenoids with PVA. The slight increase in band intensity in the C–H bands (2850-2950 cm^{-1}) region with carotenoid loading was associated with the contribution of hydrophobic alkyl groups.

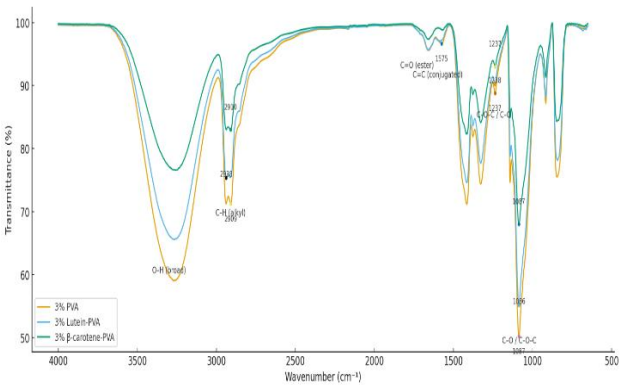

Figure 3. FTIR spectra of pure and dye-doped PVA films

X-ray diffraction (XRD) analysis was performed to investigate the crystal structure of the synthesized films. The XRD pattern of the 3 wt% pure PVA film exhibited a characteristic peak at 2θ = 19.51°, which is attributed to intermolecular hydrogen bonding within the polymer matrix. This result is consistent with previous findings, where Canan *et al.* reported a PVA characteristic peak at 2θ = 19.516° [20]. Figure 4 shows the XRD patterns of pure and dye-doped PVA films. For the 3 wt% β-carotene-doped PVA film, a single peak at 2θ = 19.60° was observed, indicating that β-carotene was homogeneously dispersed within the PVA matrix and maintained the crystalline structure. Similarly, the 3 wt% lutein-doped PVA film exhibited a peak at 2θ = 19.55°. While the addition of β-carotene increased the peak intensity, the incorporation of lutein did not significantly alter the peak intensity. These results suggest that both dyes are compatible with the PVA matrix without disrupting its crystalline structure.

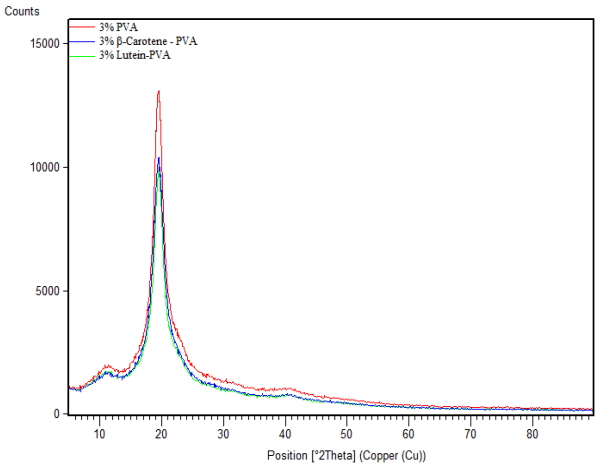

Figure 4. XRD graph of pure and dye-doped PVA films

The mechanical properties of the films were evaluated by tensile testing of pure and dye-doped PVA films. The 3 wt% pure PVA film exhibited a tensile strength of 37.97 MPa and a elasticity modulus of 158.8 MPa. For the 3 wt% β-carotene-doped PVA film, the tensile strength increased to 46.56 MPa, while the elasticity modulus decreased to 36.85 MPa, specifying that β-carotene incorporation enhanced the tensile strength but reduced stiffness. In contrast, the 3 wt% lutein-doped PVA film showed a tensile strength of 35.24 MPa and elasticity modulus of 91.61 MPa, suggesting a slight decrease in tensile strength upon lutein addition. The tensile properties of all samples are summarized in Table 1.

Table 1. Tensile strength and E modules of samples

Samples	E module (MPa)	Tensile strength (MPa)
3 wt % pure PVA film	158.89	37.97
3 wt % β-carotene-PVA film	36.85	46.56
3 wt % lutein-PVA film	91.61	35.24

Thermal characterization of the films was performed using differential scanning calorimetry (DSC) to determine their melting temperatures (T_m) and enthalpy values. The DSC curve of the 3 wt% pure PVA film is presented in Figure 5. The melting temperature of pure PVA was observed at 116.2 °C, with an enthalpy of -70.45 J/g, which is consistent with the reported T_m of ~200 °C for PVA [21]. For the 3 wt% β-carotene-doped PVA film, the melting temperature increased to 120.1 °C and the enthalpy to –104.4 J/g, as shown in Figure 6. Similarly, the 3 wt% lutein-doped PVA film exhibited a T_m of 126.5 °C and an enthalpy of -115.8 J/g (Figure 7).

The presence of endothermic peaks in all samples corresponds to phase transitions of the polymer matrix. These results indicate that the incorporation of β-carotene and lutein into PVA films increased the melting temperature, with lutein-doped films showing the highest T_m. Moreover, the enthalpy values increased upon dye addition, suggesting enhanced thermal stability of the dye-doped films compared to pure PVA.

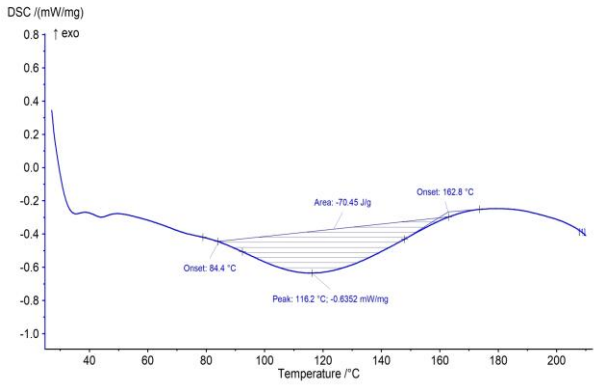

Figure 5. DSC graph of 3 wt % pure PVA film

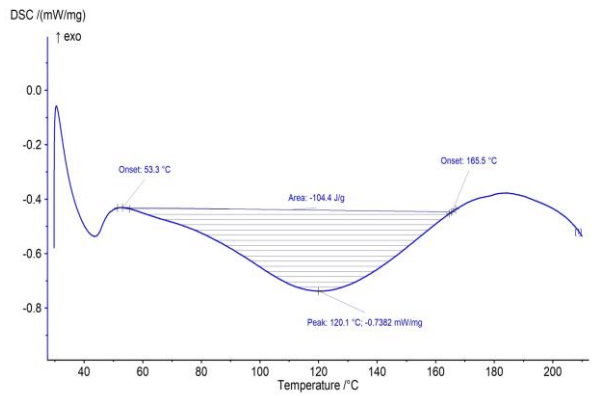

Figure 6. DSC graph of 3 wt % β-carotene dye-doped PVA film

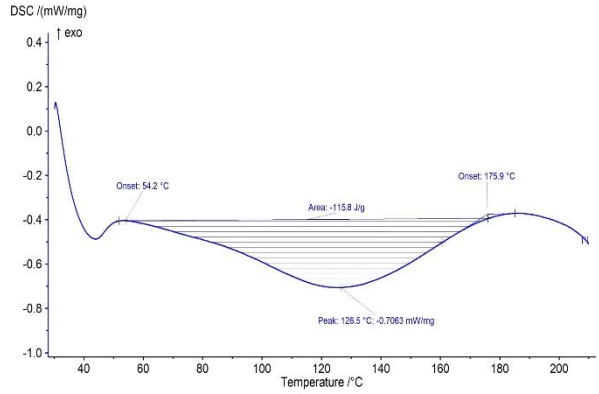

Figure 7. DSC graph of 3 wt % lutein dye-doped PVA film

CONCLUSION

In today's industry, dye-doped polymer-based films are frequently used in various areas. According to the findings of this study, the produced pure and dye-doped films exhibit favorable characteristics due to their crystal structure, smooth surface and good durability and have potential for packaging applications. Furthermore, these films have profits in terms of production conditions, usability, and biodegradability, supporting their potential use in multiple industrial areas. Considering the limitations of the solution casting method for large-scale production, alternative fabrication techniques could be explored to develop films at higher volumes. Additionally, these films may be combined as composite materials in lamination processes for various applications across different industries.

Acknowledgement: *This current study was supported by the Yildiz Technical University Scientific Research Projects Coordination Department, (Project No: FYL-2022-4877).*

Credit authorship contribution statement: *Deniz Uygunoz: Investigation, Methodology, Writing – original draft. Ibrahim Sengor: Investigation, Methodology, Writing – original draft. Emek Moroydor Derun: Methodology, Writing - Review & Editing, Supervision, Project administration.*

Declaration of competing interest: *The authors declare that they have no known competing financial interests or personal relationships that could have appeared to influence the work reported in this paper.*

Declaration of generative AI and AI-assisted technologies in the manuscript preparation: *During the preparation of this work the authors used ChatGPT to improve readability and language. The analysis data was visualized by generating Python code using Google Colab support.*

REFERENCES

1. M. Sacak, Polimer Kimyası, Gazi Kitapevi, Ankara, 2010.
2. J. R. Wagner, Multiplayer Flexible Packaging, 1st edn., Elsevier, Oxford, 2010.
3. K. Marycz, M. Maredziak, J. Grzesiak, D. Szarek, A. Lis, J. Laska, *Polymers*, **8** 175 (2016). DOI: 10.3390/polym8050175.
4. M. Ataka, K. Sasaki, *J. Membr. Sci.*, **11,** 11 (1982). DOI: 10.1016/S0376-7388(00)81239-9.
5. M. Latos-Brozio, A. Masek, *Food Chem. Toxicol*., **135** 10975 (2020). DOI: 10.1016/j.fct.2019.110975.
6. S. Patil, A. K. Bharimalla, A. Mahapatra, J. Dhakane-Lad, A. Arputharaj, M. Kumar, A. S. M. Raja, N. Kambli, *Food Biosci*., **44** 101352 (2021). DOI: 10.1016/j.fbio.2021.101352.
7. C. D. Bucak, M. O. Şahin, *Int. J. Adv. Eng. Pure Sci*., **34,** 373 (2022). DOI: 10.7240/jeps.1089688.
8. Z. A. Alrowailia, M. Ezzeldien, M. I. Mohammed, I. S. Yahiae, *Results Phys*., **18,** 103203 (2020). DOI: 10.1016/j.rinp.2020.103203.
9. H. Y. Ersan, A. Aytaç, *Eng. Sci.*, **15,** 69 (2020) DOI: 10.12739/NWSA.2020.15.2.1A0451.
10. E. M. Ahmed, *J. Adv. Res*. **6,** 105 (2015). DOI: 10.1016/j.jare.2013.07.006.
11. M. L. Di Lorenzo, L. C. Tome, A. M. Ramos, *J. Appl. Biomater. Funct. Mater*., **17,** 1 (2019).
12. J. M. Gohil, P. R. Patel, *Int. J. ChemTech Res.*, 3520 (2014).
13. D. A. Kopsell, D. E. Kopsell, M. G. Lefsrud, *J. Am. Soc. Hortic. Sci*., 527 (2009).
14. J. L. Busch, N. P. Vel, D. L. Vollmer, *Optom. Vis. Sci*., **84,** 903 (2007).
15. L. Bianchi, H. H. Schiffer, *J. Food Compos. Anal*., **17,** 221 (2004).
16. E. J. Johnson, *Nutr. Clin. Care*, **5,** 56 (2002). DOI: 10.1046/j.1523-5408.2002.00004.x.
17. B. L. L. Tan, M. E. Norhaizan, W. P. P. Liew, H. Sulaiman Rahman, *Front. Pharmacol*., **9,** 1162 (2018). DOI: 10.3389/fphar.2018.01162.
18. A. J. Meléndez-Martínez, P. Mapelli-Brahm, A. Benítez-González, C. M. Stinco, *Arch. Biochem. Biophys*., **572,** 188 (2015). DOI: 10.1016/j.abb.2015.01.003.
19. M. C. Popescu, B. I. Dogaru, M. Goanta, D. Timpu, *Int. J. Biol. Macromol*., **116,** 385 (2018). DOI: 10.1016/j.ijbiomac.2018.05.036.
20. C. A. Canbay, N. Ünlü, *Fırat Üniv. Fen Bilim. Derg*., **32**, 53 (2020).
21. E. Söylemez, Polivinil alkol-polietilenimin (PVA-PEI) kompozit nanoliflerin elektrospinleme yöntemi ile üretimi, karakterizasyonu ve çeşitli kullanım alanlarına uygulanması, MSc Thesis, Hitit University, Çorum, Türkiye, 2016.

Bulgarian Chemical Communications, Volume 58, Issue 3 (pp. 303-309) 2026 *DOI: 10.34049/bcc.58.3.D011*

Biomass energy production from sunflower plant

D. Uygunoz, S. Habibzade, E. M. Derun*

Faculty of Chemistry and Metallurgy, Department of Chemical Engineering, Yıldız Technical University, Istanbul, Türkiye

Accepted: July 28, 2026

Concerns about fossil fuel depletion and the environmental costs of petroleum combustion have steadily pushed biodiesel toward the center of renewable energy research. This study reports on the production of biodiesel from sunflower oil via base-catalyzed transesterification, using a nano-scale calcium oxide (n-CaO) catalyst prepared by the calcination of calcium carbonate ($CaCO_3$) at 900 °C. The synthesized catalyst was characterized by X-ray diffraction (XRD), Fourier-transform infrared spectroscopy (FTIR), and scanning electron microscopy (SEM) analyses. XRD patterns confirmed the formation of predominantly crystalline cubic CaO with minor carbonate and hydroxide traces, with crystallite sizes ranging from 27 to 31 nm and a mean of approximately 29 nm calculated from the Debye–Scherrer equation. FTIR data showed Ca–O stretching as the primary surface feature, with weak carbonate and hydroxyl signals attributable to limited atmospheric contact. SEM images revealed an irregular, porous, and substantially agglomerated particle morphology consistent with a high accessible surface area. The optimal conditions for transesterification were a methanol-to-oil molar ratio of 12:1, a catalyst loading of 3 wt%, a reaction temperature of 60–65 °C, and a reaction duration of 2 hours, yielding 91.0 ± 1.2% biodiesel. ASTM D6751 test methods were employed to determine significant fuel properties of the biodiesel, revealing an acid value of 0.95 mg KOH/g, the sole property exceeding the standard limit. These findings confirm that n-CaO prepared by simple thermal decomposition of an inexpensive, readily available $CaCO_3$ precursor is an easily separable heterogeneous catalyst for biodiesel production.

Keywords: nano-CaO, biodiesel, transesterification, sunflower oil, heterogeneous catalyst, acid value.

INTRODUCTION

Global energy systems are increasingly transitioning toward renewable alternatives, driven by the finite nature of fossil fuel reserves, the environmental consequences of combustion emissions on global climate, and the geopolitical vulnerabilities associated with concentrated petroleum supply chains [1-3]. Among the fuels capable of integrating into existing infrastructure without requiring wholesale engine redesign, biodiesel occupies a well-studied and practically viable position [2].

Biodiesel is produced through the transesterification of triglycerides- plant oils, animal fats, or used cooking oil- with a short-chain alcohol, typically methanol. The overall reaction, shown in Eqn. (1), yields three moles of fatty acid methyl esters (FAME) per mole of triglyceride, along with glycerol as a co-product [4, 5]:

$$C_3H_5(OOCR)_3 + 3CH_3OH \rightleftharpoons C_3H_5(OH)_3 + 3RCOOCH_3 \quad (1)$$

The chemistry is sensitive in practice: the nature and loading of the catalyst, the free fatty acid (FFA) content of the feedstock, the alcohol excess, the reaction temperature, and the contact time all affect the usable yield obtained. High FFA content is a particular complication in base-catalyzed systems, where it promotes saponification—the formation of soap rather than fuel—which reduces yield and makes subsequent separation more difficult [5].

Heterogeneous solid base catalysts, particularly calcium oxide (CaO), have attracted considerable attention for biodiesel production due to their ease of separation, recyclability, and avoidance of alkaline wastewater generation [2, 6]. Among solid bases, CaO stands out for its strong basicity, low cost, and wide availability; it can be sourced from calcium-rich waste streams such as eggshells, marine shells, and marble dust with no meaningful performance penalty [7, 8]. Calcination at approximately 900 °C is generally considered sufficient for complete $CaCO_3$-to-CaO conversion [7, 9, 10].

Nanoscale CaO particles possess higher surface-area-to-volume ratios and basic site densities, enhancing catalytic activity at lower loadings [2, 5]. Thermal decomposition is the simplest synthesis route, routinely producing crystallite sizes in the 20–31 nm range depending on calcination temperature. Degfie *et al.* [5] confirmed that nano-CaO (~29 nm, 500 °C calcination) delivers 96% yield at only 1 wt% loading and 50 °C using waste cooking oil, while Erchamo *et al*. [53] achieved 94% with eggshell-

* To whom all correspondence should be sent:
E-mail: *moroydor@yildiz.edu.tr*

© 2026 Bulgarian Academy of Sciences, Union of Chemists in Bulgaria

derived nano-CaO, showing that waste precursors match reagent-grade performance at lower cost [10].

Despite the substantial body of literature on nano-CaO-catalyzed biodiesel production, several gaps remain. First, the majority of nano-CaO studies use waste cooking oil as feedstock, while fewer systematically investigate refined sunflower oil—which, owing to its lower viscosity and negligible FFA content, provides a cleaner baseline for isolating catalyst effects from feedstock variability. Second, most comparative studies either vary feedstock or vary catalyst source, but rarely hold both constant against a nano-scale versus bulk-scale CaO comparison. Third, to the best of the authors' knowledge, limited studies have combined the 900 °C thermal decomposition route for nano-CaO synthesis with a full ASTM D6751 characterization of the resulting biodiesel from sunflower oil—including a dedicated acid value determination—while simultaneously providing a mechanistic discussion of the mass-transfer constraints that arise in the absence of a cosolvent.

This study synthesizes n-CaO from $CaCO_3$ at 900 °C, characterizes it by XRD, FTIR, and SEM, optimizes transesterification conditions for sunflower oil, evaluates fuel properties against ASTM D6751, and benchmarks yield against fifteen related CaO-based systems.

EXPERIMENTAL

Catalyst preparation

The nano-CaO catalyst was prepared by heating calcium carbonate ($CaCO_3$) powder in a muffle furnace at 900 °C for three hours. Calcination was carried out at 900 °C, which achieves complete phase conversion and peak BET surface area for carbonate-derived CaO [10]. The freshly calcined CaO was immediately transferred to a desiccator to avoid rapid atmospheric deactivation [2] . When the catalyst was to be reused, the spent material was re-calcined at 900 °C; this step thermally decomposes any accumulated $Ca(OH)_2$ and $CaCO_3$ back to the active oxide [30,31].

Feedstock characterization

Before starting the transesterification runs, the sunflower oil was characterized by acid value titration to quantify its free fatty acid content. A weighed oil sample was dissolved in a 1:1 ethanol-diethyl ether mixture and titrated with 0.1 N KOH using phenolphthalein as indicator, continuing until the endpoint color persisted for at least 30 seconds. The measured acid value was 1.40 mg KOH/g oil-low enough to proceed directly to base-catalyzed transesterification without a preliminary esterification step.

Transesterification procedure

All transesterification reactions were run in triplicate (n = 3) in a 250 mL round-bottom flask fitted with a reflux condenser to contain methanol vapor [3, 8]. In each run, the catalyst and methanol were combined first and stirred for 30 minutes at room temperature before the oil was added. This pre-activation step encourages the formation of surface methoxide species-the proximal catalytic intermediates—before the triglyceride substrate is introduced [17, 28].

The optimized reaction conditions are summarized in Table 1. The 60-65 °C range was chosen because it sits just below methanol's atmospheric boiling point of 64.7 °C, keeping the system at a kinetically favorable temperature while the reflux condenser recaptures any vapor that forms [5, 24]. In the absence of a cosolvent, agitation at 800 rpm was relied upon to maintain contact between the oil and methanol phases [3]. After two hours the flask was removed from the heating plate and allowed to cool before the product was worked up. Biodiesel yield was calculated gravimetrically as the mass of purified, dried biodiesel obtained relative to the initial oil mass, as shown in Eqn. (2) [5, 8]:

$$Yield\ (\%) = \frac{m_b}{m_0} \times 100 \qquad (2)$$

where: m^b = mass of purified, dried biodiesel (g); m_0 = initial oil mass (g).

Table 1. Optimized transesterification reaction conditions

Parameter	Value
Oil amount (g)	100
Methanol volume (mL)	55
Methanol-to-oil molar ratio	12:1
Catalyst loading, n-CaO (wt%)	3
Reaction temperature (°C)	60–65
Reaction time (h)	2
Stirring speed (rpm)	800

Product separation and purification

The cooled reaction mixture was poured into a separatory funnel and left undisturbed for 12 h [3, 29]. Two layers developed: a lighter, FAME-rich biodiesel phase on top and a denser phase below containing glycerol, unreacted methanol, and dissolved impurities [3, 8].

Catalyst characterization

Phase composition and crystallite size were determined using a Malvern PANalytical X'Pert

PRO diffractometer with Cu Kα radiation (λ = 1.54059 Å) [10, 24]. Crystallite size was calculated by applying the Debye–Scherrer equation to the five most prominent reflections [17, 24]. Surface functional groups were identified with a PerkinElmer Spectrum 100 FT-IR spectrometer, scanning from 4000 to 400 cm^{-1} [2, 17]. Particle morphology was examined using a Thermo Scientific Apreo 2S field-emission SEM; images were collected at four magnifications of ×5,000, ×20,000, ×30,000, and ×60,000 [5, 7].

RESULTS AND DISCUSSION

Catalyst characterization results

XRD spectra of the synthesized nano-CaO are presented in Fig. 1. Sharp peaks at 2θ = 32.2°, 37.3°, 47.3°, 53.8°, 64.1°, 67.3°, 82.2°, and 86.5° index to the cubic rock-salt structure of CaO (JCPDS No. 37-1497), confirming that 900 °C calcination converted $CaCO_3$ predominantly to CaO [10, 17]. Two lower-intensity peaks near 29.4° and 18.0° are assignable to trace $CaCO_3$ and $Ca(OH)_2$, characteristic surface species formed during handling [2, 17]. Applying the Debye–Scherrer equation to the five strongest reflections gave crystallite sizes of 27.02–31.21 nm (mean: 29.41 nm), consistent with the ~29 nm reported by Degfie *et al.* [5] for nano-CaO prepared by thermal decomposition.

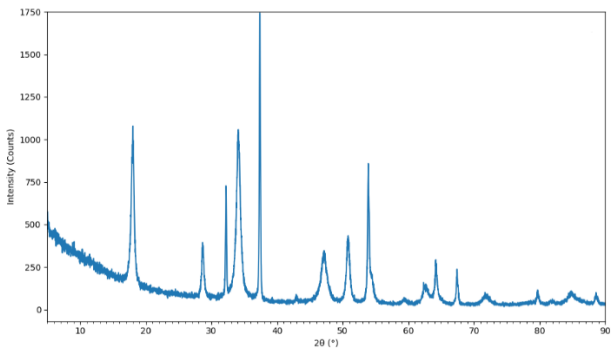

Fig. 1. XRD pattern of nano-CaO catalyst.

The FTIR spectrum (Fig. 2) shows a prominent Ca–O stretching absorption at 500–600 cm^{-1}, confirming CaO as the dominant phase [2, 17]. A band at 3640 cm^{-1} indicates O–H stretching in surface $Ca(OH)_2$, while features at 1400–1470 cm^{-1} and 870 cm^{-1} arise from carbonate species. The relative weakness of these secondary bands confirms that surface carbonation and hydroxylation are superficial and do not compromise bulk catalytic activity [2, 17]. These FTIR features are consistent with published spectra of nano-CaO prepared by thermal decomposition [5, 10].

SEM images at ×5,000, ×20,000, ×30,000, and ×60,000 (Fig. 3) revealed an irregular, porous, and substantially agglomerated particle morphology, typical of thermally synthesized nano-scale oxide powders [8, 21]. The rough, textured surface and visible porosity support high accessible surface area for contact with the oil–methanol mixture. The agglomerated morphology also explains why 3 wt% catalyst loading is required to achieve maximum yield, as the true accessible surface area is lower than what the mean crystallite size alone would suggest [5, 24].

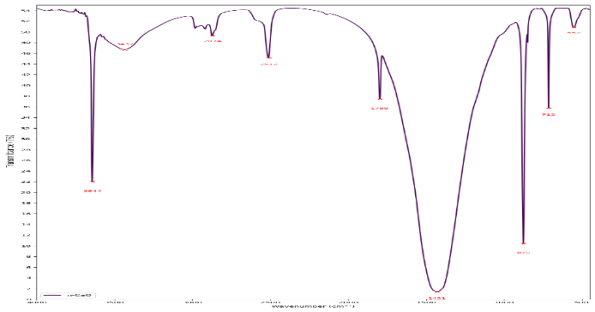

Fig. 2. FTIR spectrum of the nano-CaO catalyst.

Table 2 summarizes the catalytic performance of CaO derived from diverse calcium-rich sources, as reported across the literature. As shown in Table 2, yields consistently exceed 90% across a wide range of precursor types and feedstocks when calcination is carried out at or near 900 °C, confirming the robustness of the thermal decomposition route [36, 37].

Table 2. Catalytic performance of CaO derived from diverse calcium-rich sources

CaO source	Feedstock	MeOH:Oil	Cat. (wt%)	Temp (°C)	Time (h)	Yield (%)	Ref.
Egg/mollusk shell (800°C)	Palm olein	9:1	3	65	2	>90	[7]
Chicken eggshell (900°C)	Sunflower	9:1	3	60	3	94.73	[10]
Quail eggshell (900°C)	Sunflower	10.5:1	2	60	2	99.0	[38]
River snail shell (900°C)	Palm olein	12:1	5	65	1.5	98.5	[40]
Cockle shell (900°C)	Palm olein	9:1	10	65	4	94.47	[42]
Chicken bone (900°C)	WCO	15:1	5	65	4	89.33	[31]
Oyster shell (combusted)	Soybean	24:1	2	65	5	98.0	[43]
n-CaO – 29 nm	Waste cooking oil	8:1	1	50	1.5	96	[5]

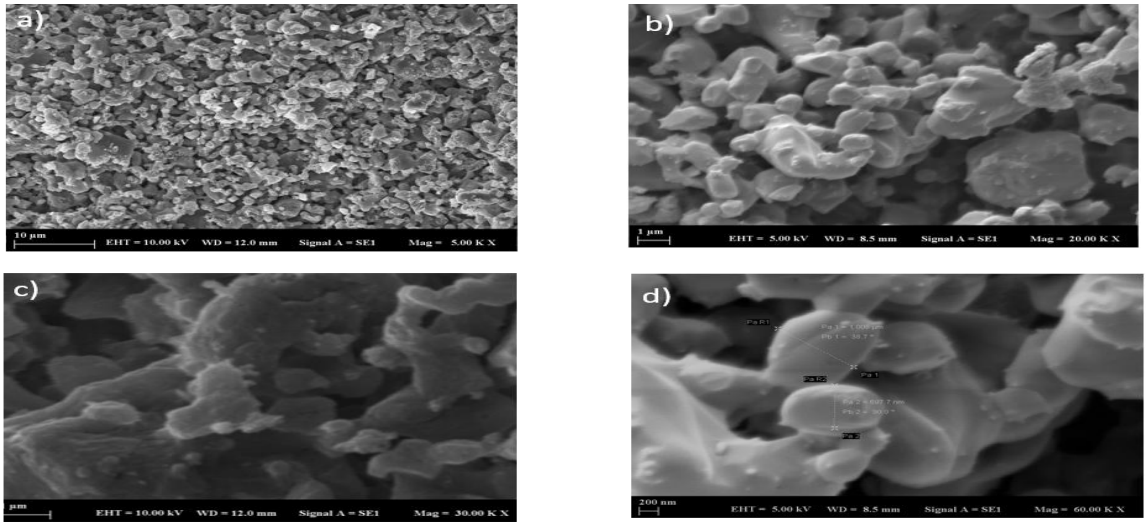

Fig. 3. (a–d) SEM images of synthesized nano-CaO catalyst at magnifications of ×5,000, ×20,000, ×30,000 and ×60,000, respectively.

Table 3. Biodiesel yield: this work alongside selected CaO-based literature systems

Feedstock / catalyst	MeOH:oil	Catalyst load (wt%)	Temperature (°C)	Time (h)	Yield (%)	Ref.
Sunflower oil / n-CaO (29 nm, 900°C)	12:1	3	60–65	2	91.0 ± 1.2	This work
Sunflower oil / CaO (eggshell, 900°C)	9:1	3	60	3	97.75	[10]
Sunflower oil / CaO (quail eggshell, 900°C)	10.5:1	2	60	2	99.0	[19]
Waste cooking oil / n-CaO (29 nm)	8:1	1	50	1.5	96	[5]
WCO / lime-based Zn-CaO	14:1	5	57.5	2	96.5	[33]
Argemone mexicana / eggshell CaO	9.7:1	3.05	60	3	99.07	[50]
Sunflower oil / CaO (marble dust)	15:1	5	60	2	89.14	[12]
Sunflower oil / CaO (eggshell)	15:1	5	60	2	73	[12]
Sunflower oil / CaO (sugar industry)	15:1	5	60	2	87.64	[12]
Sunflower oil, NaOH	6:1	1	65	1	90.9	[14]
Soybean oil / CaO (snail shell)	6:1	3	28	7	98	[51]
WCO / CaO (chicken manure)	15:1	7.5	65	5	90	[29]
Canola oil / CaO (ultrasound)	7.48:1	5.35	60	2.5	99.4	[4]
WCO / nano CaO+MgO	7:1	1.5	75	6	94.4	[24]
Rapeseed oil / Eggshell CaO	9:1	4	60	1	95.12	[52]
WCO / eggshell nano-CaO (MeOH/EtOH)	12:1	2.5	60	2	94	[53]
WCO / white bivalve clam shell CaO	12:1	7	65	1	94.25	[53]

Effect of reaction parameters on biodiesel yield

- *Catalyst loading.* Yield increased with catalyst loading up to 3 wt%, beyond which excess solid raised mixture viscosity and promoted saponification, both reducing yield. The 3 wt% optimum is notably lower than the 5 wt% required by bulk CaO systems [7, 33], reflecting the higher surface area per gram of the nano-scale material [5, 24].
- *Methanol-to-oil molar ratio.* Yield increased with methanol-to-oil ratio up to 12:1, beyond which excess methanol dissolved glycerol into the biodiesel phase and impeded separation. The 12:1 optimum exceeds the 8:1 reported by Degfie *et al.* [5] for waste cooking oil, which is attributed to the absence of a cosolvent here: without a phase-bridging agent the oil–methanol boundary imposes a mass-transfer penalty that a larger methanol excess compensates for [40, 51].
- *Reaction temperature.* Yield improved up to 60–65 °C, where reduced oil viscosity improves mass transfer and thermal energy accelerates the reaction rate. The reflux condenser retained methanol vapor, keeping the effective molar ratio at the optimum. The higher optimum compared with the 50 °C of Degfie *et a*l. [5] reflects sunflower oil's lower viscosity requiring more thermal driving force [4, 46].
- *Reaction time*. Yield increased over the first 2 h as the reaction approached equilibrium; extending beyond this added no conversion and risked reverse reaction. The 2 h optimum falls within the 1.5–2.5 h window reported for comparable CaO systems [5, 48].
- *Acid value of the produced biodiesel.* The acid value of the biodiesel produced under the optimized transesterification conditions (Table 1) was determined according to BS EN 14104:2021, the international standard method for the determination of acid value in fatty acid methyl esters. A weighed biodiesel sample was dissolved in a neutralized 1:1 (v/v) mixture of ethanol and diethyl ether and titrated against 0.1 N potassium hydroxide solution using phenolphthalein as the visual endpoint indicator. The acid value was calculated using the standard relationship given in Equation (3):

$$\mathrm{AV\ (mg\ KOH/g)} = \frac{\mathrm{V \times N \times 56.1}}{\mathrm{m}} \qquad (3)$$

where: V = volume of KOH solution consumed (mL); N = normality of the KOH solution (0.1 N); 56.1 = molar mass of KOH (g/mol); m = mass of the biodiesel sample (g).

However, the measured value of 0.95 mg KOH/g remains slightly above the maximum limit of 0.50 mg KOH/g specified by both ASTM D6751 and EN 14214 for finished biodiesel. This result suggests the presence of residual free fatty acids or minor acidic by-products remaining in the final product. In addition, process variables such as reaction efficiency, phase separation behavior, and the extent of impurity removal may also contribute to the observed acid number.

The acid value result is consistent with that of Bedir and Doğan [7], who also reported finished fuel properties within EN 14214 and ASTM D6751 limits only after additional purification optimization; and with Degfie *et al.* [5], who reported an acid number below 0.50 mg KOH/g for nano-CaO-catalyzed biodiesel from waste cooking oil after an extended purification protocol.

CONCLUSION

This study synthesized and characterized a nano-CaO catalyst by thermal decomposition of $CaCO_3$ at 900 °C and evaluated its catalytic performance in the transesterification of sunflower oil. XRD confirmed predominantly crystalline cubic CaO with a mean crystallite size of 29.41 nm; FTIR and SEM analyses showed a porous, agglomerated morphology consistent with high accessible surface area. Under optimized conditions (12:1 methanol-to-oil, 3 wt% catalyst, 60–65 °C, 2 h), a biodiesel yield of 91.0 ± 1.2% was achieved. The acid value of 0.95 mg KOH/g, determined by BS EN 14104:2021, was marginally above the ASTM D6751 limit of 0.50 mg KOH/g, indicating that downstream purification remains the primary optimization target. The 3 wt% optimum catalyst loading—below the 5 wt% typically required for bulk CaO—confirms the surface-area advantage of the nano-scale morphology. Future work should focus on targeted purification steps, systematic reusability testing, and the use of waste-derived $CaCO_3$ precursors to further reduce production cost.

Acknowledgement: *This study was supported by Yildiz Technical University Scientific Research Projects Coordination Unit under project number FYL-2025-6639.*

Credit authorship contribution statement: *D. Uygunoz: methodology, ınvestigation, visualization, formal analysis, conceptualization, writing-review & editing. S. Habibzade: methodology, ınvestigation, visualization, formal analysis, conceptualization, writing-original draft. E. Moroydor Derun: conceptualization, writing-review & editing, supervision.*

Conflict of interest: *The authors declare that they have no known competing financial interests or*

personal relationships that could have appeared to influence the work reported in this paper.

Declaration of generative ai and ai-assisted technologies in the manuscript preparation: *During the preparation of this work the authors used ChatGPT to improve readability and language. The analysis data was visualized by generating Python code using Google Colab support.*

ORCIDs:

D. Uygunoz: https://orcid.org/0000-0001-8936-6284

E. Moroydor Derun: https://orcid.org/0000-0002-8587-2013

REFERENCES

1. IEA, Renewables 2024, IEA Publications, Paris, 2024.
2. J.S.J. Ling, Y.H. Tan, N.M. Mubarak, J. Kansedo, A. Saptoro, C. Nolasco-Hipolito, *SN Appl. Sci.*, **1**, 810 (2019).
3. A.P.S. Chouhan, A.K. Sarma, *Renew. Sustain. Energy Rev.*, **15**, 4378 (2011).
4. I. Korkut, M. Bayramoglu, *Renew. Energy*, **116**, 543 (2018).
5. T.A. Degfie, T.T. Mamo, Y.S. Mekonnen, *Sci. Rep.*, **9**, 18982 (2019).
6. A.A. Refaat, *Int. J. Environ. Sci. Technol.*, **7**, 183 (2010).
7. N. Viriya-empikul, P. Krasae, B. Puttasawat, B. Yoosuk, N. Chollacoop, K. Faungnawakij, *Bioresour. Technol.*, **101**, 3765 (2010).
8. J. Boro, A.J. Thakur, D. Deka, *Fuel Process. Technol.*, **92**, 2061 (2011).
9. I.B. Bankovic-Ilic, M.R. Miladinovic, O.S. Stamenkovic, V.B. Veljkovic, *Renew. Sustain. Energy Rev.*, **72**, 746 (2017).
10. L.M. Correia, R.M.A. Saboya, N.S. Campelo, J.A. Cecilia, E. Rodriguez-Castellon, C.L. Cavalcante Jr., R.S. Vieira, *Bioresour. Technol.*, **151**, 207 (2014).
11. A. Islam, Y.H. Taufiq-Yap, E.S. Chan, M. Moniruzzaman, S. Islam, M.N. Nabi, *Energy Convers. Manage.*, **88**, 1200 (2014).
12. O. Bedir, T.H. Dogan, *Energy Sources, Part A*, **43**, 1 (2021).
13. M.D. Kostic, A. Bazargan, O.S. Stamenkovic, V.B. Veljkovic, G. McKay, *Fuel*, **163**, 304 (2016).
14. E. Emmanouilidou, A. Lazaridou, S. Mitkidou, N.C. Kokkinos, *J. Mol. Struct.*, **1306**, 137870 (2024).
15. S. Islam, B. Basumatary, S.L. Rokhum, P.K. Mochahari, S. Basumatary, *Clean. Chem. Eng.*, **3**, 100043 (2022).
16. S. Niju, K.M.M.S. Begum, N. Anantharaman, *J. Saudi Chem. Soc.*, **18**, 702 (2014).
17. E. Emmanouilidou, S. Mitkidou, A. Agapiou, N.C. Kokkinos, *Sustainability*, **15**, 1042 (2023).
18. S. Niju, S.K.M. Meera, K.M.M.S. Begum, N. Anantharaman, *Arab. J. Chem.*, **9**, 633 (2016).
19. L. Macheli, M.E. Malefane, L.L. Jewell, *Bioresour. Technol. Rep.*, **29**, 102021 (2025).
20. V. Mandari, S.K. Devarai, *BioEnergy Res.*, **15**, 935 (2022).
21. J. Goli, O. Sahu, *Renew. Energy*, **128**, 142 (2018).
22. A. Birla, B. Singh, S.N. Upadhyay, Y.C. Sharma, *Bioresour. Technol.*, **106**, 95 (2012).
23. H.H. Abdelhady, H.A. Elazab, E.M. Ewais, M. Saber, M.S. El-Deab, *Fuel*, **261**, 116481 (2020).
24. K. Tahvildari, Y.N. Anaraki, R. Fazaeli, S. Mirpanji, E. Delrish, *J. Environ. Health Sci. Eng.*, **13**, 73 (2015).
25. V.M. Melo, G.F. Ferreira, L.V. Fregolente, *Renew. Sustain. Energy Rev.*, **189**, 114042 (2024).
26. Y. Wang, D. Li, D. Zhao, Y. Shang, Y. Li, *ACS Omega*, **5**, 17471 (2020).
27. M.L. Granados, M.D.Z. Poves, D.M. Alonso, R. Mariscal, F.C. Galisteo, R. Moreno-Tost, J. Santamaria, J.L.G. Fierro, *Appl. Catal. B*, **73**, 317 (2007).
28. R. Foroutan, R. Mohammadi, J. Razeghi, B. Ramavandi, *Renew. Energy*, **168**, 1207 (2021).
29. T. Maneerung, S. Kawi, Y. Dai, C.H. Wang, *Energy Convers. Manage.*, **123**, 487 (2016).
30. X. Liu, H. He, Y. Wang, S. Zhu, X. Piao, *Fuel*, **87**, 216 (2008).
31. M. Farooq, A. Ramli, A. Naeem, *Renew. Energy*, **76**, 362 (2015).
32. M. Kouzu, T. Kasuno, M. Tajika, Y. Sugimoto, S. Yamanaka, J. Hidaka, *Fuel*, **87**, 2798 (2008).
33. M.G. Weldeslase, N.E. Benti, M.A. Desta, Y.S. Mekonnen, *Sci. Rep.*, **13**, 4430 (2023).
34. M. Kouzu, J. Hidaka, *Fuel*, **93**, 1 (2012).
35. W. Roschat, S. Phewphong, A. Thangthong, P. Moonsin, B. Yoosuk, T. Kaewpuang, V. Promarak, *Energy Convers. Manage.*, **165**, 1 (2018).
36. W. Roschat, M. Kacha, B. Yoosuk, T. Sudyoadsuk, V. Promarak, *Fuel*, **98**, 194 (2012).
37. M. AlSharifi, H. Znad, *Renew. Energy*, **136**, 856 (2019).
38. L. Marques Correia, J.A. Cecilia, E. Rodriguez-Castellon, C.L. Cavalcante Jr., R.S. Vieira, *J. Chem.*, **2017**, 5679512 (2017).
39. Y.H. Tan, M.O. Abdullah, C. Nolasco-Hipolito, Y.H. Taufiq-Yap, *Appl. Energy*, **160**, 58 (2015).
40. W. Roschat, T. Siritanon, T. Kaewpuang, B. Yoosuk, V. Promarak, *Bioresour. Technol.*, **209**, 343 (2016).
41. Y.C. Sharma, B. Singh, J. Korstad, *Energy Fuels*, **24**, 3223 (2010).
42. A. Buasri, N. Chaiyut, V. Loryuenyong, P. Worawanitchaphong, S. Trongyong, *Sci. World J.*, **2013**, 460923 (2013).
43. N. Nakatani, H. Takamori, K. Takeda, H. Sakugawa, *Bioresour. Technol.*, **100**, 1510 (2009).
44. Z.L. Chung, Y.H. Tan, Y.S. Chan, J. Kansedo, N.M. Mubarak, M. Ghasemi, M.O. Abdullah, *Biocatal. Agric. Biotechnol.*, **21**, 101317 (2019).
45. F. Ashine, Z. Kiflie, S.V. Prabhu, B.Z. Tizazu, V. Varadharajan, M. Rajasimman, S.W. Joo, Y. Vasseghian, M. Jayakumar, *Fuel*, **332**, 126166 (2023).
46. A.A. Ayoola, F.K. Hymore, C.A. Omonhinmin, O.C. Olawole, O.S.I. Fayomi, D. Babatunde, O. Fagbiele, *Chem. Data Collect.*, **22**, 100238 (2019).

47. A. Attari, A. Abbaszadeh-Mayvan, A. Taghizadeh-Alisaraie, *Biomass Bioenergy*, **158**, 106357 (2022).
48. W. Roschat, T. Siritanon, B. Yoosuk, V. Promarak, *Energy Convers. Manage.*, **108**, 459 (2016).
49. N. Ghosh, G. Halder, *Energy Convers. Manage.*, **270**, 116292 (2022).
50. M.J. Borah, A. Das, V. Das, N. Bhuyan, D. Deka, *Fuel*, **242**, 345 (2019).
51. I.B. Laskar, K. Rajkumari, R. Gupta, S. Chatterjee, B. Paul, L. Rokhum, *RSC Adv.*, **8**, 20131 (2018).
52. H.I. Mahdi, N.N. Ramlee, J.L. da Silva Duarte, Y.S. Cheng, R. Selvasembian, F. Amir, L.H. de Oliveira, N.I. Wan Azelee, L. Meili, G. Rangasamy, *Chemosphere*, **319**, 138003 (2023).
53. Y.S. Erchamo, T.T. Mamo, G.A. Workneh, Y.S. Mekonnen, *Sci. Rep.*, **11**, 6708 (2021).

Bulgarian Chemical Communications, Volume 58, Issue 3 (pp. 310-314) 2026 *DOI: 10.34049/bcc.58.3.D012*

Evaluation of the inhibitory effects of phenolic compounds on calcium oxalate crystallization

S. Simsek, O. Y. Usoğlu, E. Akyol*

Yildiz Technical University, Chemical Engineering Department, Davutpasa Campus, Esenler, Istanbul 34210, Türkiye

Accepted: July 28, 2026

Kidney stone disease, a widespread condition with a history dating back to ancient civilizations, remains a significant global health issue. Among the various types of kidney stones, calcium oxalate (CaOx) stones are predominant, accounting for the majority of urinary tract stones. Alongside conventional treatment methods such as surgery, medication, and lithotripsy, there is growing interest in complementary and alternative therapies, including herbal remedies. This study evaluates the inhibitory effects of phenolic compounds on calcium oxalate crystallization—a process of great importance in biomineralization—and assesses their drug-likeness using in silico approaches. The study aims to predict the potential pharmacokinetic properties of flavonoid compounds in the human body using an *in-silico* ADME (absorption, distribution, metabolism, and excretion) approach. *Helichrysum arenarium* (immortelle/golden everlasting), a plant native to various regions of Turkey, was used as the source of the plant extract. The extract was obtained *via* supercritical CO_2 extraction, and the study elucidates, at the molecular level, how flavonoids (such as quercetin, kaempferol, and naringenin) and phenolic compounds (such as chlorogenic acid and caffeic acid) inhibit CaOx crystal formation.

Keywords: Calcium oxalate (CaOx), kidney stone, *Helichrysum arenarium* extract, flavonoids, phenolic compounds.

INTRODUCTION

Crystallization is the process by which a substance separates from a more disordered structure into more ordered solid particles. It basically consists of three stages: nucleation, crystal growth, and aggregation [1, 2]. Although crystallization is an effective method used in fields such as the pharmaceutical industry and purification, food production, or materials science, there are also situations where its effects can be negative and lead to serious problems. Two of these are industrial crystallization and kidney stone formation, a urinary system disorder [3, 4]. Calcium oxalate, particularly in its monohydrate phase, is the main component of typical kidney Stones [5, 6]. Kidney stone formation is one of the most significant clinical problems in the human body. Kidney stone disease reduces a person's healthy life expectancy and places a heavy financial burden on healthcare systems; both of these significantly lower an individual's quality of life [7, 8]. Therefore, calcium oxalate crystallization has become an important topic of interest to researchers in biomineralization. Research indicates that traditional medicine, including herbal remedies, is used by individuals in various cultures and countries to treat kidney stones. *Helichrysum arenarium* possesses antibacterial, antiviral, antifungal, anti-inflammatory, antimicrobial, anti-allergic and antioxidant properties and is used in folk medicine for the treatment of liver and gallbladder disorders, stomach ache, asthma, cystitis and jaundice, skin infections, respiratory and digestive system disorders, kidney stone treatment and urogenital disorders [9, 10].

Recent studies have shown that SwissADME outcomes are widely used in evaluating the bioavailability, renal distribution, and safety characteristics of naturally occurring phenolic compounds and flavonoids investigated as kidney stone inhibitors. In particular, performing SwissADME analyses in conjunction with *in vitro* crystallization experiments allows for the evaluation of active compounds not only as crystal inhibitors but also as potential therapeutic candidates [11-14].

EXPERIMENTAL

Materıals and method

- *Extraction of Helichrysum arenarium using supercritical fluid extraction (SFE) method*. The leaves of the *Helichrysum arenarium* plant were sourced from a local herbalist in Uşak. The *Helichrysum arenarium extract*, used as a potential inhibitor of calcium oxalate monohydrate growth, was obtained using a supercritical fluid extraction method. Food-grade carbon dioxide (CO_2) with 99.9% purity, stored in a bottom tube, was used as the extraction solvent; ethanol with 99.9% purity was used as a co-solvent to increase the solubility of polar compounds in supercritical CO_2.

* To whom all correspondence should be sent:
E-mail: *eakyol@ yildiz.edu.tr*

© 2026 Bulgarian Academy of Sciences, Union of Chemists in Bulgaria

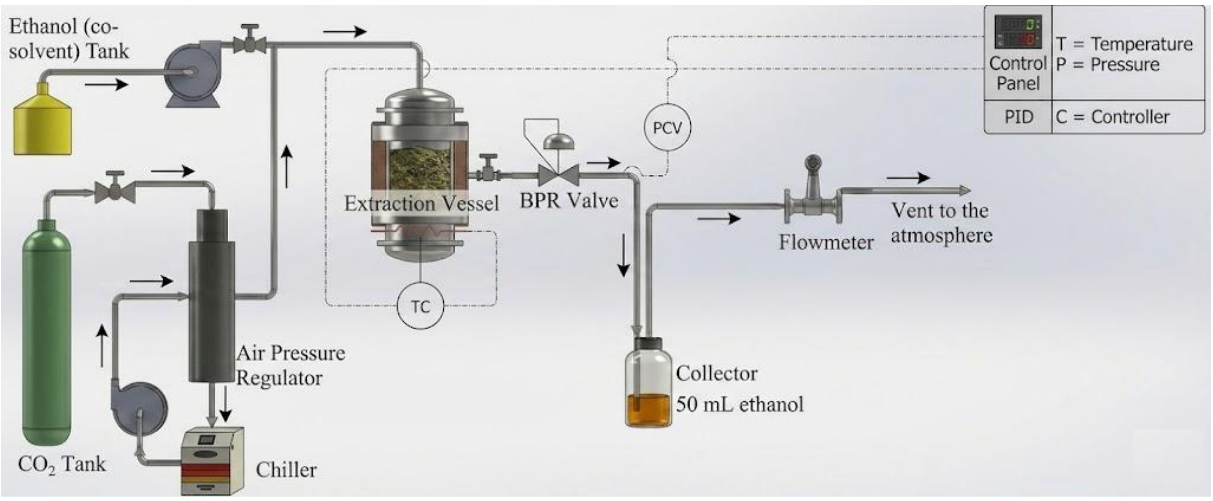

Figure 1. Experimental setup

Supercritical CO_2 extraction (SCF) conditions were as follows: 5 L/min CO_2 flow rate, 15% v/w ethanol ratio, 400 bar extraction pressure and 40 °C temperature. Supercritical fluid extraction experiments on *Achillea millefolium* were conducted using a laboratory-scale supercritical fluid extraction system (Applied Separations, USA), as shown schematically in Figure 1.

- *Phenolic content analysis by LC-HRMS:* The phenolic component profile of *Helichrysum arenarium*, *Thymus vulgaris* L., and *Achillea millefolium* extracts obtained by supercritical CO_2 extraction was determined using the LC-HRMS (liquid chromatography–high resolution mass spectrometry) (Thermo ORBİTRAP Q-EXACTIV) method, which combines liquid chromatography with high-resolution mass spectrometry.
- *In-silico evaluation of the inhibitory effects of flavonoids and phenolic compounds:* In evaluating the therapeutic potential of phenolic compounds and flavonoids that exhibit efficacy in preventing kidney stone formation, their *in vitro* crystallization inhibitory activity alone is insufficient. Candidate molecules are expected to demonstrate adequate absorption after oral administration, enter the circulation, reach kidney tissue, and possess acceptable pharmacokinetic properties. Therefore, the SwissADME platform has been widely used in natural product research in recent years.
- *Gastrointestinal (GI) absorption*: Since most natural compounds used in kidney stone treatment are planned to be administered orally, high GI absorption is one of the most important parameters. High gastrointestinal absorption allows the molecule to pass into the systemic circulation at a higher rate, increasing the effective concentration reaching the kidney. In the literature, gastrointestinal absorption has been the first characteristic evaluated in SwissADME analyses of quercetin, kaempferol, hesperidin, rutin, and various phenolic acids.
- *Bioavailability score:* The bioavailability score indicates the likelihood of bioavailability after oral administration. For phenolic compounds, value of 0.55 is generally considered suitable. It is reported that flavonoids with low bioavailability may have limited in vivo efficacy despite being effective *in-vitro*.
- *Lipinski rule of five:* Kidney stone inhibitor candidates should be evaluated for compliance with the Lipinski rules in terms of exhibiting drug-like properties. Parameters to be evaluated: molecular weight (<500 Da), H-bond donor, H-bond acceptor, LogP (<5). Lipinski violation can occur in most flavonoid glycosides due to increased molecular weight. In contrast, aglycone forms (e.g., quercetin and kaempferol) generally exhibit more favorable pharmacokinetic properties.
- *Consensus logP:* The logP value indicates lipophilicity. Moderate lipophilicity is preferred for kidney stone inhibitors. Very low logP may make it difficult to cross the cell membrane. Very high logP may reduce solubility. Generally, logP values in the range of 1–3 are considered advantageous in terms of reaching kidney tissue.
- *Water solubility:* For phenolic compounds to be effective in the urinary environment, it is important that they have sufficient water solubility. High solubility facilitates transport in urine, reaching the renal tubules, and interacting with crystals.
- *Topological polar surface area (TPSA):* The TPSA value is an important molecular descriptor associated with membrane permeability and oral absorption. Generally, a TPSA value in the range of

20–140 Å² is considered favorable for oral bioavailability, although this depends on other molecular properties. A high TPSA may reduce passive membrane permeability and intestinal absorption because highly polar molecules have limited ability to partition into the lipophilic environment of biological membranes. Flavonoid glycosides generally exhibit higher TPSA values than their corresponding aglycones because the sugar moiety introduces additional hydroxyl groups and other oxygen-containing functional groups, thereby increasing the polar surface area. Consequently, the relatively high TPSA of flavonoid glycosides may contribute to their lower passive membrane permeability and oral absorption compared with the corresponding aglycones.

- *Rotatable bonds:* A low number of rotatable bonds ensures that the molecule is more stable and has better bioavailability. According to Veber's rule, ≤10 is preferred.
- *P-glycoprotein (P-gp) substrate:* Molecules with a P-gp substrate can be pumped back into the lumen from the intestines. This situation reduces bioavailability. Therefore, being non-substrate provides an advantage.
- *Cytochrome P450 inhibition:* SwissADME; CYP1A2, CYP2C9, CYP2C19, CYP2D6, CYP3A4 predicts enzyme inhibition. The presence of numerous CYP inhibitors in natural products that can be used in kidney stone treatment is a disadvantage in terms of drug interactions.
- *PAINS and Brenk alerts:* Structures that may cause false positive biological activity in phenolic compounds are evaluated with PAINS filters. Brenk alerts, on the other hand, show functional groups that may cause potential toxicity. Both parameters are important in the selection of new drug candidates.
- *Lead-likeness:* Indicates whether natural compounds are drug candidates that can be optimized in the future. Phenolic compounds that meet the lead-likeness criteria are more suitable for structural optimization studies.
- *Synthetic accessibility:* Not directly related to biological activity. However, it is important in terms of ease of industrial synthesis and cost of drug development.

Lipinski violations may be observed in most flavonoid glycosides due to their increased molecular weight. In contrast, aglycone forms (e.g., quercetin and kaempferol) generally exhibit more favorable pharmacokinetic properties [15-19].

RESULTS AND DISCUSSION

According to LC-HRMS analysis, naringenin was detected in the highest concentration among the flavonoids frequently reported in the literature for their potential to prevent kidney stone formation in *Helichrysum arenarium* extract, with an amount of 104,410 µg/g dry plant. In contrast, kaempferol and quercetin were found at lower levels, measured as 3,673 µg/g and 0,203 µg/g dry plant, respectively. Regarding phenolic compounds, caffeic acid was detected in the extract at a level of 6,248 µg/g dry plant, while chlorogenic acid was not detected. These results indicate that the extract is particularly rich in naringenin in terms of its kidney stone-preventing effect, while quercetin, kaempferol, and caffeic acid are present in lower concentrations.

SwissADME-predicted pharmacokinetic and drug-likeness properties of major flavonoids and phenolic compounds identified in *Helichrysum arenarium* is given in Table 1. Quercetin, kaempferol, and naringenin generally exhibit favorable absorption characteristics as kidney stone-preventing agents. The estimated human intestinal absorption (HIA) of all three flavonoids is over 70%, with naringenin showing the highest gastrointestinal absorption potential at 91.31%. This suggests that naringenin may have a higher rate of systemic circulation after oral administration and a higher probability of reaching kidney tissue. Quercetin (77.21%) and kaempferol (74.29%) also show acceptable levels of intestinal absorption. CaCO-2 permeability results also support these findings. In contrast, chlorogenic acid exhibited low gastrointestinal absorption, while caffeic acid showed a high absorption potential. Naringenin's log Papp value of 1.029 indicates a very high passive diffusion through the intestinal epithelium.

Table 1. SwissADME-predicted pharmacokinetic and drug-likeness properties of major flavonoids and phenolic compounds identified in *Helichrysum arenarium*

ADME property	Quercetin	Kaempferol	Naringenin	Chlorogenic acid	Caffeic acid
Gastro-intestinal absorption (GI)	High	High	High	Low	High
Bioavail-ability score	0.55	0.55	0.55	0.11	0.56
Lipinski rule of five	Yes; 0 violation	Yes; 0 violation	Yes; 0 violation	Yes; 1 violation (NH/OH>5)	Yes; 0 violation
Consensus logP	0.79	1.20	1.87	-0.71	0.92
ADME property	Quercetin	Kaempferol	Naringenin	Chlorogenic acid	Caffeic acid

Water solubility (ESOL)	-3.19 Soluble	-3.33 Soluble	-3.49 Soluble	-1.62 Very soluble	-1.89 Very soluble
TPSA	131.36	111.13	86.99	164.75	77.76
Rotatable bonds	1	1	1	5	2
P-gp substrate	No	No	Yes	No	No
PAINS	1 alert	0	0	1 alert	1 alert
Brenk	1 alert	0	0	2 alerts	2 alerts
Lead-likeness	Yes	Yes	Yes	No	No
Synthetic accessibility	3.23	3.14	3.01	4.16	1.81

Kaempferol's log P value of 0.032 suggests moderate permeability, while quercetin's log P value of -0.229 indicates relatively lower intestinal permeability. Therefore, naringenin can be considered advantageous in terms of bioavailability compared to the other two flavonoids. All three flavonoids have moderate water solubility, with log mol/L values ranging from −2.925 to −3.224. Quercetin has the highest solubility (−2.925 log mol/L), while naringenin shows the lowest solubility (−3.224 log mol/L). However, naringenin's high intestinal permeability can significantly offset the negative impact of its low solubility on bioavailability. In terms of water solubility, chlorogenic acid and caffeic acid are classified as "very soluble," while quercetin, kaempferol, and naringenin are classified as "soluble." The high solubility of chlorogenic acid and caffeic acid, in particular, can be considered an advantage, facilitating their transport in the urine and their interaction with calcium oxalate crystals. However, high solubility alone does not necessarily mean high bioavailability, as seen in the case of chlorogenic acid, which exhibits low gastrointestinal absorption. The fact that the skin permeability (log Kp) values are quite similar for the three compounds (approximately −2.74) indicates that they have similar characteristics in terms of transdermal application. However, since the primary route of administration in kidney stone treatment is oral, the clinical significance of this parameter is limited. The fact that all three flavonoids are predicted to be P-glycoprotein (P-gp) substrates suggests that they may be subject to P-gp-mediated efflux in the intestinal epithelium, which could somewhat reduce their bioavailability. However, the fact that none of them are predicted to be P-gp inhibitors (Type I or Type II) suggests that these compounds are unlikely to disrupt drug transport mechanisms by suppressing P-gp function, and may therefore offer an advantage in terms of drug interactions.

CONCLUSION

All three flavonoids exhibit favorable pharmacokinetic properties in terms of kidney stone prevention potential. However, naringenin stands out as the most advantageous candidate in terms of oral bioavailability due to its highest HIA and CaCO-2 permeability. Quercetin and kaempferol, despite lower intestinal permeability, have acceptable absorption properties. When these pharmacokinetic findings are considered together with the antioxidant, anti-inflammatory, and calcium oxalate crystallization inhibitory biological effects reported in the literature, it suggests that naringenin, in particular, may have higher therapeutic potential for preventing kidney stone formation. However, these predictions need to be confirmed by crystallization experiments, cell culture studies, and *in vivo* models.

REFERENCES

1. C.J. Geankoplis, Transport Processes and Separation Process Principles (Includes Unit Operations), 4th edn., Prentice Hall PTR, New Jersey, 2003.
2. W.L. McCabe, J.C. Smith, P. Harriott, Unit Operations of Chemical Engineering, 7th edn., McGraw-Hill, Boston, 2005.
3. V. Romero, H. Akpinar, D.G. Assimos, *Rev. Urol.*, **12**, e86 (2010).
4. T. Alelign, B. Petros, *Advances in Urology*, **2018**, 3068365 (2018).
5. S.R. Khan, M.S. Pearle, W.G. Robertson, G. Gambaro, B.K. Canales, S. Doizi, O. Traxer, H.-G. Tiselius, *Nat. Rev. Dis. Primers*, **2**, 16008 (2016)
6. E. Akyol, M. Danisman, M. Oner, *Urolithiasis*, **53**, 133 (2025).
7. C. A. Suijker, C. van Mazijk, S. Roemeling, *Med. Health Care Philos*., **29**, 39 (2026).
8. M. Akram, B. Somani, *Res. Rep. Urol.*, **17**, 449 (2025).
9. L. C. Klein-Junior, M. R. de Souza, J. Viaene, T. M. B. Bresolin, A. L. de Gasper, A. T. Henriques, Y. Vander Heyden, *Planta Med.*, **87**, 964 (2021).
10. I M. Ivanović, A. Albreht, P. Krajnc, I. Vovk, M. I. Razboršek, *Ind. Crops Prod.*, **160**, 113102 (2021).
11. X. Zeng, Y. Xi, W. Jiang, *Crit. Rev. Food Sci. Nutr.*, **59**, 2125 (2019).
12. T. Yasui, A. Okada, S. Hamamoto, R. Ando, K. Taguchi, K. Tozawa, K. Kohri, *Biomed. Pharmacother.*, **106**, 1292 (2018).
13. S. Mushtaq, A. A. R. Siddiqui, S. A. R. Naqvi, R. Ahmed, A. M. Alqahtani, M. A. Alghamdi, *Nutrients*, **15**, 3753 (2023).

14. P. Peerapen, P. Putpeerawit, W. Boonmark, V. Thongboonkerd, *Curr. Res. Food Sci.*, **12,** 101326 (2026).
15. A. Daina, O. Michielin, V. Zoete, *Sci. Rep.*, **7**, 42717 (2017).
16. C. A. Lipinski, F. Lombardo, B. W. Dominy, P. J. Feeney, *Adv. Drug Deliv. Rev.*, **46**, 3 (2001).
17. D. F. Veber, S. R. Johnson, H. Y. Cheng, B. R. Smith, K. W. Ward, K. D. Kopple, *J. Med. Chem.*, **45**, 2615 (2002). A. K. Ghose, V. N. Viswanadhan, J. J. Wendoloski, *J. Comb. Chem*., **1**, 55 (1999).
18. A. K. Ghose, V. N. Viswanadhan, J. J. Wendoloski, *J. Comb. Chem*., **1**, 55 (1999).
19. S. Simsek, E. Akyol, I. Kucuk, *J. Med. Food*, **29**, 1 (2026).

Bulgarian Chemical Communications, Volume 58, Issue 3 (pp. 315-319) 2026 DOI: 10.34049/bcc.58.3.D013

Sustainable heavy metal ion detection of waste-based carbon quantum dots

N. A. Saleha, E. Akyol*

Yildiz Technical University, Chemical Engineering Department, Davutpasa Campus, Esenler, Istanbul 34210, Turkey

Accepted: July 28, 2026

Heavy metals contamination represents one of the noticeable challenges of the environmental pollution due to its persistence, toxicity and negative impacts on ecosystem and human health. Because of the high cost, limited sustainability of the traditional detection methods the need of green and sustainable methods has increased. In the recent years Carbon quantum dots CQDs have emerged as a valuable fluorescent nanomaterial owning to their strong photoluminescence, low toxicity, high biocompatibility, and the presence of surface functional groups that enable effective interactions with metal ions [1] In this work CQDs were green-synthesized from olive seeds kernels which consists of holocellulose, lignin, and proteins [2] using a hydrothermal method at different parameter conditions (time, temperature and citric acid) to find the best conditions that gives the higher fluorescence intensities, the CQD sample exhibiting the highest sensing performance toward Fe^{3+} ions was selected for further detection and adsorption studies.

The interaction between CQDs and Fe^{3+} ions induced pronounced photoluminescence quenching, enabling sensitive detection. The adsorption behavior of Fe^{3+} onto the selected CQDs was investigated to assess their potential not only as fluorescent sensors but also as sustainable adsorbents for heavy metal removal from aqueous solutions. Lastly olive seeds are new and friendly alternative as carbon source to synthesis CQDs and is a low-cost and sustainable solution for water quality monitoring, supporting biomass waste valorization while minimizing environmental impacts.

Keywords*:* carbon quantum dots (CQDs, heavy metal contamination, fluorescence intensities, photoluminescence quenching.

INTRODUCTION

Carbon quantum dots and their history

Carbon dots (CDs), also known as carbon quantum dots (CQDs), are a relatively new category of zero-dimensional fluorescent carbon-based nanomaterials, generally possessing particle sizes below 10 nm. These nanostructures were first identified in 2004 [3] marking the initial discovery of CQDs.

Properties and structure of carbon quantum dots

Carbon quantum dots (CQDs) possess unique physicochemical and optical properties, along with a nanoscale size and a high surface area, which contribute to their efficient electron transfer and strong adsorption capability. They exhibit excellent chemical stability, good water solubility and low toxicity [4].The general structure of CQDs is shown in Fig 1. [4]

- *Green synthesis of carbon quantum dots.* Carbon quantum dots (CQDs) can be synthesized using two main approaches: top-down and bottom-up methods. The top-down approach produces CQDs by breaking down bulk carbon materials small molecular precursors using methods including irradiation, combustion, and pyrolysis [6] Compared with top-down techniques, bottom-up methods are generally simpler, more cost- through techniques such as laser ablation, arc discharge, and electrochemical or chemical oxidation [5]. In contrast, the bottom-up approach forms CQDs from small molecular precursors using methods including hydrothermal/solvothermal synthesis, microwave irradiation, combustion, and pyrolysis [6]. Compared with top-down techniques, bottom-up methods are generally simpler, more cost-effective, scalable, and well suited for green synthesis.

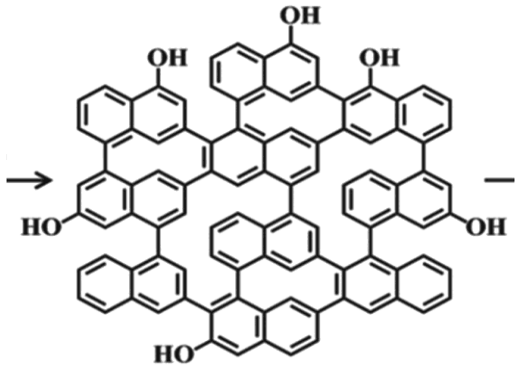

Figure 1. General chemical structure of CQD

- *Hydrothermal method.* In this method, precursor materials are dispersed in an aqueous solution, transferred into a Teflon-lined stainless-

* To whom all correspondence should be sent:
E-mail: *eakyol@ yildiz.edu.tr*

© 2026 Bulgarian Academy of Sciences, Union of Chemists in Bulgaria

steel autoclave, and heated under elevated temperature and pressure for a specified reaction time. Owing to its simple operation, low cost, and environmentally friendly one-step process, the hydrothermal method has become one of the most widely used techniques for CQD synthesis. It also enables the efficient conversion of various organic precursors into CQDs with desirable optical properties hydrothermal method has become one of the most widely used techniques for CQD synthesis. It also enables the efficient conversion of various organic precursors into CQDs with desirable optical properties [7].

- *Olive pits as a biomass for green synthesis of CQD.* Olive pits are an abundant agricultural by-product rich in cellulose, hemicellulose, lignin, proteins, and other natural compounds, making them an attractive renewable precursor for the green synthesis of carbon quantum dots. Their utilization not only provides a low-cost carbon source but also contributes to biomass waste valorization and reduces the environmental impact associated with olive oil production [2].

Applications of carbon quantum dots

Because of the remarkable properties of the CQDs they have applications in a wide range of fields, including sensing, biomedicine, energy and catalysis. Sensing is one of the most extensively studied areas for heavy metal ion detection due to their strong photoluminescence and abundant surface functional groups, which facilitate interactions with metal ions and induce fluorescence quenching through electron or energy transfer mechanisms.

EXPERIMENTAL CALCULATIONS

Overview of the study

In this work CQDs were greenly synthesized from olive seeds kernels using a hydrothermal method. The schematic of green synthesis of CQDs used in this article is shown in Fig. 2. and evaluate their performance as a fluorescent nano sensor and adsorbent for Fe^{3+} ions in aqueous solutions. The synthesized CQDs were characterized using various analytical techniques to investigate their optical and physicochemical properties. Subsequently, their fluorescence sensing performance toward Fe^{3+} ions was evaluated, and adsorption experiments were conducted to assess their efficiency in removing iron ions from water. The effects of synthesis parameters, including temperature, reaction time, and citric acid addition, were investigated using an experimental design approach to optimize the properties of the obtained CQDs.

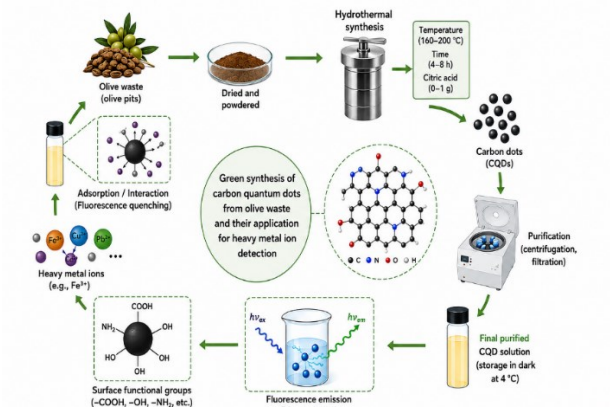

Figure 2. Schematic illustration of the green synthesis of carbon quantum dots from olive waste and their application for heavy metal ion detection.

Materials and chemicals

Olive seed kernels; citric acid; ferric chloride hexahydrate ($FeCl_3 \cdot 6H_2O$); deionized water.

Preparation of olive seed kernel powder

Olive stones were collected as agricultural waste, washed thoroughly with distilled water to remove residual oil and organic impurities, approximately 60 g of olive pits were dried in a conventional laboratory oven at 60 °C for 6 h until constant weight was achieved, the olive pits were allowed to cool inside the closed oven to prevent moisture absorption, finally the dried pits were ground into a fine powder. The ground powder was sifted by mesh number 45 (345 μm) [8] to obtain homogeneous particle size and then stored in an airtight container for further use in carbon quantum dot synthesis.

Synthesis of carbon quantum dots

- *Experimental design.* A design of experiments (DOE) approach was employed using Central Composite Design (CCD) within the response surface methodology to optimize the CQD synthesis parameters, as illustrated in Table 1. Independent variables included: A: reaction temperature, B: reaction time, C: citric acid. The response variable chosen was: fluorescence intensity (1/s).

- *Hydrothermal synthesis procedure.* Carbon quantum dots (CQDs) were synthesized using the hydrothermal method. Initially, 1.5 g of olive pit powder was weighed and dispersed in 25 mL of deionized water, followed by magnetic stirring for 15 min to obtain a homogeneous suspension. The resulting mixture was then transferred into a 50 mL Teflon-lined stainless-steel autoclave as shown in

Figure 3, which was sealed and placed in a laboratory oven.

Table 1. Design of experiments by design expert software program

Experiment number	Factor A Temperature (°C)	Factor B Time (h)	Factor C Citric acid (g)
1	180	6	0.5
2	180	8	1
3	180	4	1
4	200	6	1
5	180	6	0.5
6	180	6	0.5
7	200	4	0.5
8	160	6	1
9	160	8	0.5
10	160	4	0.5
11	180	4	0
12	180	6	0.5
13	200	6	0
14	200	8	0.5
15	180	8	0
16	180	6	0.5
17	160	6	0

The hydrothermal treatment was carried out at temperatures ranging from 160 to 200 °C for 4–8 h, depending on the experimental conditions defined by the design of experiments. In selected experiments, citric acid was used as a catalyst, and amounts of 0, 0.5, or 1.0 g were added according to the experimental design. In these cases, the required amount of citric acid was first dissolved in deionized water using a magnetic stirrer for 15 min. Subsequently, the olive pit powder was added to the solution and stirred for an additional 15 min before transferring the mixture into the hydrothermal autoclave for synthesis.

- *Purification of CQDs.* After completion of the hydrothermal reaction, the autoclave was allowed to cool naturally to room temperature. The obtained product was carefully collected and initially filtered using Whatman 44 filter paper to remove large particulates. Subsequently, the filtrate was subjected to centrifugation at 15,000 rpm for 30 min to further eliminate residual solids. The supernatant was then passed through 0.22 µm membrane filters to ensure complete removal of nanoscale impurities. Finally, the purified CQD solution was stored in clean, dark glass bottles at 4°C for further characterization as shown in Fig. 4.

- After confirming that the absorbance of all samples was ≤ 0.1 to minimize inner-filter effects, as shown in Table 2, photoluminescence measurements were performed using a fluorescence spectrophotometer at an excitation wavelength of 360 nm. The resulting fluorescence intensities are presented in Table 3.

Figure 3. Hydrothermal synthesis procedure of CQD samples

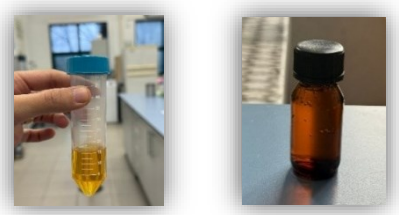

Figure 4. Final purified CQD solution

Ferric ion detection experiment

- *Selection of the optimum CQD sample.* Prior to the iron ion detection experiments, the optimum carbon quantum dot (CQD) sample was selected from the seventeen samples previously synthesized under different preparation conditions. The selection process was based on the optical properties of the prepared samples, particularly their fluorescence performance. UV–Visible absorption spectra were recorded, and the absorbance of each sample was adjusted through appropriate dilution to achieve suitable values for fluorescence measurements and to minimize inner filter effects. The absorbance was evaluated at 360 nm according to the reported literature [9]. Before proceeding with the iron ion detection and adsorption studies, all synthesized carbon quantum dot (CQD) samples were evaluated based on their photoluminescence (PL) properties. Comparison of the PL emission spectra shown in Fig. 5 revealed that sample No. 4 exhibited the highest fluorescence intensity among all prepared samples. Sample No 4 was synthesized using 1 g of citric acid as a catalyst under hydrothermal conditions at 200 °C for 6 h. The enhanced fluorescence intensity can be as a result of the combined effect of the citric acid and the synthesis temperature, which promoted carbonization,

improved surface passivation, and facilitated the formation of highly emissive surface states. Therefore, sample No (4) was selected as the optimal sample and employed in the ferric ion Fe^{3+} sensing and adsorption studies.

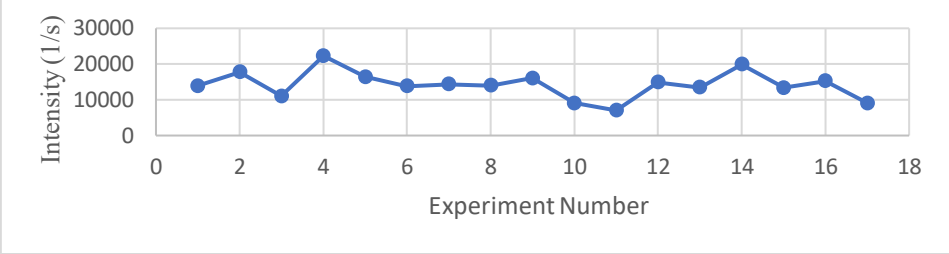

Fig. 5. Fluorescence intensity of carbon quantum dots (CQDs) prepared under different experimental conditions.

Table 2. Absorbance measurements for CQDs samples at wavelength of 360 nm before adding ferric ions

Sample	Abs. 1	Abs. 2	Abs. 3	Mean abs.
1	0.1166	0.1167	0.1170	0.11677
2	0.1104	0.1096	0.1100	0.11000
3	0.1212	0.1212	0.1215	0.12130
4	0.1051	0.1052	0.1066	0.10563
5	0.1217	0.1217	0.1207	0.12137
6	0.1116	0.1107	0.1114	0.11123
7	0.1202	0.1200	0.1193	0.11983
8	0.1167	0.1162	0.1176	0.11683
9	0.1074	0.1087	0.1088	0.10830
10	0.1157	0.1159	0.1185	0.11670
11	0.1210	0.1231	0.1221	0.12207
12	0.1124	0.1128	0.1134	0.11287
13	0.1143	0.1145	0.1148	0.11453
14	0.1072	0.1076	0.1073	0.10737
15	0.1122	0.1118	0.1112	0.11173
16	0.1120	0.1124	0.1120	0.11213
17	0.1174	0.1172	0.1173	0.11730

Table 3. Fluorescence measurements and emission wavelength for all samples

Sample No	$\lambda_{emision}$	Intensity (1/s)
1	435	13921
2	431	17723
3	431	11062
4	428	22286
5	434	16436
6	433	13850
7	426	14385
8	427	13982
9	426	16063
10	429	9102
11	425	7028
12	432	14867
13	426	13448
14	427	19909
15	428	13362
16	433	15261
17	424	9042

Preparation of Fe^{3+} solutions

- *1000 mg/L Fe^{3+} stock solution.* To prepare a 1000 mg/L Fe^{3+} stock solution ferric chloride hexahydrate ($FeCl_3 \cdot 6H_2O$) was used.

Table 4. Molecular weight calculation of ferric chloride hexahydrate ($FeCl_3 \cdot 6H_2O$)

Component	Molecular weight (g/mol)
Fe	55.85
3Cl	106.35
$6H_2O$	108.00
Total	270.20

Using the molecular weights provided in Table 4, the mass fraction of iron in $FeCl_3 \cdot 6H_2O$ is: $\frac{55.85}{270.20} = 0.2067$. Thus, 1 g of $FeCl_3 \cdot 6H_2O$ contains $1 \times 0.2067 = 0.2067$ g Fe. To prepare a stock solution containing 1000 mg/L (1.0 g/L) Fe^{3+}, the required mass of $FeCl_3 \cdot 6H_2O$ is:

$$\text{Mass of } FeCl_3 \cdot 6H_2O = \frac{1.0}{0.2067} = 4.84 \text{ g}$$

A 1000 mg/L Fe^{3+} stock solution was prepared by dissolving 4.84 g of ferric chloride hexahydrate ($FeCl_3 \cdot 6H_2O$) in deionized water. The salt was first dissolved in approximately 200 mL of deionized water and then transferred to a 1000 mL volumetric flask. The container was rinsed several times with deionized water, and the washings were added to the flask. The solution volume was adjusted to 1000 mL with deionized water and mixed thoroughly to ensure homogeneity.

The prepared stock solution was stored in an amber bottle at room temperature until use.

- *Preparation of calibration standards.* Calibration standards of 0.1, 0.2, 0.3, 0.4, 0.5, 0.6, 0.7, 0.8 and 0.9 mg/L Fe^{3+} can be prepared using the dilution equation:

$$C_1V_1 = C_2V_2$$

For the preparation of the calibration standards, an intermediate solution was prepared by pipetting 10 mL of the 1000 mg/L stock solution into a 100

mL volumetric flask. The solution was subsequently diluted to volume with deionized water and mixed thoroughly before use. Using the 100 mg/L intermediate solution of Fe^{3+}, standard solutions were prepared at different concentrations as illustrated in Table 5.

Table 5. Preparation of Fe^{3+} standard solutions at different concentrations from a 100 mg/L stock solution

Desired concentration (mg/L)	Volume of 100 mg/L solution (mL)	Dilute to
0.1	0.1	100 mL
0.2	0.2	100 mL
0.3	0.3	100 ml
0.4	0.4	100 ml
0.5	0.5	100 ml
0.6	0.6	100 ml
0.7	0.7	100 ml
0.8	0.8	100 ml
0.9	0.9	100 ml

These standards can then be used to construct the calibration curve for Fe^{3+} determination and adsorption experiments involving carbon quantum dots synthesized from olive seed biomass.

• *Ferric ion detection procedure.* For the iron ion sensing study, a series of Fe^{3+} standard solutions with different concentrations was prepared from $FeCl_3 \cdot 6H_2O$ using deionized water. A fixed volume of the selected CQD solution was mixed with each iron standard solution and allowed to interact for a predetermined period under identical experimental conditions. The fluorescence emission spectra of the CQD solutions were recorded before and after the addition of Fe^{3+} ions, the maximum emission wavelength (λ_{em}=428 nm) of the selected sample was used as the analytical emission wavelength in the fluorescence-based detection studies to monitor the response of the CQDs toward different concentrations of Fe^{3+} ions. The sensing performance was evaluated by monitoring the fluorescence quenching effect induced by Fe^{3+} ions. The relative fluorescence response $(F_0 - F)/F_0$, where F_0 and F represent the fluorescence intensities before and after iron addition, respectively, were calculated. A calibration curve was constructed by plotting the fluorescence response against the Fe^{3+} concentration. The linear relationship obtained from the calibration plot was used to determine the CQDs performance for ferric ion detection in aqueous media.

CONCLUSION AND FUTURE WORK

In this work CQDs, which are fluorescent carbon-based nanomaterials with particle sizes below 10 nm, were green-synthesized by a hydrothermal method using olive seed kernels as a carbon source The CQDs were used as a sensor for detection and removal of ferric ions (Fe^{3+}) from aqueous systems. At the current stage of the study the best CQD samples was selected using photoluminescence spectrometry according to the increase in fluorescence intensities. The quenching experiments for the sensing applications are still in progress.

The next step of the work will focus on adsorption experiments and evaluation of the CQDs for the removal of ferric ions from water and aqueous systems. Ultimately, this work seeks to contribute to improving water quality and reducing potential health and environmental risks associated with excessive ferric contamination in water resources.

Acknowledgement: *This work was supported by the Scientific Research Projects Coordination Unit of the Yildiz Technical University. Project Number FYL-2025-7278.*

REFERENCES

1. M. Hamed, S. Chinnam, A. Bedair, S. Emara, F. R. Mansour, *Talanta Open*, **10,** 100348 (2024). https://doi.org/10.1016/j.talo.2024.100348
2. D. A. Sousa, L. F. V. Ferreira, A. A. Fedorov, A. M. B. do Rego, A. M. Ferraria, A. B. Cruz, M. N. Berberan-Santos, J. V. Prata, *Molecules,* **27**(19), 6768 (2022). https://doi.org/10.3390/molecules27196768
3. X. Xu, R. Ray, Y. Gu, H. J. Ploehn, L. Gearheart, K. Raker, W. A. Scrivens, *Journal of the American Chemical Society*, **126,** 12736 (2004).
4. C. H. Hak,K. H. Leong, Y. H. Chin, P. Saravanan, S. T. Tan, W. C. Chong, L. C. Sim, *SN Applied Sciences*, **2**, 2023 (2023).
5. M. Pan, X. Xie, K. Liu, J. Yang, L. Hong, S. Wang, *Nanomaterials*, **10**, 930 (2020).
6. P. Iqbal, J. A. Preece, P. M. Mendes, Supramolecular Chemistry: From Molecules to Nanomaterials, J. W. Steed, Ph. A. Dale (eds.), Wiley, 2012.
7. B. Zhang, C. Liu, Y. Liu, *European Journal of Inorganic Chemistry*, **2010**, 4411 (2010). https://doi.org/10.1002/ejic.201000622
8. R. Ashouri, S. A. Hajiseyed Mirzahosseini, H. Shirkhanloo, A. Rashidi, N. Mansouri, *Journal of Nano Structures*, **11**(3), 480 (2021).
9. P. Wu, W. Li, Q. Wu, Y. Liu, S. Liu, *RSC Advances*, **7,** 44144 (2017). https://doi.org/10.1039/C7RA08400E

Bulgarian Chemical Communications, Volume 58, Issue 3 (pp. 320-324) 2026 *DOI: 10.34049/bcc.58.3.D014*

Modification of bitumen by adding reactive terpolymer, polyolefin elastomer and thermoplastic

H. İ. Özgündüz*, B. D. Corbacioglu, S. Keyf

Yildız Technical University, Department of Chemical Engineering, Istanbul, Turkey

Accepted July 28, 2026

In this study, 50/70 penetration grade TÜPRAŞ bitumen was modified. The reactive elastomeric terpolymer of DuPont (Elvaloy RET), Dow Engage 8411 polyolefin elastomer and Atactic Polypropylene (PP) polymers were used for bitumen modification. Each of the polymers elastomeric terpolymer (Elvaloy RET), Engage 8411 polyolefin elastomer, and atactic polypropylene (PP) was added to the 50/70 penetration grade bitumen at proportions of 0.5%, 1%, 1.5%, 2%, and 2.5% by weight. Additionally, 1% by weight of the other two polymers was added to obtain modified bitumen samples. The samples were subjected to oenetration (TS 118 EN 1426) and softening point (TS 120 EN 1427) tests in accordance with the Turkish General Directorate of Highways Modified Bitumen Specification. With the decrease in penetration values and the increase in softening point values, modified bitumen that is more resistant to stress, shock waves, and impacts was obtained. Moreover, the modified bitumen exhibited greater resistance in regions with high air temperatures.

Keywords: Bitumen modification, penetration value, softening point, reactive, elastomeric terpolymer, polyolefin elastomer

INTRODUCTION

The use of pure bitumen as a pavement surface material has been widespread since ancient times [1]. Bitumens generally have complex compositions. Pure bitumen contains high levels of hydrocarbons in varying proportions, primarily asphaltenes and maltenes, and these hydrocarbon compounds form a colloidal dispersion medium [2]. The complex composition of pure bitumen used in asphalt, mainly consisting of asphaltenes and maltenes, provides adequate performance against temperature and load in highway pavements and airport runway application [3]. However, over time, increases in vehicle loads and tire pressures due to the growing mass of road traffic, insufficient maintenance services, rapidly changing climatic conditions, and construction and design errors cause premature deterioration of asphalt pavements, thereby reducing their service life [4–7].

With the increasing demand for higher performance from pure bitumen used in asphalt, polymers with different properties are added to pure bitumen to produce polymer-modified bitumen. The increased resistance of polymer-modified bitumen under load is expected to extend its service life. Furthermore, as a result of modification, the aim is to improve the asphalt's resistance to cracking and fatigue at low temperatures and to increase its stability duration with minimal creep at high temperatures [8–10]. Polymers used in bitumen modification are generally classified into two groups, namely elastomers and plastomers, and their common disadvantage is phase separation at high temperatures. Among the polymers used to modify bitumen are styrene-butadiene-styrene (SBS), styrene-butadiene rubber (SBR), rubber, ethylene-vinyl acetate (EVA), polyethylene, and others [1, 11–14].

The feasibility of using polyolefin elastomers with a two-phase molecular structure to improve the performance of bitumen at different environmental temperatures has been investigated. The use of polyolefin elastomers (POEs) as different elastomers has demonstrated flexibility, processability, impact resistance, and low-temperature performance.

In the study conducted by Ye and Zhao, polyolefin elastomers with two different molecular structures were used to simultaneously improve both the high- and low-temperature performance of asphalt. Following the evaluation, the storage stability, workability, and rheological properties of asphalt modified with modified polyolefin were measured through the softening point difference test [15]. POE and SBS modified pure bitumen have been used to increase resistance to aging, environmental temperature, and UV radiation, as well as to slow down the degradation of styrene-butadiene-styrene caused by oxygen in the air [16].

* To whom all correspondence should be sent:
E-mail: *ozgunduz@yildiz.edu.tr*

© 2026 Bulgarian Academy of Sciences, Union of Chemists in Bulgaria

Among commercially developed polymer-modified bitumens, reactive ethylene terpolymers containing ethylene, glycidyl methacrylate (GMA), and an ester group (generally methyl or butyl acrylate) have gained increasing importance over the last 25 years. The Elvaloy series produced by Dow Chemicals are widely used reactive terpolymers in the literature [17].

Bulatovic *et al*. produced polymer-modified bitumen by adding Elvaloy AM and Elvaloy 4170 reactive ethylene terpolymers, which contain different percentages of the reactive functional group glycidyl methacrylate (GMA), to two types of pure bitumen with different asphaltene and maltene contents. It was observed that polymer modification improved the penetration, softening point, and temperature susceptibility performance of the base bitumen [18].

Recent studies have emphasized the effect and importance of reactive terpolymers in polymer-bitumen modification. Geckil and Seloglu [19] highlighted the importance of reactive terpolymers in their study. They determined that the penetration value of polymer-modified bitumen produced by adding Elvaloy RET 4170 at concentrations of 0.5%, 0.75%, and 1% to pure bitumen with a penetration value of 146 decreased by 23% for the 0.5% composition and by 31% for the 1% composition [19].

In the study conducted by Morova and Özel [20], polymer-modified bitumen was produced by adding 1.6%, 1.7%, and 1.8% Elvaloy RET 5160 reactive terpolymer and 0.2% polyphosphoric acid (PPA) as a catalyst to pure bitumen under appropriate temperature, mixing speed, and mixing duration conditions. With the addition of Elvaloy RET 5160 and PPA, the penetration value decreased from 58 (for pure bitumen) to approximately 45–48 (a reduction of about 17–22%). Therefore, a significant increase in hardness and load resistance was achieved. The softening point increased markedly from 51 °C to 60– 62.4 °C (an increase of approximately 18–22%), confirming that Elvaloy RET 5160 and PPA significantly improve the high-temperature stability of bitumen [20].

In the study by Taciroğlu [21], the penetration value of 50/70 penetration grade pure bitumen was determined as 53, and its softening point was measured as 52 °C. When 1.6% Elvaloy RET was added to the pure bitumen, the penetration value decreased to 45.5, while the addition of 1.8% Elvaloy RET reduced the penetration value further to 31.7. In terms of softening point values, according to the "Polymer Modified Bitumen (PMB) Technical Specification" table included in the 2013 Highway Technical Specifications of the General Directorate of Highways of Türkiye, the PMB produced with 1.6% Elvaloy RET falls within the usable range for PMB 58-28, PMB 64-28, PMB 70-16, PMB 70-20, and PMB 70-22 classes among the ten different polymer-modified bitumen classes. The sample containing 1.8% Elvaloy RET could not be used for PMB 82-16 and PMB 82-22 classes, but it was suitable for the other eight PMB classes.

Regarding penetration values, all samples containing 1.6% Elvaloy RET were suitable for nine PMB classes except PMB 58-28. The sample containing 1.8% Elvaloy RET satisfied the requirements for PMB 76-16, PMB 76-22, PMB 76-28, PMB 82-16, and PMB 82-22 classes. The sample containing 1.6% Elvaloy RET can be used for the PMB 58-28 class, as it satisfies both the softening point and penetration value requirements, while the sample containing 1.8% Elvaloy RET is suitable for the PMB 82-16 and PMB 82-22 classes [21]. In this study, polymer-modified bitumen was produced using 50/70 penetration grade raw bitumen (RAWB) produced at the Tüpraş Refinery, Dow Engage 8411 polyolefin elastomer, reactive terpolymer (Elvaloy RET 4170), and atactic polypropylene (PP) [22].

Fifteen polymer-modified bitumen (WPMB) samples were produced by separately incorporating three different polymers with distinct properties: reactive elastomeric terpolymer (Elvaloy RET), Engage 8411 polyolefin elastomer, and atactic polypropylene (PP). Penetration and softening point tests specified in the 2013 Highway Technical Specifications of the General Directorate of Highways of Türkiye for polymer-modified bitumen were conducted. The changes in the softening point and penetration values of the fifteen polymer-modified samples were evaluated and compared with the requirements of the ten different PMB classes specified in the bitumen standards.

EXPERIMENTAL

The General Directorate of Highways (KGM) has prepared the "Technical Specification for Modified Bitumen" to delay common pavement distresses such as rutting and cracking observed in hot mix asphalt layers and to enhance traffic safety by increasing skid resistance. Therefore, the bitumen grades used on Turkish highways, as specified by KGM, as well as the test criteria for polymer-modified bitumen applied in Turkey, are given in Tables 1 and 2, respectively [23].

Table 1. Bitumen grades used on Turkish highways

Experiment name (E.N.)	Standard (S.T)	Types of bitumen				
		B 40/60	RAW B 50/70	B 70/100	B 100/150	B 160/220
Penetration (P.N.T), (25°C), 0,1 mm	TS 118 EN 1426 ASTM D5	40-60	50-70	70-100	100-150	160-220
Softening point (S.P.), °C	TS 120 EN 1427 ASTM D36	48-56	46-54	43-51	39-47	35-43

Table 2. Physical properties of polymer-modified bitumen used on Turkish highways (TS EN 14023)

E.N	WPMB	PMB 58-28	PMB 64-28	PMB 70-16	PMB 70-22	PMB 70-28	PMB 76-16	PMB 76-22	PMB 76-28	PMB 82-16	PMB 82-22
P.N.T (25°C, 100g, 5sn.), 0.1mm	26-39	90-150	40-100	45-80	45-80	45-80	25-55	25-55	25-55	25-55	25-55
S.P., ^{0}C	58-74.6	45	50	60	60	55	65	65	60	70	70

Penetration (TS 118 EN 1426)

Penetration is a measure of the hardness and consistency of bitumen. The penetration test consists of measuring the depth to which a standard needle penetrates vertically into a bitumen sample under specified temperature, load, and time conditions. The bituminous material is tested at 25 °C under a load of 100 g for a duration of 5 sec.

Softening point (TS 120 EN 1427)

The softening point is generally defined as the temperature at which a bituminous material, placed in a standard mold with a steel ball on top and immersed in a water bath, softens upon heating at a controlled rate and reaches the bottom. This temperature is recorded from a thermometer at the moment the material touches the base.

Preparation of PMB samples

Experimental procedure

A total of 4–5 kg of 50/70 penetration grade bitumen produced by TÜPRAŞ is weighed, and polymers with predetermined percentages are added sequentially. The mixture is heated up to 200 °C and stirred at a speed of 120 rpm.

- Start: At 200 °C, ENGAGE 8411, at a specified percentage, is added to the base bitumen.
- 2nd hour: The base bitumen and ENGAGE are mixed for 2 hours. A 200 g sample is taken (1). The temperature is then reduced to 195 °C and maintained at this level until the end of the experiment. Polypropylene (PP), at a specified percentage, is added to the mixture.
- 3rd hour: ENGAGE 8411and PP are mixed. A 200 g sample is taken (2), and Elvaloy RET along with super polyphosphoric acid (SPFA) are added and mixed.
- 4th hour: A 200 g sample (3) is taken from the mixture containing ENGAGE, PP, and Elvaloy RET. SPFA is then added at the same temperature and mixing continues.
- 5th hour: A 200 g sample (4) is taken from the mixture containing ENGAGE, PP, and Elvaloy RET. Then, 0.2% super polyphosphoric acid (SPFA) is added, and mixing is continued at the same temperature. SPFA accelerates the reaction of Elvaloy RET 4170 with asphaltenic acids.
- 6th hour: A 200 g sample (5) is taken from the mixture containing ENGAGE, PP, and Elvaloy RET reacted with asphaltenic acids.
- 7th hour: A 200 g sample (6) is taken from the same mixture. The process is continued until no further change is observed in the softening point based on physical testing.

RESULTS AND DISCUSSION

The penetration and softening point test results of bitumen containing 0.5%, 1%, 1.5%, 2%, and 2.5% ENGAGE 8411, polypropylene (PP), and Elvaloy RET 4170 are presented below. The penetration and softening point tests applied to the modified bituminous binders yielded the following results (Figs. 1-6).

Penetration for polymer matrix (TS 118 EN 1426, ASTM D5

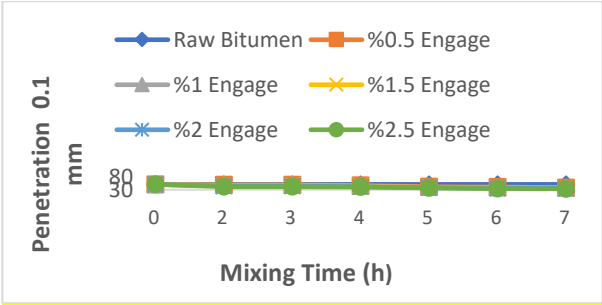

Figure 1. Penetration change for Engage 8411 Series and 1% PP 1% RET

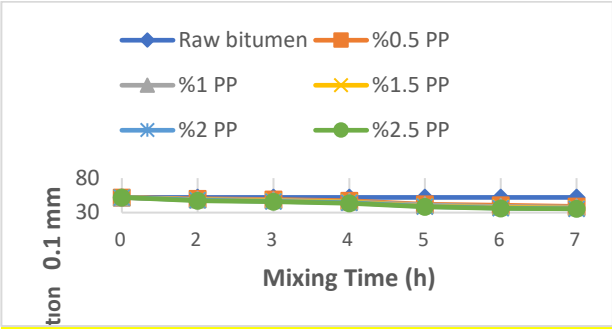

Figure 2. Penetration change for PP Series and 1% Engage 1% RET.

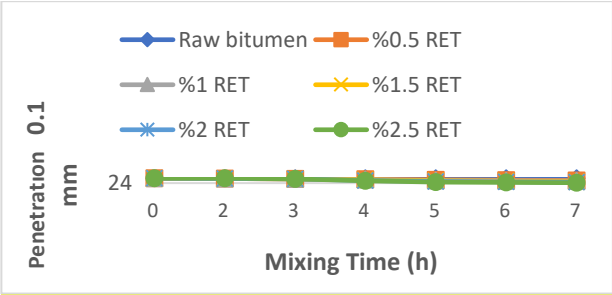

Figure 3. Penetration change for RET Series and 1% Engage 1% PP.

Softening point (TS EN 1427, ASTM D36)

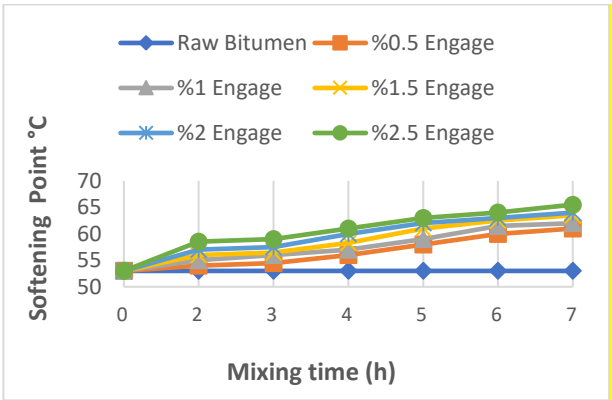

Figure 4. Softening point for Engage 8411 Series and 1% PP 1% RET.

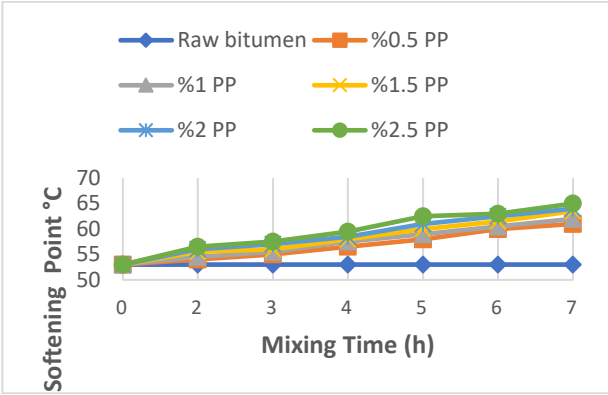

Figure 5. Softening point for PP Series and 1% Engage 8411 1% RET.

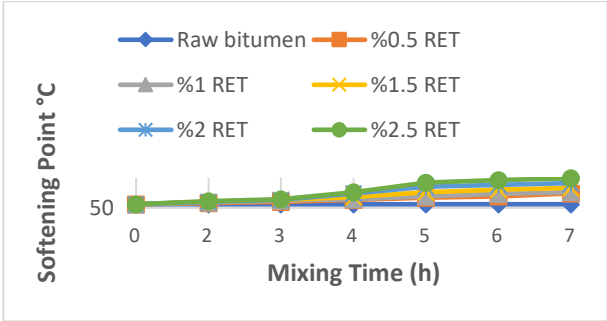

Figure 6. Softening point for RET Series and 1% Engage 1% PP.

Table 3 summarizes the maximum and minimum ranges of the penetration and softening point values.

Table 3. Minimum and maximum values of softening point and penetration according to the percentage composition of polymers by weight.

Composition of polymers by weight	Penetration, 25°C, 100 g, 5 sn, 0.1 mm	Softening point, °C
0.5 % Engage 8411, 1% PP, 1% RET.	39	61
2.5 % Engage 8411, 1% PP, 1% RET.	33	64.5
0.5 % PP, 1% Engage 8411 1% RET.	39	61
2.5 % PP, 1% Engage 8411, 1% RET.	36.2	64
0.5 % RET, 1% Engage 8411, 1% PP.	39	58
2.5 % RET, 1% Engage 8411, 1% PP.	26	74.5

CONCLUSION

The physical properties of the base bitumen were enhanced through the incorporation of a reactive elastomeric terpolymer (Elvaloy RET), Dow Engage 8411 polyolefin elastomer, and atactic polypropylene (PP). The evaluation of polymer-modified bitumen performance relies significantly on penetration and softening point tests. For the RAWB 50/70 base bitumen used in Turkish highways, the penetration value was determined to be 52 (0.1 mm), while the softening point was measured at 53°C. The incorporation of varying proportions of Engage 8411, PP, and RET into the neat bitumen resulted in an increase in softening point values ranging from 15% to 40.7%. Conversely, the addition of these polymers in different compositions led to a reduction in penetration values, with decreases observed in the range of 25% to 50%. When the PMB classes in Table 2 were evaluated together with the softening point values obtained in this study, the penetration and softening point values of fifteen different polymer-modified bitumen (WPMB) compositions were determined. The polymer-modified bitumen containing 1.5% RET, 1% Engage 8411, and 1% PP exhibited a softening point of 66.5 °C; the sample containing 2% RET, 1% Engage 8411, and 1% PP showed a softening point of 70.5 °C; and the sample containing 2.5% RET, 1% Engage 8411, and 1% PP had a softening point of 74.5 °C. These values were found to be suitable for all PMB class requirements. The other twelve polymer-modified bitumen samples produced in this study were suitable for all PMB classes except PMB 82-16, PMB 82-22, PMB 76-16, and PMB 76-22. When the PMB classes in Table 2 were compared with the penetration values obtained in this study, it was observed that all fifteen polymer-modified bitumen (WPMB) samples satisfied the penetration requirements for all ten PMB classes.

In the studies on polymer-modified bitumen (WPMB) produced using a blend of ENGAGE 8411, polypropylene (PP), and Elvaloy RET 4170, the softening point increased additionally due to the synergistic effect caused by the intertwining of the chemical bond chain of Elvaloy RET with the two polymer chains.

In contrast, the penetration value decreased further. Compared with the Elvaloy RET studies and polymer-modified bitumen studies obtained from different polymer blend systems reported in the literature, improvements in both penetration and softening point values were observed.

REFERENCES

1. J. Zhu, B. Birgisson, N. Kringos, *Eur. Polym. J.*, **54,** 18 (2014).
2. M. Jasso, R. Hampl, O. Vacin, D. Bakos, J. Stastna, L. Zanzotto, *Fuel Process. Technol.,* **140**, 172 (2015).
3. G. D. Airey, *Constr. Build. Mater.,* **16(8)**, 473 (2002).
4. U. Isacsson, X. Lu, *Mater. and Struct.*, **28(177)**, 139 (1995).
5. Ş. Oruc, B. Yılmaz, K. Sancak, *Road Mater. Pavement Des*., **17(4)**, 810 (2016).
6. Z. Suo, W. G. Wong, *Constr. Build. Mater.*, **23(12)**, 3492 (2009).
7. S. Tayfur, H. Ozen, A. Aksoy, *Constr. Build. Mater.*, **21(2)**, 328 (2007).
8. Y. Yıldırım, *Constr. Build. Mater*., **21**, 66 (2007).
9. X. Li, C. Ouyang, Y. Yuan, Q. Gaoa, K. Zhenga, J. Yan, *Constr. Build. Mater.*, **90**, 44 (2015).
10. V. Mouillet, F. Farcas, S. Besson, *Fuel,* **87**, 2408 (2008).
11. B. Sengoz, G. Isikyakar, *Constr. Build. Mater.*, **22(9)**, 1897 (2008).
12. G. Polacco, J. Stastna, Z. Vlachovicova, D. Biondi, L. Zanzotto, *Polym. Eng. Sci*., **44**, 2185 (2004).
13. A. Pérez-Lepe, F. J. Martínez-Boza, C. Gallegos*, J. Appl. Polym. Sci.,* **103(2)**, 1166 (2007).
14. D. Gama, Y. Yan, J. K. G. Rodrigues, R. Roque, *Constr. Build. Mater*., **169**, 522 (2018).
15. Z. Ye, Y. Zhen, *Buildings*, **13**, 1291 (2023).
16. G. Zeng, A. Shen, Z. Lyu, C. Kang, H. Cui, G. Ren, G. Yue, *Const. Build. Mater.,* **376**, I3I060 (2023).
17. https://www.dow.com/en-us/search.html#q=elvaloy%20ret&t=All&sort=relevancy)
18. V. O. Bulatović, V. Rek, J. Marković, *Poly. Eng. and Sci.*, **54(5),** 1056 (2014a).
19. T. Geckil, M. Seloglu, *Const. Build. Mater*., **173**, 262 (2018).
20. H. Varol Morova, C. Özel, *Materials*, **26**, 2 (2025**).**
21. M. V. Taciroğlu, *J. Innov. Trans.*, **4(2)**, 25 (2023).
22. https://www.dow.com/en-us/pdp.engage-8411-polyolefin-elastomer.102461z.html#tech-content.
23. https://www.tamyol.com.tr/Karayollari-Teknik-Sartnamesi-2013

Bulgarian Chemical Communications, Volume 58, Issue 3 (pp. 325-330) 2026 *DOI: 10.34049/bcc.58.3.D015*

Effect of hemp filler on the mechanical and physical properties of PLA/PBAT composite films

O. Tavlıbıyık, İ. Küçük*

Chemical Engineering Department, Yıldız Technical University, İstanbul, Turkey

Accepted: July 28, 2026

Advances in packaging materials and plastic waste management have recently been driven by the increasing use of bio-based biodegradable polymers such as polylactic acid (PLA) and poly (butylene adipate-co-terephthalate) (PBAT). Although these biopolymers are considered environmentally friendly due to their biodegradability, their limited mechanical performance restricts their broader application in flexible packaging systems.

In this study, industrial hemp (*Cannabis Sativa*) was incorporated as a natural filler into PLA/PBAT polymers to improve the mechanical properties of biodegradable films intended for sustainable packaging applications.

Polyethylene glycol (PEG200) was used as a plasticizer, and 20 µm thick films were fabricated *via* the solution casting method. Alkali treatment of hemp was applied to improve interfacial compatibility between hemp fibers and the polymer matrix. Structural, morphological, thermal, and mechanical characterizations of the hemp-incorporated composite films were performed using Fourier-transform infrared spectroscopy (FTIR), field-emission scanning electron microscopy (FE-SEM), differential scanning calorimetry (DSC), and mechanical testing

The results showed that the formulation with a PLA/PBAT ratio of 25/75 and 0.15% hemp exhibited the highest tensile strength of 12.18 MPa. Compared to the reference sample, the addition of 0.15% alkali-treated hemp increased tensile strength by up to 61%, whereas the incorporation of PEG200 negatively affected mechanical performance. These findings demonstrate the potential of hemp-reinforced PLA/PBAT composites as sustainable materials for flexible packaging applications.

Keywords: PLA (polylactic acid), PBAT (poly-butylene adipate-co-terephthalate), bio-based filler, mechanical properties.

INTRODUCTION

Plastic pollution, defined as the accumulation of plastics in the ecosystem in a manner that negatively impacts the environment, has become one of the most widespread global environmental challenges. Plastic products released into the environment are highly persistent; however, through processes such as photochemical oxidation and mechanical abrasion, they gradually fragment into microplastics (1 µm–5 mm) and nanoplastics (<1 µm) [1-3].

Due to their high mobility and resistance to natural degradation, these small particles enter aquatic food webs and accumulate in sediments. Furthermore, their high surface area-to-volume ratio enhances their capacity to adsorb heavy metals and persistent organic pollutants, posing significant ecological risks to aquatic organisms and water quality[4, 5].

Increasing concerns over the sustainability of petroleum-based feedstocks have intensified efforts to develop renewable bio-based polymer systems. Compared to fossil-derived materials, bio-based alternatives offer reduced environmental burden, lower carbon footprint, and decreased reliance on finite fossil resources, aligning with sustainable material engineering principles [6, 7].

The extensive use of ecoplastic materials based on naturally derived polymers and fillers contributes to addressing ecological concerns through the utilization of renewable resources and components that are part of the natural environment [8-10]. Advancements in the processing technologies and property enhancement of biodegradable materials will enable the widespread utilization of products based on naturally derived components. This may lead to the partial or complete replacement of synthetic polymers with ecoplastics. Among these materials, polylactic acid (PLA) and poly(butylene adipate-co-terephthalate) (PBAT) have attracted significant attention for the development of sustainable products [11, 12].

The development of polymer composites with novel chemical compositions requires the investigation of their structure and properties as influenced by technological factors, thereby enabling the production of defect-free materials through consideration of phase transformation behavior under external physical fields.

* To whom all correspondence should be sent:
E-mail: *kucuk@yildiz.edu.tr*

© 2026 Bulgarian Academy of Sciences, Union of Chemists in Bulgaria

The high quality and durability of products and structures fabricated from the investigated environmentally friendly composite materials are almost always achieved through the proper selection of the material composition in combination with the most effective processing method. Therefore, it is possible to produce eco-friendly composites by incorporating hemp fibers, with varying compositions, morphologies, and particle sizes, as fillers into a renewable bioplastic blend composed of poly(butylene adipate-co-terephthalate) and poly(lactic acid) (PBAT/PLA composites) [13-16].

This study aims to fabricate biofilms with varying PLA and PBAT ratios by using alkali-treated hemp as a reinforcing filler in a matrix, employing the solution casting method. Biodegradable polymer formulations will be developed, and their morphological, physical, thermal, and mechanical properties will be characterized.

EXPERIMENTAL

Materials and methods

In this study, industrial hemp (*Cannabis Sativa*) stalks obtained from the Black Sea Agricultural Research Institute (Samsun, Türkiye) were used as the filler material. During the preparation phase, the outer bark layers of the stalks were peeled; after being soaked in water for 24 hours and cleaned, they were dried at ambient temperature for 2 days, followed by 48 h in an oven at 80°C. The dried samples were then ground to a particle size of less than 20 µm using a laboratory grinder. Since hemicellulose, lignin, and pectin contribute to the hydrophilic nature of natural fibers and may hinder adhesion to the polymer matrix, an alkaline treatment was applied using a 10% NaOH solution for 30 min. Following this, the samples were washed with distilled water at 40°C, neutralized to pH 7 with acetic acid, and dried again at 80°C for 48 h.

To form the composite structure, PLA, PBAT, treated hemp, and PEG200 plasticizer were mixed in chloroform until complete dissolution was achieved. The resulting solution was cast onto Teflon-coated glass plates using an applicator to obtain films with a thickness of 20 µm. The samples were dried in a fume hood for 24 hours, followed by 6 hours of oven drying at 40°C to obtain the final films. In the final stage, the films were characterized using FTIR, DSC, and FE-SEM analyses, in addition to the evaluation of mechanical properties.

All biodegradable films were coded as shown in Table 1, and the preparation scheme of the hemp-incorporated films is presented in Figure 1.

RESULTS AND DISCUSSION

Structural analyses of biopolymer film samples were carried out in the 4000 – 400cm^{-1} spectral range using a Spectrum Two Fourier transform ınfrared (FTIR) spectrometer (Perkin Elmer, USA). The measurements were performed in accordance with the ASTM E168 standard.

FTIR spectra of both the pure materials and hemp incorporated films are compared in Figure 2. The presence of similar characteristic peaks in the FTIR spectra of all samples indicates that they possess the same or highly similar chemical structures. The carbonyl (C=O) peak at 1711 cm^{-1}, together with the C–O stretching bands in the 1268–1101 cm^{-1} range, confirms that the material is predominantly an ester-based polyester. The band observed at 727–728 cm^{-1}, attributed to CH_2 rocking vibrations, suggests the presence of long aliphatic chains, supporting a structure with ordered chain segments and a potentially semi-crystalline character.

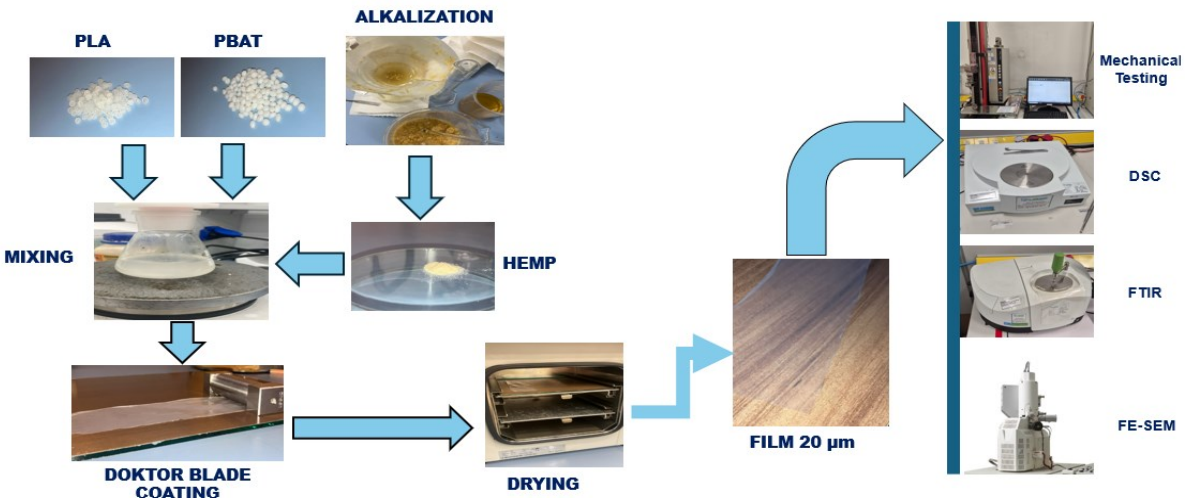

Figure 1. Schematic representation of composite films

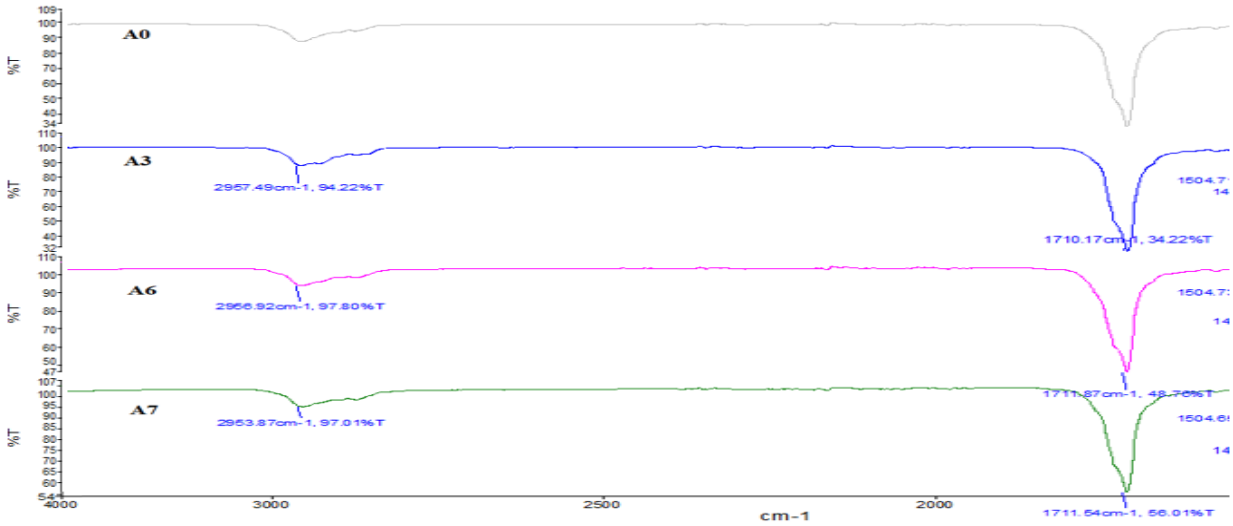

Figure 2. FTIR spectra of PLA/PBAT-based composite films

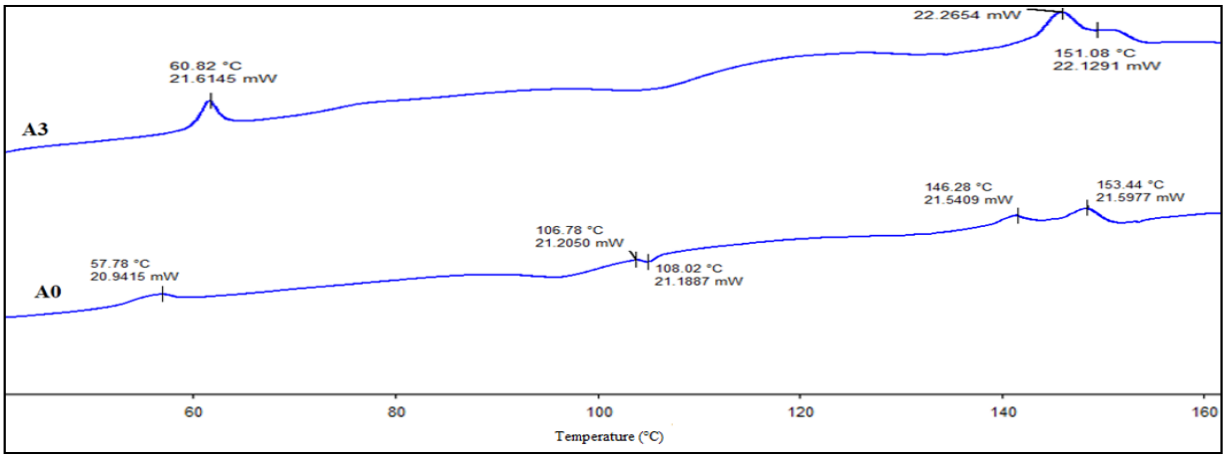

Figure 3. DSC curves of PLA/PBAT films: control (A0) and hemp-incorporated (A3)

RESULTS AND DISCUSSION

Structural analyses of biopolymer film samples were carried out in the 4000 – 400 cm^{-1} spectral range using a Two Fourier transform ınfrared (FTIR) spectrometer (Perkin Elmer, USA). The measurements were performed in accordance with the ASTM E168 standard.

FTIR spectra of both the pure materials and hemp-incorporated films are compared in Figure 2. The presence of similar characteristic peaks in the FTIR spectra of all samples indicates that they possess the same or highly similar chemical structures. The carbonyl (C=O) peak at 1711 cm^{-1}, together with the C–O stretching bands in the 1268–1101 cm^{-1} range, confirms that the material is predominantly an ester-based polyester. The band observed at 727–728 cm^{-1}, attributed to CH_2 rocking vibrations, suggests the presence of long aliphatic chains, supporting a structure with ordered chain segments and a potentially semi-crystalline character.

Thermal behavior of the biofilms was characterized using a DSC 4000 (PerkinElmer) instrument under a nitrogen atmosphere, in accordance with ASTM D3417. The sample masses used for the analyses ranged from 1.7 to 2.5 mg. During the measurements, the samples were first heated from 30 °C to 200 °C at a heating rate of 10 °C/min and held at 200 °C for 5 min, followed by cooling to the initial temperature at a cooling rate of 20 °C/min.

The thermal behavior of the samples is presented in the DSC thermograms (Figure 3). Based on the DSC thermograms, differences in the thermal response of the films were observed depending on the presence of alkali-treated hemp. The composite containing alkali-treated hemp exhibited higher heat flow intensities compared to the hemp-free sample, suggesting changes in the thermal transitions and possible variations in the degree of molecular ordering within the polymer matrix. The thermal events observed in the range of 106–108 °C may be associated with alterations in the crystallization or

relaxation behavior of the polymer chains induced by the presence of hemp fibers.

Mechanical properties of the film specimens were measured at room temperature (25 °C) using a Zwick Roell universal testing machine at a crosshead speed of 500 mm/min in accordance with ASTM D882. The film dimensions were prepared for uniaxial tensile testing with dimensions of 50 × 25.4 × 0.02 (mm), corresponding to the specimen length, width, and thickness, respectively. For the mechanical tests, three specimens were prepared for each formulation. Differences among the formulations were discussed based on the magnitude of the observed changes and the non-overlapping nature of the standard deviation values.

Analysis of the mechanical test results indicated that both the hemp filler and PEG200 plastizer had a significant influence on the mechanical performance of the composite structure. For the 20-micrometer-thick films prepared via the solution casting method, the PLA/PBAT ratio and hemp content were found to be key parameters governing the overall performance, as summarized in Table 1.

The highest tensile strength of 12.18 MPa was obtained for the formulation containing 25% PLA, 75% PBAT, and 0.15% hemp. This improvement is attributed to enhanced fiber–matrix interactions and a more uniform dispersion of hemp fibers within the polymer matrix, as evidenced by FE-SEM analyses (Figure 4).

Overall, these results suggest that a small amount of alkali-treated hemp can contribute to mechanical reinforcement in PLA/PBAT-based biodegradable films.

In contrast, the lowest mechanical strength was observed for the film containing 20% PLA, 80% PBAT, 5% PEG200, and 0.25% hemp, and was determined to be 2.45 MPa. The presence of PEG200 was found to exert an negative effect on the mechanical strength. Although PEG200 was incorporated into the matrix as a plasticizer, its use beyond certain concentrations reduced the stiffness of the matrix, resulting in a decrease in tensile strength.

Furthermore, increasing the hemp ratio to 0.25% may have prevented the fibers from being fully wetted by the matrix at lower polymer ratios and created stress concentration points within the structure, leading to premature failure

Table 1. Compositions and mechanical properties of PLA/PBAT/hemp composite films

	PLA(w%)	PBAT% (w%)	PEG200 (V%)	Hemp (W%)	Tensile Strength N (Newton)	Tensile Strength MPa
A0	25	75			3,84	7,56
A1	25	75		0,25	3,23	6,36
A2	25	75		0,2	3,68	7,25
A3	25	75		0,15	6,19	12,18
A4	25	75		0,1	4,25	8,86
A5	25	75		0,05	5,86	11,53
A6	25	75	5		2,41	4,75
A7	25	75	5	0,25	5,48	4,31
B0	20	80			14,52	9,68
B1	20	80		0,25	45,43	9,49
B2	20	80		0,2	9,27	7,32
B3	20	80		0,15	3,97	7,81
B4	20	80		0,1	4,78	9,42
B5	20	80		0,05	5,04	9,92
B6	20	80	5		2,45	4,82
B7	20	80	5	0,25	3,11	2,45

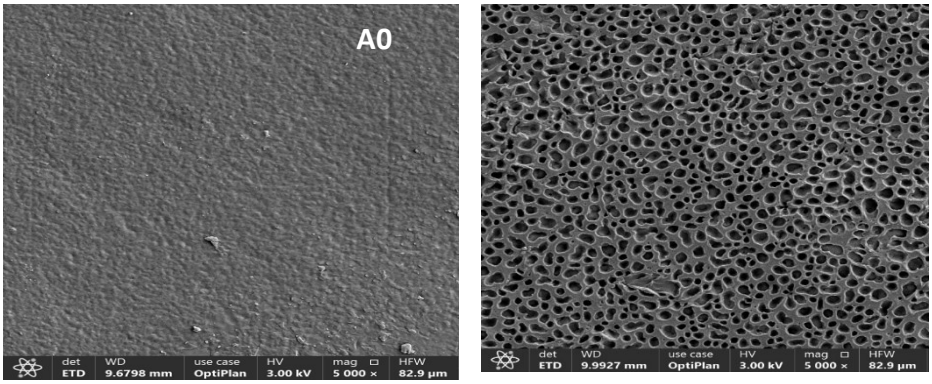

Figure 4. FE-SEM images of PLA/PBAT films: control (A0) and hemp-incorporated (A3)

The field-emission scanning electron microscopy (FESEM) images clearly reveal the significant morphological influence of hemp incorporation on the PLA/PBAT matrix structure. The observed morphology of A0 corresponds to a neat polymer matrix without reinforcing additives, characterized by a smooth surface.

In image A3, corresponding to the 0.15% hemp content (where the highest tensile strength of 12.18 MPa was obtained), a marked change in the matrix morphology is observed. The structure exhibits a more heterogeneous and porous, honeycomb-like network compared to the neat sample. This morphological change suggests improved fiber dispersion within the polymer matrix following alkali treatment, which removes surface impurities such as lignin and hemicellulose from the fibers.

The relatively uniform porous structure observed in the FE-SEM micrographs indicates better filler distribution within the matrix. The presence of finely ground hemp fibers (<20 μm) may contribute to improved stress transfer efficiency, which is consistent with the higher tensile strength observed for this formulation.

The 10% NaOH alkali treatment applied to the hemp fibers constitutes an important preliminary step in this study. The removal of components such as hemicellulose, lignin, and pectin, which are present in natural fibers and may limit interaction with the polymer matrix, modified the hydrophilic nature of the fibers and is expected to improve interfacial adhesion with the matrix. This process, also known as mercerization in the literature, helps to clean the fiber surface by removing waxes and oils and may enhance stress transfer by affecting the structural organization of cellulose.

The results indicate that incorporating hemp fibers into PLA/PBAT improved the tensile strength and elastic modulus. These findings suggest that hemp can act as a sustainable, lightweight, and promising filler material, offering potential for use as an alternative reinforcing agent in biodegradable plastic systems for flexible packaging applications.

CONCLUSION

Reinforcing biodegradable polymers (PLA/PBAT) with industrial hemp fibers may offer a promising approach to addressing plastic pollution in sustainable packaging applications. In this study, hemp fibers were used as a filler material in the development of eco-friendly biocomposite films as an alternative to fossil-fuel-based plastics.

The 10% NaOH alkali treatment purified the hemp fibers and may improve their interaction with the polymer matrix, contributing to enhanced mechanical performance. Among the films prepared *via* the solution casting method, the formulation containing 25% PLA, 75% PBAT, and 0.15% hemp exhibited the highest tensile strength of 12.18 MPa. In contrast, the addition of PEG200 negatively influenced the tensile strength, while certain hemp contents supported the structural integrity of the composites.

Overall, industrial hemp fibers have shown potential as a cost-effective and sustainable reinforcing component for biopolymer matrices. These biocomposites may contribute to reducing packaging waste and increasing the value of locally available renewable resources. The developed formulations provide a basis for future studies on sustainable packaging materials.

Acknowledgement: *Thanks to the Black Sea Agricultural Research Institute and Huhtamaki for their contributions to this study.*

REFERENCES

1. C.-G. Miriam, R. Marci, C. Lanna, *Biol. Lett.* **8**, 817 (2012). https://doi.org/10.1098/rsbl.2012.0298
2. R.-G. Lisa, D.-O. Mark, L.-D.Miriam, W.Watson, *CalCOFI Rep.* **50**, 123 (2009)
3. H.-R. Valeria, G. Lars, C.-T. Richard, T. Martin, *Environ. Sci. Technol.* **46**, 3060 (2012). https://doi.org/10.1021/es2031505
4. M. Rebecca M, M.-R. Saymur, *J. Hazard. Mater. Adv.* **18**, 100663 (2025). DOI: https://doi.org/10.1016/j.hazadv.2025.100663
5. C. Klára, V. Martina, M. Tomáš, Z. Lukáš, B. Lucia, *Life* **11**, 1349 (2021). DOI: https://doi.org/10.3390/life11121349
6. K.-A. Syed, A.-A. Abdullah, A. Faris, M.-A. Hassien, P. Humaira, M. Sayeed, Shaily, A.-K. Liyaqat, W. Mohd, S. Adnan, *J. Environ. Chem. Eng.* **14**, 121722 (2026), https://doi.org/10.1016/j.jece.2026.121722
7. M. Olczyk, M. Kuc-Czarneck, *J. Clean. Prod.* **495**, 145077 (2025). https://doi.org/10.1016/j.jclepro.2025.145077
8. M.-D. Banea, *Polymers* **15**, 1185 (2023). https://doi.org/10.3390/polym15051185
9. A.-L.Pereira, M.-D. Banea, J.-S. Neto, D.K.-K Cavalcanti, Polymers **12**, 866 (2020). https://doi.org/10.1016/j.jclepro.2025.145077
10. J.S.-S. Neto, H.F.-M. de Queiroz, R. A.-A. Aguiar, M.D. Banea, *Polymers* **13**, 4425 (2021). https://doi.org/10.3390/polym13244425
11. J.-B.Mu'azu, S.-D Adamu, S.-B. Mamudu, A. Dalhatu, H. Ataitiya, M.-Y. Abubakar, A.-B. Adam, *J. Chem. Technol.* **2**, 48 (2026). https://doi.org/10.22034/jchemtech.2025.556439.1030
12. N.-A. Asri, N.A.-A. Sezali, H.-L. Ong, M.-H. M. Pisal, Y.-H. Lim, J. Fang, *Macromol. Res.,* **45**, 202400475 (2024). https://doi.org/10.1002/marc.202400475

13. A. Kariev, V. Lebedev, D. Miroshnichenko, Y. Sokol, M. Gasanov, A. Cherkashina, Y. Lutsenko, S. Pyshyev *Tech Sci. Press.* **13**, (2025). https://doi.org/10.32604/jrm.2025.02025-0049
14. O. Boughanmi, L. Allegue, H. Marouani, A. Koubaa, Y. Fouad, *Polym. Eng. Sci.* **64**, 5613 (2024). https://doi.org/10.1002/pen.26938
15. V. Lebedev, D. Miroshnichenko, N. Vytrykush, S. Pyshyev, A. Masikevych, O. Filenko, O. Tsereniuk, L. Lysenko, *Mater. Chem. Phys.* **313**, 128778 (2024). https://doi.org/10.1016/j.matchemphys.2023.128778
16. Y.G.-T. Girijappa, R.-S. Mavinkere, J. Parameswaranpillai, S. Siengchin, *Front. Mater.* **6**, 226 (2019). https://doi.org/10.3389/fmats.2019.00226

Bulgarian Chemical Communications, Volume 58, Issue 3 (pp.331-336) 2026 *DOI: 10.34049/bcc.58.3.D016*

Synthesis and characterization of eco-friendly edible films based on pistachio shell

K. Akdemir, H. Gonultas, B. K. Isik, N. Tugrul*

[1]*Yıldız Technical University, Faculty of Chemistry and Metallurgy, Department of Chemical Engineering, Davutpaşa Campus, 34220 Esenler, Istanbul, Türkiye*

Accepted: July 28, 2026

The transition toward biopolymer-based packaging is critical to mitigate the ecological crisis caused by petrochemical plastics. This study valorizes pistachio shells (*Pistacia vera* L.), a prominent agrowaste, as a lignocellulosic matrix to develop active edible films. Micronized shell powder was integrated into sodium alginate and carrageenan networks, plasticized with glycerol, and modified with peanut oil. Glycerol provided superior flexibility and structural integrity over sorbitol. Incorporating peanut oil yielded an exceptional moisture barrier, reducing the water vapor permeability (WVP) to 0.704–2.593 g/m²·h. Water solubility was highly controllable (48.67–86.90%), suiting diverse food moisture demands. *In vivo* 14-day trials on fresh produce confirmed that the carrageenan-based formulation (Car-S2.0-G10) substantially suppressed weight loss from ~70% to 40.51% in strawberries and from ~90% to 70.06% in apples compared to uncoated controls. These findings demonstrate a scalable, circular economy strategy for fruit preservation using agro-industrial residues.

Keywords: Edible film; pistachio shell; peanut oil; biodegradable packaging; nut waste

INTRODUCTION

Packaging is essential to extend food shelf life, maintain quality, and ensure transport safety. However, the non-biodegradable nature of petrochemical plastic packaging induces severe global ecological crises, driving intense interest in sustainable biopolymer-based edible films [1, 2]. These green technologies effectively valorize agricultural residues into high-performance coatings [3, 4]. Derived from natural polysaccharides, proteins, or lipids, edible films form physical barriers that regulate gas or moisture transfer while serving as structures for active additives [5-7]. Successful film fabrication requires precise control over core processing variables, including matrix optimization, formulation engineering, and barrier characterization [8-10]. Mapping molecular cross-linking networks in hydrocolloids is essential to design dynamic barrier configurations capable of replacing fossil-resource frameworks [11-14]. Agricultural residue recycling forms a core cornerstone of the circular economy. As a leading global producer of pistachios (*Pistacia vera* L.), Türkiye generates thousands of tons of hard shell waste annually during industrial processing [2], emphasizing their structural utility and widespread biomass availability [15]. These residues are highly rich in structural cellulose (30–50%), hydrophobic lignin (20–35%), and hemicellulose (15–25%) [2]. Due to this rigid lignocellulosic architecture, pistachio shell pieces can be effectively upcycled as natural fillers in biodegradable film design [16]. economic, and biocompostable reinforcement phase for polymer matrices [17].

The primary objective of this study was to develop eco-friendly edible films by utilizing micronized pistachio shell powder as a functional matrix reinforcement. Peanut oil was incorporated as a hydrophobic lipid phase to minimize water vapor permeability, while glycerol, kappa-carrageenan, and sodium alginate established structural flexibility and gel matrix stability. The films were systematically characterized *via* FT-IR, thickness, water solubility, moisture content, and WVP analyses, and validated through *in vivo* shelf-life trials on fresh strawberry and apple slices.

EXPERIMENTAL

Materıals

Pistachio shells (domestic agrowaste) and peanut oil (Nkaresabun) served as raw materials. Kappa-carrageenan (Model: 316, Benosen), sodium alginate (Alfasol), sorbitol (Zag Kimya), and glycerol (Merck) formed the film matrix. Distilled water was used as the solvent. Fresh strawberry and apple slices were selected as target food models to evaluate shelf-life extension performance.

Preparation of pistachio shell powder

The endocarp of pistachio shells was mechanically ground using a ring mill and sieved through a 250 μm mesh to obtain a uniform particle size distribution for optimal dispersion.

* To whom all correspondence should be sent:
E-mail: *ntugrul@yildiz.edu.tr*

© 2026 Bulgarian Academy of Sciences, Union of Chemists in Bulgaria

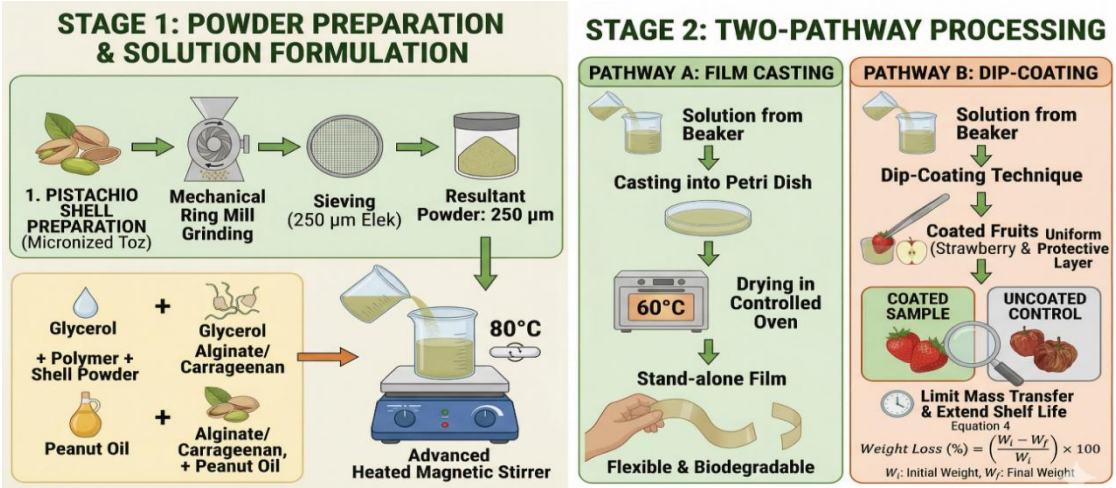

Figure 1. Schematic representation of the fabrication process of edible films

Table 1. Detailed formulations and component ratios of the edible films

Sample	Shell (g)	Polymer (g)	Glycerol (mL)	Additive (wt%)*	Plasticizer (wt%)*
Car-P2.5-G8	2.4	2.5	8	16.02%	67.29%
Car-P1.5-G8	2.4	1.5	8	17.17%	72.10%
Car-P1.0-G8	2.4	1.0	8	17.80%	74.78%
Car-S2.0-G10	2.0	1.0	10	12.82%	80.77%
Car-S1.5-G10	1.5	1.0	10	9.93%	83.44%
Alg-G6	2.4	2.5	6	19.26%	60.68%
Alg-G8	2.4	2.5	8	16.02%	67.29%

*Weight percentages (wt%) for additives (shell powder) and plasticizers (glycerol) are calculated relative to the total solid weight (W_{total} = Polymer + Shell + Glycerol). Glycerol density was taken as 1.26 g/mL.

The resulting micronized powder was stored in a desiccator at room temperature (22±0.5°C) to prevent moisture absorption prior to formulation

Synthesis of edible films

The edible films were synthesized *via* the solvent casting method based on the formulations detailed in Table 1. Glycerol concentrations varied between 60.68% and 80.77% (w/w) relative to the total solid content. A multi-stage thermal dissolution protocol was executed at 80°C under continuous magnetic stirring. For the alginate series, glycerol, sodium alginate, and carrageenan were sequentially dissolved in 100 mL of distilled water for 30, 15, and 15 min, respectively (60 min total). For the carrageenan (Car) series, carrageenan was pre-dissolved at 80 °C for 30 min before adding the other components. Subsequently, pistachio shell powder (1.5, 2.0, or 2.4 g; representing 9.93% to 21.90% of total solids) and peanut oil (2 mL) were incorporated into the mixture.

The final film emulsion was stirred at 80°C for an additional 15 min to achieve homogeneous lipid phase distribution. The mixtures were cast into molds and dehydrated in a controlled oven at 60 °C for 24 h until a stable weight was reached. The dried films were equilibrated in a desiccator (22±0.5°C) before characterization. Fig. 1 depicts the detailed schematic workflow of the multi-stage fabrication and casting process of the pistachio shell-reinforced edible films. A systematic coding system was applied: Car and Alg denote carrageenan and sodium alginate matrices, respectively, while P, G, and S represent polymer weight (g), glycerol volume (mL), and pistachio shell powder load (g), respectively.

The macrostructural appearance and physical flexibility of the fabricated edible films are illustrated in Fig. 2.

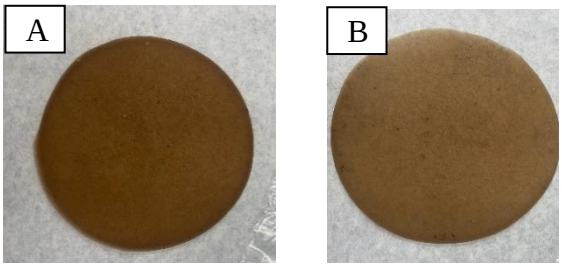

Figure 2. Macrostructural appearance of the produced A) Car-P2.5-G8 and B) Car-P1.0-G8

Characterization of edible films

- *Fourier transform infrared spectroscopy (FT-IR).* The chemical structures and functional group interactions of the synthesized edible films were analyzed using a Perkin Elmer Spectrum 100 FT-IR spectrometer. Spectral data were acquired *via* the attenuated total reflectance (ATR) technique by scanning over a wavenumber range of 4000 cm^{-1} to 650 cm^{-1} [18, 19].
- *Water vapor transmission rate (WVTR).* The moisture barrier capacity of the films was gravimetrically determined according to the modified ASTM E96 standard [20, 21]. Film samples (2×2 cm^2) were dried at 105 °C for 24 h to reach a constant mass, and then fixed airtight with parafilm to the mouths of test tubes containing 5 g of silica gel. The assemblies were placed in a constant humidity desiccator for 5 days. The weight change (ΔW) was recorded and the WVTR was calculated *via* Eqn. 1 [22]:

$$\text{WVTR} = \frac{\Delta W/\Delta t}{A} \quad (1)$$

where ΔW is the mass change (g), A is the exposed surface area (0.00015393 m^2), and Δt is the total experimental time (120 h).

- *Moisture content.* The moisture retention of the films was determined gravimetrically. Film specimens were dried at 105 °C until a constant weight was achieved. The moisture content percentage was calculated using Eqn. 2 [23, 24]:

$$\text{Moisture content (\%)} = \frac{M_1 - M_2}{M_1} \times 100 \quad (2)$$

where M_1 and M_2 represent the weights of the film before and after drying, respectively.

- *Water solubility.* To evaluate water resistance, dried film samples (2×2 cm^2, 105°C for 24 h) were immersed in 50 mL of distilled water and stirred at 150 rpm for 1 h using a magnetic stirrer. The insoluble fraction was separated via filter paper and dried at 105°C for 24 h to determine the final dry weight. The water solubility (WS) percentage was calculated using Eqn. 3 [24, 25]:

$$\text{WS (\%)} = \frac{W_0 - W_t}{W_0} \times 100 \quad (3)$$

where M_1 is the initial dry weight and M_2 is the remaining dry weight after dissolution.

- *Thickness.* The film thickness was measured at three random points using a digital micrometer (0.1 mm precision) to determine the average value [23, 26].
- *Fruit coating application.* The protective efficacy of the selected carrageenan and sodium alginate based formulations was evaluated on fresh strawberry and apple slices. The fruit samples were treated using a standardized dip-coating technique to ensure a uniform surface layer. An uncoated control group was maintained under identical environmental conditions for validation. Over a 14-day storage period, the physical barrier performance against moisture transfer was quantitatively assessed by monitoring the weight loss percentage according to Eqn. 4 [27-29]:

$$\text{Weight loss (\%)} = \frac{W_i - W_f}{W_i} \times 100 \quad (4)$$

where W_i is the initial weight and W_f denotes the weight at day 14.

RESULTS AND DISCUSSION

Fourier transform infrared spectroscopy (FT-IR)

The molecular architecture and functional group interactions of the synthesized edible films were monitored *via* FT-IR spectroscopy (Fig. 3). All membranes exhibited a prominent, broad absorption band at 3280–3307 cm^{-1}, corresponding to the O–H stretching vibrations of adsorbed water, glycerol, and the hydrophilic polymer backbones [18]. The successful integration of components was confirmed by the aliphatic C-H stretching peaks observed at 2925–2926 cm^{-1}, inherent to the $-CH_2-$ groups of carrageenan and alginate chains [19].

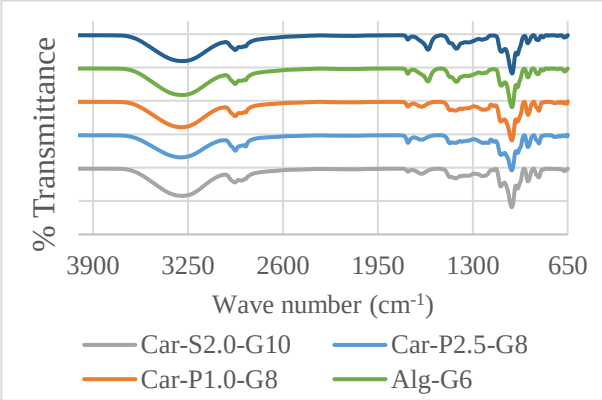

Figure 3. FTIR spectra of samples Car-S2.0-G10, Car-P2.5-G8, Car-P1.0-G8 and Alg-G6, Alg-G8

The presence of ester-based constituents was evidenced by the characteristic C=O stretching band between 1743–1746 cm^{-1}. Notably, the carrageenan-based formulations displayed a distinct peak at 1647–1648 cm^{-1} along with a symmetrical stretching band at 1412–1417 cm^{-1}, signifying the presence of carboxylate (COO^-) or sulfate (SO_3^-) groups. These shifts and peak combinations imply the formation of a robust intermolecular hydrogen-bonding network between the plasticizer and the biopolymer matrix, which is crucial for film flexibility. The fingerprint region further elucidated the polysaccharide skeleton and filler interactions. The absorption bands

in the 1103–1109 cm^{-1} and 1031–1034 cm^{-1} ranges are assigned to C–O stretching and glycosidic linkages (C–O–C), respectively, reflecting glycerol-matrix coordination [19]. Structural bending of the polymer chains was detected at 993–995 cm^{-1} and 922–924 cm^{-1} the latter specifically confirms the 3,6-anhydro-D-galactose units of carrageenan. Furthermore, the active SO_3^- stretching vibrations at 847–853 cm^{-1} validated the integrity of the carrageenan matrix. Finally, the spectral region between 670–730 cm^{-1} exhibited the aromatic C–H out-of-plane bending [30], confirming the successful incorporation of the lignocellulosic pistachio shell filler within the edible film framework. This structural consolidation is consistent with spectral parameters validated for extracted pistachio shell films [17]. Recent structural data by carbohydrate and hydrocolloid researchers [31-33] confirm that incorporating natural cross-linkers, chitosan networks, and polyphenolic agrowastes induce positive molecular assembly shifts without breaking the core polysaccharide skeleton.

Barrier properties and hydrolytic stability

The physical dimensions, moisture resistance, and hydrolytic stability of the synthesized edible films are consolidated in Table 2. The film thicknesses spanned a spectrum between 0.6 mm and 1.3 mm, where the sodium alginate series formed more compact layers (0.6–0.8 mm) than the carrageenan counterparts due to denser molecular packing during dehydration. This structural arrangement directly governed the barrier dynamics; the water vapor permeability (WVP) values ranged from 0.704 to 2.593 $g/m^2 \cdot h$, demonstrating superior efficiency over conventional benchmarks.

Table 2. Comprehensive physical, barrier, and stability results of the edible films

Sample	Thickness (mm)	WVP ($g/m^2 \cdot h$)	Moisture loss (%)	Water solubility (%)
Alg-G8	0.6	0.704	32.63	81.52
Alg-G6	0.8	1.998	30.77	86.90
Car-P1.0-G8	1.3	1.608	28.26	48.67
Car-P2.5-G8	0.9	1.424	24.02	59.94
Car-P1.5-G8	1.0	2.409	41.23	77.19
Car-S2.0-G10	1.0	0.861	35.62	84.19
Car-S1.5-G10	1.0	2.133	25.71	65.30

This high-efficiency performance is fundamentally driven by the inclusion of peanut oil as a hydrophobic lipid phase [20], which establishes a tortuous path for water molecules within the polymer network [21, 34]. Similar structural designs utilizing active lipid barriers and agro-industrial particles have been shown to drastically restrict internal moisture transport channels [34-36].

The interplay between plasticization, matrix density, and filler load revealed clear correlations among WVP, moisture retention, and water solubility. In the alginate series, increasing glycerol from 6 mL to 8 mL minimized internal friction of the casting solution, yielding a thickness of 0.6 mm and optimizing interfacial adhesion with the lipid phase to achieve the minimum WVP of 0.704 $g/m^2 \cdot h$. Strategic plasticizer adjustment expands the free volume between polymer chains [22, 23, 26], defining the physical assembly and water affinity of the sheets. Due to the hygroscopic nature of glycerol and the hydrophilicity of the sodium alginate backbone, both alginate formulations exhibited a high-water affinity, leading to elevated moisture content [23] and water solubility rates exceeding 81% [25]. This balance matches conventional biopolymer paradigms noting that natural hydrophilic hydrocolloids require precise formulation adjustments to withstand aqueous erosion [35-38]. Conversely, structural stability in carrageenan systems was governed by the density of the polysaccharide network and the lignocellulosic filler load rather than plasticizer dominance alone. Increasing carrageenan content reinforced the matrix; a comparative analysis between Car-P2.5-G8 and Car-P1.0-G8 showed an 11% reduction in water solubility due to a dense, dispersion-resistant gel network. The micronized pistachio shell powder functioned as a pivotal regulator of internal porosity and water resistance. Increasing the shell load by 0.5 g (comparing Car-S1.5-G10 and Car-S2.0-G10) tightened the biopolymer matrix, restricting free volume for vapor transport to lower the WVP to 0.861 $g/m^2 \cdot h$. Concurrently, the hydrophobic lignin fraction of the higher filler load restricted moisture absorption—inducing a 10% shift in moisture content—and enhanced resistance against aqueous erosion to lower water solubility by 19%. A similar physical paradigm confirms that the strategic dispersion of crystalline shell residues within polymer networks modifies thermal stability, matrix spacing, thickness parameters, and subsequent moisture flux behavior depending on the absolute loading ratio [17, 39]. These findings show that balancing hydrophobicity, water resistance (48.67% to 86.90%), and barrier parameters can be precisely tailored by optimizing glycerol-lipid-filler ratios to satisfy active packaging specifications.

Practical application: shelf-life extension of perishable fruits

The practical efficacy of the synthesized edible films was demonstrated by monitoring the weight loss of highly perishable strawberry and apple slices over a 14-day storage period (Table 3). While uncoated control strawberries suffered a severe mass reduction of ~70%, the application of the Car-S2.0-G10 formulation successfully restricted this loss to 40.51%, significantly outperforming the Alg-G6 coating (68.03%). A similar trend was observed for apple slices; uncoated samples reached a near-total mass reduction of 90%, whereas the Car-S2.0-G10 coating provided superior moisture retention by limiting the loss to 70.06%, outperforming the 86.59% loss recorded for the Alg-G6 formulation. These suppression trends align with recent active coatings outlined for post-harvest preservation using agrowaste residues [1, 27, 31, 32], as well as sustainable green packaging paradigms [34, 40].

Table 3. Weight loss analysis of coated strawberry and apple samples over a 14-day storage period

Sample	Initial weight (g)	Weight at day 14 (g)	Weight loss (%)
Strawberry samples			
Car-S1.5-G10	11.11	6.33	43.02
Car-S2.0-G10	10.96	6.52	40.51
Alg-G5 (GA-2)	13.04	4.40	66.26
Alg-G6 (GA-3)	20.24	6.47	68.03
Apple samples			
Car-S1.5-G10	6.67	1.85	72.26
Car-S2.0-G10	8.75	2.62	70.06
Alg-G5 (GA-2)	10.11	1.76	82.59
Alg-G6 (GA-3)	15.21	2.04	86.59

The variation in these results is governed by the interplay between the polymer matrix, plasticizer concentration, and filler load. The carrageenan-based Car-S2.0-G10 formulation emerged as the most effective coating because the inherently denser structural network of carrageenan, when reinforced with a 2.0 g pistachio shell load, forms a robust physical barrier that regulates respiration rates and minimizes transpiration-induced mass transfer. In contrast, the higher weight loss in the sodium alginate-based series is attributed to high glycerol concentrations, which enhance the hygroscopic nature of the coating and facilitate rapid moisture exchange with the environment. Furthermore, variations among the carrageenan recipes suggest that structural stabilization provided by the pistachio shell powder is a critical regulator of film porosity; formulations with optimized filler-to-plasticizer ratios showed a more consistent ability to seal the fruit surface against mass loss. As established by innovative packaging reviews [3, 4, 29], upcycling fibrous wastes creates complex tortuous paths that retard environmental gas diffusion, stabilizing the post-harvest cellular integrity of perishable horticultural matrices [28, 33]. Although these loss percentages exceed some literature benchmarks due to experimental variables—such as high initial fruit moisture, specific plasticizer types, and ambient humidity—the substantial relative improvement over the control groups confirms the commercial potential of these waste-derived films as sustainable active coatings.

CONCLUSION

In this study, novel bio-based edible films were successfully developed by reinforcing sodium alginate and carrageenan matrices with micronized pistachio shell powder, plasticized with glycerol, and hydrophobic-modified using peanut oil. FT-IR spectroscopic analysis verified the successful integration of the lignocellulosic filler and the formation of a robust intermolecular hydrogen-bonding network within the biopolymer matrices. The structural modification significantly enhanced the functional packaging parameters, yielding exceptional moisture barrier efficiencies with tailored WVP values between 0.704 and 2.593 $g/m^2 \cdot h$, alongside highly tunable water solubility profiles (48.67–86.90%). *In vivo* post-harvest storage trials on fresh strawberry and apple slices over a 14-day period validated the practical efficacy of the developed coatings. The optimized carrageenan-based formulation (Car-S2.0-G10) emerged as the most efficient protective layer, substantially suppressing critical mass losses to 40.51% in strawberries and 70.06% in apples compared to ~70% and ~90% reductions in uncoated control groups, respectively. Consequently, this study demonstrates that upcycling abundant agro-industrial residues into high-performance edible coatings offers a scalable, circular-economy-driven strategy to extend the shelf life of perishable horticultural produce while mitigating environmental plastic waste.

REFERENCES

1. V. Gigante, B. Dal Pont, A. Cavallero, C. Sbrana, L. P. Fabbri, M. Gabriele, L. Aliotta, *Carbohydr. Polym. Technol. Appl.*, **11**, 100984 (2025).

2. F. Demirbaş, F. Kalkan, *Gıda Bilimi ve Teknolojileri Dergisi*, **9(2)**, 45 (2021).
3. R. Kumar Gupta, E. AE Ali, F. Abd El Gawad, V. Mecheal Daood, H. Sabry, S. Karunanithi, P. Prakash Srivastav, *Waste Manage. Bull.*, **2(4)**, 21 (2024).
4. [D. Gupta, A. Lall, S. Kumar, T. D. Patil, K. K. Gaikwad, *Sustainable Food Technol.*, **2(5)**, 1428 (2024).
5. M. E. Embuscado, K. C. Huber, *Edible Films and Coatings for Food Applications*, Springer Science & Business Media (2009).
6. S. Burt, *Int. J. Food Microbiol.*, **94(3)**, 223 (2004).
7. V. Siracusa, *Trends Food Science Technol.*, **19(12)**, 634 (2008).
8. R. Sothornvit, J. M. Krochta, *Plasticizers in edible films and coatings*, **23** (2005).
9. G. W. Padua, Q. Wang, *Protein-based films and coatings*, CRC Press, New York, 43 (2002).
10. M. A. Pascall, S.-J. Lin, *Food Process. Technol.*, (2013).
11. M. G. de Morais, B. S. Vaz, S. Silva de Souza, K. M. de Medeiros, I. de L. M. Ferreira, A. G. B. de Lima, V. O. Santos, J. A. V. Costa, *Sustainable Food Technol.*, **2**, 98 (2024).
12. Y. Zhao, *Int. J. Food Sci. Technol.*, **47(6)**, 1250 (2012).
13. M. A. García, M. N. Martino, N. E. Zaritzky, *J. Food Sci.*, **65(6)**, 941 (2000).
14. R. Zafar, K. M. Zia, S. Tabasum, F. Jabeen, A. Noreen, M. Zuber, *Int. J. Biol. Macromol.*, **92**, 1012 (2016).
15. G. Mandalari, D. Barreca, T. Gervasi, M. A. Roussell, B. Klein, M. J. Feeney, A. Carughi, *Plants*, **11(1)**, 18 (2021).
16. W. Liu, *J. Appl. Polym. Sci.*, **111(1)**, 113 (2009).
17. S.-Y. Park, H.-L. Kim, J.-Y. Her, *Carbohydr. Polym. Technol. Appl.*, **7**, 100423 (2024).
18. C. Berthomieu, R. Hienerwadel, *Photosynth. Res.*, **101(2-3)**, 157 (2009).
19. J. Smith, Infrared Spectra of Some Common Functional Groups, Organic Chemistry, 2001, p. 11.
20. N. Gontard, S. Guilbert, J. L. Cuq, *J. Agric. Food Chem.*, **42(12)**, 2857 (1994).
21. D. Kowalczyk, B. Baraniak, *Food Hydrocolloids*, **41**, 195 (2014).
22. H. Gidik, O. Vololonirina, R. M. Ghantous, A. Ankou, *Int. J. Cloth. Sci. Technol.*, **31(4)**, 528 (2019).
23. R. Sothornvit, J. M. Krochta, *J. Food Eng.*, **50(3)**, 149 (2000).
24. M. Rahmawati, M. Arief, W. H. Satyantini, *IOP Conf. Ser.: Earth Environ. Sci.*, **236**, 012129 (2019).
25. S. Galus, A. Lenart, *J. Food Eng.*, **115(4)**, 459 (2013).
26. S. Mali, *Food Sci. Technol.*, **38(5)**, 564 (2005).
27. C. Han, *J. Food Sci.*, **70(3)**, 1492 (2005).
28. M. Ma, Y. Liu, Z. Zhang, *Foods*, **13(1)**, 1177 (2024).
29. P. Oğuzhan, F. Yangılar, *Bitlis Eren Üniversitesi Fen Bilimleri Dergisi*, **5(1)**, 65308 (2016).
30. R. Smith, D. Jones, *J. Postharvest Biol.*, **12(3)**, 155 (2023).
31. N. Harrazi, H. N. Özbek, D. K. Yanık, I. Zaghbib, F. Göğüş, *J. Food Sci. Technol.*, **61(10)**, 1919 (2024).
32. A. Taye, U. Kalita, P. P. Dutta, D. Haloi, *Packag. Technol. Sci.*, (Early View), 10.1002/pts.2855 (2025).
33. S. Roy, J.-W. Rhim, *Carbohydr. Polym.*, **350**, 122846 (2025).
34. M. B. Perez-Gago, J. M. Krochta, *J. Agric. Food Chem.*, **49(2)**, 996 (2001).
35. C. W. Wang, *J. Food Process.*, **23(4)**, 230 (2000).
36. S. Pan, L. Zhang, Y. Wang, *Food Chem.*, **470**, 36817 (2025).
37. R. Sharma, S. Kumar, K. K. Gaikwad, *Sustainable Food Technol.*, **2**, 378 (2025).
38. A. Syarifuddin, N. Haliza, N. Izzah, M. M. Tahir, A. Dirpan, *Foods*, **14(7)**, 1219 (2025).
39. B. A. Salazar-Cruz, M. Y. Chávez-Cinco, A. B. Morales-Cepeda, C. E. Ramos-Galván, J. L. Rivera-Armenta, *Molecules*, **27(2)**, 426 (2022).
40. M. B. Perez-Gago, J. M. Krochta, *J. Agric. Food Chem.*, **49(2)**, 996 (2001).

Bulgarian Chemical Communications, Volume 58, Issue 3 (pp.337-341) 2026 DOI: 10.34049/bcc.58.3.D017

From orange peel to sustainable biocomposite: production and characterization of pectin/CMC films with matcha tea extract

Ö. İpsalalı[1]*, B. Okyay[2], F. U. Nigiz[2]

[1]*Faculty of Graduate Studies, Department of Chemical Engineering, Çanakkale Onsekiz Mart University, Turkey*
[2]*Faculty of Engineering, Department of Chemical Engineering, Çanakkale Onsekiz Mart University, Turkey*

Accepted: July 28, 2026

This study aims to evaluate the production of polysaccharide-based films obtained from orange peel waste, combining pectin (P) and a synthesized carboxymethyl cellulose (C) matrix with matcha tea extract (M). P was recovered from orange peel waste using an acid extraction technique. The extraction yield has been established at 23.37% and 67.38% esterification (DE). Biopolymer films named C/P and C/P/M were produced using the solvent casting method. In the films, C and P solutions were employed at different concentrations (80/20 w/w C:P) to achieve a total biopolymer content of 2% by weight. M was included into the film at concentrations of 0.2%, 0.4%, and 0.6% (w/w relative to total biopolymer weight). This work proposes to develop biocomposite films from C-P and investigate the effect of M on their structural and functional characteristics. Evaluations of opacity, moisture content, thickness, and water vapour transfer rate (WVTR) were performed to describe the films. M in the films, opacity and film thickness increased, but moisture content and WVTR values diminished. The reduction in WVTR, along with diminished moisture content, indicates an improved water vapour barrier resulting from the establishment of a dense network of new hydrogen bonds between M and the C-P matrix. Moreover, the increased film thickness and compact internal structure significantly impeded the transfer of water molecules within the matrix.enhanced its barrier characteristics. These biocomposite films, distinguished by improved water vapour barrier characteristics and heightened opacity, have significant potential as environmentally acceptable, sustainable for synthetic plastics in the food packaging sector.

Keywords: Orange peel, Polysaccharide-based, Pectin, Matcha tea

INTRODUCTION

The food packaging sector is among the largest consumers of plastic. It constitutes over 40% of overall plastic use, with a significant fraction of this packaging becoming waste in a relatively short duration [1]. Food packaging is essential for maintaining product quality, facilitating traceability, and protecting consumer safety. Nevertheless, the majority of conventional packaging materials are derived from petroleum and are non-biodegradable, so presenting an environmental hazard. In formulating sustainable solutions for the food packaging industry, it is essential to account for both the packaging materials and the waste produced by the food sector [2, 3]. In this context, by contributing to the circular economy in line with sustainability principles, high-value-added packaging materials (biopolymers, bioactive materials) can be produced [4].

The utilization of pectin extracted from fruit and vegetable peel waste in the fabrication of polysaccharide-based films is regarded as possessing considerable potential for the advancement of sustainable packaging materials. Diverse sources of pectin may be utilized, including by-products from juice production, as well as peels and seeds from oranges, mangoes, bananas, limes, and pomegranates [5-7]. The fruit juice sector utilizes approximately 40% of global citrus production. The operation generates substantial quantities of citrus (orange, lemons/limes, mandarines) byproducts, including peels, pulp, and seeds. Peels constitute roughly 20% of an orange's (*Citrus sinensis*) total weight and, if inadequately processed, could result to water contamination and environmental damage. This waste represents an exceptional source for pectin extraction due to its diverse biological properties and significant economic worth. [8, 9]. Acidic extraction using citric acid, nitric acid, or hydrochloric acid is acknowledged as one of the most cost-effective and efficient techniques for separating high-yield and high-quality pectin. Among these methods, acidic extraction utilizing such as citric acid is distinguished as an environmentally sustainable and economically viable approach for obtaining high-quality pectin with a sustainable production [10].

Pectin's linear chain structure provides it with significant film-forming potential, excellent

* To whom all correspondence should be sent:
E-mail: *ozdeipsalali@gmail.com*

© 2026 Bulgarian Academy of Sciences, Union of Chemists in Bulgaria

biodegradability, and biocompatibility. The main approach employed in the creation of pectin-based films is the casting process. Biocomposite films can be made by assuring optimal compatibility with biopolymers, including proteins, lipids, and other polysaccharides. Films produced from pectin demonstrate low gas permeability barrier characteristics which are significant, especially in food packaging applications. To mitigate the limitations of pure pectin films, including their elevated water vapor permeability and fragile mechanical properties, novel films are being formulated in the literature through the integration of diverse biopolymers (starch, cellulose, alginate, chitosan) and active compounds (organic acids, phenolic compounds) [7, 10, 11].

Furthermore, a robust film matrix can be successfully formed by utilizing various biopolymers such as carboxymethyl cellulose (CMC), offering significant potential to enhance the mechanical and barrier performance of cost-effective, non-toxic, renewable, and biodegradable packaging materials [12, 13]. Pure CMC, an anionic cellulose derivative, often demonstrates limited mechanical strength; however, this property is enhanced when integrated with other biopolymers, such as pectin [14]. Matcha (*Camellia sinensis*) is a natural green tea produced by carefully grinding tea leaves, historically cultivated in Japan. It is highly abundant in natural antioxidants, particularly polyphenols, which constitute almost 30% of its dry mass [15, 16] The elevated biological activity of matcha, along with its soluble powder form, has significant promise for stabilizing functional food ingredients and incorporating them into biodegradable packaging methods [16, 17].

This work developed films utilizing a polysaccharide-based matrix, utilizing the film-forming, non-toxic and biocompatible characteristics of pectin and carboxymethyl cellulose. Pectin was extracted from orange peel waste, and created by including matcha tea extract into the film matrix. The films were submitted to characterization tests, including thickness, moisture, water vapor transfer rate (WVTR) and opacity, to assess their suitability for food packaging. The incorporation of matcha tea extract contributes to the existing literature by providing further insight into its effects on the physicochemical, optical, and barrier properties of biodegradable films. Furthermore, the use of pectin extracted from orange peel, a juice-industry byproduct, supports the valorization of food waste.

EXPERIMENTAL

- *Pectin extraction.* Pectin was extracted from orange peel with 1 N citric acid (1:25 w/v) at 80°C and pH 1.2 for 60 min. Following extraction, the mixture underwent filtering using Whatman No. 1 filter paper and was permitted to cool to room temperature. Ethanol was added to the cooled solution at a 1:2 (v/v) ratio and allowed to precipitate at +4 °C for 24 h. The precipitate was acquired using centrifugation at 1000 g for 15 min, washed with distilled water, and then dried in an air oven at 40 °C for 24 h to produce pectin. The pectin yield was calculated by the mass difference between the dried pectin and the initial dry raw material.

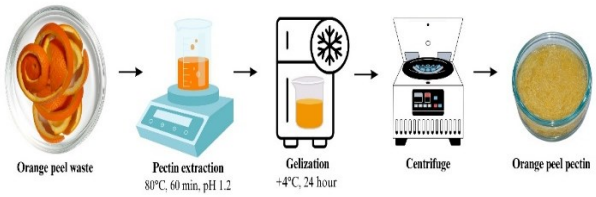

Figure 1. Schematic representation of the carrot pectin extraction

The extent of esterification of orange peel pectin was assessed utilizing a modified approach based on [18]. The dehydrated pectin was solubilized in 20 mL of distilled water and ethanol at a temperature of 40°C and titrated with 0.1 M NaOH. Upon the color shift, the volume of NaOH was noted as V_1. Subsequently, 10 mL of 0.1 M HCl was introduced, and the solution was vortexed until the pink hue vanished. The titration with NaOH was conducted once more, and the volume was noted as V_2. The DE was computed by Equation 1.

$$DE\ (\%) = \frac{V_2}{V_1+V_2} \times 100 \quad (1)$$

- *Matcha tea extraction.* Matcha extract (ME) was produced by dissolving 3 g of matcha in 150 mL of boiling distilled water, subjecting the mixture to a water bath for 45 min, filtering it, and subsequently evaporating it with a rotary evaporator [19].
- *Production of films.* Film-forming solutions were prepared with a total polymer concentration of 2% (w/v) by adjusting the weight ratio of pectin (P) to carboxymethyl cellulose (C) as detailed below: Formulations of 80:20 (C:P, w/w) were prepared, incorporating matcha tea extract (M) abundant in polyphenols, at concentrations of 0.2%, 0.4%, and 0.6% (w/w based on total biopolymer weight. A and P were utilized in 80:20 (C:P w/w) ratios.

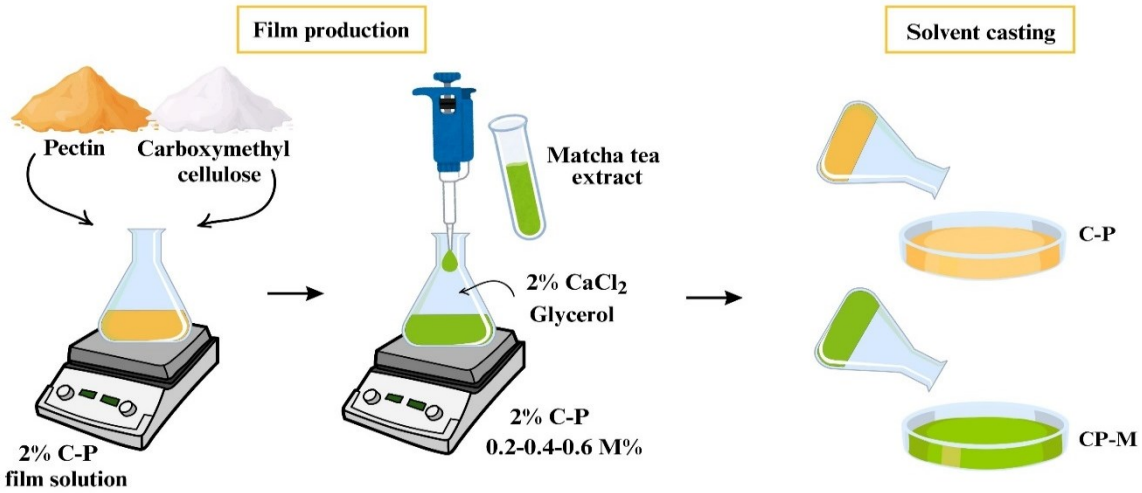

Figure 2. Schematic representation of the orange P, C and M composite films production

The film solution was stirred at 50 °C for 1 h and cross-linked with 2% $CaCl_2$ [20]. The films were produced using the cast film method. Glycerol is preferred as a plasticiser to impart flexibility and films drying oven at 40 °C. The films produced were assigned as C-P (C8-P2), CP-M2, CP-M4 and CP-M6 accordingly.

- *Film characterization.* The film thickness was measured with the Dasqua 4310 digital micrometre gauge. The thickness of each film has been evaluated at three locations: one at the centre and two next to it. The films' opacity, or light transmittance, was assessed utilizing a UV-Vis spectrophotometer (UV1280, Shimadzu, Japan). The opacity in absorbance at 600 nm was calculated utilizing Equation 1.

$$Opacity = \frac{Abs_{600}}{x} \quad (2)$$

where: Abs_{600}: absorbance of the film at 600 nm, x: thickness of the film (mm). The colors of the films were determined using a portable colorimeter (Linshang LS173). Before measuring the color parameters of the prepared films, the device was calibrated using a white standard plate.

The moisture content was determined by drying the films in an oven at 105 °C for 24 h until a constant weight was achieved. The moisture content was determined by dividing the difference between the starting weight (Wi) and the weight lost during drying (Ws) by the starting weight (Wi) (Equation 2).

$$Moisture\ content\ (\%) = \frac{W_i - W_s}{W_s} x100 \quad (3)$$

The water vapor transfer rate (WVTR) was assessed utilizing the usual gravimetric approach. Film samples were positioned in a Petri dish holding a prescribed volume of water. The films were trimmed to a precise dimension and affixed to the inner surface of the Petri dish lid with a waterproof hydrophobic glue. The cover was affixed to the Petri dish, which was maintained at 25 °C in a controlled-humidity laboratory; the weights of the films were recorded after 24 h. Equation 4 was used to determine the WVTR.

$$WVTR\ (\%) = \frac{\Delta m}{A \times \Delta t} \quad (4)$$

where: Δm (g): weight of the container or film being tested, A (m²): surface area of the film, Δt (s): test duration.

Materıals

Carboxymethyl cellulose from Sigma Aldrich, citric acid, ethanol, calcium chloride ($CaCl_2$) were of analytical grade and were purchased from Merck Chemicals, Türkiye. Fresh oranges (*Citrus sinensis*) and matcha tea powder (*Camellia sinensis*) were purchased at a local market in Çanakkale.

RESULTS AND DISCUSSION

Many factors affect pectin yield. The factors encompass the supply of pectin, pH, temperature, extraction duration, and the type of acid utilized. Literature indicates that pectin yield increases inversely with decreasing pH. This could be attributed to the limited solubility and degradation of pectin at elevated pH levels. The extent of pectin esterification is also affected by pH. Pectin is categorized into low-methoxyl pectin (DE < 50%) and high-methoxyl pectin (DE > 50%) [21, 22]. At the end of the study, the degree of esterification of pectin was calculated to be 67.38%, and the gelling ability of pectin was high (Table 1). Generally, an increase in pectin extraction yield was observed as extraction temperatures rose. At low temperatures, pectin yield decreases because acids cannot hydrolyze the insoluble form of pectin. Additionally, longer extraction times at constant temperature and pH increase pectin yield [9]. Yields and degrees of esterification of pectin derived from orange peels

under different conditions with those reported in the literature are summarized in Table 1.

Table 1. Literature review of pectin extraction parameters and yields from orange peels.

Type	Extraction method	Yield	DE (%)	Ref.
Orange peels	Citric acid 80°C-90 min-pH 2.0	18.27	61.65	[9]
Orange peels	Hydrochloric acid 95°C-60 min-pH 1.5	21.53	74.02	[21]
Orange peels	Citric acid 70°C-60 min-pH 3.2	29.41	-	[22]
Orange peels	Citric acid 80°C-60 min-pH 1.2	23.37	67.38	This study

Compared to the reference film, the thickness values of the CP-M films are gradually increasing (Table 2). The observed increase in film thickness corresponding to the rise in matcha tea extract (M) concentration can be attributed to the increased total solids integrated into the matrix. The polyphenolic components in M enter the polymer matrix (C-P), modifying the dense arrangement of the chains and resulting in a more expansive internal structure through intermolecular interactions, so directly increasing the film thickness [23].

The addition of matcha to the C-P film resulted in enhanced opacity values, signifying low light transmission, a conclusion that aligns with existing research [16]. The reduction in optical performance is attributable to the colour of the matcha itself. As the amount of matcha added to the films increases, they take on a greener color, and their opacity increases in direct proportion to the amount of matcha (Fig. 3). The decrease in light transmittance can be considered as beneficial for packing materials. By shielding shelf-packaged food from sunlight, it captures consumer attention, enhancing the product's visibility on the shelf [17].

Table 2. Film thickness values

Film code	Thickness (mm)
CP	0.029
CP-M2	0.027
CP-M4	0.031
CP-M6	0.049

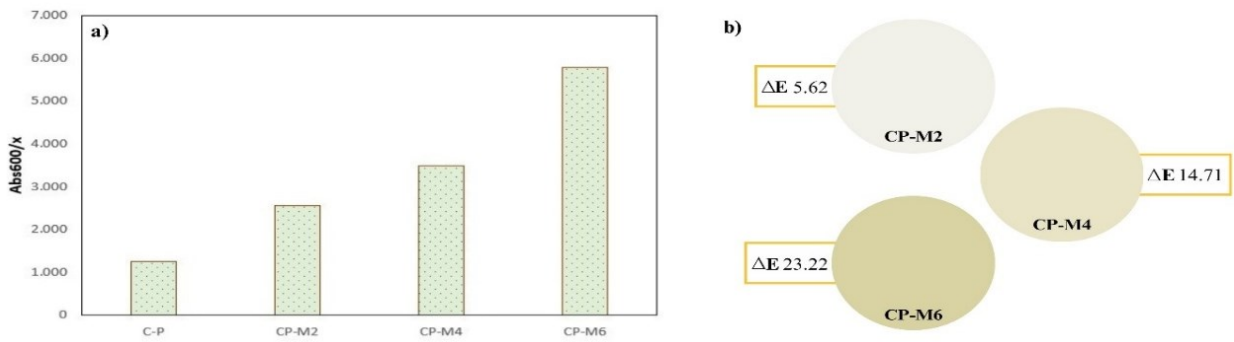

Figure 3. Films' opacity values (a) and color values (b)

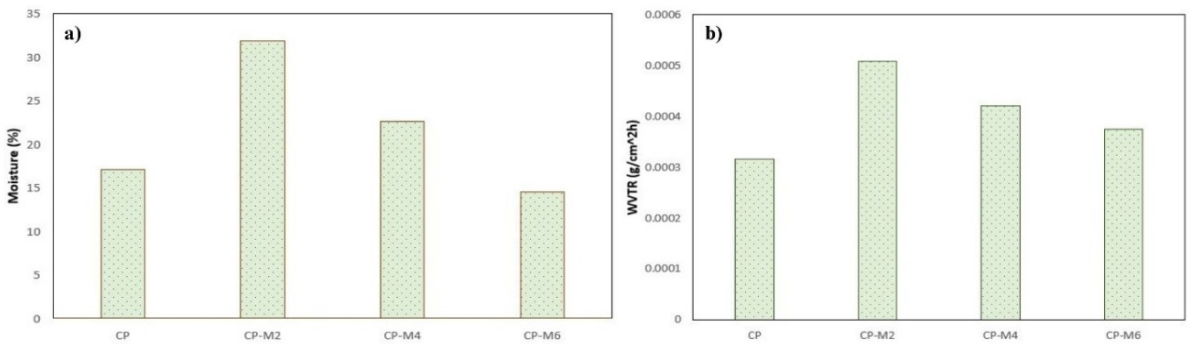

Figure 4. Moisture content (a) and vapor transmission rate (b) of the C-P and CP-M film series

The water vapor transmission rate (WVTR) diminished in accordance with the films' moisture content (Fig. 4b). Matcha is rich in polyphenolic compounds and has enhanced the water barrier qualities of films [24]. This results from the extensive network of hydrogen bonds established between the matcha polyphenols and the C-P matrix, along with the augmented film thickness. The polyphenol-rich M phase, at elevated concentrations, made the matrix more compact, hence inhibiting the transfer of water molecules and enhancing the films' water barrier capabilities. A lower permeability value of a packaging material indicates high resistance to water vapour intrusion [25].

CONCLUSION

This work involves the extraction of pectin from orange peel waste using hot acid extraction with citric acid at 80°C for 60 minutes at a pH of 1.2. The yield of the produced pectin (P) was 23.37%, and the degree of esterification (DE) was 67.38%, categorizing it as high-methoxyl pectin. Biocomposite packaging films were established by integrating pectin into a carboxymethyl cellulose-based film matrix and enhancing it with Matcha tea extract. The incorporation of M has modified the structural and functional characteristics of the C-P film. The M addition resulted in heightened opacity and thickness of the films, concurrently decreasing moisture content and water vapour transmission rate (WVTR). The films' efficacy as a water vapour barrier has been improved.

Acknowledgement: *This study was financially supported by the TÜBİTAK 2209 (Grant Number: 1139B412401793) and Çanakkale Onsekiz Mart University Scientific Research Project Coordination (Grant Number: FLÖAP-2026-5549)*

REFERENCES

1. L. Operato, A. Panzeri, G. Masoero, A. Gallo, L. Gomes, W..Hamd, *Front. Food Sci. Technol.,* **5,** 1520532 (2025).
2. L. Hakim, K. K. Gaikwad, Food Packaging Safety and Health Risks, in: Concepts of Food Packaging. Apple Academic Press; 2025. p. 317.
3. A. Dirpan, Y. Deliana, A. F. Ainani, N. A. Irwan Bahmid, *Polymers,* **16**(19), 2783 (2024).
4. M. A. Zainal Arifin, N. Mohd Adzahan, N. H. Zainal Abedin, M. Lasik-Kurdyś, *Foods,* **12**(3), 456 (2023).
5. R. D. Baron, L. L. Pérez, J. M. Salcedo, L. P. Córdoba, P. J. do Amaral Sobral, *Int. J. Biol. Macromol.,* **98**, 676 (2017).
6. S. R. Kanatt, *Packag. Technol. Sci.,* **37**(6), 487 (2024).
7. C. Mellinas, M. Ramos, A. Jiménez, M. C. Garrigós, *Materials,* **13**(3), 673 (2020).
8. M. Jridi, O. Abdelhedi, A. Salem, H. Kechaou, M. Nasri, Y. Menchari, *Food Hydrocoll.,* **103**, 105688 (2020).
9. R. Bocker, E. K. Silva, *Food Biosci.,* **61**, 104526 (2024).
10. M. J. Akhter, S. Sarkar, T. Sharmin, S. C. Mondal, *Appl. Food Res.,* **4**(2), 100614 (2024).
11. W. Y. Tong, A. R. A. Rafiee, C. R. Leong, W. N. Tan, D. J. Dailin, Z. M. Almarhoon, M. Shelkh, A. Nawaz, L. F. Chuah, *Chemosphere*, **336**, 139212 (2023).
12. T. Zhang, H. Wang, H. Hu, W. Li, X. Zhang, X. Zhang, *Int. J. Biol. Macromol.,* **282**, 136740 (2024).
13. J. S. Yaradoddi, N. R. Banapurmath, S. V. Ganachari, M. E. M. Soudagar, N. M. Mubarak, S. Hallad, S. Hugar, H. Fayaz, *Sci. Rep.*, **10**(1), 21960 (2020).
14. S. Sabzevari, H. Farrokhzad, A. Poorkhalil, *Carbohydr. Polym. Technol. Appl.,* **11**, 100983 (2025).
15. R. Dobrucka, M. Pawlik, M. Szymański, *Molecules,* **29**(19), 4699 (2024).
16. A. N. Zambak, S. Samatya Yilmaz, H. Uzuner, A. Aytac, *J. Thermoplast. Compos. Mater.,* **39**(5), 2566 (2026).
17. G. Y. Akal, P. Akbaş, *Int. J. Biol. Macromol.,* **332**, 148710 (2025).
18. S. Bilraheem, S. Srinuanpan, B. Cheirsilp, A. Upaichit, F. Kawai, U. Thumarat, *Foods,* **13**(16), 2554 (2024).
19. P. Xu, L. Ying, G. Hong, Y. Wang, *Food Funct.,* **7**(1), 294 (2016).
20. Ö. Ipsalalı, F. U. Nigiz, *Bulg. Chem. Commun.,* **11**, 218 (2025).
21. M. M. Kamal, J. Kumar, M. A. H. Mamun, M. N. U. Ahmed, M. R. I. Shishir, S. C. Mondal, *J. Biosyst. Eng.*, **46**(1), 16 (2021).
22. P. Kanmani, E. Dhivya, J. Aravind, K. Kumaresan, *Iran J. Energy Environ.,* **5**(3), e64538 (2014).
23. M. C. Chalapud, M. D. L. P. Salgado-Cruz, E. R. Baümler, A. A. Carelli, E. Morales-Sánchez, G. Calderón-Domínguez, A. B. García-Hernández, *Membranes,* **13**(10), 846 (2023).
24. M. Szymański, M. Pawlik, R. Dobrucka, *Food Biosci.,* **62**, 105047 (2024).
25. M. N. Aga Pranata, W. Supartono, M. R. Tanuputri, *IOP Conf. Ser.: Earth Environ. Sci.,* **1485**(1), 012006 (2025).

Bulgarian Chemical Communications, Volume 58, Issue 3 (pp. 342-347) 2026 *DOI: 10.34049/bcc.58.3.D018*

Effect of tannic acid concentration on structural, mechanical, and antibacterial properties of polyvinyl alcohol/chitosan/pomegranate peel-based biocomposite films

N. İşman[1], Ö. Işık[2], P. Terzioğlu[1]*, M. Orhan[2,3,4]

[1] *Bursa Technical University, Faculty of Engineering and Natural Sciences, Department of Polymer Materials Engineering, Bursa, Türkiye*
[2] *Graduate School of Natural and Applied Sciences, Department of Biotechnology, Bursa Uludag University, Bursa, Türkiye*
[3] *Bursa Uludag University, Faculty of Engineering, Department of Textile Engineering, Bursa, Türkiye*
[4] *Faculty of Textiles, Engineering and Business, Department of Textile Technology, University of Borås, Borås, Sweden*

Accepted: July 28, 2026

Tannic acid is a plant-derived natural crosslinker and active agent, generally improving the properties of biodegradable films. This study investigated the effect of tannic acid (TA) incorporation on the mechanical, structural, and antibacterial properties of biocomposite films based on polyvinyl alcohol (PVA), chitosan (CS), and pomegranate peel powder (PPP). Tannic acid was added to the film-forming solution at concentrations ranging from 6% to 10% (w/w), based on the total polymer weight. The mechanical performance of the films was evaluated in terms of elastic modulus, tensile strength, and elongation at break. The addition of tannic acid resulted in improved mechanical performance, as evidenced by higher elastic modulus and tensile strength values relative to those of the control film. The highest elastic modulus and tensile strength values were obtained for the films containing 10% (w/w) tannic acid. FT-IR results revealed the formation of hydrogen bonding interactions between the functional groups of tannic acid and polymers. The antibacterial activity of the control film and the film containing the highest concentration of tannic acid was evaluated against *Escherichia coli* and *Staphylococcus aureus* by the modified ISO 20645 disc diffusion method. The film samples did not exhibit any antibacterial activity.

Keywords: Polyvinyl alcohol, Chitosan, Tannic acid, Pomegranate peel powder

INTRODUCTION

Packaging is a method or material that plays a critical role in protecting products from environmental effects, extending the shelf life of food products, and enabling safe global distribution [1]. Globally, approximately half of the packaging industry consists of conventional petroleum-based plastics due to their low cost, durability, and ease of processability. Nevertheless, these conventional plastics have led to significant environmental and economic challenges such as long degradation times, micro-plastic pollution, and their high carbon footprint in production processes [2–5]. Similar to the situation with petroleum-based plastics, agricultural food waste and agro-industrial by-products also constitute a significant global problem affecting national economies, world resources, and public health [6–8]. A promising solution involves recycling/reusing/upcycling food waste and by-products to develop sustainable, biodegradable packaging, which directly aligns with circular economy strategies [2]. In this context, there is a growing demand for eco-friendly, sustainable, and functional bio-based packaging materials developed using biopolymers, biodegradable polymers, and biocomposites. PVA is one of the most preferred and commonly used biodegradable polymers in biocomposite films due to its unique properties such as high chemical resistance, non-toxicity, and biocompatibility [9]. Another biodegradable and bio-based polymer commonly used, and also preferred in this study, is chitosan. Chitosan is a linear polysaccharide derived from chitin with exceptional properties such as biodegradability, biocompatibility, and antibacterial activity [9]. However, food packaging films based on a single biopolymer component may have various disadvantages that limit their practical applications and functional properties in the food packaging industry. Polymer blending is the preferred first choice and a promising strategy for the development of biodegradable food packaging films. Blending different polymers makes it possible to create films with unique properties while preserving the distinctive properties of each polymer [10, 11]. In recent years, especially in the food packaging field, biocomposite film structures have begun to be developed with various organic or inorganic additives at the micro- or nano-level, incorporated into polymer blends to improve

* To whom all correspondence should be sent:
E-mail: *pinar.terzioglu@btu.edu.tr*

© 2026 Bulgarian Academy of Sciences, Union of Chemists in Bulgaria

several properties (thermal, barrier, mechanical, antibacterial, etc.) of the films.

Biocomposites are materials composed of at least two components, referred to as the polymer matrix and the reinforcement material, at least one of which is bio-based [12]. With the above-mentioned environmental concerns, the use of food waste (fruit peels, ground seeds, etc.) and agricultural by-products (stems, stalks, etc.) as reinforcement materials in synthetic or bio-based polymer matrices is gaining attention [13, 14].

Pomegranate peel powder, a by-product of the pomegranate fruit, has gained significant attention as an organic reinforcement material in the food packaging, cosmetic, and medical fields, owing to its valuable antioxidant, antibacterial, anti-inflammatory, and anticancer properties [15. Pomegranate peel powder contains phenolic compounds and flavonoids such as apigenin, caffeic acid, chlorogenic acid, ellagic acid, gallic acid, quercetin, and punicalagin [17]. Active packaging films containing pomegranate peel powder exhibit excellent antimicrobial and antioxidant activity, which makes them an attractive option for extending the shelf life of food products.

Tannic acid is a natural green crosslinker used in polymeric films. Tannic acid is a plant-derived polyphenolic compound, consisting of polymerized flavonoids with varying degrees of polymerization, and containing catechol and pyrogallol aromatic rings [18]. As one of the most abundant naturally occurring compounds, it offers economic advantages and exhibits excellent biocompatibility along with antioxidant, anti-inflammatory, and antimicrobial properties [19]. Due to its rich phenolic hydroxyl content, tannic acid can readily associate with biological macromolecules through various intermolecular interactions. As a crosslinker, it has a tendency to form more stable structures [20]. In the literature, food packaging films/coatings based on biopolymers cross-linked with tannic acid have shown good effects in preserving fresh foods, as tannic acid improves the mechanical, barrier, and thermal properties of the films [21, 22].

The aim of this study is to develop and characterize PVA/CS/PPP composite films incorporated with varying concentrations of tannic acid (0, 6, 8, and 10% w/w) for food packaging applications. The physicochemical, mechanical, and antibacterial properties of the films were evaluated through Fourier-transform infrared spectroscopy (FT-IR), scanning electron microscopy (SEM), hydrophilicity measurements, mechanical testing, and antibacterial assays against *Escherichia coli* and *Staphylococcus aureus*.

EXPERIMENTAL

Materials

Chitosan (CS) with a deacetylation degree of at least 75% was obtained from Sigma-Aldrich (Darmstadt, Germany). Polyvinyl alcohol (PVA, 87.8% purity) was supplied by Zag Kimya (Istanbul, Türkiye). Pomegranate peel powder (PPP) was procured from Naturşah (Izmir, Türkiye). Tannic acid (TA) was purchased from Sentez Lab. Company (Istanbul, Türkiye), while glycerol, used as a plasticizing agent, was acquired from Merck (Darmstadt, Germany).

PVA/CS/PPP and PVA/CS/PPP/TA biocomposite film production

Figure 1 illustrates the general fabrication workflow of the biocomposite film production. Initially, a 5% (w/v) PVA solution was prepared by dissolving polymer granules in distilled water at 90 °C under continuous stirring at 400 rpm for 3 h. In parallel, a 1% (w/v) chitosan (CS) solution was obtained using a 1% (v/v) aqueous acetic acid solvent at 50 °C. These two polymeric solutions were subsequently blended and stirred at 50 °C for 1 h. To prepare the control film, pomegranate peel powder (PPP) was added into the neat PVA/CS blend at 3% (w/w, based on total polymer weight) concentration. Tannic acid was used in liquid form; therefore, a 5% (w/v) tannic acid stock solution was prepared with distilled water. After stirring the PPP-loaded polymer solution at 250 rpm and 25 °C for 24 h, tannic acid was added separately at concentrations of 6, 8, and 10% (w/w). The tannic acid-containing polymer solutions were stirred again at 40°C for 2 h. In the next step, glycerol (20% w/w) was incorporated as a plasticizer, followed by an additional 30 min of stirring at room temperature. Finally, the prepared solutions were poured into circular glass Petri dishes with a diameter of 11.5 cm and dried in an oven at 50 °C for 24 h and 35 °C for 18 h, respectively [23].

Fourier transform infrared spectroscopy (FT-IR)

The biocomposite films (PCPT-0 and PCPT-10) were analyzed by FT-IR spectroscopy (Thermo Nicolet iS50 FT-IR, USA). The measurements were taken between 500-4000 cm^{-1} wavenumbers at 4 cm^{-1} resolution in transmission mode [13, 23].

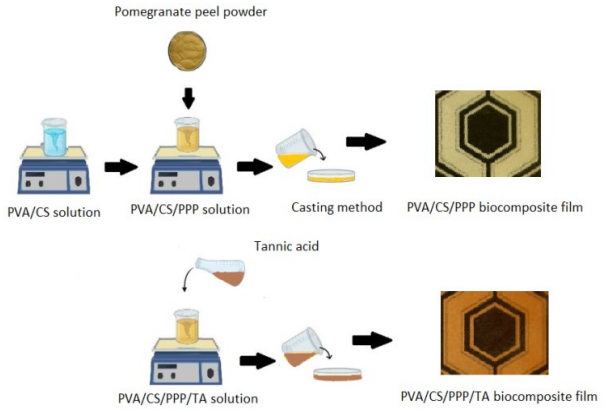

Figure 1. Schematic illustration of PPP- and TA-loaded biocomposite film preparation.

The resulting film samples were designated as PCPT-0, PCPT-6, PCPT-8, and PCPT-10, respectively, as shown in Table 1.

Table 1. Biocomposite film compositions

Sample code	PVA % (w/v)	CS % (w/v)	PPP % (w/w)	TA % (w/w)	Glycerol % (w/w)
PCPT-0	5	1	3	0	20
PCPT-6	5	1	3	6	20
PCPT-8	5	1	3	8	20
PCPT-10	5	1	3	10	20

Surface morphology analysis (SEM)

The surface morphology of the biocomposite films (PCPT-0 and PCPT-10) was analyzed on a Gemini 300 scanning electron microscope (SEM, Carl Zeiss, Germany) operating with a 5 kV acceleration voltage. The film samples were coated with gold before scanning to eliminate charge effects [13, 23].

Mechanical properties

The tensile properties of the biocomposite films were presented in terms of tensile strength, elongation at break, and Young's modulus. The tests were performed according to the ASTM D882 standard with some modifications using a 1 kN load cell and a 15 mm/min crosshead speed. A one-way ANOVA test was performed in the statistical analyses [13, 23].

Water contact angle measurements

Water contact angle measurements were conducted to determine the hydrophobic or hydrophilic character of the biocomposite films. An automatic dispensing unit coupled to an optical tensiometer (Biolin Scientific, Gothenburg, Sweden) was employed for the measurements. The measurements were taken from three points on one film, and the results were given as average data with standard deviations [13, 23].

Antibacterial activity

The antibacterial activity of the biocomposite films (PCPT-0 and PCPT-10) was evaluated against ATCC 25922 *E. coli* and ATCC 6538 *S. aureus* bacteria using the modified ISO 20645 agar diffusion method. Bacterial suspensions prepared from test microorganisms were adjusted to a final concentration of 10^5 CFU/mL. A 1 mL aliquot of this prepared inoculum was homogeneously spread onto the surface of Mueller Hinton Agar (BD, Germany) using a sterile swab. Then, ~~the~~ film samples were cut into 2×2 cm dimensions and placed onto the agar surface. After the plates were gently pressed to ensure full contact of the samples with the surface, they were left for incubation at 37°C for 18–24 h. At the end of the incubation period, the clear zones formed around the film samples were measured in millimeters by two independent researchers, and the antibacterial activity was evaluated.

RESULTS AND DISCUSSION

FT-IR analysis of the biocomposite films

The FT-IR spectra of tannic acid, control film (PCPT-0), and the film with the highest tannic acid concentration (PCPT-10) are given in Figure 2. The band shift and intensity alterations around 3000-3500 cm^{-1} (O-H stretching) could be attributed to the increase in hydrogen bonding between the polymer matrix and the tannic acid functional groups. Peaks at 1605 and 1519 cm^{-1} in the spectrum of TA are classic indicators of the C=C stretching peak and aromatic ring vibrations [24, 25]. The FT-IR spectrum of the film loaded with 10% (w/w) tannic acid showed a new peak around 1622-1615cm^{-1} compared to the control film. This newly formed peak could be attributed to the stretching vibrations of the aromatic C=C bonds originating from the polyphenolic structure of tannic acid or amide I/C=O stretching of chitosan. Moreover, this band could be the result of the shifted carbonyl (C=O) stretching vibrations, involved in intermolecular hydrogen bonding between the polymer matrix and phenolic hydroxyl groups (-OH) of tannic acid [24, 26].

SEM analysis of the biocomposite films

The micrographs of the surface views of PCPT-10 and PCPT-0 biocomposite films are shown in Figure 3. As can be seen from the SEM images, the control film has a rougher and slightly heterogeneous surface; however, PCPT-10 exhibits

a smooth, uniform, and continuous surface morphology without any visible phase separation. The reason for this could be the good compatibility and homogeneous dispersion of tannic acid within the PVA/CS/PPP polymer matrix. This morphological result is supported by literature findings and attributed to the abundance of (-OH) groups [24, 25].

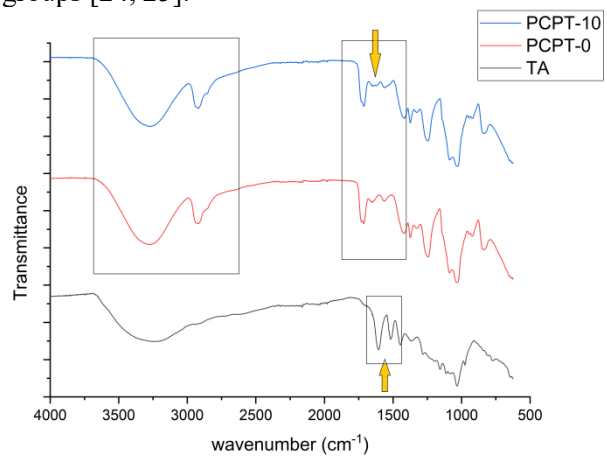

Figure 2. FT-IR spectra of tannic acid powder and biocomposite films

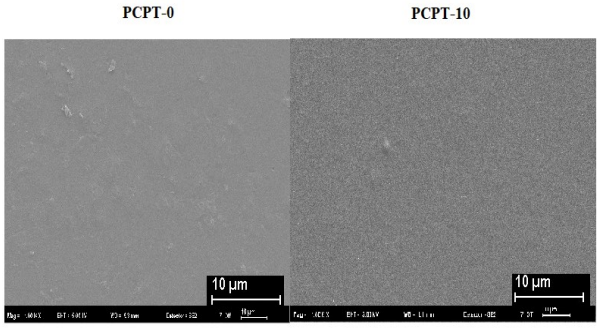

Figure 3. SEM images of the surface morphology of the biocomposite films

Mechanical properties of biocomposite films

Mechanical test results are presented in Table 2. It can be seen that tannic acid addition significantly enhanced the tensile strength and Young's modulus, thus the stiffness, of the PVA/CS/PPP biocomposite films, whereas the elongation at break values remained nearly unchanged ($p>0.05$). The highest values of tensile strength and Young's modulus were obtained for the PCPT-10 sample, owing to the highest tannic acid concentration. This enhancement could be due to the improved intermolecular interactions such as hydrogen bonding established between the hydroxyl groups of TA and the polymer matrix, PVA/CS/PPP [26]. These interactions could lead to the development of a more compact and rigid network within the polymeric structure [24]. Initially, the elongation at break value of the 6% (w/w) tannic acid-containing film increased compared to the control film. Then, the elongation at break values remained nearly unchanged; the control film, PCPT-0, had a value of 290.18%, and the film with the highest tannic acid concentration, PCPT-10, had 292.56%. Tensile strength and Young's modulus values of PCPT-10 reached the highest levels ($p<0.05$) among the films. It can be said that tannic acid addition improves the mechanical strength and stiffness of the biocomposite films. In the literature, tensile strength and Young's modulus values increased with an increase in tannic acid concentration [27, 28]. However, at low tannic acid concentrations, the elongation at break value stayed almost the same compared with the control film [27].

Table 2. Mechanical test results of biocomposite films

Sample code	TA content (%)	Young's modulus (MPa)	Tensile strength (MPa)	Elongation at break (%)
PCPT-0	0	$25.01^{c} \pm 1.88$	$20.23^{b} \pm 2.96$	$290.18^{a} \pm 65.65$
PCPT-6	6	$34.11^{b} \pm 3.11$	$22.87^{ab} \pm 3.06$	$298.25^{a} \pm 42.11$
PCPT-8	8	$31.44^{bc} \pm 3.16$	$21.49^{ab} \pm 2.06$	$290.01^{a} \pm 40.81$
PCPT-10	10	$48.90^{a} \pm 6.07$	$25.33^{a} \pm 1.28$	$292.56^{a} \pm 33.68$

Water contact angle measurement of biocomposite films

Water contact angle is a parameter that defines the hydrophilic ($\theta< 90°$) or hydrophobic ($\theta> 90°$) character of a material. Contact angle values and droplet images are shown in Figure 4. It can be seen that the water contact angle values decreased from 83.1° in PCPT-0 to 75.75° in PCPT-10 with tannic acid addition. This reduction indicates an increase in the hydrophilicity of the film surfaces, which can be directly related to the hydrophilic hydroxyl (-OH) groups introduced by the tannic acid molecules [25, 28].

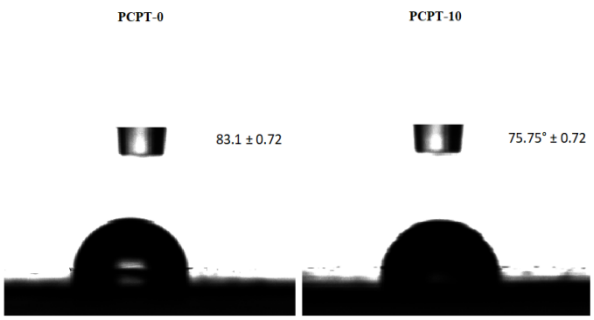

Figure 4. Water contact angle of biocomposite films

Antibacterial activity of biocomposite films

The antibacterial activity of the biocomposite films, PCPT-0 and PCPT-10, was evaluated against *E. coli* and *S. aureus* using the modified disc diffusion method on Mueller-Hinton Agar. Both the control film (PCPT-0) and the tannic acid-incorporated film (PCPT-10) swelled in the agar, and PCPT-10 migrated through the agar surface. Despite this physical migration into the agar, no zones of inhibition were observed for any of the film samples. The highly hydrophilic character of tannic acid (contact angle of 75.75°) could trigger rapid water uptake and macroscopic dissolution on the agar. Even in the dissolved state, the active phenolic hydroxyl groups of TA might be locked within the polymer-tannic acid macromolecular structure, or they might migrate in insufficient quantity to inhibit bacterial growth [29, 30]. Consequently, the active sites of tannic acid and bioactive molecules might never be released freely to interact with the bacterial cell membranes to inhibit their activity [29, 31]. In the literature, there are limited studies showing that bioactive compounds do not inhibit bacterial growth. These studies attribute this situation to the release profile of bioactive compounds and dose dependency [24, 32].

CONCLUSION

In this study, eco-friendly biocomposite films based on PVA/CS polymer blends enriched with pomegranate peel powder and different concentrations of tannic acid were successfully produced by the solution casting method for sustainable food packaging applications. Structural, mechanical, and antibacterial analyses were performed. FT-IR and SEM analyses confirmed a homogeneous and continuous film structure with good molecular compatibility between the polymer matrix and the fillers. The tannic acid incorporation improved the mechanical properties of the films, significantly increasing Young's modulus (up to 48.90 MPa) and tensile strength; however, no significant difference was observed in the elongation at break values compared to the control film. Although ~~the~~ tannic acid addition increased the hydrophilic character (water contact angle 75.75°) of the films due to the presence of phenolic hydroxyl groups and led to film dissolution during the modified disc diffusion tests, no antibacterial inhibition zones were observed against *E. coli* and *S. aureus*. Future studies should focus on the evaluation of antioxidant activity, barrier properties, and food shelf-life tests of the developed biocomposite films to characterize their preservation potential. Moreover, antibacterial tests should be performed according to the ASTM E2149 Dynamic Contact Method as a complementary approach. The multifunctional biocomposite films could be sustainable alternatives to conventional synthetic packaging, with the potential to improve food preservation and reduce environmental impact; moreover, tannic acid could be a good alternative as a low-cost natural crosslinker for the polymer systems.

Acknowledgement: *This research was supported by the Research Fund of Bursa Technical University (Project Number: 230D014).*

REFERENCES

1. P. Hariharan, G. S. S. Sathyan, S. V. Sathyaprakash, K. Rinchen, R. S. Lokesh, A. Shiju, K. Agilandeswari, *J. Packag. Technol. Res.*, **9**, 141 (2025).
2. M. Qasim, A. Noormazlinah, A. Mohd, A. Azhar, M. Sakinah, A. Munaim, A. Hussain, A. Ali, *Discov. Food*, (2024). doi:10.1007/s44187-024-00117-4
3. C. L. Reichert, E. Bugnicourt, M. Coltelli, P. Cinelli, A. Lazzeri, I. Canesi, F. Braca, R. Alonso, L. Agostinis, S. Verstichel, L. Six, S. De Mets, E. Cantos, C. Ißbrücker, R. Geerinck, D. F. Nettleton, I. Campos, E. Sauter, P. Pieczyk, M. Schmid, *Polymers (Basel)*, **12**, 1 (2020).
4. A. Marotta, A. Borriello, M. R. Khan, S. Cavella, V. Ambrogi, E. Torrieri, *Polymers (Basel)*, **17**, 1 (2025).
5. J. Cheng, R. Gao, Y. Zhu, Q. Lin, *Alexandria Eng. J.*, **91**, 70 (2024).
6. D. Xie, M. Guo, *Compr. Rev. Food Sci. Food Saf.*, 1 (2024). doi:10.1111/1541-4337.13334.
7. S. L. d. S. C. Carnaval, A. K. Jaiswal, *J. Compos. Sci.*, **8**, 1 (2024).
8. D. B. Pal, A. Kapoor, A. K. Arya, R. K. Arya, A. K. Tiwari, *Biomass Convers. Biorefin.*, **15**, 24403 (2025).
9. O. Fakraoui, L. I. Atanase, S. Salhi, M. Arous, Z. Ayadi, *J. Polym. Sci.*, 1 (2024). doi:10.1002/pol.20240268.
10. W. Zhang, H. Ahari, Z. Zhang, S. Mahdi, *Trends Food Sci. Technol.*, **133**, 75 (2023).
11. W. Zhang, A. Khan, P. Ezati, R. Priyadarshi, M. Alizadeh, *Food Chem.*, **443**, 138506 (2024).
12. L. G. Moutinho, E. Soares, M. Oliveira, *Polym. Compos.*, **46**, 9703 (2025).
13. P. Terzioğlu, F. Güney, F. N. Parın, İ. Şen, S. Tuna, *Food Packag. Shelf Life*, **30**, 100742 (2021).
14. E. Messinese, O. Pitirollo, M. Grimaldi, D. Milanese, C. Sciancalepore, *Food Bioprocess Technol.*, 606 (2024).
15. F. Azmat, M. Safdar, H. Ahmad, M. Rizwan, J. Khan, J. Abid, M. Sadiq, N. Saurabh, A. Ali, U. Khalid, S. Mahvish, F. Islam, S. A. Cheema, U.

Shehzadi, R. Ali, A. Befa, K. Yuosra, A. Ali, *Food Sci. Nutr.*, 661 (2024).
16. P. Rasane, S. Kaur, J. Kaur, M. Gunjal, S. Ercisli, R. Choudhary, *ACS Omega*, (2023). doi:10.1021/acsomega.3c02586.
17. P. Monika, M. N. Chandraprabha, R. Hari Krishna, M. Vittal, C. Likhitha, N. Pooja, V. Chaudhary, C. Manjunatha, *Biotechnol. Genet. Eng. Rev.*, **00**, 1 (2022).
18. C. Chen, H. Yang, X. Yang, Q. Ma, *RSC Adv.*, **12**, 7689 (2022).
19. J. Feng, Y. Yu, S. Huang, N. Zhu, A. Mojiri, D. Ge, *J. Environ. Manage.*, **375**, 124390 (2025).
20. M. Hosseini, L. Moghaddam, L. Barner, S. Cometta, D. W. Hutmacher, F. Medeiros Savi, *Prog. Polym. Sci.*, **160**, 101908 (2025).
21. W. Zhang, S. Roy, P. Ezati, D. P. Yang, J. W. Rhim, *Trends Food Sci. Technol.*, **136**, 11 (2023).
22. G. S. Maia, L. Marangoni Júnior, R. P. Vieira, *Adv. Colloid Interface Sci.*, **339**, 103428 (2025).
23. N. İşman, Y. Sıcak, P. Terzioğlu, *Mater. Today Commun.*, **48**, 113542 (2025).
24. S. Jasrotia, S. Gupta, M. L. Kudipady, Y. M. Puttaiahgowda, *ACS Omega*, **10**, 19361 (2025).
25. S. J. Lee, M. A. Gwak, K. Chathuranga, J. S. Lee, J. Koo, W. H. Park, *Food Hydrocoll.*, **136**, 108249 (2023).
26. Z. Qin, Y. Huang, S. Xiao, H. Zhang, Y. Lu, K. Xu, *Int. J. Mol. Sci.*, **23**, 9284 (2022).
27. M. Sultan, A. Youssef, R. A. Baseer, *Sci. Rep.*, **14**, 1 (2024).
28. S. Tanpichai, K. Yuwawech, E. Wimolmala, Y. Srimarut, W. Woraprayote, Y. Malila, *RSC Adv.*, **15**, 30742 (2025).
29. B. P. Genesi, R. de Melo Barbosa, P. Severino, A. C. D. Rodas, C. M. P. Yoshida, M. B. Mathor, P. S. Lopes, C. Viseras, E. B. Souto, C. Ferreira da Silva, *Int. J. Pharm.*, **634**, 122648 (2023).
30. S. Moreira Gonçalves, J. F. Gomes Motta, R. Ribeiro-Santos, D. W. Hidalgo Chávez, N. Ramos de Melo, *Curr. Res. Food Sci.*, **3**, 1 (2020).
31. N. Xu, Y. Yuan, L. Ding, J. Li, J. Jia, Z. Li, D. He, Y. Yu, *Burns Trauma*, **10**, 1 (2022).
32. R. Zhou, J. Huang, W. Zhang, W. Wang, W. Peng, J. Chen, C. Yu, R. Bo, M. Liu, J. Li, *Mater. Today Bio*, **29**, 101315 (2024).

Bulgarian Chemical Communications, Volume 58, Issue 3 (pp. 348-351) 2026 *DOI: 10.34049/bcc.58.3.D019*

Synthesis and characterization of boron-containing benzoxazine resins for advanced thermal protection systems

R. Ozdemir*, D. Unlu

Bursa Technical University, Faculty of Engineering and Natural Sciences, Chemical Engineering Department,16310, Bursa, Turkey

Accepted: July 28, 2026

The material systems used in aerospace and defense vehicles are of critical importance for ensuring reliable operation under both atmospheric and extra-atmospheric conditions. In particular, severe aerodynamic heating caused by surface friction during atmospheric entry and exit exposes these vehicles to extreme thermal loads. Preserving structural integrity and functional performance under such conditions requires the development of advanced thermal protection systems (TPS). Among the candidate materials, carbon fiber-reinforced phenolic resin composites have attracted considerable attention due to their high thermal resistance, ablative characteristics, and excellent mechanical properties. In this study, phenylboronic acid-modified benzoxazine resins were synthesized to enhance the thermal performance of composite materials intended for TPS applications. Neat benzoxazine and phenylboronic acid-modified benzoxazine resin systems were successfully prepared and comparatively investigated. The structural, morphological, and thermal properties of the synthesized resins were characterized using Fourier transform infrared spectroscopy (FTIR), thermogravimetric analysis (TGA), and scanning electron microscopy (SEM). The incorporation of phenylboronic acid significantly improved the thermal behavior of the benzoxazine resin systems, indicating enhanced thermal stability and potential for high-temperature applications. The obtained results demonstrate that the developed resin systems are promising candidates for advanced thermal protection composites and contribute to the ongoing development of high-performance phenolic matrix materials for aerospace applications.

Keywords: Benzoxazine, Phenolic resin, Thermal properties, Phenylboronic acid

INTRODUCTION

The high velocities reached by spacecraft and aircraft during atmospheric flight expose these vehicles to severe environmental stresses. Aerodynamic heating, oxidative environments, high pressure, and plasma effects collectively threaten the structural and thermal integrity of the system [1]. The simultaneous presence of such extreme conditions necessitates the development of advanced engineering materials capable of maintaining performance under harsh operational environments.

In this context, thermal protection systems have been developed to provide effective thermal shielding by preventing excessive heat transfer from the vehicle's outer surface to its internal structure during hypersonic flight [2]. TPS materials are typically designed as multiphase composite systems consisting of a reinforcement phase (carbon, glass, or kevlar fibers) and a matrix phase (polymeric or ceramic resins) that provides structural cohesion and load transfer capability. Among these constituents, the matrix phase plays a critical role in determining overall performance, as it is the most susceptible component to thermal degradation, ablation, and surface erosion under extreme temperature conditions. Therefore, the selection or modification of high-temperature-resistant polymer matrices is of paramount importance.

Thermoset and thermoplastic polymers are widely used as matrix materials in composite systems [3]. Among thermosets, phenolic resins exhibit superior thermal stability and high char yield compared to other polymer classes. Their dense aromatic structures provide resistance to thermal degradation, while their low thermal conductivity and ability to absorb heat generated during decomposition further enhance their suitability for high-temperature applications. Owing to these advantages, phenolic resins are commonly used as matrix materials in modern aerospace thermal protection systems.

However, inherent limitations such as brittleness and processing constraints have encouraged researchers to explore alternative high-performance polymer systems. In this regard, polybenzoxazine (PBZ) resins have emerged as promising candidates to replace or complement conventional phenolic

* To whom all correspondence should be sent:
E-mail: *ruozdemir@hotmail.com*

© 2026 Bulgarian Academy of Sciences, Union of Chemists in Bulgaria

resins. Benzoxazine monomers, synthesized *via* the Mannich reaction of formaldehyde, phenol (or phenol derivatives), and primary amines, undergo ring-opening polymerization to form phenolic-like PBZ networks under thermal curing conditions [4]. Compared to conventional phenolic systems, benzoxazine resins offer advantages such as reduced shrinkage, absence of volatile by-products during curing, and elimination of acidic catalysts. These characteristics make PBZ resins attractive candidates for advanced thermal protection composite applications.

In this study, boron-modified and unmodified benzoxazine resins were synthesized, and the resulting systems were characterized.

EXPERIMENTAL

Materials

Phenol (90%) supplied by Kimetsan Kimya, aniline (≥99.5%) obtained from Merck, and 37% formaldehyde solution containing 10% by weight of methanol purchased from Tekkim Kimya were used as the primary precursors for benzoxazine synthesis. Magnesium hydroxide (95%) was supplied by Sigma-Aldrich, while N, N-dimethylformamide (≥99%) was obtained from Carlo Erba and used as solvent without further purification. Phenylboronic acid (PBA) (98%) was purchased from BLDpharm and utilized as a thermal performance-enhancing modifier in the benzoxazine structure.

Synthesis of the resins

For the synthesis of benzoxazine resin, phenol and aniline were first weighed at appropriate molar ratios and mixed until a homogeneous solution was obtained. After continuous stirring for a predetermined period, formaldehyde solution was slowly added dropwise to the reaction medium using a burette under controlled conditions. Subsequently, magnesium hydroxide ($Mg(OH)_2$) was introduced as a catalyst to promote the reaction and optimize the polymerization process. The pH of the reaction medium was adjusted to 6.0–6.5 to provide suitable synthesis conditions. The reaction mixture was then gradually heated to 80 °C and maintained at this temperature for a specific duration to complete the polymerization process [5]. Upon completion of the reaction, the reactor was cooled to room temperature, and the benzoxazine resin was successfully obtained.

For the modification process, phenylboronic acid was incorporated into the synthesized benzoxazine resin at predetermined concentrations. To ensure complete dissolution and homogeneous dispersion of phenylboronic acid within the resin matrix, the reaction temperature was increased to 80–85 °C and the system was continuously stirred for approximately 1 h. After completion of the modification step, the resin mixture was cooled to room temperature, resulting in the successful synthesis of phenylboronic acid-modified benzoxazine resin.

Characterization of the resins

The synthesized benzoxazine resin systems were characterized to evaluate their structural, thermal, and morphological properties. Fourier transform infrared spectroscopy (FTIR) analyses were carried out using a Thermo Scientific Nicolet iS50 instrument to identify the chemical structures and functional groups present in the resins. The measurements were performed at room temperature within the scanning range of 4000–650 cm^{-1}.

Thermogravimetric analysis (TGA) was conducted to investigate the thermal stability and degradation behavior of the synthesized samples. The analyses were performed under a nitrogen atmosphere from room temperature to 900 °C at a heating rate of 10 °C min^{-1}.

The surface morphology of the samples was examined by scanning electron microscopy (SEM). Prior to SEM imaging, the sample surfaces were coated with a thin gold layer using a Leica ACE600 sputter coater to improve electrical conductivity and obtain high-quality micrographs.

RESULTS AND DISCUSSION

FTIR spectroscopy

The chemical bond structures and functional group properties of benzoxazine (BZ) resin and phenylboronic acid (PBA)-doped benzoxazine (PBZ) resin were investigated using FTIR. The measurements were performed at room temperature within a scanning range of 4000–650 cm^{-1}, and the FTIR spectra of benzoxazine resins containing BZ and 10% by weight of PBA are shown in Figure 1.

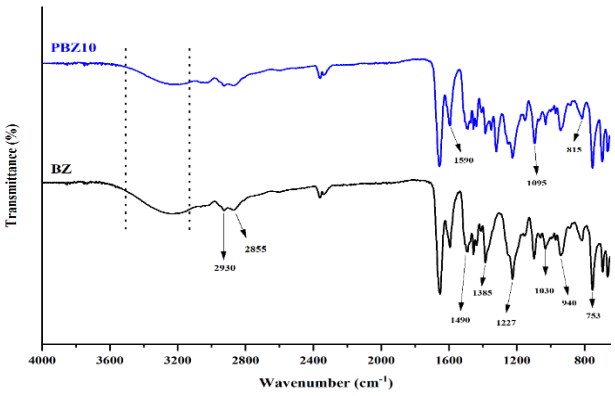

Figure 1. FTIR spectra of the resins

The FTIR spectra of the synthesized benzoxazine resin systems were analyzed to investigate the structural changes induced by phenylboronic acid modification. The broad absorption band observed in the 3500–3200 cm^{-1} region was attributed to hydrogen-bonding interactions between the phenolic hydroxyl groups formed after ring-opening polymerization of the benzoxazine ring and the B–OH functionalities of the PBA structure. The characteristic absorption bands detected at 2930 cm^{-1} and 2855 cm^{-1} correspond to the aliphatic C–H stretching vibrations of methylene groups and alkyl side chains associated with the oxazine ring structure, confirming the formation of methylene bridges within the polymer network [6]. The bands appearing in the 1590–1490 cm^{-1} range are assigned to aromatic C=C skeletal vibrations, indicating the preservation of the benzoxazine aromatic structure [7]. In addition, the band located at approximately 1385 cm^{-1} is related to methylene ($–CH_2–$) groups generated during the ring-opening polymerization process. The characteristic benzoxazine bands observed at 1227 cm^{-1} and 1030 cm^{-1} were attributed to asymmetric and symmetric C–O–C stretching vibrations, respectively, and were retained in all resin systems. Furthermore, the absorption band around 940 cm^{-1}, corresponding to out-of-plane bending vibrations of the oxazine ring C–H bonds, was clearly observed in the neat benzoxazine resin [8-9]. However, this band became weaker or partially disappeared in the PBA-containing samples, suggesting that boronic acid incorporation altered the chemical environment surrounding the oxazine ring [10-11]. Additional bands observed near 815 cm^{-1} and 753 cm^{-1} were attributed to aromatic C–H vibrations and ortho-disubstituted benzene structures containing oxazine functionalities [12-13]. Moreover, the relative intensity of the C–O–C vibrational band around 1095 cm^{-1} decreased after PBA modification, indicating possible intermolecular interactions between the benzoxazine network and phenylboronic acid molecules [14].

SEM analysis

The morphological properties of phenylboronic acid-modified benzoxazine resin systems were investigated by scanning electron microscopy (SEM) analysis of the fracture surfaces. SEM micrographs of the cured neat BZ resin and the BZ resin containing 10 wt.% phenylboronic acid (PBZ10) are presented in Figure 2.

As shown in Figure 2(a), the fracture surface of the cured neat BZ resin exhibits a relatively rough and heterogeneous morphology with noticeable agglomerated domains distributed across the surface. In contrast, the PBZ10 sample displayed a more homogeneous and comparatively smoother fracture surface morphology, as illustrated in Figure 2(b). This morphological change suggests that phenylboronic acid was successfully incorporated, at least partially, into the benzoxazine network during the synthesis and curing processes.

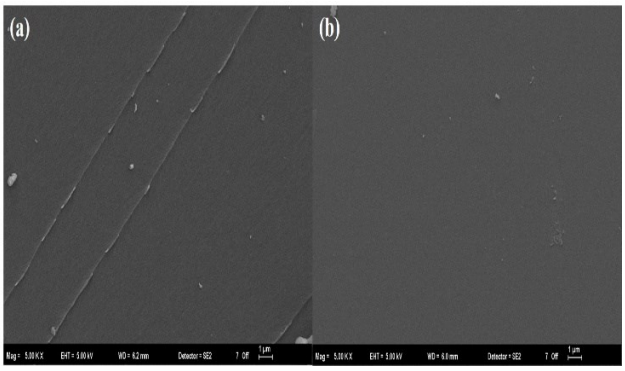

Figure 2. SEM images of resins (a) neat benzoxazine (b) benzoxazine resin containing 10 wt.% phenylboronic acid.

The improved surface homogeneity observed in the modified resin system may be attributed to enhanced intermolecular interactions and improved structural compatibility between the benzoxazine matrix and the phenylboronic acid component. These findings indicate that phenylboronic acid modification can influence the microstructural organization of the cured resin system and potentially contribute to improved thermal and structural properties.

TGA

The thermal decomposition behavior of neat BZ and phenylboronic acid-modified PBZ resins was investigated by thermogravimetric analysis (TGA) under a nitrogen atmosphere. The TGA curves presented in Figure 3 demonstrate that the incorporation of phenylboronic acid significantly influences the thermal degradation behavior of the benzoxazine resin systems.

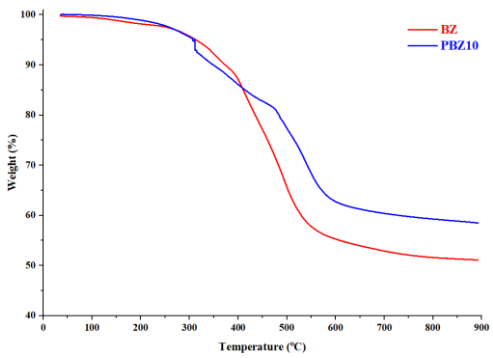

Figure 3. TGA results of the resins.

The results indicate that phenylboronic acid addition considerably enhances the char-forming ability of the benzoxazine matrix. While the neat benzoxazine resin exhibited a residual char yield of 51.08% at 900 °C, the residue amount increased to 58.49% for the resin containing 10 wt.% boron additive. This improvement suggests that boron-containing structures promote the formation of a more thermally stable carbonaceous layer during thermal decomposition and suppress the generation of volatile degradation products.

The primary weight loss region observed between approximately 400 and 600 °C corresponds to the pyrolytic decomposition of the benzoxazine-based polymer network. The higher char residue obtained at elevated temperatures for the boron-modified resin systems can be attributed to the relatively high bond dissociation energies of boron–oxygen (B–O) and boron–carbon (B–C) bonds introduced into the polymer structure [15]. These thermally stable boron-containing structures contribute to improved thermal resistance and enhanced carbonization behavior of the resin system.

CONCLUSION

In this study, phenylboronic acid-modified benzoxazine resin systems were successfully synthesized and evaluated for potential thermal protection system applications. The effects of phenylboronic acid incorporation on the structural, thermal, and morphological properties of benzoxazine resins were systematically investigated using FTIR, TGA, and SEM analyses.

FTIR results confirmed the successful modification of the benzoxazine structure through interactions between phenolic hydroxyl groups and boronic acid functionalities. Changes observed in the characteristic oxazine-related absorption bands indicated that the incorporation of phenylboronic acid altered the chemical environment of the polymer network. TGA analyses demonstrated that boron modification significantly enhanced the thermal stability and char-forming capability of the resin systems. The char residue increased from 51.08% for neat benzoxazine resin to 58.49% for the resin containing 10 wt.% phenylboronic acid, indicating the formation of more thermally stable boron-containing structures during decomposition. SEM observations further revealed that the modified resin exhibited a more homogeneous and smoother fracture surface morphology compared to the neat benzoxazine resin, suggesting improved structural compatibility and network organization.

Overall, the obtained results demonstrate that phenylboronic acid incorporation effectively improves the thermal resistance and microstructural characteristics of benzoxazine-based resin systems. These findings indicate that the developed boron-modified benzoxazine resins are promising candidates for high-temperature composite and thermal protection applications in aerospace and defense industries. Future studies may focus on the incorporation of reinforcing fibers and ceramic fillers, as well as the evaluation of ablative and mechanical performance under extreme thermal environments.

Acknowledgement: *This study was supported by TÜBİTAK (Project No: 224M331) and Bursa Technical University Scientific Research Projects Unit (Project No: 250Y005).*

REFERENCES

1. A. Daniel, Y. Badhe, I. Srikanth, S. Gokhale, K. Balasubramanian, *Ind. Eng. Chem. Res.*, **55**, 10645 (2016).
2. H. Cheng, Z. Fan, C. Hong, X. Zhang, *Compos. - A: Appl. Sci. Manuf.,* **143**, 106313 (2021).
3. Y. Zhang, Q. Shen, X. Li, L. Wang, C. Nie, *Mater. Chem. Front.,* **5**, 4214 (2021).
4. T. Guo, Y. Fan, C. Bo, Z. Qi, H. Tao, C. Ziran, X. Youhui, *High Perform. Polym.*, **33**, 825 (2021).
5. Z. Deliballi, B. Kiskan, Y. Yagci, *Macromolecules*, **53**, 2354 (2020).
6. H. Hu, W. Wang, L. Jiang, L. Liu, Y. Zhang, Y. Yang, J. Wang, *Polym. Polym. Compos.* **30**, 1 (2022).
7. Y. Guo, X. Wang, X. Wang, R. Wei, X. *J.* Zhang, *J. Harbin Inst.,* **49**, 165-172 (2017).
8. Y. Liu, L. Yuan, G. Liang, A. Gu, *J. Polym. Sci.*, **61**, 1279-1288 (2023).
9. J. Wang, Q. Liu, J. Yu, R. Xu, C. Wang, J. Xiong, *Materials*, **15**, 8364 (2022).
10. T. Agag, T. Takeichi, *Polymer,* **52**, 2757 (2011).
11. B. Kiskan, B. Koz, Y. Yagci, *J. Polym. Sci. A Polym. Chem.,* **47**, 6955 (2009).
12. H. X. Ma, C. Zhao, J. J. Qiu, Y. Liu, C. M. Liu, *J. Appl. Polym. Sci.,* 134 (2017).
13. H. Wang, X. Xiu, Y. Wang, Q. Xue, W. Ju, W. Che, S. Liao, H. Jiang, M. Tang, J. Long, J. Hu, *Compos. B: Eng.,* **202**, 108378 (2020).
14. S. M. Attia, M. S. Abdelfatah, M. M. Mossad, *J. Phys. Conf. Ser.,* **869**, 012036 (2017).
15. S. Wang, C. Bian, B. Jia, Y. Wang, X. Jing, *Polym. Degrad. Stab.,* **130**, 328 (2016).

Bulgarian Chemical Communications, Volume 58, Issue 3 (pp. 352-358) 2026 DOI: 10.34049/bcc.58.3.D020

Activated carbon from gypsophila roots: a sustainable adsorbent for dye removal

M. Kocaoğlu, S. N. Karabekiroğlu*

Yildiz Technical University, Faculty of Chemical Metallurgical Engineering, Chemical Engineering, Istanbul, Türkiye

Accepted: July 28, 2026

This study investigates the production and characterization of activated carbon derived from the roots of *Gypsophila* spp., an endemic genus of flowering plants belonging to the Caryophyllaceae family. Due to their high saponin content and abundant biomass in the Anatolian region of Türkiye, Gypsophila roots represent a sustainable precursor for carbon-based adsorbent materials. In this work, the effects of activating agent type and dosage on pore formation during the preparation of activated carbon from Gypsophila roots were examined. For this purpose, chemical activation was carried out using potassium hydroxide (KOH), phosphoric acid (H_3PO_4), sulfuric acid (H_2SO_4), and citric acid ($C_6H_8O_7$) at various concentrations. To achieve the desired porous structure, the process parameters activation temperature, activation time, and impregnation ratio were optimized using the Box–Behnken experimental design. The activated carbons produced under optimal conditions were characterized using Brunauer–Emmett–Teller (BET) surface area analysis and a series of complementary tests to evaluate their textural properties. The sample exhibiting the most developed porous structure was selected for further adsorption studies. In particular, the performance of the Gypsophila-derived activated carbon in removing cationic and anionic dyes from aqueous solutions will be investigated to assess its potential application in wastewater treatment.

Keywords: *Gypsophila* spp., activated carbon, wastewater treatment, dye, environmental

INTRODUCTION

Dye compounds are essential chemicals widely used in various industries such as textiles, paper, plastics, and cosmetics, and they represent one of the major pollutants in industrial wastewater [1]. Due to their high solubility in water, chemical stability, and resistance to biological degradation, these compounds are considered particularly hazardous organic pollutants to the environment [2,3]. Therefore, the removal of dyes from wastewater is of great importance in terms of environmental protection and sustainable water management. Various chemical and physical treatment methods such as flocculation, coagulation, sedimentation, ozonation, and adsorption are commonly employed for this purpose [2,4]. However, adsorption using activated carbon has been shown to be a more effective and economical treatment technique compared to other methods, owing to its high efficiency in removing a wide range of adsorbates, operational simplicity, and ease of design [1,4,5].

Activated carbon (AC) is a carbon-based material characterized by its high porosity, large surface area, high adsorption capacity, mechanical strength, and surface reactivity [6]. Nevertheless, the high cost of commercial activated carbon and its reliance on non-renewable precursors have prompted researchers to explore low-cost, sustainable alternatives derived from agricultural and natural biomass [4,7,8]. In recent years, growing research interest has been directed toward the production of activated carbon from renewable biomaterials such as coconut husk [4], palm seed shells [9], jute fibers [10], olive stones [11], plum kernels [12], and bamboo [13].

The Gypsophila plant (*Gypsophila* spp.), belonging to the *Caryophyllaceae* family, is a perennial herbaceous species that grows 40–100 cm tall, has a deep taproot system, and produces white flowers between June and July [14,15]. Native to the Mediterranean basin, Western Asia, and parts of Europe, Gypsophila is widely distributed in Türkiye, where it is also considered an economically valuable export product. The high saponin content found particularly in its roots is the main factor contributing to its commercial importance [16–18]. Owing to its high saponin concentration and abundant root biomass, Gypsophila species can be regarded as promising and sustainable raw materials for various industrial and environmental applications. However, despite their availability and chemical richness, studies investigating the use of *Gypsophila* roots as precursors for activated carbon production remain limited in the literature. This makes the utilization of this plant both innovative and environmentally significant.

* To whom all correspondence should be sent:
E-mail: *senanurk@yildiz.edu.tr*

© 2026 Bulgarian Academy of Sciences, Union of Chemists in Bulgaria

In this study, Gypsophila roots were selected as a novel and sustainable precursor for the production of activated carbon. Since the adsorption capacity of activated carbon is highly influenced by preparation conditions, optimization of the production process is essential [6]. For this purpose, chemical activation was carried out using potassium hydroxide (KOH), phosphoric acid (H_3PO_4), sulfuric acid (H_2SO_4), and citric acid ($C_6H_8O_7$) as activating agents. To optimize the structural and adsorption properties of the obtained materials, key process parameters activation temperature, activation time, and impregnation ratio were systematically investigated using response surface methodology (RSM). RSM is a statistical optimization technique used to evaluate the effects of independent variables on response outputs, and the Box–Behnken design (BBD) is an efficient approach within this methodology that enables the determination of optimum conditions with fewer experimental runs [19]. After determining the optimal conditions, the resulting activated carbons were characterized using various analytical techniques.

This study aims to address the existing gap in the literature regarding the utilization of endemic Turkish plant species as precursors for activated carbon production and to contribute to the development of cost-effective, sustainable, and high-performance adsorbents for the removal of both cationic and anionic dyes from textile wastewater.

MATERIALS AND METHODS

Gypsophila roots and cultivation conditions

Roots of Gypsophila were procured in Kalealtı Çöğen and Dried Nuts Import Export Industry and Trade Ltd. Co. (Kalealtı Çöğen ve Kuruyemiş İth. İhr. San. ve Tic. Ltd. Şti.). The roots of Gypsophila were subjected to a grinding process in an industrial disc mill operating at a high speed. This resulted in the formation of particles measuring between 3-5 millimeters in size, which were then prepared for experimental use.

Preparation of activated carbon

The following substances were utilised as activation agents for the activation of *Gypsophila* root: potassium hydroxide (KOH), sulfuric acid (H_2SO_4), citric acid ($C_6H_8O_7$), and phosphoric acid (H_3PO_4). The root mass of *Gypsophila* was impregnated with activation agents at ratios of 0:1, 0:3, and 0:5 (w:w). The impregnated *Gypsophila* root was subjected to a 24-h mixing process in a shaker. Subsequently, the samples were subjected to filtration and maintained within an oven (NUVE FN 500 dry air sterilizer) set at 60°C until a complete desiccation had been achieved. The activated carbons were finally ground.

Impregnated samples obtained from *Gypsophila* roots were evaluated in terms of various process parameters to optimize the preparation conditions of activated carbon after the activation process (Table 1). In this study, the primary factors presumed to influence adsorption capacity were identified as impregnation ratio, carbonization temperature, and carbonization time. Consequently, root samples that had been treated with a range of activation agents and impregnation ratios were subjected to carbonization at varying temperatures and times. The performance of the resulting activated carbons was then evaluated based on their adsorption capacities.

Table 1. Factors of carbonization of *Gypsophila* root

Levels	Impregnation ratio (w:w)	Carbonization time (min)	Carbonization temperature (°C)
1	0:1	30	450
2	0:3	60	525
3	0:5	90	600

Adsorption studies

- *Methylene blue test.* Methylene blue (MB) (methylthioninium chloride) was utilised as an adsorbent. Samples of the optimised AC, with a mass of 10 mg, were introduced to 25 mL of dye solution, which had an initial concentration of 100 mg/L. The suspension was stirred for 24 h in order to achieve equilibrium. Subsequently, the solution was separated from the sorbent through centrifugation at 5000 rpm for 5 min. The concentration of the dye solutions was determined by means of a UV-Vis spectrophotometer. Adsorption capacity (q) was calculated using Equation 1.

$$q = \frac{C_0 - C_e.V}{m} \quad (1)$$

where q is adsorption capacity (mg/g), C_0 is initial methylen blue concentration (mg/L), C_e *is* the metyhlene blue concentration after adsorption process has been completed (mg/L), V is solution volume (L), m is activated carbon amount (g).

Based on the methylene blue results, the samples exhibiting the best performance for each chemical were selected and characterized using iodine number analysis.

- *Iodine number test.* Iodine number analysis was carried out to determine the adsorption capacity of the activated carbon samples. In order to achieve this objective, 0.1 N sodium thiosulphate, 0.1 N

iodine solution and a 1% starch indicator were meticulously prepared. For the 0.1 N sodium thiosulphate solution, 6.21 g of $Na_2S_2O_3 \cdot 5H_2O$ was dissolved in distilled water, and the volume was made up to 250 mL. The 0.1 N iodine solution was prepared by means of the following procedure. A quantity of 5–6 g of KI was dissolved in 10–15 mL of distilled water, after which 3.17 g of I_2 was added. The solution was stirred using a magnetic stirrer until no iodine crystals remained, at which point the volume was made up to 250 mL. The solution was then stored in an amber bottle. For the experiment, 0.1 g of each activated carbon sample was weighed into falcon tubes, and 25 mL of 0.1 N iodine solution was added to each tube. A control sample without activated carbon was also prepared under the same conditions. The tubes were mixed in an orbital shaker at 170 rpm for 2 hours. At the end of the period, the samples were centrifuged at 5000 rpm for 5 minutes to allow the solid phase to settle.

Following centrifugation, 10 mL of each sample's superior layer was extracted and titrated with a 0.1 N sodium thiosulphate solution. During the titration process, when the solution assumed a pale straw-yellow hue, 3–4 drops of 1% starch indicator were introduced, and the titration was continued until the dark blue colour was fully dissipated. The volumes of sodium thiosulphate consumed were recorded, and the iodine adsorption capacity of the activated carbons was calculated by comparison with a blank sample.

Statistical analysis

In order to systematically investigate the effects of three parameters (impregnation ratio, carbonization temperature, and carbonization time) which have been identified as the most important factors affecting adsorption capacity in activated carbon production from gypsophila roots, and to optimise the number of experiments, a Box-Behnken experimental design (BBD) was used, with adsorption capacity (q) evaluated as the response variable. A second-order mathematical model was developed to predict adsorption capacity using the experimental data obtained with BBD. However, an examination of the model outputs revealed that the Box-Behnken approach did not adequately represent the adsorption system. This phenomenon is hypothesized to be attributable to the non-dependence of the adsorption mechanism on a single experimental parameter. Rather, it is theorized that multiple factors, including pore structure, surface functional groups, carbonization degree, and adsorbent-adsorbate interactions, collectively exert an effect. Consequently, it was determined that the classical RSM approach is constrained by the nonlinear and complex nature of the system. To address this limitation, machine learning methods were employed in the subsequent stages of the study.

RESULTS AND DISCUSSION

Methylene blue adsorption results

The adsorption performance of activated carbons produced from *Gypsophila* roots using different chemical activation agents was evaluated through methylene blue (MB) adsorption experiments. The resulting adsorption capacity data are presented in Fig. 1.

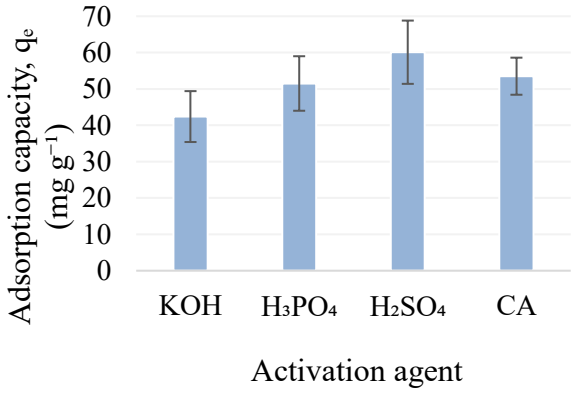

Figure 1. Effect of activation agent on methylene blue adsorption capacity.

The average adsorption capacity of activated carbons treated with H_2SO_4 was approximately 60 mg g^{-1}. The lowest adsorption performance was observed for KOH activated samples, with an average adsorption capacity of approximately 42 mg g^{-1}. Samples activated with H_3PO_4 and citric acid exhibited moderate adsorption performance.

The higher adsorption performance of H_2SO_4 activation can be attributed to sulfuric acid due to the strong dehydration effect during carbonization, resulting in a more developed pore structure. Oxygen-containing surface functional groups formed during H_2SO_4 activation may enhance electrostatic interactions with cationic methylene blue molecules.

In contrast, excessive pore expansion or partial collapse of the carbon structure may occur during KOH activation at high temperatures, resulting in lower adsorption capacity.

The highest adsorption capacity obtained in the study was 78.5 mg g^{-1}, achieved in H_2SO_4 activated carbon prepared at 525°C, with a 30-min activation time, and a 0.1 impregnation ratio. This result suggests that low impregnation rates may be suitable for effective pore formation.

Evaluation of process parameters using the Box–Behnken experimental design

A Box-Behnken experimental design was applied to investigate the effect of activated carbon production parameters on adsorption performance. The three parameters considered to have the greatest impact on adsorption performance were identified as temperature, activation time, and impregnation ratio. Accordingly, a range of 450–600 °C for temperature, 30–90 min for time, and 0.1–0.5 for the impregnation ratio was selected (Table 2).

Table 2. Box-Behnken experimental design plan for activated carbon production

Run	Temperature (°C)	Time (min)	Impregnation ratio
1	450	30	0.3
2	600	30	0.3
3	450	90	0.3
4	600	90	0.3
5	450	60	0.1
6	600	60	0.1
7	450	60	0.5
8	600	60	0.5
9	525	30	0.1
10	525	90	0.1
11	525	30	0.5
12	525	90	0.5
13	525	60	0.3
14	525	60	0.3
15	525	60	0.3

The experimental results show that adsorption capacity is significantly influenced by the process parameters. In general, increasing the activation temperature improved adsorption performance by promoting pore formation. However, excessively high temperatures had the opposite effect, causing pore collapse in some samples and consequently reducing adsorption capacity.

Similarly, increasing the activation time did not always lead to a linear increase in adsorption capacity. In some cases, longer carbonization times resulted in a reduction of the active surface area, thereby limiting adsorption performance.

The results also indicated that the impregnation ratio played an important role in determining adsorption performance. While more balanced pore development is achieved at low impregnation ratios, excessive chemical degradation of the carbon structure may occur at high impregnation ratios.

The RSM model did not adequately represent the adsorption system. The nonlinear behavior of the system may be associated with the combined effects of pore structure, surface functional groups, carbonization degree, and adsorbent–adsorbate interactions. These results suggest that classical RSM approaches may be insufficient for modeling complex adsorption systems involving multiple interactions.Therefore, machine learning approaches were adopted to better model the adsorption system.

Machine learning modeling of adsorption performance

Due to the limitations of the classical RSM approach, machine learning methods were evaluated to model adsorption performance.. In this context, linear model (LM), support vector machine (SVM), GLMNET, and random forest (RF) algorithms were compared.

The performance results for the evaluated models are shown in Figure 2. Among the evaluated models, RF demonstrated the highest predictive performance, with an R^2 of 0.7295 and an RMSE of 5.3159.

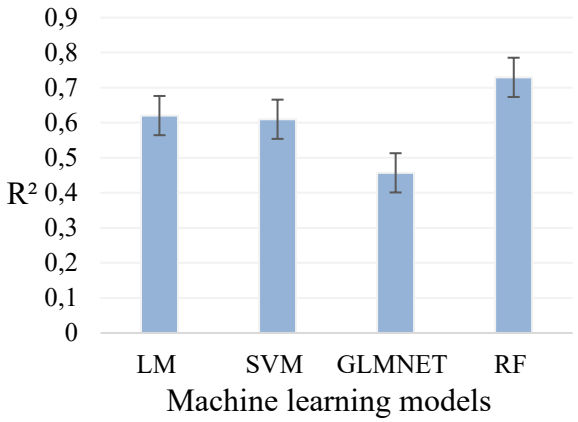

Figure 2. Comparison of machine learning model performances based on R^2 values.

Unlike traditional statistical models, the Random Forest model has yielded more successful results because it can more effectively model the complex, nonlinear interactions between process parameters and adsorption capacity. The optimum production conditions were determined as follows:

- H_2SO_4 activation,
- 0.1 impregnation ratio,
- 525–600 °C temperature range,
- 60–90 min activation time.

These results indicate that machine learning approaches can provide more reliable predictions for complex adsorption systems.

Iodine number analysis of selected activated carbons

The activated carbon samples exhibiting the highest methylene blue adsorption performance were examined in greater detail using iodine number analysis to evaluate the development of microporosity. The resulting iodine number values are presented in Figure 3.

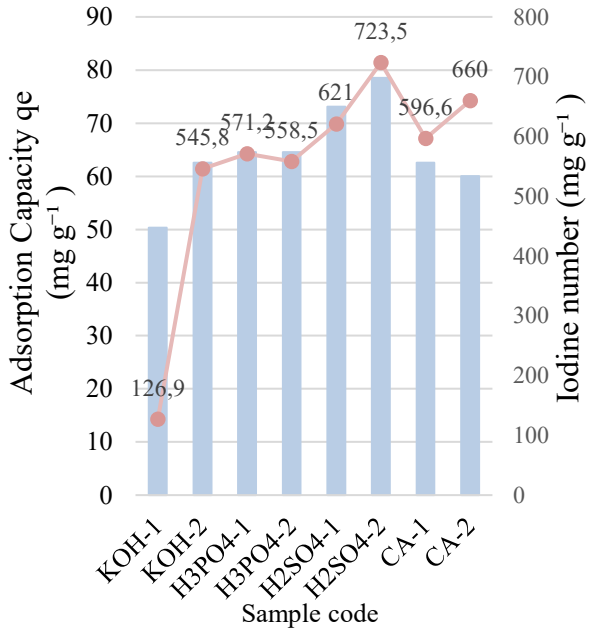

Figure 3. Comparison of adsorption capacity and iodine number values of selected activated carbon samples.

The iodine number values of the samples range from 126.9 to 723.5 mg g^{-1}. The highest iodine number was obtained from the sample activated with H_2SO_4, and this result indicates that activation with H_2SO_4 promotes the formation of micropores.

Owing to their small size, iodine molecules are primarily adsorbed in micropores. Therefore, high iodine numbers are generally associated with high micropore volume and increased surface area.

The results generally indicate a parallel relationship between the iodine number and the methylene blue adsorption capacity. However, it was found that this relationship is not entirely linear. Since methylene blue molecules are larger in size compared to iodine molecules, it is believed that the mere presence of micropores is insufficient. It is believed that mesopores and an appropriate pore size distribution are also important for the effective adsorption of methylene blue. The fact that the adsorption capacity remains limited in some samples despite a high iodine number may be due to the pore entrances not being sufficiently accessible to large dye molecules. These results demonstrate that the coexistence of micro- and mesopores is important in dye adsorption applications.

BET surface area analysis

The textural properties of the selected activated carbon samples were determined using nitrogen adsorption–desorption analyses. The micropore and BET surface area results for the samples are presented in Table 3. It is observed that the BET surface areas of the samples range from 5.17 to 87.90 m^2/g. The highest BET surface area of 87.90 m^2/g was obtained for the H_2SO_4-1 sample, followed by the H_3PO_4-2 (65.71 m^2/g) and CA-2 (54.98 m^2/g) samples. The lowest surface areas were determined for the KOH-1 and KOH-2 samples.

Table 3. Textural properties of activated carbon samples determined by BET analysis

Sample code	BET surface area (m^2/g)	Micropore area (m^2/g)
KOH-1	5.17	–
KOH-2	5.66	1.04
H_3PO_4-1	10.72	0.84
H_3PO_4-2	65.71	41.69
H_2SO_4-1	87.90	59.81
H_2SO_4-2	22.60	6.49
CA-1	40.33	15.40
CA-2	54.98	36.94

When the BET results were evaluated in conjunction with iodine number analyses, a direct relationship was not observed between the two methods. Although the highest BET surface area and micropore area were obtained for the H_2SO_4-1 sample, the highest iodine number was determined for the H_2SO_4-2 sample. This suggests that iodine adsorption is influenced not only by the total surface area but also by the pore size distribution and surface properties. However, it can be stated that samples with high BET surface areas generally exhibit more developed pore structures and support adsorption performance.

In conclusion, the H_2SO_4-1 sample exhibited the most advanced textural properties among the studied samples due to its highest BET surface area and micropore area.

Comparison with literature

The adsorption capacity and iodine number results obtained in this study were compared with

those reported in the literature for biomass-based activated carbons (Table 4).

The methylene blue adsorption capacity of activated carbons derived from Gypsophila roots ranged from 50 to 78 mg g^{-1}, showing similar performance to sawdust-based activated carbons. However, lower capacity values were obtained compared to highly porous activated carbons derived from certain biomass sources such as coconut shells, rice husks, and corn cobs.

Table 4. Comparison of biomass-derived activated carbons reported in the literature

Precursor	Activation	MB adsorption (mg g^{-1})	Iodine number (mg g^{-1})	Ref.
Various biomass	Chemical / thermal	30–50	500–1200	[7]
Sawdust	$ZnCl_2$	78	650	[20]
Gypsophila (This study)	Chemical activation	50–78	546–723	*This work*
Corn cob	KOH	92	850	[21]
Rice husk	H_3PO_4	104	720	[22]
Coconut shell	Steam activation	120–150	900–1100	[23]

The iodine number values, fell within the typical range reported in the literature for biomass-based activated carbons. In particular, the fact that the highest iodine number was at a level similar to that of rice husk-based activated carbon indicates successful microporous development.

The results obtained demonstrate that *Gypsophila* roots are a suitable, low-cost, and sustainable biomass source for activated carbon production.

CONCLUSION

In this study, activated carbon was successfully produced from *Gypsophila* roots using a chemical activation method. The adsorption performance of the produced activated carbons was evaluated using methylene blue.

It was determined that the activation agent had a significant effect on adsorption performance. Among the chemicals examined, the highest adsorption capacity was obtained in samples activated with H_2SO_4. The highest adsorption capacity was determined to be 78.5 mg g^{-1}, and this value was obtained from a sample prepared at 525 °C, with an activation time of 30 minutes and an impregnation ratio of 0.1.

The effects of process parameters were evaluated using a Box–Behnken experimental design. However, it was determined that the classical RSM approach could not adequately represent the adsorption behavior due to the system's nonlinear nature.

For this reason, various machine learning models were applied, and the best predictive performance was achieved using the Random Forest model. For the RF model, the R^2 value was calculated as 0.7295 and the RMSE value as 5.3159.

It was observed that the iodine number analysis applied to the selected samples yielded results similar to those obtained from methylene blue adsorption following H_2SO_4 activation. BET analysis revealed that H_2SO_4-1 possessed the highest BET surface area (87.90 m^2 g^{-1}) and micropore area (59.81 m^2 g^{-1}), indicating the development of a more porous structure compared with the other activated carbons.

The results indicate that *Gypsophila* roots are a low-cost and sustainable biomass source for activated carbon production. Furthermore, it was determined that machine learning methods constitute an effective approach for modeling complex adsorption systems.

Future studies are recommended to focus on enhancing mesopore formation, investigating adsorption performance with different pollutants, and testing in real-world wastewater applications.

Author contributions: *All authors have accepted responsibility for the entire content of this manuscript and approved its submission.*

Conflict of interest: *The authors state no conflict of interest.*

REFERENCES

1. H. Jawad, N. F. H. Mamat, B. H. Hameed, K. Ismail, *J. Environ. Chem. Eng.*, **7** (2), 102965 (2019), doi: 10.1016/J.JECE.2019.102965.
2. L. Zhai, Z. Bai, Y. Zhu, B. Wang, W. Luo, *Chin. J. Chem. Eng.*, **26** (3), 657 (2018), doi: 10.1016/J.CJCHE.2017.08.015.
3. T. Robinson, G. McMullan, R. Marchant, P. Nigam, *Bioresour. Technol.*, **77** (3), 247 (2001), doi: 10.1016/S0960-8524(00)00080-8.
4. W. Tan, A. L. Ahmad, B. H. Hameed, *Chemical Engineering Journal,* **137** (3), 462 (2008), doi: 10.1016/J.CEJ.2007.04.031.
5. A. Demirbas, *J Hazard Mater,* **167** (1-3), 1 (2009), doi: 10.1016/J.JHAZMAT.2008.12.114.
6. M. Ghazoui, R. Elkacmi, A. S. Sylla, K. Moulakhnif, I. Touzani, O. Boudouch, *Desalination Water Treat.,* **318**, 100378 (2024), doi: 10.1016/J.DWT.2024.100378.

7. G. Crini, *Bioresour. Technol.,* **97** (9), 1061 (2006), doi: 10.1016/J.BIORTECH.2005.05.001.
8. M. J. Martin, A. Artola, M. D. Balaguer, M. Rigola, *Chemical Engineering Journal,* **94** (3), 231 (2003), doi: 10.1016/S1385-8947(03)00054-8.
9. S. Rengaraj, S. H. Moon, R. Sivabalan, B. Arabindoo, V. Murugesan, *Waste Management*, **22** (5), 543 (2002), doi: 10.1016/S0956-053X(01)00016-2.
10. S. Senthilkumaar, P. R. Varadarajan, K. Porkodi, C. V. Subbhuraam, *Colloid Interface Sci.,* **284** (1), 78 (2004), doi: 10.1016/J.JCIS.2004.09.027.
11. A. H. El-Sheikh, A. P. Newman, H. K. Al-Daffaee, S. Phull, N. Cresswell, *J. Anal. Appl. Pyrolysis,* **71** (1), 151 (2004), doi: 10.1016/S0165-2370(03)00061-5.
12. F. C. Wu, R. L. Tseng, R. S. Juang, *J. Hazard. Mater.,* **69** (3), 287 (1999), doi: 10.1016/S0304-3894(99)00116-8.
13. F. C. Wu, R. L. Tseng, R. S. Juang, *Journal of Environmental Science & Health Part A*, **34** (9), 1753 (1999), doi: 10.1080/10934529909376927.
14. G. Burak ÇAM, *Graduate School of Natural and Applied Sciences*, (2010).
15. G. İpek, B. Gürbüz, *Journal of Agricultural Engineering*, **359**, 26 (2012).
16. M. Korkmaz *et al.*, *Journal of Biological Sciences Research*, **5** (2), 111 (2012), [Online].
17. E. Sezik, *Ankara Journal of Faculty of Pharmacy*, 41 (1982), doi: 10.1501/Eczfak_0000000277
18. H. Özçelik, B. Yıldırım, *SDÜ Journal of Forestry*, 57 (2011).
19. D. C. Montgomery, *Mycol. Res.*, **106** (11), 1323 (2017), [Online].
20. P.K. Malik, *J. Hazard. Mater.*, **113**. 81 (2004), doi: 10.1016/j.jhazmat.2004.05.022.
21. S. Yorgun, D. Yıldız, *J. Taiwan Inst. Chem. Eng*., **53**, 122 (2015), doi: 10.1016/j.jtice.2015.02.032
22. D. Kalderis, S. Bethanis, P. Paraskeva, E. Diamadopoulos, *Bioresour. Technol.,* **99**, 6809 (2008), doi: 10.1016/j.biortech.2008.01.041.
23. O.Ioannidou, A. Zabaniotou, *Renew. Sustain. Energy Rev*., **11**, 1966 (2007), doi: 10.1016/j.rser.2006.03.013.

Bulgarian Chemical Communications, Volume 58, Issue 3 (pp. 359-364) 2026 *DOI: 10.34049/bcc.58.3.D021*

Production and characterization of a double-layered wound dressing containing electrospun polylactic acid and hypericum-infused alginate hydrogel

S. Kahraman[1]*, E. Özbey[2], S. Uzun[2], F. U. Nigiz[2]

[1]*Çanakkale Onsekiz Mart University, School of Graduate Studies, 17100, Merkez/Çanakkale, Türkiye*
[2]*Çanakkale Onsekiz Mart University, Chemical Engineering Department, 17100, Merkez/Çanakkale,Türkiye*

Accepted: July 28, 2026

This study presents the development of a double-layered, natural-based wound dressing designed to enhance healing and reduce infection risk. The aim is to combine key dressing properties—moisture retention, high absorption capacity, optimal porosity, and antimicrobial activity—within a synergistic structure. The outer layer was fabricated from polylactic acid (PLA) *via* electrospinning. Characterization results revealed a highly porous structure (>85%) and a contact angle of 128°, indicating hydrophobic behavior that provides an effective barrier against external fluids while maintaining gas permeability. Mechanical testing demonstrated a tensile strength of approximately 4 MPa, ensuring sufficient durability for practical applications. Morphological analyses using scanning electron microscopy (SEM) and optical microscopy confirmed uniform nanofiber distribution and structural integrity, while Fourier-transform infrared (FTIR) analysis verified the preservation of PLA's chemical structure after electrospinning. The inner layer consists of an alginate-based hydrogel, selected for its excellent moisture retention and biocompatibility. This layer was functionalized with Hypericum perforatum extract at concentrations ranging from 1% to 4%. Swelling studies showed that the 2% extract formulation exhibited the highest swelling capacity (652%), along with improved flexibility and reduced hardness. FTIR results confirmed the successful incorporation of the extract into the hydrogel matrix. Overall, the combination of mechanically robust PLA nanofibers and bioactive, highly absorbent hydrogel demonstrates a promising double-layered wound dressing with potential applications in advanced wound care and tissue engineering.

Keywords: Alginate hydrogel, Bilayer wound dressing, Electrospinning, *Hypericum perforatum* extract, Polylactic acid

INTRODUCTION

Skin is the largest organ of the human body and acts as the first protective barrier against external pathogens, mechanical injuries, and environmental stressors. Damage to skin tissue caused by burns, surgical interventions, trauma, or chronic diseases may disrupt this barrier and significantly increase the risk of infection and delayed healing. Therefore, the development of advanced wound dressing materials capable of accelerating tissue regeneration while preventing microbial contamination has attracted considerable attention in recent years [1, 2].

An ideal wound dressing should maintain a moist environment, absorb excess wound exudate, permit oxygen exchange, prevent bacterial invasion, and possess sufficient mechanical integrity [3]. Traditional wound dressings such as cotton gauze often fail to provide these multifunctional properties because of their low bioactivity and poor moisture management capacity [4]. Consequently, modern wound care approaches increasingly focus on bioactive and multifunctional dressing systems that can mimic the extracellular matrix (ECM) and support cellular activities during healing [5].

Electrospun nanofibrous membranes have emerged as promising materials for wound healing applications due to their high porosity, interconnected structure, and large surface-area-to-volume ratio [6]. These characteristics enable effective gas permeability, fluid management, and cell attachment while structurally resembling the native ECM [7]. Among biodegradable polymers, polylactic acid (PLA) has been extensively investigated because of its biodegradability, biocompatibility, non-toxicity, and favorable mechanical properties [8]. Electrospun PLA membranes additionally provide hydrophobic barrier properties that can protect wounds against external fluid penetration while maintaining adequate breathability [9].

Hydrogels are another widely studied class of wound dressing materials owing to their excellent swelling behavior, flexibility, and capacity to maintain a moist wound environment [10]. Sodium alginate, a naturally derived polysaccharide extracted from brown algae, is particularly attractive for biomedical applications due to its biocompatibility, non-toxicity, and mild gelation ability in the presence of divalent cations such as

* To whom all correspondence should be sent:
E:-mail Seniyecan18@gmail.com

© 2026 Bulgarian Academy of Sciences, Union of Chemists in Bulgaria

Ca^{2+} [11]. Alginate hydrogels can efficiently absorb wound exudates and promote tissue regeneration through their soft and hydrated structure [12].

Recently, increasing attention has been directed toward incorporating natural bioactive compounds into wound dressings to improve antibacterial and healing performance. *Hypericum perforatum* L. (St. John's Wort) is a medicinal plant known for its antimicrobial, antioxidant, anti-inflammatory, and tissue regenerative activities [13]. The therapeutic effects of *Hypericum* extract are mainly associated with bioactive compounds such as hypericin, hyperforin, and flavonoids [14]. Previous studies have demonstrated that *Hypericum*-based formulations can enhance fibroblast proliferation, collagen formation, and wound contraction while reducing microbial growth [15, 16].

Although electrospun nanofibers and hydrogel systems have individually demonstrated promising wound healing performance, studies focusing on bilayer structures that combine the protective advantages of electrospun PLA membranes with the bioactive and highly absorbent characteristics of *Hypericum*-loaded alginate hydrogels remain limited. Therefore, the present study aims to develop and characterize a double-layered wound dressing composed of an electrospun PLA outer layer and a *Hypericum* extract-incorporated alginate hydrogel inner layer. The structural, chemical, mechanical, swelling, wettability, and antibacterial properties of the developed system were comprehensively investigated to evaluate its potential for advanced wound care applications.

EXPERIMENTAL

Materials

Polylactic acid (PLA 2003D, Mw: 120,000–160,000 g/mol) was procured from NatureWorks. Dimethylformamide (DMF) and chloroform ($CHCl_3$) were acquired from Isolab (Turkey). Methanol, ethanol, sodium alginate (alginic acid sodium salt, Sigma-Aldrich, CAS No: 9005-38-3), and polyethylene glycol 400 (PEG 400) were purchased from Merck Chemicals (Turkey). St. John's Wort extract (*Hypericum perforatum* L.) was obtained from Selen Biokimya (Istanbul, Turkey) with lot number S007.R40101.G0034.231220.

Fabrication of electrospun PLA membranes

The outer protective layer of the bilayer wound dressing was produced using an electrospinning machine (IDASONIC NanoWeaver®-Pro). A polymer solution was prepared by dissolving 12.5 wt% PLA in a solvent system consisting of DMF and chloroform (70% chloroform by volume) and stirred for 4 h at 50 °C to ensure complete dissolution. To improve the fiber morphology and act as a pore forming agent, 20 wt% PEG 400 (relative to the PLA weight) was incorporated into the homogeneous solution and stirred at room temperature [17]. The electrospinning process was conducted under optimized conditions to ensure bead-free and uniform nanofibers. The solution was fed at a constant flow rate of 0.02 mL/min through a syringe pump. A high voltage of 18 kV was applied, and the distance between the needle tip and the flat aluminum collector was maintained at 18 cm. The production was carried out for 15 min to reach the desired membrane thickness. Figure 1 shows a schematic diagram of the formation of the outer layer of the PLA electrospun fiber *via* the electrospinning process.

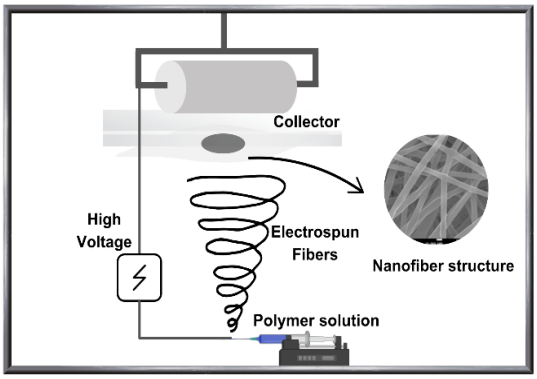

Figure 1. Schematic illustration of the electrospinning setup used for producing the protective PLA outer layer of the bilayer wound dressing.

Preparation of alginate hydrogels containing Hypericum extract

The inner healing layer, composed of sodium alginate (SA) hydrogel, was enriched with varying concentrations of St. John's Wort extract. A1% (w/v) SA solution was initially prepared in distilled water at 50 °C. The St. John's Wort extract was dissolved in a 70:30 ethanol-water mixture and added to the SA solution at ratios ranging from 1% to 4% (v/v). The mixture was then homogenized using an ultrasonic homogenizer to ensure uniform distribution of the plant extract. The solution was cast into petri dishes and ionically cross-linked via the dropwise addition of 0.03 M $CaCl_2$. Following the gelation process, the hydrogels were washed with methanol to eliminate unreacted residues and rinsed three times with distilled water to remove excess Ca^{2+} ions and remaining solvents [18]. The visual appearances of the prepared hydrogels are shown in Figure 2, where A0 represents the pure alginate (control), and A1, A2, A3, and A4

correspond to the hydrogels enriched with 1%, 2%, 3%, and 4% *Hypericum* extract, respectively.

Figure 2. Physical appearance of the synthesized hydrogel samples: Pure alginate (A0) and *Hypericum* extract-incorporated alginate hydrogels (A1–A4).

RESULTS AND DISCUSSION

The surface morphology and structural characteristics of the electrospun membranes were evaluated using scanning electron microscopy (SEM) and optical microscopy. Figure 3 presents the SEM and optical microscope images of the PLA membrane at various magnification ratios. The SEM analysis reveals that the PLA membrane possesses high porosity, a homogeneous fiber distribution, and well-maintained structural integrity. Furthermore, the absence of significant beading indicates that the electrospinning parameters were optimally selected. High-magnification SEM images show that the fibers have a smooth and even surface, forming an interconnected, porous network structure. These properties contribute to the membrane's gas and water vapor permeability while providing a barrier behavior that restricts liquid passage. The optical microscope images corroborate the fibrous and porous architecture observed in the SEM analysis, confirming a homogeneous overall surface and structural continuity. The fibers are randomly but stably distributed, with no excessive concentration or dilution in specific regions, indicating a successful production process. The obtained bead-free and uniformly distributed PLA nanofibers are consistent with previous electrospinning studies reported in the literature. Similar smooth and interconnected PLA nanofibrous structures were observed by Abrigo *et al*. [7], who stated that optimized electrospinning parameters significantly improve fiber homogeneity and porosity, which are essential for wound healing applications.

The chemical structures and functional groups of the PLA membranes and bioactive hydrogels were identified using Fourier transform infrared spectroscopy (FTIR), as presented in Figure 4. For the alginate-based hydrogels (A0–A4), the broad absorption band between 3200–3500 cm^{-1} is attributed to the stretching vibrations of hydroxyl (OH^-) groups, indicating the polysaccharide nature and water content within the alginate chains.

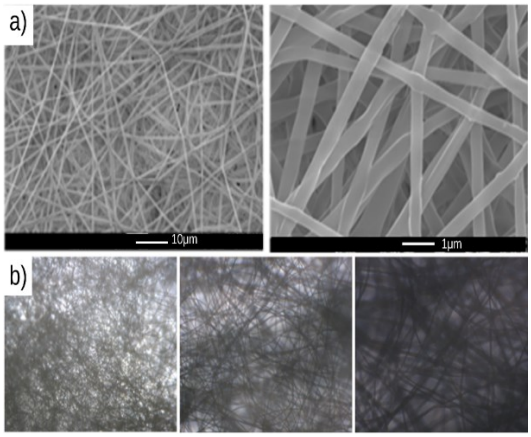

Figure 3. SEM (a) and optical microscopy (b) images of electrospun PLA membranes.

The characteristic peaks at 1600 cm^{-1} and 1000–1100 cm^{-1} correspond to the carboxylate groups (-COO^-) and the C–O–C stretching of the G and M blocks, respectively [19]. With increasing concentrations of *Hypericum* extract (A1–A4), a notable increase in peak intensity at 1400 cm^{-1} was observed, suggesting enhanced interactions between the phenolic components of the extract and the alginate carboxyl groups. The intensified OH^- band in the enriched samples further confirms the successful integration of the extract through hydrogen bonding [20]. Regarding the PLA membrane, the intense and sharp peak at 1750–1760 cm^{-1} represents the C=O stretching, serving as the primary evidence for the ester structure of PLA. The range of 1080–1185 cm^{-1}, known as the "fingerprint region," shows strong C-O and C-O-C asymmetric vibrations characteristic of PLA [8]. Peaks at 2995 cm^{-1} and 2945 cm^{-1} correspond to asymmetric and symmetric -CH stretching, while the broad, weak peak at 3400–3600 cm^{-1} is attributed to the -OH stretching of the PEG 400 chain ends. The results indicate that the high-voltage electrospinning process and solvent evaporation did not lead to chemical degradation or undesired side reactions.

The swelling tests of pure (A0) and *Hypericum* extract-incorporated (A1–A4) alginate hydrogels were evaluated, and the results are summarized in Figure 5. All samples exhibited a time-dependent increase in their swelling ratios, reaching equilibrium within 24 h. This behavior is primarily attributed to the high hydrophilicity of the alginate polymer chains, while the $CaCl_2$ cross-linking mechanism effectively regulated the overall water absorption capacity. The addition of *Hypericum* extract significantly altered the swelling performance.

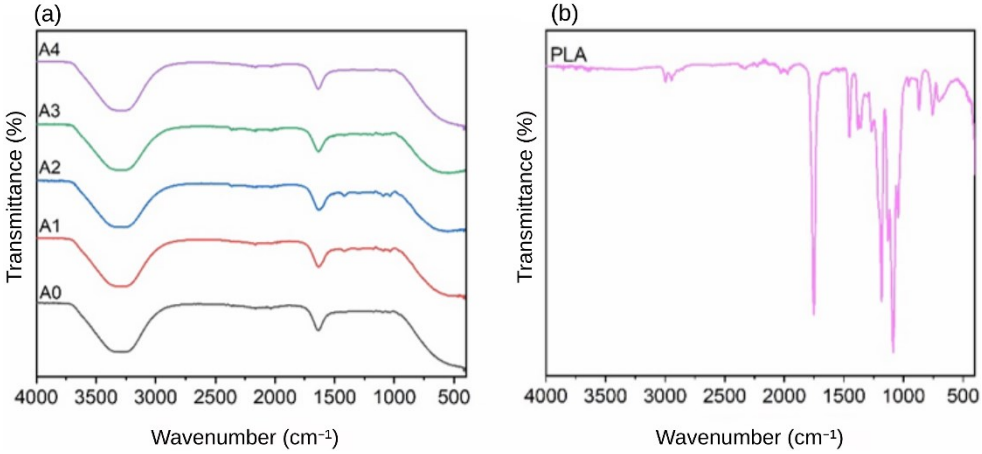

Figure 4. FTIR spectra of (a) *Hypericum* extract-incorporated alginate hydrogels and (b) electrospun PLA membranes.

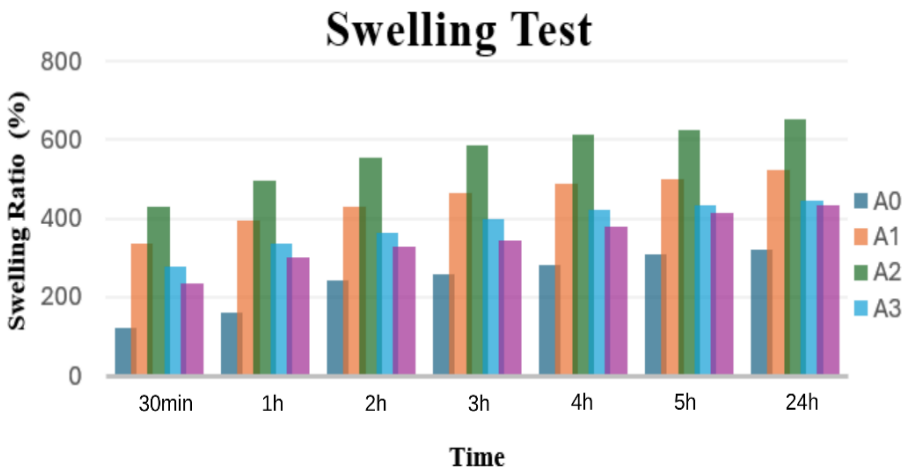

Figure 5. Percent swelling ratios of hydrogel samples at different time intervals

The A2 formulation (2% extract) achieved the highest swelling ratio of 652%. This enhancement is likely due to the phenolic and flavonoid components within the extract forming additional hydrogen bonds, which expand the hydrogel matrix and facilitate water uptake. However, a decrease in swelling was observed at higher concentrations (A3 and A4). This reduction stems from increased molecular interactions and enhanced Ca^{2+} binding activity, leading to a more densely packed and rigid network. This tighter structure restricts water diffusion into the matrix, thereby limiting the total swelling capacity. The high swelling behavior of alginate-based hydrogels is mainly associated with the hydrophilic hydroxyl and carboxyl groups present in the polymer backbone. Similar swelling trends were reported by Ahmed [10], who demonstrated that hydrogel swelling capacity strongly depends on crosslinking density and polymer-network flexibility. The enhanced swelling observed in the A2 formulation may be attributed to the phenolic compounds in *Hypericum* extract, which likely increased intermolecular spacing and water uptake capacity.

The structural properties of the electrospun PLA membranes were evaluated through swelling and porosity tests. The membranes exhibited a high average porosity of 85.35%, indicating a fibrous and open-pore architecture produced via the electrospinning process. This high porosity level ensures that fluids can easily diffuse into the inter-fiber voids. Furthermore, the membranes demonstrated a significant average swelling ratio of 507.22%, which confirms the high specific surface area and porous morphology of the nanofibrous structure [6,17]. A direct correlation was observed between the porosity and swelling behavior; higher porosity provides more internal void volume, thereby enhancing the water retention capacity of the membrane. These results indicate that the PLA outer layer possesses the necessary morphological features to support gas exchange while effectively managing fluid interactions at the wound site.

The mechanical performance of the electrospun PLA membranes was evaluated to determine their structural suitability for wound dressing applications. The membranes, with an average thickness of 0.06 mm, exhibited a tensile strength of

4 MPa. During the tensile tests, the samples demonstrated significant elongation before failure, reaching a strain value of 1.348. This high strain indicates a ductile mechanical behavior, where the nanofibers rearrange and distribute the applied load gradually rather than failing abruptly. Such mechanical durability and flexibility are essential for maintaining the integrity of the dressing while conforming to the dynamic contours of the wound site [21, 22]. The surface wettability of the PLA outer layer was characterized by contact angle measurements to evaluate its protective barrier function. The membrane exhibited a high contact angle of 128°, confirming its hydrophobic nature. This hydrophobicity is attributed not only to the intrinsic chemical properties of the PLA but also to the rough, fibrous morphology created by the electrospinning process [17]. In a bilayer system, this hydrophobic outer layer serves as a controlled barrier that protects the wound from external liquid contaminants while simultaneously preserving the moist microenvironment provided by the underlying *Hypericum*-incorporated alginate hydrogel.

The antibacterial performance of the electrospun PLA membranes was evaluated using the agar disk diffusion method against Gram-negative *Escherichia coli* (*E. coli*) and Gram-positive *Staphylococcus aureus* (*S. aureus*). The membranes exhibited a distinct inhibition zone with a diameter of 1.4 cm against E. coli. The fact that the inhibition zone was larger than the membrane diameter indicates that the active components effectively diffused into the agar medium, preventing bacterial growth beyond the immediate contact area. In contrast, no inhibition zone was observed against S. aureus. This suggests that while the membrane possesses significant antibacterial efficacy against Gram-negative bacteria, its activity against Gram-positive strains was limited under the tested conditions. These results demonstrate that the PLA-based layer contributes to the wound dressing's protective function by inhibiting specific bacterial growth, thereby reducing the risk of infection at the wound site [17, 22, 23]. Figure 6 shows the antibacterial test.

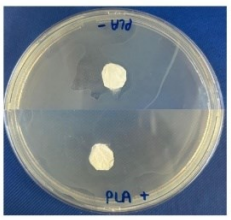

Figure 6. Antibacterial activity test

The mechanical hardness of the hydrogels was measured using a texture analyzer, and the results are presented in Table 1. The peak force required to compress the samples was recorded as the hardness value. The pure alginate hydrogel (A0) exhibited a hardness of 0.49 kg. The addition of *Hypericum* extract led to a decrease in hardness, with the A2 sample (2% extract) showing the minimum value of 0.36 kg. This trend suggests that the extract components may interfere with the Ca^{2+} cross-linking process, resulting in a more compliant network. However, at higher concentrations (A4), the hardness slightly recovered to 0.44 kg, which may be attributed to a more crowded molecular environment hindering deformation [10, 11].

Table 1. Hardness values of the hydrogel formulations.

Sample code	*Hypericum* extract concentration (%)	Hardness (kg)
A0	0	0.49
A1	1	0.43
A2	2	0.36
A3	3	0.39
A4	4	0.44

The color properties of the hydrogel samples were evaluated based on the CIELAB (L*, a*, b*) color space, and the results are summarized in Table 2. The incorporation of *Hypericum* extract significantly altered the transparency and optical characteristics of the alginate hydrogels. Pure alginate (A0) exhibited the highest brightness (L*) value, while a substantial decrease was observed in all extract-incorporated samples. The lowest L* value was recorded for the A2 formulation, indicating that the extract components interact with the polymer matrix to absorb or scatter light, thereby reducing light transmittance. The a* (redness) and b* (yellowness) values reached their peak in the A1 sample, which is directly correlated with the natural pigments found in the *Hypericum* extract [20, 24]. The total color difference (ΔE) for the enriched samples (A1–A4) ranged between 32.15 and 38.59 relative to the control group (A0). The maximum ΔE value was observed in the A2 sample, suggesting that a 2% concentration induces the most significant morphological and chemical color transition. The stabilized ΔE values observed in A3 and A4 indicate that a color saturation point is reached beyond a certain extract concentration.

Table 2. *Hypericum*-alginate color test

Alginate code	L*	a*	b*	ΔE
A0	55.74	0.8	0.38	2.85
A1	28.4	8.67	14.39	32.15
A2	18.37	4.01	8.7	38.59
A3	22.48	2.95	4.66	33.74
A4	23.09	3.16	6.71	33.49

CONCLUSION

In this study a bioactive bilayer wound dressing consisting of an electrospun PLA outer layer and a *Hypericum* extract-incorporated alginate hydrogel was successfully developed. The PLA layer provided a protective hydrophobic barrier with a 128° contact angle, high porosity (85.35%), and a tensile strength of 4 MPa. The A2 formulation (2% extract) emerged as the optimum inner layer, exhibiting the highest swelling capacity (652%) and improved flexibility. The electrospun PLA outer layer exhibited antibacterial activity against *E. coli*, whereas no inhibition zone was observed against *S. aureus.* FTIR analysis confirmed the stable integration of the extract into the matrix, while mechanical and color tests showed that the extract significantly influenced the structural and optical properties of the hydrogels. Overall, the synthesized bilayer system effectively combines protective barrier functions with high exudate management, making it a promising candidate for advanced wound care applications.

Acknowledgement: *This research was supported by the Çanakkale Onsekiz Mart University Scientific Research Projects Coordination Unit (BAP) under Grant Number FHD-2026-5584, and by the Scientific and Technological Research Council of Türkiye (TÜBİTAK) under the 2209-B Industry Oriented Research Project Support Programme for University Students (Grant Number 1139B412401793).*

REFERENCES

1. J. S. Boateng, K. H. Matthews, H. N. Stevens, G. M. Eccleston, *J. Pharm. Sci.*, **97**, 2892 (2008).
2. S. Dhivya, V. V. Padma, E. Santhini, *BioMedicine*, **5**, 22 (2015).
3. L. I. Moura, A. M. Dias, E. Carvalho, H. C. De Sousa, *Acta Biomater.*, **9**, 7093 (2013).
4. V. Jones, J. E. Grey, K. G. Harding, *BMJ*, **332**, 777 (2006).
5. S. A. Guo, L. A. DiPietro, *J. Dent. Res.*, **89**, 219 (2010).
6. N. Bhardwaj, S. C. Kundu, *Biotechnol. Adv.*, **28**, 325 (2010).
7. M. Abrigo, S. L. McArthur, P. Kingshott, *Macromol. Biosci.*, **14**, 772 (2014).
8. S. Farah, D. G. Anderson, R. Langer, *Adv. Drug Deliv. Rev.*, **107**, 367 (2016).
9. M. Liu, X. P. Duan, Y. M. Li, D. P. Yang, Y. Z. Long, *Mater. Sci. Eng. C*, **76**, 1413 (2017).
10. E. M. Ahmed, *J. Adv. Res.*, **6**, 105 (2015).
11. K. Y. Lee, D. J. Mooney, *Prog. Polym. Sci.*, **37**, 106 (2012).
12. J. Boateng, O. Catanzano, *J. Pharm. Sci.*, **104**, 3653 (2015).
13. Z. Saddiqe, I. Naeem, A. Maimoona, *J. Ethnopharmacol.*, **131**, 511 (2010).
14. A. Nahrstedt, V. Butterweck, *J. Nat. Prod.*, **73**, 1015 (2010).
15. B. Farasati Far, G. Gouranmohit, M. R. Naimi-jamal, E. Neysani, H. A. El-Nashar, M. El-Shazly, K. Khoshnevisan, *Phytother. Res.*, **38**, 3271 (2024).
16. N. Yildirim, İ. Küçük, *J. Fac. Eng. Archit. Gazi Univ.*, **35**, 1 (2020).
17. S. Kahraman, A. Katırcı, A. Aytaç, S. Veli, F. U. Nigiz, *Appl. Clay Sci.*, **268**, 107756 (2025).
18. H. Malektaj, A. Dec Drozdov, J. deClaville Christiansen, *Int. J. Mol. Sci.*, **24**, 5064 (2023).
19. G. Lawrie, I. Keen, B. Drew, A. Chandler-Temple, R. Rintoul, P. Fredericks, L. Grøndahl, *Biomacromolecules*, **8**, 2533 (2007).
20. M. Jarzębski, W. Smułek, H. M. Baranowska, Ł. Masewicz, J. Kobus-Cisowska, M. Ligaj, E. Kaczorek, *Food Hydrocoll.*, **104**, 105748 (2020).
21. X. Zhang, Y. Wang, Z. Gao, X. Mao, J. Cheng, L. Huang, J. Tang, *J. Appl. Polym. Sci.*, **141**, e54746 (2024).
22. J. Yang, L. Xu, *Materials*, **16**, 6021 (2023).
23. A. Pakolpakçıl, Z. Draczyński, J. Szulc, D. Stawski, N. Tarzyńska, A. Bednarowicz, B. Gutarowska, *Appl. Sci.*, **11**, 8219 (2021).
24. A. Gavan, L. Colobatiu, H. Hanganu, C. Bogdan, N. K. Olah, M. Achim, S. Mirel, *Processes*, **10**, 242 (2022).

Bulgarian Chemical Communications, Volume 58, Issue 3 (pp. 365-370) 2026 DOI: 10.34049/bcc.58.3.D022

Synthesis and *in vitro* characterization of quercetin-loaded alginate-keratin composite hydrogels for enhanced wound healing applications

S. Yiğit, T. E. Bektaş[2], S. Kahraman[2], F. Uğur Nigiz[2]*

[1]*Çanakkale Onsekiz Mart University, School of Graduate Studies, 17100, Merkez/Çanakkale, Türkiye*
[2]*Çanakkale Onsekiz Mart University Chemical Engineering Department, 17100, Merkez/Çanakkale,Türkiye*

Accepted: July 28, 2026

The effective management of cutaneous wounds remains a significant clinical challenge because traditional dressings, such as cotton gauze, often fail to maintain an optimal moisture balance, leading to secondary tissue trauma and delayed healing. This study details the synthesis and characterization of a novel hybrid hydrogel, formulated as a bioactive component for a multilayered wound dressing. The preparation protocol consisted of blending a 1% (w/v) sodium alginate solution, with a series of concentrations of keratin (1%; 2%; 3%) at 45 °C, before ionic cross-linking with $CaCl_2$. The delivery of an anti-oxidant and anti-inflammatory agent was achieved by loading quercetin (0.1%) within the matrix. Spectroscopic analysis by FTIR showed the successful entrapping of quercetin and the molecular stability of the compound was confirmed by the presence of the characteristic aryl ether (C-O-C) peak at 1271 cm-1. The swelling profile of the formulations demonstrated a maximum swelling ratio of 293% after 48 h with the optimum formulation (2%) showing an excellent rate of control over excess wound exudates. Following in vitro release into PBS of pH 7.4, an increase in keratin content was shown to influence the diffusion coefficient with the greatest release profile being achieved by the 3% keratin formulation. The alginate-keratin-quercetin hydrogel system presents a biocompatible, chemically stable and therapeutically active alternative for advanced wound care.

Keywords: Hydrogel, Sodium alginate, Keratin, Quercetin, Drug release, Wound care.

INTRODUCTION

Hydrogels, due to their three-dimensional network structure and high water retention capacity, are promising biomaterials for wound care applications, as they provide a moist environment and enable controlled drug delivery. Re-epithelialization is greatly accelerated by their innate capacity to provide a moist milieu at the site of injury, which also makes regulated medication administration possible [1]. Hydrogels are structurally incredibly versatile, with thicknesses varying from nanometers to centimeters. Additionally, they can conform to complex, irregular, and constrained wound geometries due to their exceptional deformability and relatively low shear modulus. Because of these special physicochemical characteristics, hydrogels are widely used as structural matrices in biomedical engineering, especially for pressure ulcers, severe burns, cutaneous blisters, and surgical wounds [2]. Hydrogels have a huge variety of structures and thicknesses, ranging from nanometers to centimeters. Their excellent deformability and relatively low shear modulus also allow them to conform to complex, irregular and constrained wound geometries. These unique physicochemical properties have made hydrogels widely used as structural matrices in biomedical engineering, especially for pressure ulcers, severe burns, cutaneous blisters, and surgical wounds [3].

In recent years, the development of drug-eluting wound dressings has significantly improved the clinical efficiency of these matrices. These technologies offer significant advantages over traditional delivery routes by maintaining appropriate plasma medication levels within a predefined therapeutic window over extended periods of time by directly incorporating therapeutic agents into the polymeric network [4]. Microbial infection is a major impediment to the physiological cascade of healing. Hydrogel dressings are often combined with antimicrobial and anti-inflammatory drugs to eradicate microorganisms from the wound bed and to reduce delays caused by infection [3]. Besides their great biocompatibility, hydrogel-based dressings are usually transparent, which enables medical professionals to non-invasively monitor the course of wound healing in real time without the need for painful or premature dressing changes [3]. To improve biological affinity and biodegradability, present research has turned to natural polymers such

* To whom all correspondence should be sent:
E-mail: *sezeryigit059@gmail.com*

© 2026 Bulgarian Academy of Sciences, Union of Chemists in Bulgaria

as chitosan and alginate. For instance, recent developments disclose the development of hybrid dressings based on alginate containing green-synthesized metallic nanoparticles, including copper, in addition to bioactive plant extracts [5]. The phytochemical profiling through liquid chromatography-mass spectrometry (LC-MS/MS) reveals that the phenolics, flavonoids, and glycosidic chemicals present in these natural extracts are very effective reducing and stabilizing agents while synthesis [5]. The exploitation of the synergistic potential of biopolymer matrices and natural bioactive compounds is essential for the development of next-generation multifunctional wound treatments.

EXPERIMENTAL

Materials

The functional biomaterial matrix was synthesized using sodium alginate as a main, non-toxic polymeric backbone for the controlled therapeutic delivery.

Keratin was added to the matrix as structural additive in different percentages of 1%, 2% and 3% (w/v) to improve biocompatibility and structural integrity. Encapsulation of a potent natural antioxidant, quercetin, at a defined concentration of 0.1% (w/v) was provided with bioactive healing properties to the composite system. Then, the alginate polymer chains were ionically cross-linked by using a 0.1 M calcium chloride ($CaCl_2$) solution to fabricate a flexible and mechanically stable three-dimensional hydrogel scaffold.

In Fig. 1, the aforementioned composite hydrogels (1K1A, 2K1A and 3K1A) were prepared by incorporating different levels of keratin into a constant 1% (w/v) sodium alginate suspension and entrapment of 0.1% (w/v) quercetin, at optimum pH. The ultimate architectural stabilization was achieved by salt-mediated ionic cross-linking with Ca^{2+}, converting the polymeric mixture into a resilient bioactive 3D matrix. Purification steps, and final controlled thermal drying at 45 °C were performed.

The first step in the preparation of the bioactive composite hydrogels was the preparation of the main polymer components. To maintain a constant baseline concentration of 1% (w/v), sodium alginate was continuously dissolved in deionized water, resulting in a homogeneous, viscous polymeric matrix (Fig. 2a). At the same time, different concentrations of 1%, 2%, and 3% (w/v) keratin stock solutions were prepared (Fig. 2b).

Hydrogel material preparation process

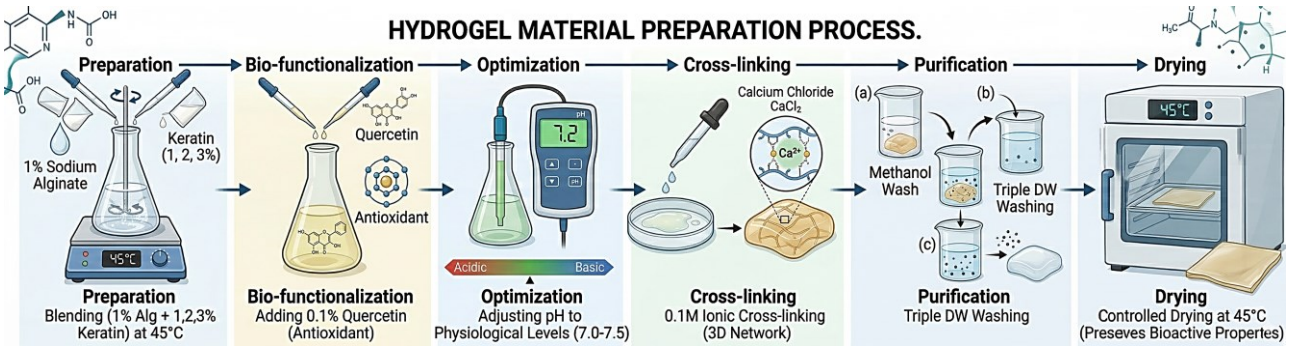

Figure 1. Hydrogel material preparation process.

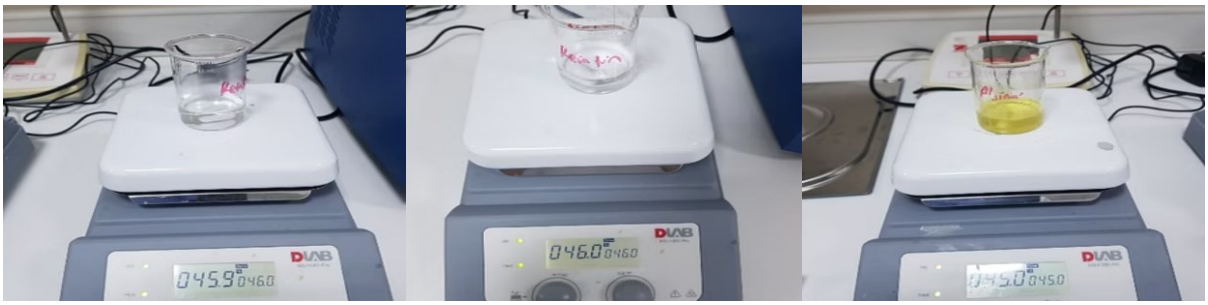

Figure 2. (a) 1% sodium alginate solution, (b) keratin solution, (c) mixture of all solutions with pH adjusted and 0.1% quercetin added

The different keratin solutions were methodically added to the fixed sodium alginate matrix under constant, regulated magnetic stirring to produce the hybrid polymeric matrices—designated as 1K1A, 2K1A, and 3K1A, respectively—to guarantee total structural homogeneity.

Quercetin was added to the composite mixes at a specific concentration of 0.1% (w/v) in order to give the scaffold medicinal effectiveness (Fig. 2c). This powerful natural polyphenol was chosen to reduce localized oxidative stress at the site of injury and quicken the physiological wound healing cascade. The dense polymer matrix in this engineered configuration performs two functions: it creates a convoluted pathway that controls the sustained, controlled release kinetics of the sensitive polyphenol while acting as a protective barrier to prevent oxidative degradation under harsh physiological conditions.

The pH of the solution was carefully optimized during the mixing process (Fig. 2c). This parameter must be controlled accordingly during the blending stage, as it is known to influence the compatibility of the blend with tissues, prevent the premature alkaline degradation of quercetin, and identify the optimal ionization of the functional groups implicated in the cross-linking process.

Standard neutralization of the blends was followed by ionic cross-linking of the liquid polymers to form a stable three-dimensional gel network. These hydrated alginate polymers can be cross-linked using divalent calcium ions. This commences with the immersion of the gels within a 0.1 M $CaCl_2$ clone solution whereupon the ionic calcium (Ca^{2+}) effectively forms ionic bridges between the blocks of neighboring alginate chains. The use of a 0.1 M concentration was chosen with the utmost care, as the higher concentrations (0.2 and 0.3 M) observed to lead to inhomogeneous, rapid curing of the polymer. This concentration was optimal for covalent gel formation, achieving the higher levels of cross-linking producing gel medium with an efficient quercetin encapsulation ability, while leaving the medium easily maneuvered for a prolonged, efficacious diffusion. After the cross-linking procedure, the hydrogels were filtered, treated with methanol, and then incubated for 30 min at 4 °C in a refrigerator to aid in precipitation and purification. Following the incubation period, the hydrogels were taken out of the refrigerator, washed once with methanol, and carefully cleaned three times with distilled water to get rid of any remaining ions and unreacted species. Structural scaffolds were created by drying the hydrogels in a controlled oven at 45 °C for 1 h in order to eliminate excess moisture without causing thermal degradation of the encapsulated bioactive chemicals. The final appearance and structural morphology of the obtained hydrogels are presented in Fig. 3.

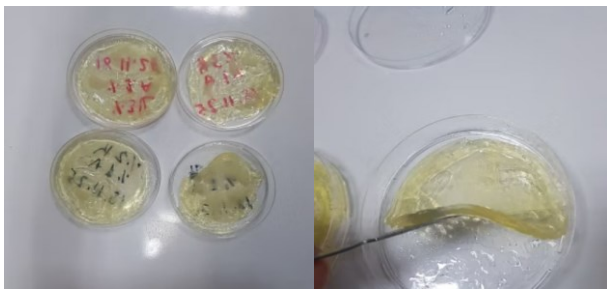

Figure 3. (a) The lower ones have 2% K%1A, and the upper ones have 3% K%1A; (b) These are hydrogels containing 1% keratin and 1% alginate.

RESULTS AND DISCUSSION

The synthesized alginate-keratin-quercetin composite hydrogels were comprehensively investigated for characterization and functional assessment to ascertain their suitability for advanced wound therapies, as schematically shown in Fig. 4. The experimental workflow includes swelling analysis, in vitro drug release techniques, and FTIR spectroscopy for the characterization of hydrogels.

The confirmation of the polymeric matrix at the molecular level, its macro-scale physical swelling behavior, and finally its functional drug release performance under physiologically simulated settings are all logical steps in the experimental workflow. It includes swelling analysis, *in vitro* drug release techniques, and FTIR spectroscopy for the characterization of hydrogels.

FTIR was used to determine the chemical structures and functional groups of the produced composite hydrogels.

The three critical spectral zones over which the experimental spectra were systematically analyzed were the hydroxyl area, the carbonyl/carboxylate region and the fingerprint region, all of which together provide a clear insight into the structural organization of the composite matrix.

- *Hydroxyl area (3000 3600 cm^{-1})* The stretched vibrations of the hydroxyl (–OH) groups are illustrated by the broad absorption between 3000 and 3600 cm^{-1}, as seen in Fig. 5. As keratin content increased from 1K1A to 3K1A formulations the broad OH band is significantly increased in both size and intensity. This is indicative of the formation of a dense network of inter-molecular hydrogen bonds involving the keratin functional groups, the backbone of the sodium alginate and the phenolic hydroxyl groups of quercetin [6].

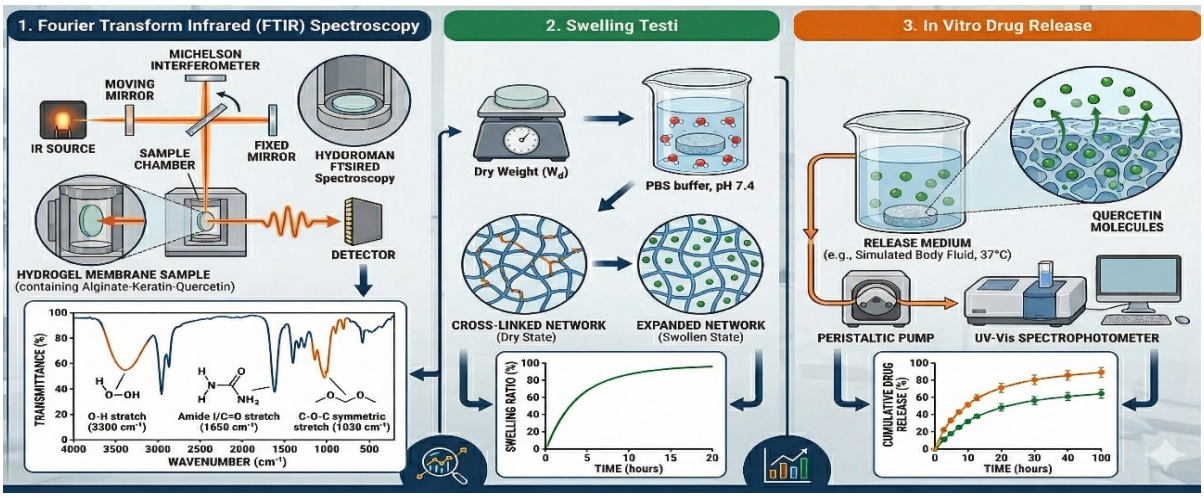

Figure 4. Characterization of hydrogels using; FTIR spectroscopy, swelling analysis, and *in vitro* drug release methods

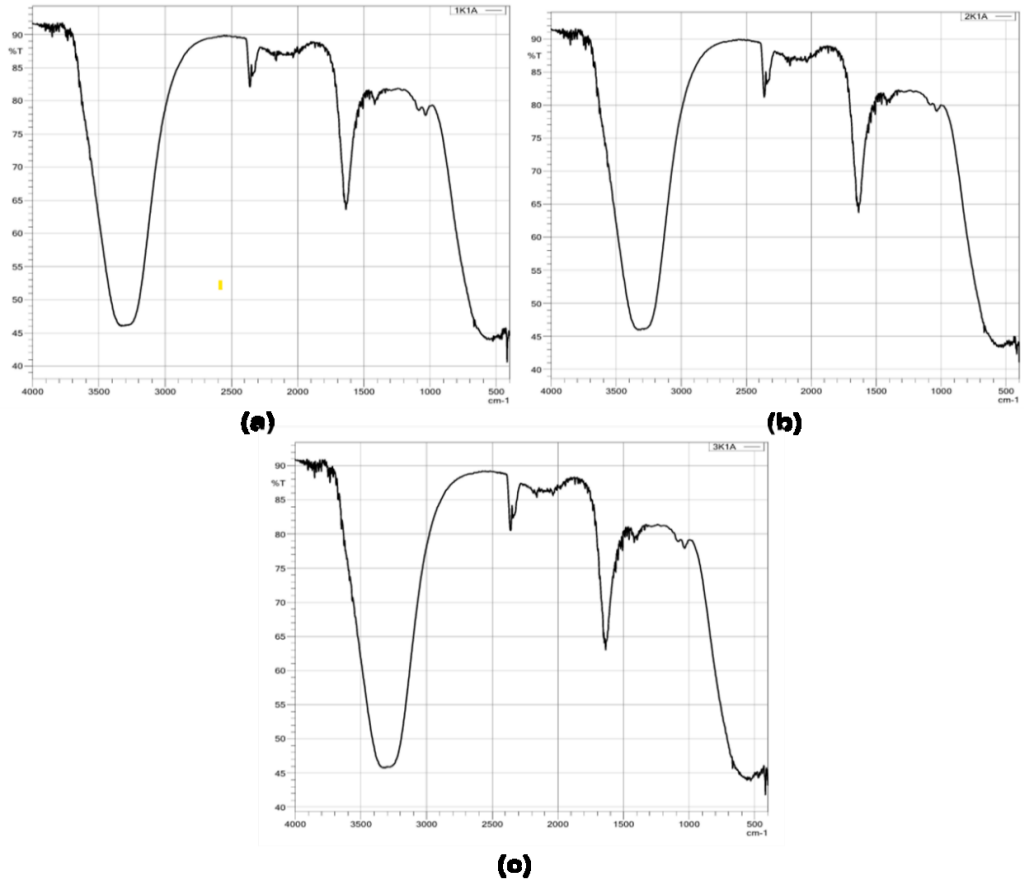

Figure 5. FTIR spectra of (a) 1K1A (1% keratin, 1% alginate), (b) 2K1A, and (c) 3K1A hydrogels.

- *At the carbonyl and carboxylate regions* (1500–1700 cm $^{-1}$) all alginate carboxylate peaks identified in these regions in Fig. 6 showed substantial displacements to higher wave numbers (blue shifts). These consistent modifications confirm the successful co-ordination and molecular mixing between biopolymer chains and consequently they are indicative of a change in the nearby ion environment. However, the encapsulated drug exhibited an interesting behavior in this same region; it appeared that even at the highest level of polymer loading, as evidenced by the 3K1A formulation (Fig. 6 c), the crystalline peaks of pure quercetin had become masked. The polyphenol was successfully entrapped within the polymer matrix at a molecular, amorphous level.

Table 1. Swelling test of 1K1A (1% keratin, 1% alginate), 2K1A, and 3K1A hydrogels.

Time	1%			2%			3%		
	Dry Weight (W0) (g)	Swollen Weight (W1)(g)	Swelling Ratio (%)	Dry Weight (W0) (g)	Swollen Weight (W1)(g)	Swelling Ratio (%)	Dry Weight (W0) (g)	Swollen Weight (W1)(g)	Swelling Ratio (%)
30 min	0,5821	1,1970	105,6348	0,5438	1,0672	96,2486	0,5270	1,1063	109,9241
1h	0,5548	1,4700	164,9603	0,5755	1,0581	83,8575	0,3920	0,8460	115,8163
2h	0,4557	1,1235	146,5438	0,5177	1,2965	150,4346	0,4281	0,9360	118,6405
3h	0,3738	0,8075	116,0246	0,4998	1,3115	162,4050	0,3200	0,8170	155,3125
4h	0,6110	1,0967	79,4926	0,6260	1,2304	96,5495	0,3838	0,8982	134,0281
5h	0,4195	0,7558	80,1669	0,5462	1,1375	108,2570	0,4432	0,7120	60,6498
6h	0,6763	0,9075	34,1860	0,4540	1,1680	157,2687	0,2480	0,5808	134,1935
24h	0,4305	0,9603	123,0662	0,5050	1,2900	155,4455	0,5167	1,2537	142,6360
48h	0,4890	1,0675	118,3027	0,4920	1,9380	293,9024	0,4843	1,1180	130,8486

- *The fingerprint region* provides the strongest evidence of drug loading and chemical stability. The most direct evidence of chemical loading and stability within the polymeric matrix is a well-defined prominent peak at 1271 cm^{-1}, a characteristic aryl ether (C–O–C) stretching vibration. The similar representation of this peak in the 1K1A, 2K1A and 3K1A spectra confirms the bioactive compound maintained chemical stability inside the polymeric matrix in the course of loading and polymerization processes, since there is an absence of this particular signal within free alginate. The relative intensity of this peak increased linearly with increased drug loading, providing further confirmation of its use as a reliable indicator of drug loading and structural stability [7]. It becomes more intense as the drug concentration increases. To summarize our FTIR results, we see three major phenomena: broadening of the OH band which indicates improved physical stability, shift and masking of the drug peaks provides evidence that the drug is encapsulated in our system, and finally the baseline insertion of the 1271 cm^{-1} peak shows that quercetin is indeed present and chemically stable [6].

Swelling ratio and water absorption capacity measurements were performed to evaluate the structural features (such as polymer network structure) of the biopolymer composite hydrogels. The dried hydrogels were weighed to determine the initial weight (W_0). The samples were then immersed in distilled water for periods ranging from 30 minutes to 48 hours, after which the swollen weight (W_1) was measured. The swelling percentage was calculated using the following formula:

$$Percentage\ Swelling\ (\%) = \left(\frac{W_1 - W_0}{W_0}\right) \times 100$$

The hydration profiles varied considerably depending on the exact keratin concentration, as summarized in the quantitative data presented in Table 1. The changing biopolymer ratios yielded distinct performance behaviors for each formulation:1% keratin, fluctuating swelling was observed throughout the testing time. Apart from some clinical situations which require an initial fast drug release profile upon first contact with moisture, the relatively weak network stability may impede its broad use 2% keratin, The matrix demonstrated an optimum initial balance between overall hydrophilicity and structural elasticity, with a maximum swelling ratio of 293% at 48 h. 2% keratin matrix is the most desirable one for further application in advanced wound dressing purpose as it harbors fluid well without any compromise in the matrix structure. 3% keratin swelling behavior was very stable and well-controlled for this gel. For certain biomedical applications requiring a higher degree of mechanical strength and structural durability, the dense network structure of the macromolecules provides a great advantage by restricting rapid water transport [8].

According to the swelling experiments (Table 1), the formulation with 2% keratin is the ideal option for wound care, when fluid absorption is crucial, while the formulation with 3% keratin is the pick when some degree of structure needs to be preserved [9].

In vitro drug release, test for quercetin release once removed from the hydrogel, 0.5 g of the hydrogel was introduced to 10 m L of PBS (pH 7.4). To observe and monitor the release of quercetin, samples of 1 m L were taken at 15, 30, and 45 min, then in hours from 1 5 h and in half-hour time periods between 2 and 5 h. The samples were diluted with ethanol and spectrophotometric analysis was then conducted at 370 nm. All caps were covered with aluminum.

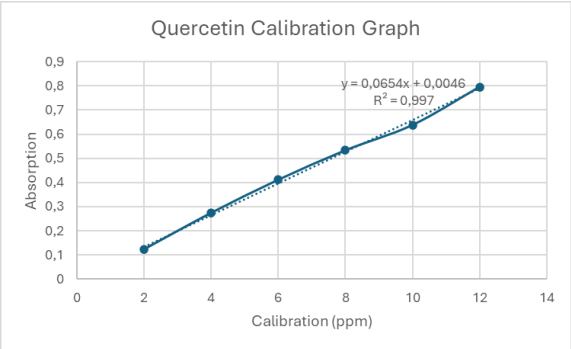

Figure 6. Quercetin calibration graph.

Table 2. Calculation of the concentration values of hydrogels containing 1% (w/v), 2% (w/v), and 3% (w/v) keratin.

	Absorption			Concentration (ppm)		
Time	1%	2%	3%	1%	2%	3%
15m	0,573	0,703	0,800	8,697	10,671	12,164
30m	0,504	0,723	0,928	7,636	10,990	14,124
45m	0,612	0,761	0,935	9,280	11,566	14,226
1h	0,573	0,711	0,930	8,693	10,798	14,154
2h	0,596	0,702	0,964	9,046	10,663	14,665
3h	0,621	0,747	0,886	9,427	11,344	13,472
4h	0,622	0,823	0,880	9,447	12,508	13,378
5h	0,595	0,604	0,759	9,034	9,157	11,534

The absorbance data demonstrated that there was a continuous release of quercetin from polymer matrix. However, fluctuations in concentration indicate quercetin's oxidative instability under physiological conditions. According to Table 2, release is time-dependent and positively correlated with keratin content (1% < 2% < 3%), with the 3% (w/v) formulation yielding the highest release. While increasing keratin concentration enhanced the release rate, observed fluctuations highlight the drug's oxidative instability. The profile exhibited an initial burst release followed by a more controlled release phase. However, fluctuations in concentration indicate quercetin's oxidative instability under physiological conditions [10].

CONCLUSION

In this study, we successfully created a set of sodium alginate-keratin composite hydrogels that are bioactive and loaded with quercetin, specifically designed for advanced wound care. The results demonstrate that by varying the biopolymer ratios, the scaffolds' structural performance may be precisely adjusted. Interestingly, the formulation stabilized with 2% (w/v) keratin achieved an excellent swelling capacity of 293%, providing the perfect hydrophilic balance needed to control wound exudates while maintaining the proper moisture content at the injury site. As demonstrated by the masking of its distinctive spectral peaks, FTIR analysis verified that quercetin was successfully and thoroughly entrenched inside the cross-linked networks of the 1K1A and 2K1A samples.

Importantly, the distinct presence of important phenolic groups in the spectra demonstrates that the polyphenol's strong antioxidant ability was unaffected by the encapsulation process. The unique protein-drug synergy seen when the keratin concentration was raised is one of the study's main highlights. Strong connections between the drug molecules and the protein chains in the 3K1A matrix effectively reduced the rate of diffusion. The gradual swelling and structural deterioration of the keratin network in this particular structure directly controls the therapeutic release profile, enabling a highly controlled and prolonged delivery phase. When combined, these findings show that these composite hydrogels offer a very flexible, biocompatible platform. The interaction between the proteins and the medications appears to be favored by an increase in keratin content, which effectively lowers the drug's diffusion rate. It is also this connection that makes the hydrogel more stable, which explains why the pharmaceuticals within have longer biological activity. Consequently, hydrogels with a high keratin concentration may be viable options for treating wounds.

Strong connections between the drug molecules and the protein chains in the 3K1A matrix effectively reduced the rate of diffusion.

Acknowledgement: *This research was supported by the Çanakkale Onsekiz Mart University Scientific Research Projects Coordination Unit (BAP) and Grant Number FBA-2025-5202.*

REFERENCES

1. K. Modi, M. Modi, D. Mishra, P. Mittal, U. Sorathiya, P. Shelat, *Int. Res. J. Pharm.*, **4**(3), 1 (2013).
2. J. H. Lee, Y. Yeo, *Chem. Eng. Sci.*, **125**, 120 (2015).
3. R. G. Erfan, Wound dressings: Current advances and future directions, Wiley Online Library, 2019.
4. J. S. Boateng, K. H. Matthews, H. N. Stevens, G. M. Eccleston, *J. Pharm. Sci.*, **97**, 2892 (2008).
5. H. Ngoc-Dung, N. Minh, Y. Ngu, D. Le Hang, *J. Appl. Polym. Sci.,* **141**, e54201 (2024).
6. M. Jarzębski, W. Smułek, H. M. Baranowska, Ł. Masewicz, J. Kobus-Cisowska, M. Ligaj, E. Kaczorek, *Food Hydrocoll.*, **104**, 105748 (2020).
7. G. Lawrie, I. Keen, B. Drew, A. Chandler-Temple, R. Rintoul, P. Fredericks, L. Grøndahl, *Biomacromolecules*, **8**, 2533 (2007).
8. E. M. Ahmed, *J. Adv. Res.,* **6**, 105 (2015).
9. S. Kahraman, A. Katırcı, A. Aytaç, S. Veli, F. U. Nigiz, *Appl. Clay Sci.,* **268**, 107756 (2025).
10. N. Dossi, et al., *Molecules*, **23**(11), 3020 (2018).

Bulgarian Chemical Communications, Volume 58, Issue 3 (pp. 371-377) 2026 *DOI: 10.34049/bcc.58.3.D023*

Investigation of the correlation between skin permeation and global reactivity descriptors in phenolic antioxidants: a comparative DFT and ADMET study

B. Kemanci[1], S. Kurumoglu[1]*, B. Gurkan[2]

[1]*Namik Kemal University, Department of Chemistry, Tekirdag, Turkey*
[2] *Gebze Technical University, Department of Physics, Gebze, Turkey*

Accepted: July 28, 2026

In the present work the relationship between the skin permeation potential and global reactivity descriptors of four structurally different phenolic compounds, namely ethyl guaiacol, carvacrol acetate, caffeic acid and syringic acid, is explored. Molecular geometries were optimized at the B3LYP/6-311G(d,p) level of density functional theory (DFT). The global reactivity descriptors such as chemical hardness, softness and electrophilicity index were obtained from the frontier molecular orbitals (FMO). The percutaneous permeability coefficients, pharmacokinetic parameters and toxicological profiles were predicted through SwissADME and ProTox-3.0 computational platforms. Marked difference in skin permeability was observed for the alkylated/esterified derivatives as compared to the carboxylic acid analogues. Carvacrol acetate and ethyl guaiacol exhibited higher permeability, whereas caffeic and syringic acids exhibited poor barrier penetration. DFT analysis revealed low chemical hardness and less dipole moments as important electronic factors for diffusion through lipophilic *stratum corneum*. All compounds were predicted to be in Toxicity Class 4 or 5, which confirms their safety for topical applications. Results demonstrate that skin permeability is not only determined by lipophilicity, but also by intrinsic electronic 'softness'. This "Quantum-Permeability" concept provides a predictive approach for the rational design of bioactive molecules for cosmeceutical and transdermal drug delivery systems. The study also shows the utility of DFT with ADMET analysis for the evaluation of their pharmacological potential.

Keywords: ADMET, skin permeation, antioxidants, DFT, electronic reactivity, quantitative surface descriptors

INTRODUCTION

Herbal-derived antimicrobial chemicals (phytochemicals are divided into three main groups; phenolic compounds, terpenes and alkaloids. These compounds have beneficial antioxidant, antibacterial, and antifungal activities and, when combined with antibiotics, can act as effective resistance-altering agents [1]. Phenolic compounds with antioxidant activity are one of the main substances formed as a result of secondary metabolism of plants [2]. Polyphenols, an important subgroup within phytochemicals, are structurally characterized by their inclusion of one or more phenolic units and are among the most abundant antioxidants in the human diet [3]. Polyphenols have been proposed as one of the most effective functional components with anti-aging properties due to their anti-inflammatory effects, their capacity to neutralize reactive oxygen species (ROS), absorb UV radiation and interact with dermal enzymes involved in connective tissue reconstruction [4]. Naturally occurring antioxidants offer remarkable medical applications in wound healing. But the encapsulation of these phytochemical components their natural properties such as low molecular weight, poor water solubility and inadequate skin permeability, has always been challenging [5]. For example, syringic acid (SA) is a phenolic acid found in abundance and is derived from olives, spices, grapes, dates and other plants. SA has been proven to have biological effects in a variety of diseases due to its anti-inflammatory, antioxidant and antitumor properties [6]. In one study, a high SA% ratio was observed in different skin layers with limonene-based SA-NE and did not cause dermal irritation. A preclinical study also showed that limonene-based SA-NE was effective in alleviating psoriasis-like skin lesions and against psoriasis caused by imiquimod in rats [7].

Caffeic acid (CA), its protective mechanism, includes direct free radical cleansing and inhibition of nuclear factor kappa-B (NF-isab)-driven pro-inflammatory pathways; this helps to collectively protect skin cells from UV-induced oxidative stress and MMP-mediated ECM degradation [8]. The human skin can be affected by a wide range of ailments ranging from inflammatory diseases to skin cancer, and no effective treatment has been found for many of them. In particular, some studies have

* To whom all correspondence should be sent:
E-mail: *skurumoglu@nku.edu.tr*

© 2026 Bulgarian Academy of Sciences, Union of Chemists in Bulgaria

shown the potential of CA in the treatment of inflammatory pathologies of the skin, such as psoriasis. Moreover, thanks to its antioxidative power, CA can photocorrotect against DNA damage, protecting the skin from aging and preventing melanoma [9]. Similarly, ferulic acid is a powerful antioxidant with scientifically proven skin care effects. However, the instability of this active ingredient in skin care products has restricted its wide use in the beauty and skin care industries. The average particle size of ferulic acid-laden nanocapsules is optimized at <300 nm [10]. Caffeic acid is also a powerful antioxidant molecule that is difficult to apply through the skin due to its low solubility and little stability. Franz cell results showed that caffeic acid diffusion from ethosomes was 18 times slower than solid lipid nanoparticles [11]. Dermal absorption is defined as the transport of substances from the outer surface of the skin into the skin and into the circulatory system. This process is divided into penetration (introduction to a specific layer), permeability (penetration from one layer to another) and resorption (intake to the vascular system) [12]. Topical and transdermal drug administration is an effective, safe and preferred way of administering drugs. Therefore, skin permeability is one of the critical parameters to consider in the process of drug discovery and development. Various in vitro, in vivo and ex vivo test systems have been developed to assess drug retention and skin permeability in the skin layers [13]. The benefits of transdermal delivery of active ingredients include a comparatively large absorption surface area and non-invasiveness. The lipophilicity and molecular size of these compounds have a major impact on the permeability of the active ingredient. Compounds having molecular weight less than 600 may be able to get through the skin's lipophilic barrier [14].

Fatty acid vesicles (FAVs) have lately gained interest as a substitute for conventional delivery methods including liposomes and synthetic polymers. Since FAVs are composed of fatty acids (such oleic acid) and non-ionic stabilizers rather than the phospholipids and cholesterol found in liposomes, they have clear advantages for cutaneous distribution. Fatty acid intermolecular hydrogen bonds and hydrophobic interactions are primarily responsible for their stability, which may provide formulation advantages [15]. Since caffeic acid is characterized by its antioxidant potential but also has high instability, its encapsulation appears to be an interesting strategy. Etosomes are produced by adding water to the solution of phosphatidylcholine ethanol under magnetic mixing. Ethanol also increases the passage of drugs through the skin from topical formulations. Although it is well known that ethanol penetrates the skin and increases the permeability of both polar and non-polar molecules, the mechanism to increase permeability is not fully explained [16]. One of the more straightforward and all-encompassing methods for transdermal drug delivery (TDD) is the use of chemical penetration enhancers (CPEs), which are preferred in topically administered formulations. These are compounds that interact with intracellular lipids or proteins in the *stratum corneum* (*SC*) (lipid-protein cleavage theory) or facilitate the drug's percutaneous penetration by rapidly and reversibly boosting the drug's solubility in *SC* lipids [17].

In *in vitro* permeability studies, vertical Franz diffusion cells are often used to assess the permeability of drugs through the skin or other biologically relevant membranes [18]. Diffusion cell is a simple test that can reliably measure in vitro and *ex vivo* drug release from topical preparations such as creams, ointments, liposome formulations and gels [19]. In recent years, computational methods have emerged as powerful tools to explain the hidden mechanisms of skin diseases and advance discoveries concerning current treatments. Overall, the integration of computational chemistry into dermocosmetic research has tremendous potential to accelerate the discovery and development of innovative treatments to improve skin health and address dermatological problems [20].

One of the most applicable and versatile of existing theories in its field is the density functional theory (DFT) which provides an understanding of chemical selectivity through the study of properties of a compound. This method facilitates the explanation of the reactivity of simple and complex systems without a detailed explanation of the reaction pathway [21]. The chemical reactivity of a molecule has been defined through various concepts, such as electronegativity, chemical hardness and softness along with the principle of equalization, and the hard-soft acid-base principle [22]. For example, the free radical scavenging activity of a phenolic antioxidant *via* the HAT reaction can be assessed by measuring the bond dissociation enthalpy (BDE) associated with the homolytic breakage of the O-H bond to form stable phenolic radicals [23]. Propolis contains a naturally occurring phenolic chemical molecule called caffeic acid phenethyl ester (CAPE). By blocking the free radicals of DPPH, peroxide, carboxyl, and hydroxide, CAPE's antioxidant activity is determined. The B3LYP/6-31+G* technique is used to calculate CAPE's performance on free radicals. Caffeic acid phenethyl ester

(CAPE) may have a potent antioxidant impact on the aforementioned radicals, according to the data [24].

Estimating the skin permeability of chemicals is very time consuming and expensive. There are also many ethical challenges associated with human and animal testing for the assessment of skin permeability. Experimental evaluation of ADMET-related traits may be a time-consuming and costly process that requires extensive animal experiments at the early stage of drug discovery [25]. Quantitative structure-activity/toxicity relation (QSAR/QSTR) models can be used to estimate the physicochemical properties of compounds, even for undiagnosed compounds [26].

The main originality of this study; it gives a new perspective to the literature by linking the skin permeability potential not only through classical physicochemical descriptors (logP, TPSA) but with quantum mechanical based global reactivity parameters. While percutaneous transition is usually analyzed by empirical methods, the electronic structure of the molecules by DFT calculations performed at B3LYP/6-311G(d,p) level in this research; chemical hardness, softness and electrophilicity index were examined in depth through dynamic indicators. In particular, the correlation of low dipole moment and the decisive role of reduced chemical hardness in overcoming the lipophilic stratum corneum barrier by classical ADMET parameters provides a more precise and predictive set of criteria for the design of the cosmetological and transdermal drug. By considering both passive diffusion and the possibility of electronic interaction with the molecule's biological environment, this "Quantum-Passioned" approach develops a novel evaluation framework for the logical design of upcoming bioactive compounds.

Materıals and methods

Gaussian 09W software with the DFT/B3LYP approach and the 6-311++G(d,p) basis set was used to optimize molecules [27]. The basic dyes used to compute quantum chemical characteristics have had their molecular structures, optimized structures, and HOMO and LUMO orbitals characterized. The HOMO–LUMO energy gap values, including global softness (η), global softness (S), electronic chemical potential (μ), electrophilic index (Ψ), electronegativity (χ), ionization energy (IE), and electron affinity (EA), were roughly calculated using the following equations in terms of HOMO and LUMO orbital energies after the frontier molecular orbital (FMO) was used to estimate the E_{homo}(energy of the highest occupied molecular orbital) and E_{lumo} (energy of the lowest unoccupied molecular orbital [28].

To evaluate the biological correlation of these electronic parameters, pharmacokinetic profiles and skin permeability coefficients (logKp) were predicted using the SwissADME platform (https://www.swissadme.ch/index.php).

Toxicological safety profiles, including acute oral toxicity classes (Class 1-6) and organ toxicity parameters, were determined *via* the ProTox-3.0 computational database (https://tox.charite.de/protox3/). This integrated approach elucidates the relationship between molecular reactivity and percutaneous absorption potential on a quantum mechanical basis. following equations in terms of HOMO and LUMO orbital energies.

Quantitative surface descriptors, including the total surface variance (σ_{tot}^2) and molecular polarity index (MPI), were calculated using the Multiwfn software package (version 2026.3.27) [29-30] to evaluate the distribution and variability of the electrostatic potential on the molecular surface. These parameters were determined according to the quantitative analysis of molecular surfaces as described by Bulat *et al*. [31] and the fundamental roles of electrostatic potential established by Politzer and Murray [32].

Analysis was carried out on the 0.001 a.u. isodensity surface as defined by the van der Waals surface. The three-dimensional visualization of the ESP maps and surface projections were generated using UCSF ChimeraX (version 1.11.1) [33].

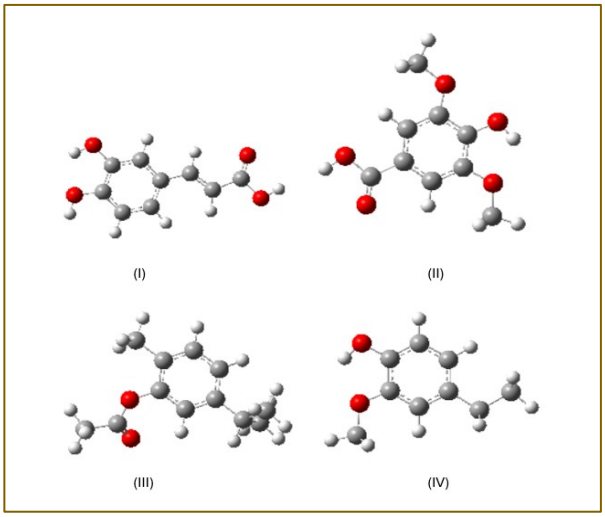

Figure 1. Optimized structures of (i) caffeic acid; (ıı) syringic acid; (ııı) carvacryl acetate; (ıv) ethylguaiacol (grey, C; white, H; red, O)

RESULTS AND DISCUSSION

The distribution of electrostatic potential on the surface of a molecule has a direct effect on the

electrostatic resistance that is met during passive transport. Caffeic acid has the highest total surface variance (σ_{tot}^2= 303.12 $kcal^2/mol^2$) and the highest molecular polarity ındex (MPI = 13.63 kcal/mol) of all the compounds we looked at. These quantitative results strongly support the strong charge polarization seen in Figure 2. High variance and MPI values indicate substantial interaction with the polar components of the skin's lipid matrix, leading to an electrostatic retention effect that obstructs efficient diffusion.

Conversely, ethylguaiacol and carvacryl acetate have the lowest values of variance on the surface (102.38 and 112.52, respectively).

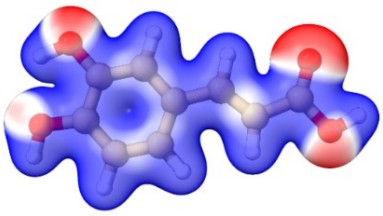

Figure 2. ESP map of caffeic acid projected onto their van der Waals (0.001 a.u. isodensity) surface

This structural feature appears as large electrostatic neutrality regions (white domains) in Figures 3 and 4. Particularly carvacryl acetate has the maximum nonpolar surface area (%73.15) and therefore is determined as the most compatible derivative for rapid transportation through lipophilic extracellular pathways.

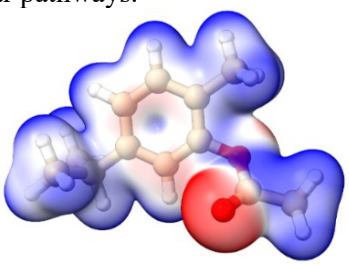

Figure 3. ESP map of carvacryl acetate projected onto their van der Waals (0.001 a.u. isodensity) surface

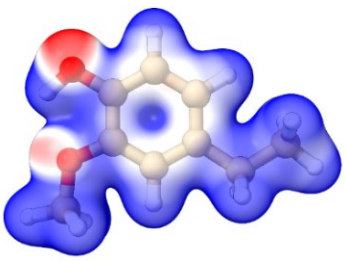

Figure 4. ESP map of ethylguaiacol projected onto their van der Waals (0.001 a.u. isodensity) surface

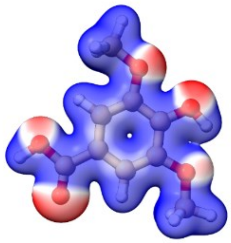

Figure 5. ESP map of syringic acid projected onto their van der Waals (0.001 a.u. isodensity) surface

The values of E_{HOMO}, E_{LUMO} and energy gap (ΔE) of the frontier molecular orbitals of the target compounds are presented in Figure 6. The E_{HOMO} levels range from -6.21 eV to -5.38 eV, with the higher position of ethylguaiacol indicating its greater ability to donate electrons. The calculated energy gaps also show a clear trend in chemical reactivity and kinetic stability, increasing from caffeic acid (4.19 eV) to syringic acid (4.70 eV), ethylguaiacol (5.69 eV) and finally carvacryl acetate (6.02 eV). These observations confirm the fact that the narrow HOMO-LUMO gap makes caffeic acid the most reactive species whereas the wider gap of carvacryl acetate indicates its better structural stability.

Global reactivity parameters were calculated using frontier molecular orbital energies according to the Koopmans' theorem. The chemical potential (μ) is the arithmetic mean of the energies of HOMO and LUMO, while the global hardness (η) is obtained by dividing the HOMO-LUMO energy difference by two. Using these two parameters, the value of the electrophilicity index (ψ) and that of global softness (S) were obtained. Additionally, some other electronic parameters such as electronegativity (χ), ionization energy (IE) and electron affinity (EA) were calculated using the frontier orbital energies.

The equations used in these calculations are stated as follows:

$$\mu = \frac{E_{\{HOMO\}}+E_{\{LUMO\}}}{2} \quad (1)$$

$$\eta = \frac{E_{\{HOMO\}}-E_{\{LUMO\}}}{2} \quad (2)$$

$$\psi = \frac{\mu^2}{2\eta} \quad (3)$$

$$S = \frac{1}{2\eta} \quad (4)$$

$$\chi = -\frac{E_{\{HOMO\}}+E_{\{LUMO\}}}{2} = -\mu \quad (5)$$

$$IE = -E_{\{HOMO\}} \quad (6)$$

$$EA = -E_{\{LUMO\}} \quad (7)$$

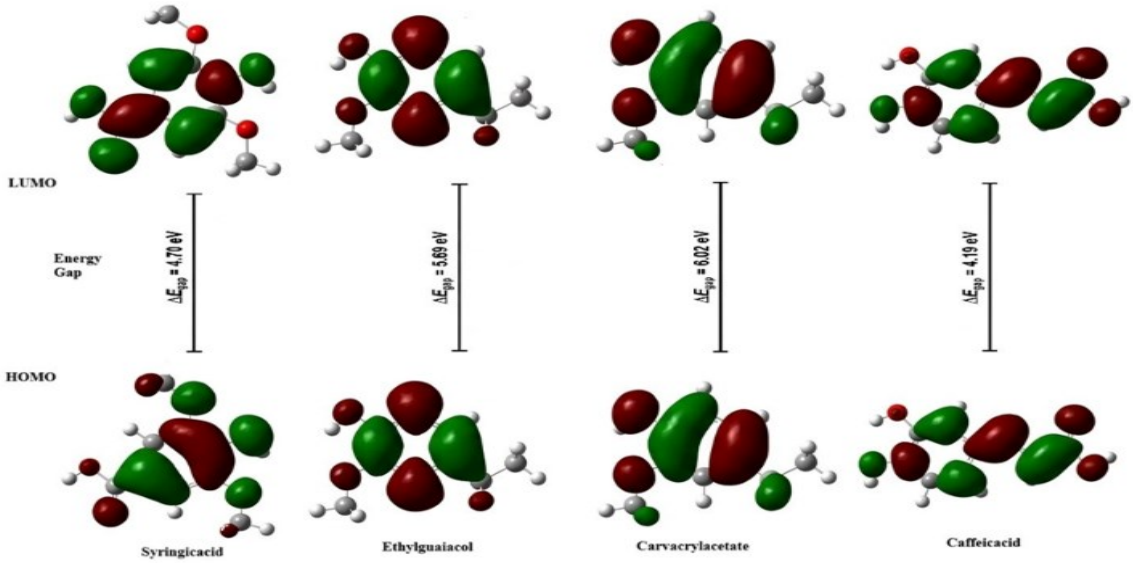

Figure 6. HOMO, LUMO and energy gap of optimized molecules

Table 1. Global reactivity descriptors of optimized molecules

Parameter (eV)	Caffeic acid	Syringic acid	Carvacryl acetate	Ethyl guaiacol
E_{HOMO}	-5.82	-5.67	-6.21	-5.38
E_{LUMO}	-1.63	-0.97	-0.19	+0.31
Energy gap	4.19	4.70	6.02	5.69
Electro-negativity (χ)	3.73	3.32	3.20	2.53
Global hardness (η)	2.10	2.35	03.01	2.84
Global softness (s)	0.48	0.43	0.33	0.35
Global electro-philicity index (Ψ)	3.31	2.34	1.69	1.13

The calculated global reactivity descriptors of the optimized molecules are shown in Table 1. Electronic descriptors displayed carvacryl acetate has the highest energy gap (Egap = 6.02 eV) and the highest Chemical Hardness (η = 3.01 eV) indicating higher chemical stability. Ethylguaiacol also has the smallest electrophilicity ındex (ω=1.13 eV) in the group. The low values of both ω and variance indicate a very low degree of non-specific interactions with the skin matrix, which makes possible passive permeability. Syringic Acid has an intermediate profile as suggested by the moderate variance (165.63) and MPI (12.85) values, which are consistent with the surface properties shown in Figure 5.

Table 2. Skin permeability of optimized molecules

Molecule	Log Kp cm/s	Consensus log Po/w	TPSA Å²
Caffeic acid	-6.58	0.93	29.46
Syringic acid	-6.77	0.99	26.30
Carvacrol acetate	-5.37	3.02	75.99
Ethyl gauaiacol	-5.81	2.02	77.76

The physicochemical parameters relevant to the absorption and permeability profiles of the target compounds are summarized in Table 2. The consensus lipophilicity (log Po/w) ranged from 0.93 to 3.02 with the most lipophilic species being carvacrol acetate (3.02) followed closely by ethyl guaiacol (2.02). The lipophilic behavior observed is also related to the skin permeability, where carvacrol acetate and ethyl guaiacol showed a higher diffusion capacity, with log Kp values of -5.37 and -5.81 cm/s, respectively. In contrast, the more hydrophilic nature of caffeic acid (0.93) and syringic acid (0.99) resulted in a notable decrease in their permeability coefficients (-6.58 cm/s and -6.77 cm/s). Additionally, the topological polar surface area (TPSA) values provided crucial insights into the molecular polarity, positioning ethyl guaiacol (77.76 Å²) and carvacrol acetate (75.99 Å²) as the structures with the most favorable surface properties among the evaluated group.

Table 3. Toxicology values of optimized molecules using SwissADME and Protox-3.0

Molecule	Rat acute toxicity (LD_{50} - mol/kg)	Max. tolerated dose (log mg/kg/day)	Skin sensitization
Caffeic acid	1.78	0.27	low
Syringic acid	1.95	1.75	low
Carvacrol acetate	1.89	1.01	low
Ethyl-guaiacol	1.99	0.88	low

The in silico toxicity endpoints evaluated for the studied compounds are compiled in Table 3. The acute toxicity in rats, quantified via LD50 values, followed the upward trend of caffeic acid (1.78 mol/kg) < carvacrol acetate (1.89 mol/kg) < syringic acid (1.95 mol/kg) < ethyl guaiacol (1.99 mol/kg). For the maximum tolerated dose (MTD), the values ranged significantly from 0.27 to 1.75 log mg/kg/day, where syringic acid emerged as the most well-tolerated structure (1.75 log mg/kg/day) and caffeic acid marked the lowest threshold (0.27 log mg/kg/day). Crucially, none of the molecules exhibited high dermatological risk, as all compounds displayed a low potential for skin sensitization. These toxicity indices collectively suggest that while dosage adjustments must consider the lower MTD of caffeic acid, the overall series maintains a promising safety profile.

CONCLUSION

This study investigated the passive diffusion mechanisms of selected phenolic compounds across the skin barrier using quantum chemical descriptors and quantitative electrostatic potential (ESP) surface analysis. The results underscore the critical influence of molecular surface electrostatic properties on permeation rates. Specifically, caffeic acid, characterized by high electrophilicity (ω) and total surface variance, exhibits substantial electrostatic resistance within the skin matrix. In contrast, carvacryl acetate and ethylguaiacol display electrostatically neutral profiles, indicated by low variance and high percentages of nonpolar surface area (73.15% and 59.76%, respectively), which facilitate their diffusion through lipophilic pathways. Structural modifications such as acetylation, exemplified by carvacryl acetate, were found to enhance skin barrier compatibility by increasing chemical hardness and reducing molecular polarity (MPI). Overall, total surface variance and the percentage of nonpolar surface area are proposed as effective predictors of the skin absorption potential of phenolic derivatives.

Acknowledgement: *The financial support provided by Tekirdag Namik Kemal University BAP unit through Project No. NKUBAP.64.GA.25.656 is gratefully acknowledged.*

REFERENCES

1. L. Dzurická, J. Hoová, B. Dribňáková, P. Skoumalová, P. Rappelli, I. Márová, *International Journal of Molecular Sciences*, **26**(19), 9485 (2025).
2. A. Butkeviciute, K. Ramanauskiene, V. Kurapkiene, V. Janulis, *Plants*, **11**(15), 1901 (2022).
3. D. H. Lee, J. W. Kim, R. Cong, J. S. Park, C. H. B. Nguyen, K. Park, ... S. M. Shim, *Journal of the Science of Food and Agriculture*, **105**(11), 6243 (2025).
4. A. L. Oliveira, D. Valente, H. R. Moreira, M. Pintado, P. Costa, *Colloids and Surfaces B: Biointerfaces*, **218**, 112779 (2022).
5. S. S. Hallan, F. Ferrara, R. Cortesi, M. Sguizzato, *Molecules*, **30**(3), 641 (2025).
6. S. Xiang, J. Xiao, *Experimental and Therapeutic Medicine*, **23**(1), 66 (2022).
7. N. Assalem, H. Abd-Allah, M. H. Ragaie, S. S. Ahmed, E. Elmowafy, *International Journal of Pharmaceutics*, **660**, 124376 (2024).
8. L. Liu, L. Zhang, Z. Liu, C. Tan, E. Lam, M. C. Ehrman, W. Ding, *Cosmetics*, **13**(1), 24 (2026).
9. S. S. Hallan, M. Sguizzato, P. Mariani, R. Cortesi, N. Huang, F. Simelière, E. Esposito, *Pharmaceutics*, **12**(8), 740 (2020).
10. S. Das, A. B. Wong, *Scientific Reports*, **10**(1), 12288 (2020).
11. S. S. Hallan, M. Sguizzato, M. Drechsler, P. Mariani, L. Montesi, R. Cortesi, E. Esposito, *Nanomaterials*, **11**(1), 171 (2021).
12. C. J. Kuster, J. Baumann, S. M. Braun, P. Fisher, N. J. Hewitt, M. Beck, M. Ernst, *Computational Toxicology*, **24**, 100242 (2022).
13. Y. W. Wu, G. H. Ta, Y. C. Lung, C. F. Weng, M. K. Leong, *Pharmaceutics*, **14**(5), 961 (2022).
14. A. Günther, E. Makuch, A. Nowak, W. Duchnik, Ł. Kucharski, R. Pełech, A. Klimowicz, *Molecules*, **26**(11), 3435 (2021).
15. X. Ma, Q. Zhang, Y. Yang, Y. Zhan, X. Zhang, Y. Zhao, J. Li, D. Wu, *Molecules*, **31**(1), 122 (2026).
16. R. Gupta, Y. Badhe, B. Rai, S. Mitragotri, *RSC Advances,* **10**(21), 12234 (2020).
17. H. Carreño, E. E. Stashenko, P. Escobar, *Molecules*, **28**(6), 2872 (2023).
18. R. S. Nair, N. Billa, A. P. Morris, AAPS *PharmSciTech*, **26**(5), 147 (2025).
19. M. Kumar, A. Sharma, S. Mahmood, A. Thakur, M. A. Mirza, A. Bhatia, *Journal of Dispersion Science and Technology*, **45**(5), 943 (2024).
20. L. El Bouamri, M. Bouachrine, S. Chtita, *Current Topics in Medicinal Chemistry*, **25**(6), 657 (2025).

21. C. Ramirez-Martinez, L. A. Zarate-Hernandez, R. L. Camacho-Mendoza, S. Gonzalez-Montiel, A. Meneses-Viveros, J. Cruz-Borbolla, *Computational and Theoretical Chemistry*, **1226**, 114211 (2023).
22. R. Pal, P. K. Chattaraj, *Journal of the Indian Chemical Society*, **98**(1), 100008 (2021).
23. R. Rohman, R. Nath, R. Kar, *Computational and Theoretical Chemistry*, **1223**, 114097 (2023).
24. K. Hachem, D. Bokov, L. Mahdavian, *Polycyclic Aromatic Compounds*, **43**(3), 2770 (2023).
25. Y. Wei, S. Li, Z. Li, Z. Wan, J. Lin, *Bioinformatics*, **38**(10), 2863 (2022).
26. R. Zeng, J. Deng, L. Dang, X. Yu, *Scientific Reports,* **11**(1), 10076 (2021).
27. M. J. Frisch, G. W. Trucks, H. B. Schlegel, G. E. Scuseria, M. A. Robb, J. R. Cheeseman, G. A. Montgomery Jr., T. Vreven, K. N. Kudin, J. C. Burant, J. M. Millam, S. S. Iyengar, J. Tomasi, V. Barone, B. Mennucci, M. Cossi, G. Scalmani, N. Rega, G. A. Petersson, H. Nakatsuji, M. Hada, M. Ehara, K. Toyota, R. Fukuda, J. Hasegawa, M. Ishida, T. Nakajima, Y. Honda, O. Kitao, H. Nakai, T. Klene, X. Li, J. E. Knox, H. P. Hratchian, J. B. Cross, C. Adamo, J. Jaramillo, R. Gomperts, R. E. Stratmann, O. Yazyev, A. J. Austin, R. Cammi, J. W. Ochterski, P. Y. Ayala, K. Morokuma, G. A. Voth, P. Salvador, J. J. Dannenberg, V. G. Zakrzewski, A. Dapprich, A. D. Daniels, M. C. Strain, O. Farkas, D. K. Malick, A. D. Rabuck, R. Raghavachari, J. B. Foresman, J. V. Ortiz, Q. Cui, A. G. Baboul, S. Clifford, G. Cioslowski, B. B. Stefanov, G. Liu, A. Liashenko, P. Piskorz, P. Komaromi, R. L. Martin, D. J. Fox, T. Keith, T. Al-Laham, C. Y. Peng, A. Nanayakkara, A. Challacombe, P. M. W. Gill, B. Johnson, W. Chen, M. W. Wong, C. Gonzalez, J. A. Pople, Gaussian 09, Revision C.01, Gaussian, Inc., Wallingford, CT, USA (2010).
28. G. Pirinççi, Ş. Kürümoğlu, *Kahramanmaraş Sütçü İmam Üniversitesi Mühendislik Bilimleri Dergisi,* **29**(1), 243 (2026).
29. T. Lu, F. Chen, *Journal of Computational Chemistry*, **33**(5), 580 (2012).
30. T. Lu, *Journal of Chemical Physics*, **161**(8), 082503 (2024).
31. F. A. Bulat, A. Toro-Labbé, T. Brinck, J. S. Murray, P. Politzer, *Journal of Molecular Modeling*, **16**(11), 1679 (2010).
32. P. Politzer, J. S. Murray, *Theoretical Chemistry Accounts*, **130**(2–3), 265 (2011).
33. E. F. Pettersen, A. Goddard, C. C. Huang, G. S. Couch, D. M. Greenblatt, E. C. Meng, T. E. Ferrin, *Protein Science*, **30**(1), 70 (2021).

Bulgarian Chemical Communications, Volume 58, Issue 3 (pp. 378-382) 2026 *DOI: 10.34049/bcc.58.3.D024*

Brain penetration in CNS and non-CNS drugs using molecular electronic parameters

C. Ergul, S. Kurumoglu*, Y. Yalcin Gurkan

Tekirdag Namik Kemal University, Department of Chemistry, Tekirdag, Turkey

Accepted: July 28, 2026

The blood-brain barrier (BBB) is a selective biological filter that protects the central nervous system, and it is important for some drugs to enter the brain while others do not. BBB permeability is conventionally predicted on the basis of physicochemical parameters, including logP, molecular weight, and total polar surface area (TPSA). However, research in this area is still in its early stages, with only a limited number of studies conducted thus far investigating the impact of these structural and reactive properties on the aforementioned process. The objective of this research endeavour was to ascertain the correlation between BBB penetration, as determined by DFT calculations, and global reactivity descriptors (i.e. η, ω, dipole moment, polarizability). A comparison with classical ADMET descriptors was also carried out. Four small molecules that have been clinically approved were selected for further investigation: Diazepam and carbamazepine exhibit high BBB permeability, while atenolol and metformin demonstrate low BBB permeability. The molecules were optimised at the B3LYP/6-311++G(d,p) DFT level, and parameters such as the HOMO-LUMO energy difference, chemical hardness, softness, electrophilic index, dipole moment, and polarizability were calculated. BBB parameters were evaluated using SwissADME via logBB, logP, and TPSA. The objective of this study was to establish a comparison that would reveal the reactivity and classical parameter differences between molecules that successfully pass the BBB and those that do not. Preliminary analyses indicate that molecules with high BBB passage exhibit reduced dipole moments and enhanced polarizability. Furthermore, it is hypothesised that the energy range and electrophilic indices may offer a superior explanation for BBB passage in comparison to classical logP and TPSA. The present study demonstrates that BBB permeability can be evaluated as a potential additional marker alongside reactivity parameters in molecular electronic parameter-based reactivity assessments and as a criterion in CNS drug design.

Keywords: ADMET, Blood–brain barrier, CNS drugs, DFT, Electronic reactivity, LogBB

INTRODUCTION

The blood-brain barrier (BBB) is a selectively permeable and highly dynamic interface that maintains homeostasis within the central nervous system (CNS) [1, 2]. This structure is vital for protecting the integrity of the nervous system by isolating the brain from potential pathogens and toxic molecules in the bloodstream. The integrity of the barrier is subject to regulation by a complex cellular network comprising endothelial cells, neurons, pericytes, and the basal laminae that tightly bind these components together. This microstructure is important for the global balance of the CNS [3]. One of the major problems in the management of CNS disorders is the low permeability of active substances through the BBB [4]. Poor pharmacokinetic behavior and undesirable safety features of potential drugs can impede the development of new pharmaceuticals [5].

The exposure of a particular compound in the brain depends on the physical characteristics of the compound [6]. In traditional literature, logBB value, the ratio between the total concentration of drug in the brain and that in the blood stream, has been used as permeability standard [7, 8]. However, it is necessary to expand the scope beyond the consideration of concentration as the standardization of geometric factors like the polar surface area (PSA) of the molecule is critical [9].

Advanced computational approaches are used in modern drug discovery to overcome the limitations of experimental methods. Hybrid techniques such as the extreme parallel graph convolutional network (XP-GCN) are employed for analyzing molecular graph data, yielding highly accurate results without the need for backpropagation techniques [10]. Artificial neural networks were also proved to be a feasible approach to predict chemical absorption using the logBB scale [11].

Density functional theory (DFT) and time-dependent density-functional theory (TD-DFT) are used to calculate the optimal coordinates of the atoms inside the molecules and the energy band analysis [12, 13]. Information obtained from such computations such as the adiabatic ionization potential (AIP), the bond dissociation enthalpy (BDE), and molecular electrostatic potential (ESP) give detailed information regarding the interaction

* To whom all correspondence should be sent:
E-mail: *skurumoglu@nku.edu.tr*

© 2026 Bulgarian Academy of Sciences, Union of Chemists in Bulgaria

of the molecule with biological entities [14, 15]. The Boiled-Egg approach is a method of *in silico* analysis that has been developed for the purpose of evaluating the absorption properties of drugs across both the gastrointestinal tract (GIT) and the blood-brain barrier (BBB). Nevertheless, the precision of such methodologies is subject to constant enhancement, in view of the challenges posed by imbalanced data sets and elevated false positive values [16].

The study of CNS permeability has a direct impact on the therapy of severe disorders such as Alzheimer's disease and epilepsy. For instance, the development of inhibitors that prevent Aβ peptide deposition and p-Tau protein phosphorylation in Alzheimer's disease requires a balance of physicochemical properties [17]. The drug carbamazepine, used to treat epilepsy, and benzodiazepines, popular due to their effectiveness in treating anxiety and insomnia, act by affecting GABA_A receptors in the brain [18-20]. The lipophilicity of beta-blockers (e.g., atenolol) can enable its penetration through the BBB, which may ultimately result in the appearance of neuropsychiatric side effects [21]. The interaction of metformin, a medication used to treat type 2 diabetes, with transporters at the blood-brain barrier (BBB), and the precise mechanism by which it penetrates the brain, remains a current area of research [22].

The primary novelty of this study is the introduction of an alternative perspective to the existing literature by correlating blood-brain barrier (BBB) permeability not only with classical physicochemical descriptors (logP, TPSA) but also with quantum mechanical-based global reactivity parameters. Although BBB crossing is usually analysed using empirical methods in the current literature, this study has conducted a thorough investigation of the electronic structure of molecules via dynamic indicators such as chemical hardness, polarizability and electrophilic index. These were investigated using DFT calculations performed at the B3LYP/6-311++G(d,p) level. In particular, the correlation of the decisive role of low dipole moment and optimised polarizability in the CNS transition with classical ADMET parameters provides a more precise and predictive set of criteria for central nervous system (CNS) drug design. This approach establishes an innovative evaluation framework for the design of future drug candidate molecules by accounting not only for passive diffusion but also for the molecule's potential for electronic interaction with its biological environment.

MATERIALS AND METHODS

Molecular optimization was performed using the Gaussian 09W software with the DFT/B3LYP method and the 6-311++G(d,p) basis set [23]. The molecular structures, optimized structures, and HOMO and LUMO orbitals of the basic dyes used to calculate quantum chemical parameters have been modeled. The frontier molecular orbital (FMO) has been used to estimate the E_{HOMO} (energy of the highest occupied molecular orbital) and E_{LUMO} (energy of the lowest unoccupied molecular orbital), followed by the values of the HOMO–LUMO energy gap, including global softness (η), global softness (S), electronic chemical potential (μ), electrophilic index (Ψ), electronegativity (χ), ionization energy (IE), and electron affinity (EA) were approximately calculated using the following equations in terms of HOMO and LUMO orbital energies [24].

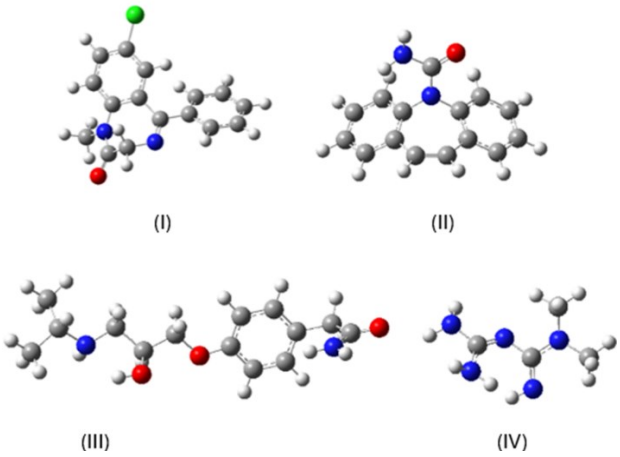

Fig. 1. Optimized structures of (I) diazepam; (ıı) carbamazepine; (ııı) atenolol; (ıv) metformin (grey, C; white, H; red, O; blue, N; green, Cl)

Following the calculation of quantum chemical parameters, the pharmacokinetic profiles and blood-brain barrier (BBB) permeability potentials of the selected molecules were evaluated *in silico*. Physicochemical parameters (lipophilicity – logP, molecular weight and total polar surface area – TPSA) were obtained using the SwissADME platform (https://www.swissadme.ch/index.php). The molecules' central nervous system (CNS) penetration capabilities were validated via numerical logBB and logPS (Permeability-Surface area product) values obtained through the pkCSM (https://biosig.lab.uq.edu.au/pkcsm/) databases. In particular, the logPS values obtained from the pkCSM platform were classified based on the critical threshold of -2 for CNS penetration. In the final stage, a correlation analysis was performed between the reactivity indices (η, S, μ, Ψ) from the Gaussian

09W output and *in silico* ADME data to investigate the decisive influence of electronic structure on the BBB crossing mechanism.

RESULTS AND DISCUSSION

The computed thermodynamic properties, which include total electronic energy (ΔE), enthalpy (ΔH), and Gibbs free energy (ΔG), for diazepam, carbamazepine, atenolol, and metformin have been given in Table 1. The calculated energy is found to be significantly negative for all molecules, thereby indicating that the optimized geometry is energetically favorable from a thermodynamic perspective.

Table 1. Gibbs free energy, enthalpy and energy values of optimized molecules

Molecule	ΔE (kcal/mol)	ΔH (kcal/mol)	ΔG (kcal/mol)
Diazepam	-792045.3	-792044.7125	-792083.5
Carbam-azepine	-478999.09	-478998.4994	-479033.15
Atenolol	-553199.19	-553198.5967	-553198.6
Metformin	-271486.21	-271485.6199	-271514.89

The analysis of the molecular structure of the pharmaceutical compound revealed that diazepam exhibited the least significant differences in enthalpy (ΔH), entropy (ΔS), and Gibbs free energy (ΔG). This finding suggests that diazepam possesses enhanced stability in comparison to the other drug molecules that were analyzed in this study. Atenolol demonstrated greater stability and exhibited higher energy levels compared to diazepam. Additionally, carbamazepine and metformin showed elevated energy levels, which can be attributed to differences in molecular size and heteroatom content.

The Gibbs free energies aligned with the trends observed in total electronic energy and enthalpy. The negative ΔG values for the analyzed compounds indicate that their molecular conformations are energetically favored. The minimal difference between ΔE and ΔH values suggests that only minor corrections are necessary when accounting for heat, whereas ΔG values incorporate entropic effects.

The results obtained in this study provide a comprehensive overview of the thermodynamics of the pharmaceutical molecules under investigation. The structural stability is confirmed by these results, which are theoretically supported for studying its further chemical reactivity, interactions with each other, and sorption characteristics.

Table 2 presents the BBB permeability characteristics of logPS, consensus Log Po/w and topological polar surface area (TPSA), values for selected pharmaceuticals.

Table 2. Prediction results of optimized molecules using SwissADME and pkCSM

Molecule	logPS	Consensus log Po/w	TPSA (Å^2)	BBB permeability
Diazepam	-0.89	2.97	32.67	yes
Carbam-azepine	-0.84	2.40	46.33	yes
Atenolol	-2.19	1.00	84.58	no
Metformin	-3.16	-0.89	91.49	no

Diazepam and carbamazepine exhibited relatively high lipophilicity values, with consensus Log Po/w values of 2.97 and 2.40, respectively. Furthermore, the two substances exhibited low TPSA values (32.67 and 46.33 Å^2, respectively), which are conducive to passive diffusion. Furthermore, both had elevated logPS values (indicative of reduced negative charge), suggesting effective permeability through the BBB. Consequently, the prediction results indicate that both substances were BBB permeable, thereby aligning with their observed pharmacological effects on the CNS.

Conversely, both atenolol and metformin exhibit comparatively low BBB permeability. Atenolol exhibits intermediate lipophilicity (Log Po/w=1.00) in conjunction with a relatively elevated TPSA value (84.58 Å^2). Consequently, the logPS value of the latter was found to be the smallest at -2.19. With regard to metformin, it possesses the lowest lipophilicity (log Po/w: -0.89) and the highest TPSA value (91.49 Å^2), indicating that the substance is highly polar and less membrane-permeable. Consequently, both substances are predicted to be unable to pass through the BBB ("no").

The results of the analysis demonstrate a strong correlation between the BBB permeability of the compounds and their lipophilicity and polarity. In general, compounds that exhibit high logP values and low TPSA values tend to demonstrate enhanced penetration into the BBB in comparison to those possessing high TPSA values and low logP values.

The global chemical reactivity descriptors were calculated by utilizing the values for the frontier molecular orbital energies in accordance with Koopmans' theorem. The chemical potential, denoted by μ, is calculated from the average value of the frontier orbital energies, while the global hardness, denoted by η, is calculated from half of the HOMO-LUMO gap energy (ΔE). The remaining parameters, namely the electrophilicity index (ψ), global softness (s), electronegativity (χ), ionization energy (IE), and electron affinity (EA), are derived

from these initial values. The equations, used in the calculations, are given below:

$$\mu = \frac{E_{\{HOMO\}}+E_{\{LUMO\}}}{2} \quad (1)$$

$$\eta = \frac{E_{\{HOMO\}}-E_{\{LUMO\}}}{2} \quad (2)$$

$$\psi = \frac{\mu^2}{2\eta} \quad (3)$$

$$S = \frac{1}{2\eta} \quad (4)$$

$$\chi = -\frac{E_{\{HOMO\}}+E_{\{LUMO\}}}{2} = -\mu \quad (5)$$

$$IE = -E_{\{HOMO\}} \quad (6)$$

$$EA = -E_{\{LUMO\}} \quad (7)$$

The global reactivity indices for diazepam, carbamazepine, atenolol and metformin, as determined using FMO theory, are presented in Table 3 below. The indices are of significance in understanding the electronic stability, reactivity, and electron transfer capability of the compounds.

Table 3. Global reactivity descriptors of optimized molecules

Global reactivity descriptors	Diazepam	Carbam azepine	Atenolol	Met formin
HOMO	-6.26	-5.78	-5.79	-5.40
LUMO	-1.70	-1.36	-0.18	0.56
ΔE	4.56	4.42	5.61	5.96
Chemical potential (μ)	-3.98	-3.57	-2.98	-2.42
Global hardness (η)	-2.28	-2.21	-2.81	-2.98
Global softness (s)	-162.29	-167.50	-131.91	-124.22
Global electrophili-city index (ψ)	-0.01	-0.01	-0.01	-0.02
Electronega-tivity (χ)	3.98	3.57	2.98	2.42
Ionization energy (IE)	6.26	5.78	5.79	5.40
Electron affinity (EA)	1.70	1.36	0.18	-0.56

The HOMO energies of the studied molecules were found to vary between −6.26 and −5.40 eV. Diazepam has the minimum HOMO energy levels (−6.26 eV) which represents low energy required to remove an electron. Conversely, metformin had the maximum HOMO energy level (−5.40 eV), indicative of the strongest electron donor. LUMO Energies Diazepam and carbamazepine had negative LUMO energy indicating strong propensity to accept electrons. On the other hand, metformin had the highest LUMO energy, which was positive value (0.56 eV).

The energy difference between HOMO and LUMO (denoted by ΔE) is considered as an important parameter for estimating the molecular stability and chemical reactivity. As for the energy gap atom, the result indicates that carbamazepine has the steepest energy gap (4.42 eV), while diazepam has the second largest energy gap just a little higher than carbamazepine (4.56 eV), that means carbamazepine low and so that of diazepam have high chemical reactivity and low kinetic stabilities. The energy difference between the highest occupied and the lowest unoccupied state of metformin is the highest (5.96 eV), implying that metformin is the most kinetically stable and least reactive molecule. Atenolol also had a relatively large ΔE value (5.61 eV), indicating that its electronic structure was more stable relative to others.

The values for the chemical potential (μ) and electronegativity (χ) also supported the electronic nature of these complexes. Among these molecules, diazepam had the maximum electronegativity value (3.98 eV), so it has the strongest pull on electrons. Conversely, the lowest electronegativity value was observed in metformin (2.42 eV), revealing a weakened ability to attract electrons. In addition, the more negative chemical potentials of diazepam and carbamazepine imply greater electronic-structure stabilization relative to atenolol and metformin.

Based on the global hardness values, metformin and atenolol were proposed as more stable molecules with high energy gap between HOMO and LUMO and low reactivity. However, carbamazepine and diazepam exhibited lower global hardness values, indicating a more flexible electronic structure. The same behavior was observed in the context of global softness (s) values of these molecules, with carbamazepine exhibiting the highest value.

The electrophilicity indices obtained are relatively low for all chemicals, thus demonstrating moderate electrophilicity behavior. With regard to the ionization energy, it was established that in order to strip off its electrons, Diazepam requires elevated levels of energy. Conversely, metformin exhibited the lowest ionization energy, thereby demonstrating a pronounced propensity for electron donation. The electron acceptor behavior of diazepam and carbamazepine is also notably higher than that of atenolol and metformin, as evidenced by the electron acceptor values.

In conclusion, from the analysis of the global chemical reactivity descriptors, it is evident that diazepam and carbamazepine exhibit significantly higher levels of reactivity in comparison to atenolol and metformin.

CONCLUSIONS

The permeability of the blood-brain barrier (BBB) to four model compounds (diazepam, carbamazepine, atenolol, and metformin) was studied using quantum chemistry-based reactivity descriptors and *in silico* ADME tools. Compounds that exhibit a higher BBB permeation ability (diazepam, carbamazepine) are associated with a smaller energy difference between HOMO and LUMO levels and a "softer" electronic structure. This facilitates their interaction with membranes. Conversely, BBB impermeable compounds (atenolol, metformin) exhibit a larger gap between electronic levels and higher hardness, which is consistent with increased passivity towards diffusive permeation. The results obtained via our quantum chemical study and virtual pkCSM (logPS) /SwissADME (TPSA) studies were found to be highly congruent. It has been demonstrated that global indices of reactivity can be regarded as potent, high-precision biomarkers for CNS-targeting drug discovery, which can exceed the efficacy of classical descriptors (logP/TPSA).

Acknowledgement: *The financial support provided by Tekirdag Namik Kemal University BAP unit through Project No. NKUBAP.64.YL.24.546 is gratefully acknowledged.*

REFERENCES

1. Y. Zhao, L. Gan, L. Ren, Y. Lin, C. Ma, X. Lin, *Brain Research*, **1788**, 147937 (2022).
2. R. Kumar, A. Sharma, A. Alexiou, A. L. Bilgrami, M. A. Kamal, G. M. Ashraf, *Frontiers in Neuroscience*, **16**, 858126 (2022).
3. Z. F. Gu, Y. D. Hao, T. Y. Wang, P. L. Cai, Y. Zhang, K. J. Deng, H. Lv, *BMC Biology*, **22**(1), 86 (2024).
4. D. J. Begley, *Pharmacology & Therapeutics*, **104**(1), 29 (2004).
5. M. Fridén, Prediction of Drug Exposure in the Brain from the Chemical Structure, in Drug Delivery to the Brain: Physiological Concepts, Methodologies and Approaches, Springer New York, New York, NY, 2013, p. 317.
6. M. Fridén, Prediction of Drug Exposure in the Brain from the Chemical Structure, in Drug Delivery to the Brain: Physiological Concepts, Methodologies and Approaches, Springer International Publishing, Cham, 2022, p. 437.
7. F. Meng, Y. Xi, J. Huang, P. W. Ayers, *Scientific Data*, **8**(1), 289 (2021).
8. T. Kim, B. H. You, S. Han, H. C. Shin, K. C. Chung, H. Park, *International Journal of Molecular Sciences*, **22**(20), 10995 (2021).
9. C. P. Spielvogel, N. Schindler, C. Schröder, S. L. Stellnberger, W. Wadsak, M. Mitterhauser, C. Vraka, *Journal of Chemical Information and Modeling,* **65**(6), 2773 (2025).
10. M. A. Pala, *Computational Biology and Chemistry,* **120**, 108755 (2026).
11. Q. Zhang, D. Mao, Y. Tu, Y. Y. Wu, *Journal of Chemical Information and Modeling,* **64**(15), 5853 (2024).
12. K. Asokan, S. Sivaraman, K. Nallasamy, J. Subbiah, S. Paranthaman, *Indian Journal of Biochemistry and Biophysics*, **62**(4), 406 (2025).
13. D. Şakar, E. Üstün, *Russian Journal of Inorganic Chemistry*, **68**(9), 1303 (2023).
14. B. T. Ogunyemi, *Communication in Physical Sciences,* **12**(2), 1081 (2025).
15. M. Sönmez Çelebi, M. Çol Ayvaz, D. Şakar, E. Üstün, Ö. Ertürk, *Inorganica Chimica Acta*, **585**, 122752 (2025).
16. S. Şahin, N. Dege, *Polyhedron*, **205**, 115320 (2021).
17. N. Job, V. S. Thimmakondu, K. Thirumoorthy, *Molecules*, **28**(3), 1388 (2023).
18. P. M. Burkat, *The Journal of Clinical Pharmacology*, **62**(10), 1297 (2022).
19. M. Uzzaman, A. Ahsan, M. N. Uddin, *European Journal of Chemistry*, **12**(4), 412 (2021).
20. F. Sotoudegan, M. Amini, M. Sharifzadeh, N. Samadi, F. Sotoudegan, *AAPS Open*, **10**(1), 12 (2024).
21. V. Dahiya, A. Rohilla, S. Jain, S. Rohilla, *Asian Journal of Pharmaceutical and Clinical Research*, **15**(6), 9 (2022).
22. S. Sharma, Y. Zhang, K. A. Akter, S. Nozohouri, S. R. Archie, D. Patel, T. Abbruscato, *Pharmaceutics*, **15**(5), 1357 (2023).
23. M. J. Frisch, G. W. Trucks, H. B. Schlegel, G. E. Scuseria, M. A. Robb, J. R. Cheeseman, Gaussian 09, Revision C.01, Gaussian, Inc., Wallingford, CT, USA, 2010.
24. G. Pirinççi, Ş. Kürümoğlu, *Kahramanmaraş Sütçü İmam Üniversitesi Mühendislik Bilimleri Dergisi,* **29**(1), 243 (2026).

Bulgarian Chemical Communications, Volume 58, Issue 3 (pp. 383-386) 2026 *DOI: 10.34049/bcc.58.3.D025*

Comparison of the effects of cellulase, pectinase, and xylenase enzymes on the total flavonoid content of *Helichrysum arenarium* extract obtained by enzymatically pre-treated Soxhlet extraction

S. Simsek*, E. Akyol, I. Kucuk

[1]*Yildiz Technical University, Chemical Engineering Department, Davutpasa Campus, Esenler, Istanbul 34210, Türkiye*

Accepted: July 28, 2026

Flavonoids are plant compounds that have various benefits for human health. Their benefits for human health have been supported by studies and their use has become widespread in the nutraceutical, pharmaceutical, medical and cosmetic sectors. In the present work, the flavonoid extraction from *Helichrysum arenarium* using Soxhlet extraction and single or a combination of several enzymes was achieved and the influence of enzymes types (cellulase, pectinase, and xylanase) on the flavonoid extraction efficiency was explored. The total flavonoid content was determined based on the aluminum chloride colorimetric method in terms of quercetin equivalent (mg QE/mL). Experimental data show that xylanase treatments increased the total flavonoid content to the range of 55.32–58.45 mg QE/g, yielding the highest values (58.45 mg QE/g in EA9) and providing the most significant increase compared to the control group. The enzyme-assisted extraction method has demonstrated higher extraction capacity compared to traditional Soxhlet extraction, offering high efficiency.

Keywords: *Helichrysum arenarium*, total flavonoid content, Soxhlet extraction, enzyme-assisted extraction, xylanase, cellulase, pectinase.

INTRODUCTION

Helichrysum arenarium is a medicinal plant species belonging to the Asteraceae family and is known for its high flavonoid and phenolic content. The plant's rich bioactive profile, consisting of flavanones and various polyphenolic compounds, supports its widespread use in traditional medicine [1–3]. *Helichrysum arenarium*, as a medicinal plant belonging to the Asteraceae family, is known for its diuretic, choleretic, spasmolytic, hepatoprotective and anti-inflammatory properties, can also be used as a detoxification agent, and exhibits antiviral, antibacterial, antifungal and antioxidant activities, wound healing, anti-aging, antitumor and anti-atherosclerotic effects, supporting its traditional uses [4–6]. Various phytochemical and pharmacological studies emphasize that *Helichrysum arenarium* has a rich phenolic compound content, especially flavonoids [1, 6]. However, the cellulose, hemicellulose, and pectin matrix in the cell wall forms a physical barrier that limits the passage of flavonoids into the solvent during conventional solvent extraction; the literature emphasizes that the enzymatic hydrolysis of this structure facilitates the release of bioactive compounds [5, 6]. Enzyme-assisted extraction of flavonoids is a potential alternative to traditional solvent-based extraction methods. Enzymes, by their ability to break down or disrupt cell walls and membranes, enable more efficient extraction of bioactives, thus offering a more environmentally friendly extraction method [7–9].

This study aims to improve the degradation of cell wall components and increase extraction efficiency by comparing the effectiveness of cellulase, pectinase, and xylanase enzymes individually and synergistically. These enzymes accelerate the transfer of intracellular compounds to the solvent by degrading plant tissues under mild conditions and improve extraction kinetics [10]. In this study, extraction was performed from *Helichrysum arenarium* plants using the Soxhlet extraction method after pretreatment with enzymes to increase the total flavonoid content (TFC) in terms of quercetin equivalent. The enzymes were added individually or in mixtures in various volumes, with the total activity fixed at 50 U/ml.

EXPERIMENTAL

Materıals and method

The leaves of the *Helichrysum arenarium* plant, sourced from a local herbalist called Amcahafızoğulları in Uşak, were separated from the branches and stored in an airtight bag at room temperature. Commercial enzymes cellulase (SQzyme CSL, 10,000 U/mL), pectinase (SQzyme PCL, 60,000 U/mL), and xylanase (SQzyme XSL, 50,000 U/mL) were obtained as samples from

* To whom all correspondence should be sent:
E-mail: *simseksinan@outlook.com.tr*

© 2026 Bulgarian Academy of Sciences, Union of Chemists in Bulgaria

Suntaq International Limited. Sodium hydroxide (CAS: 1310-73-2) and hydrochloric acid (CAS: 7647-01-0) were obtained from Boston Chemical, and citric acid (CAS: 5949-92-1) was obtained from Akbel Kimya, for the purpose of preparing the buffer solution. *Helichrysum arenarium* leaves were pre-treated with enzymatic treatment and then subjected to Soxhlet extraction, and the resulting extracts were analyzed using a UV spectrophotometer. Distilled water was preferred as the solvent in the Soxhlet extraction, and it was carried out at an extraction temperature of 70 °C for 4 h.

Preparation of buffer solution

A pH 5 buffer solution was prepared according to the procedure described in European Pharmacopoeia 5.0, containing 20.1 g/l citric acid and 8.0 g/l sodium hydroxide. The pH was adjusted with dilute hydrochloric acid [11].

Enzymatic pretreatment

Enzymatic pretreatment was performed by adding 99 mL of pH 5.0 citrate buffer and 1 mL of diluted enzyme solution (to ensure 50 U/mL enzyme activity in each test flask) to 5 g of dry *Helichrysum arenarium* sample for each experiment; the ratio of "dry plant mass: volume of enzyme-added buffer solution" was prepared as 1:20, the total volume in each test flask was adjusted to 100 mL, and it was applied in a shaking water bath at 37 °C for 1 hour at a stirring speed of 100 rpm.

Cellulase (10,000 U/mL), pectinase (60,000 U/mL), and xylanase (50,000 U/mL) enzymes were used, and the target activity was brought to a level of 50 U/mL in diluted solutions; in each experiment, 99 mL of buffer and 1 mL of diluted enzyme solution were applied with the enzyme loads specified in Table 1, while no enzyme was added in the control group (EA10). After the enzymatic pretreatment was completed, the buffer solution was removed from the plant leaves *via* a rotary evaporator (Heidolph Hel-VAP), and only trace amounts of buffer solution extract were obtained and included in the Soxhlet extractor along with the *Helichrysum arenarium* leaves.

Table 1. Experimental design of enzymatic pretreatment application.

Sample No.	Experimental group / enzyme ratio	Cellulase, mL	Pectinase, mL	Xylanase, mL	Total enzyme volume, mL	Total enzyme load, U	Final enzyme activity, U/mL
EA1	Cellulase	0.1	0	0	0.1	1000	50
EA2	Cellulase	0.2	0	0	0.2	2000	50
EA3	Cellulase	0.3	0	0	0.3	3000	50
EA4	Pectinase	0	0.1	0	0.1	6000	50
EA5	Pectinase	0	0.2	0	0.2	12000	50
EA6	Pectinase	0	0.3	0	0.3	18000	50
EA7	Xylanase	0	0	0.1	0.1	5000	50
EA8	Xylanase	0	0	0.2	0.2	10000	50
EA9	Xylanase	0	0	0.3	0.3	15000	50
EA10	Control	0	0	0	0	0	0
EA11	Enzyme mixture (1:1:1)	0.1	0.1	0.1	0.3	12000	50
EA12	Enzyme mixture (2:1:1)	0.2	0.1	0.1	0.4	13000	50
EA13	Enzyme mixture (1:2:1)	0.1	0.2	0.1	0.4	18000	50
EA14	Enzyme mixture (1:1:2)	0.1	0.1	0.2	0.4	17000	50

Soxhlet extraction

Helichrysum arenarium leaves, pre-treated with enzymatic methods, were loaded into a Soxhlet extractor chamber. A heated mantle placed under the solvent chamber of the Soxhlet extractor was activated, and 250 mL of distilled water was evaporated at 110 °C. The water in the vapor phase, striking the reflux surface, condensed and collected in the extraction chamber. The plants were extracted at an extraction temperature of approximately 70 °C, and 15 extraction cycles were applied for each experiment. The extracts obtained after extraction were transferred to a rotary evaporator (Heidolph Hel-VAP). Excess water was removed by the rotary evaporator, the extracts were concentrated and prepared for UV analysis, and stored in amber glass bottles at 4 °C.

Determination of total flavonoid content

To determine the total flavonoid content in terms of quercetin equivalents by colorimetric analysis using a UV-Vis spectrophotometer (Perkin Elmer Lambda 35 UV-Vis), a 12.5 mg/mL stock solution was prepared by dissolving 625 mg of standard quercetin in 50 mL of distilled water. This stock solution was then diluted to concentrations of 10; 7.5; 5; 2.5; 7.5; 5; 2; 1.5; 1.25; 1; 0.5 and 0.1 mg/mL, yielding quercetin solutions at various concentrations. Using these solutions, a calibration equation of $y = 0.3809x + 0.0697$ was obtained via UV-Vis analysis at 510 nm, with an R^2 value of 0.9919. To each 10 mL tube, 1 mL of extract (each extract obtained from the extraction processes was added separately), 4 mL of distilled water and 0.3 mL of 5% (w/v) sodium nitrite solution were added; the mixture was then thoroughly mixed and left to stand at room temperature for 5 minutes. Subsequently, 0.3 mL of a 10% (m/v) aluminium chloride solution was added to the tubes; after allowing the mixture to stand for a further 1 minute, 2 mL of 1 M sodium hydroxide and 2.4 mL of distilled water were added to adjust the total volume to 10 mL. The absorbance values of the prepared mixtures were measured at a wavelength of 510 nm using a UV-Vis spectrophotometer (Perkin Elmer Lambda 35 UV-Vis) [12], and the obtained values were applied to the calibration equation to calculate the results in terms of quercetin equivalents (mg QE/mL).

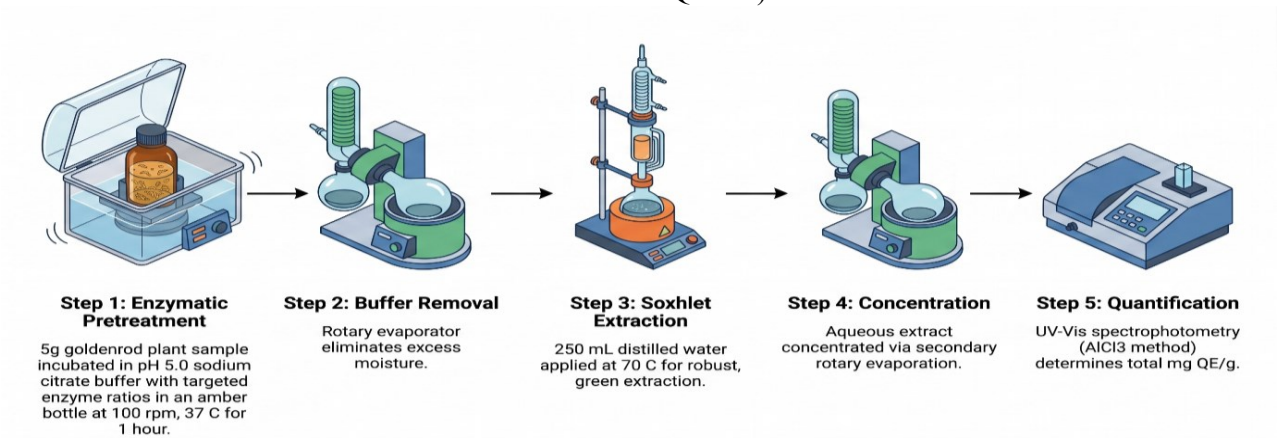

Figure 1. Experimental procedure for enzymatically pre-treated Soxhlet extraction and UV analysis

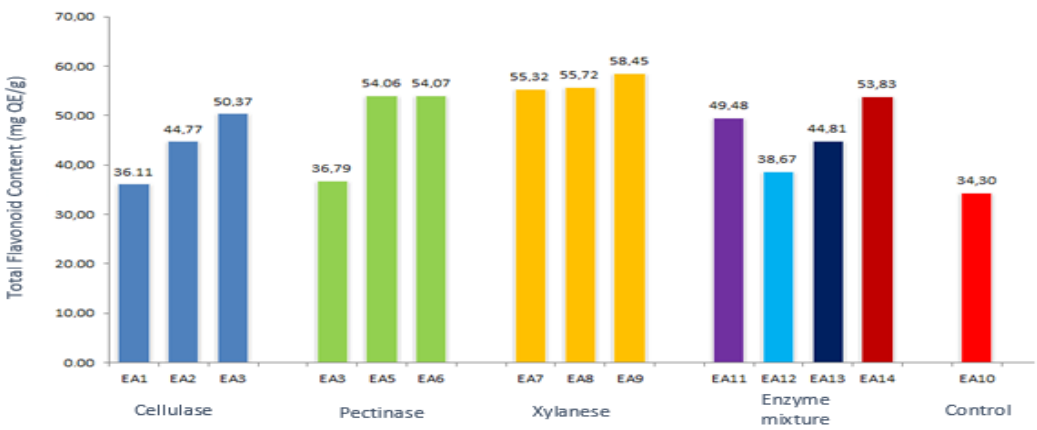

Figure 2. Effect of single enzymes and their mixtures on the extraction yields of total flavonoids.

RESULTS AND DISCUSSION

Extraction of total flavonoids from *Helichrysum arenarium* was conducted with three enzymes, cellulase, pectinase, and xylanase. A series of preliminary experiments were conducted to determine the most effective concentration and ratio for all three enzymes, both individually and in mixtures. The effect of enzyme type, enzyme quantity and ratio on flavonoid extraction yield is shown in Figure 2. It was observed that every single enzymatic condition lead to a clear and significant increase in flavonoid extraction. All enzymes significantly improved the yield, with increasing activity leading to higher flavonoid extraction. Among them, xylanase showed the strongest effect, reaching up to 58.45 mg QE/g, corresponding to 70.41% improvement. Interestingly, although multi-enzyme combinations also perform well, they do not surpass the performance of alone xylanase at optimal conditions. In the specific cellular architecture of *Helichrysum arenarium,* the hemicellulose network serves as the primary trapping matrix for phenolic compounds. Xylanase efficiently hydrolyzes the xylan structure, thereby completely isolating the structurally bound flavonoids that remain intact during Soxhlet extraction.

CONCLUSION

The main findings of this study are as follows: Every enzymatic variation tested resulted in a meaningful improvement over the baseline Soxhlet extraction. Although multi-enzyme systems perform well, xylanase provided the highest yield in this study. First, enzymatic pretreatment substantially enhances extraction performance, yielding 70.41% increase compared to direct Soxhlet extraction. Second, the results indicate a clear matrix-specific effect, where selective degradation of the hemicellulose fraction -particularly *via* xylanase- plays a dominant role in improving flavonoid accessibility.

Finally, this approach to improving the ability to obtain high flavonoid content using a Soxhlet extraction system with distilled water has the potential to be used as a simplified and efficient process alternative that does not require the use of toxic solvents.

The present study demonstrates xylanase to be a highly efficient enzyme to assist the extraction of flavonoid compounds in mild solvents like water. Overall, these findings demonstrate that targeted enzymatic pretreatment represents an effective strategy for intensifying flavonoid extraction from plant matrices.

Acknowledgement: *This work was supported by the Research Fund of the Yildiz Technical University. Project Number FCD-2025-7043.*

REFERENCES

1. K. Kramberger, Z. Jenko Pražnikar, A. Baruca Arbeiter, A. Petelin, D. Bandelj, S. Kenig, *Antioxidants*, **10**, 380 (2021).
2. S. Simsek, E. Akyol, I. Kucuk, *Journal of Medicinal Food*, 1096620X261430296 (2026).
3. S. Simsek, E. Akyol, I. Kucuk, *Bulgarian Chemical Communications*, **57**, 202 (2025).
4. D.A. Bajrami, *BJSTR*, **50**, 41270 (2023).
5. S.M. Dănăilă-Guidea, M.C. Eremia, L.D. Dinu, D.M. Miu, *Applied Sciences*, **12**, 10241 (2022).
6. D. Pljevljakušić, D. Bigović, T. Janković, S. Jelačić, K. Šavikin, *Front. Plant Sci.*, **9** (2018).
7. L. Gardossi, P.B. Poulsen, A. Ballesteros, K. Hult, V.K. Švedas, Đ. Vasić-Rački, G. Carrea, A. Magnusson, A. Schmid, R. Wohlgemuth, P.J. Halling, *Trends in Biotechnology*, **28**, 171 (2010).
8. A.S. Meyer, *Annals of the New York Academy of Sciences*, **1190**, 126 (2010).
9. M. Pinelo, A. Arnous, A.S. Meyer, *Trends in Food Science & Technology*, **17**, 579 (2006).
10. M. He, K. Yasin, S. Yu, J. Li, L. Xia, *International Journal of Molecular Sciences*, **24**, 16348 (2023).
11. European Pharmacopeia 5.0 - Buffer Solutions Notes 4.1.3, *Studocu.*
12. J. Zhishen, T. Mengcheng, W. Jianming, *Food Chemistry*, **64**, 555 (1999).

Bulgarian Chemical Communications, Volume 58, Issue 3 (pp. 387-390) 2026 *DOI: 10.34049/bcc.58.3.D026*

Determination of the chemical composition of the essential oil of the *Rubia tinctorum* plant

T. Sabudak[1]*, B. Eren[2], C. Ozcelik[3]

[1]*Tekirdag Namik Kemal University, Faculty of Arts and Sciences, Department of Chemistry, Tekirdag, Turkey*
[2] *Tekirdag Namik Kemal University, Vocational School of Social Sciences, Tekirdag, Turkey*
[3] *Tekirdag Namik Kemal University, Institute of Natural Sciences, Tekirdag, Turkey*

Accepted: July 28, 2026

From past to present, plants and plant extracts have been used in many scientific and commercial fields for various purposes. *Rubia tinctorum* L. (Rubiaceae) has a long history of traditional use as a diuretic and in the treatment of conditions such as jaundice, sciatica, and paralysis. In this study, the essential oil of *R. tinctorum* was obtained by the hydrodistillation method, and the volatile and semi-volatile compounds it contains were identified using the GC–MS technique. GC–MS analysis revealed the presence of 21 compounds in the essential oil extract of *R. tinctorum*. The chemical profile was determined by fatty acids, accounting for 89.29% of the total composition, followed by alkanes (5.32%), terpenoids (4.57%), alcohols (0.5%), and aldehydes.

Keywords: *Rubia tinctorum*, essential oil, gas chromatography, GC-MS.

INTRODUCTION

Globally, estimated 50.000–70.000 plant species are utilized for medicinal applications, while nearly 500 medicinal plants are used therapeutically in Türkiye [1]. Interest in plant-derived natural products has been steadily increasing in recent years. Plants have gained considerable scientific interest because of their wide range of biological properties, such as anti-inflammatory, anticarcinogenic, antifungal, antiallergic, antioxidant, and antibacterial activities.

Consequently, research focusing on the isolation of biologically active compounds from plants and the elucidation of their chemical structures has intensified in recent times.

The genus *Rubia* belongs to the Rubiaceae family, which comprises approximately 450 genera and around 6.500 species. The genus *Rubia* is widely distributed, encompassing over 60 species found in Africa, temperate regions of Asia, and the Americas. In India, about 15 species of *Rubia* have been reported [2]. Species of the genus *Rubia* (Figures 1 and 2) are of considerable commercial, economic, and medicinal importance, primarily due to their high anthraquinone content, which is predominantly accumulated in the roots [3].

Extracts obtained from *R. tinctorum* L. contain several bioactive constituents with notable pharmacological relevance. Traditionally, crude extracts have been used to treat bladder and kidney stones, especially calcium oxalate and calcium phosphate calculi in the urinary tract. *In vitro* investigations have shown that ruberythric acid suppresses the formation of calcium oxalate and calcium phosphate crystals [5-8].

Figure 1. Aerial parts of *R. tinctorum* [4]

Figure 2. Roots of *R. tinctorum* [4]

* To whom all correspondence should be sent:
E-mail: *tsabudak@nku.edu.tr*

© 2026 Bulgarian Academy of Sciences, Union of Chemists in Bulgaria

R. tinctorum (Rubiaceae) has traditionally been used as a diuretic and for the treatment of ailments including jaundice, sciatica, and paralysis. It has also been utilized to regulate menstruation after childbirth and to manage conditions such as rheumatism, eczema, and fungal infections [9]. Moreover, *R. tinctorum* serves as an important natural source of dye raw materials utilized in the cosmetic, textile, food, and pharmaceutical sectors. Beyond its industrial applications, the species is also well known for its diverse and beneficial biological activities [10].

The present study aims to determine the secondary metabolites found in the essential oil of *R. tinctorum* L. cultivated in the Edirne - Havsa region by using the GC–MS method. In this context, the study will contribute to the chemotaxonomic classification of *R. tinctorum*.

MATERIALS AND METHODS

Plant material and extractions

The cultivated *Rubia tinctorum* was harvested in August 2024 from the garden of Trakya University Havsa Vocational School and subsequently dried in a shaded, well-ventilated environment. The dried material was then divided into aerial parts and roots. After the aerial part of the plant was cut into small pieces, it was placed in a Clevenger apparatus and subjected to steam distillation for 12 h. Subsequently, extraction was performed on the water-oil mixture, yielding 0.074 g of crude essential oil [11].

Determination of volatile and semi-volatile compounds in essential oil of R. tinctorum by GC-MS

To determine the composition of the compounds present in the essential oil extract of the plant, a Shimadzu QP2010-Ultra model GC–MS instrument was used. GC–MS analyses were performed using a TRB-5MS capillary column (30 m × 0.25 mm × 0.25 µm) coated with 5% phenyl–95% methylpolysiloxane. The split ratio was adjusted to 10:1, with an injection volume of 1 µL. The injector temperature was kept at 250 °C, while both the ion source and interface temperatures were maintained at 280 °C. Helium was used as the carrier gas at a constant flow rate of 1 mL/min. The initial column temperature was set at 50 °C and held for 3 min. It was then increased at a rate of 3 °C/min to 100 °C and held for 5 min. Subsequently, the temperature was raised at 6 °C/min to 250 °C and held for 14.5 min. The mass spectrometer was operated in scan mode over a mass range of 45–700 m/z. The total analysis time was 64 min. The mass spectra of the compounds were identified by comparison with the Wiley 9 and NIST mass spectral libraries. In addition, the retention indices of each component in the mixture were calculated based on their retention index using a C6–C22 n-alkane standard mixture [12].

RESULTS AND DISCUSSION

GC–MS analysis revealed the presence of 21 compounds in the essential oil extract of *R. tinctorum*. The chemical profile was dominated by fatty acids, accounting for 89.29% of the total composition, followed by alkanes (5.32%), terpenoids (4.57%), alcohols (0.5%), and aldehydes (Table 1). This finding is consistent with previous reports on species within the *Rubia* genus, where fatty acids have been identified as major constituents of volatile and semi-volatile extracts. The dominance of margaric acid (67.34%) observed in the present study is particularly noteworthy, as this saturated fatty acid has been reported to exhibit antimicrobial and membrane-disrupting properties, which may contribute to the biological activity of the extract [13].

Table 1. Chemical distribution of compounds in the essential oil extract of *R. tinctorum*

Functional group	Percentage (%)
Fatty acid	89.29
Alkane	5.32
Terpenoid	4.57
Alkol	0.50
Aldehyde	0.30
Total	99.98

Oleic acid (8.17%) and myristic acid (5.08%) (Table 2), detected as other major fatty acids, are well-documented for their antimicrobial, anti-inflammatory, and antioxidant activities. The presence of these fatty acids suggests a potential role of the essential oil extract in inhibiting microbial growth and modulating oxidative processes. Compared to previously published studies on related plant species, the fatty acid profile of *R. tinctorum* appears to be distinct, especially in terms of the unusually high margaric acid content, indicating possible chemotypic variation or the influence of environmental and geographical factors[14, 15].

A review of the literature shows that Houari *et al*. [11]. analyzed the chemical composition of the essential oil obtained from *R. tinctorum* by hydrodistillation using GC–MS and reported

cyclohexanone (88.74%) as the predominant compound. Similarly, Zhaohui (2009) [16] determined the composition of *R. tinctorum* essential oil using GC-MS and observed that theaspirane, 2-furaldehyde and benzaldehyde constitute the main compounds of the essential oil. Hoseinzadeh *et al*. [17]. investigated the essential oil composition of *R. tinctorum* using GC–MS analysis and identified bornyl acetate, asarone, sabinene hydrate acetate, ocimene, thymol, methyl isoeugenol, neophytadiene, and methyl eugenol among the major constituents.

In the present study, terpenoids (4.57%) and alkanes (5.32%) were detected in lower proportions. These compounds are known to contribute to the aroma and biological functionality of essential oils. Terpenoids, even at low concentrations, may exhibit synergistic effects with fatty acids, thereby enhancing the overall antimicrobial or antioxidant potential of the extract [18].

Table 2. Identified compounds in the essential oil extract of *R. tinctorum*

No	RT (min)	RI	Compounds	Percentage
1	35.868	1574	Dodecanoic acid (lauric acid)	0.26
2	39.100	1720	Tetradecanal (myristaldehyde)	0.30
3	40.125	1769	Tetradecanoic acid (myristic acid)	5.08
4	41.665	1849	6,10,14-Trimethyl-2-pentadecanone	3.90
5	41.999	1867	Pentadecanoic acid (pentadecylic acid)	3.86
6	42.316	1885	1- hexadecanol (cetyl alcohol)	0.11
7	43.444	1948	9- Hexadecenoic acid	0.54
8	43.525	1952	Isophytol	0.26
9	43.906	1973	Heptadecanoic acid (margaric acid)	67.34
10	45.570	2073	13- Epi-manool	0.09
11	45.814	2088	1- Nonadecanol	0.30
12	46.730	2145	9- Octadecenoic acid (oleic acid)	8.17
13	46.793	2149	Heptadecen- (8)- carbonic acid- (1)	2.11
14	47.072	2166	Octadecanoic acid (stearic acid)	1.74
15	49.463	2321	cis-9,10-epoxy octadecanoic acid	0.19
16	50.015	2358	4,8,12,16-Tetramethyl heptadecan-4-olide	0.41
17	50.675	2401	Tetracosane	0.24
18	52.457	2492	Pentacosane	0.94
19	54.621	2601	Hexacosane	0.62
20	57.319	2690	Heptacosane	2.72
21	60.735	2802	Octacosane	0.80

RT: Retention time; RI: Retention index

CONCLUSION

In the present study, the chemical composition of *Rubia tinctorum* essential oil was characterized using GC–MS analysis, revealing fatty acids, terpenoids, and alkanes as the major constituents. It is well established that the production and accumulation of secondary metabolites in plants are influenced by environmental factors such as soil properties, mineral availability, and climatic conditions. Consequently, variations in the geographical origin and collection site of the plant may result in qualitative and quantitative differences in its secondary metabolite profile.

Overall, the chemical composition of *R. tinctorum* essential oil extract revealed in this study highlights fatty acids as the principal contributors to its phytochemical profile. The distinctive abundance of margaric acid differentiates *R. tinctorum* from other members of the genus and underscores its potential for further pharmacological and functional investigations. These results provide a scientific basis for future studies focusing on the biological activities and possible industrial or pharmaceutical applications of *R. tinctorum* essential oil.

Acknowledgement: *The authors would like to thank Tekirdag Namik Kemal University for financial*

support of the project (Project number: NKUBAP.00.GA.25.669).

Declaration of competing interests: *The authors declare no conflict of interest.*

REFERENCES

1. Ş. Türkan, H. Malyer, S. Öz Aydın, G. Tümen, *Süleyman Demirel Ün. FBE Derg.,* **10,** 162 (2006).
2. K.S. Krishnan Marg, The Wealth of India: Raw Materials, National Institute of Science Communication and Information Resources CSIR, New Delhi,110 012, 1985.
3. R.H. Thomson, Naturally occuring quinones, Chapman & Hall, London, 1996.
4. M. Yavuzcanli, PhD Thesis, Van Yüzüncü Yıl Ün. FBE, 2023.
5. H. Schilcher, *Deutsche Apotheker-Zeitung,* **124**, 2429 (1984).
6. V.V.S. Murti, T.R. Seshadri, S. Sivakumaran, *Indian J. Chem.,* **8,** 779 (1970).
7. B. Poginsky, J. Westendorf, B. Blomeke, H. Marquardt, A. Hewer, P.L. Grover, D.H. Phillips, *Carcinogenesis*, **72**, 1265 (1991).
8. R. Wijnsma, R. Verpoorte, in: Progress in the chemistry of organic natural products. W. Herz, H. Grisebach, G.W. Kirby, C. Tamm (eds.), Wien, Springer, vol. 49, 1986, p. 79.
9. Y. Güzel, M. Güzelşemme, M. Miski, *J. Ethnopharmacol.,* **174**, 118 (2015).
10. N. Kabaalioğlu, H. Tezcan, *Inter. Social Sci. Studies J.,* **7**, 3573 (2021).
11. F.Z. Houari, M. Brahmi, R. Erenler, A. Hariri, *Nat. Product Res.,* **39**, 5000 (2025).
12. T. Sabudak, A.C. Goren, *J. Essent. Oil-Bear. Plants,* **14**, 401 (2011).
13. Q. Lei, Y. Zhang, T. Yang, L. Chen, X. Pei, Y. Zhang, T. Ma, Y. Xie, Y. Wang, H. Li, C. Cao, B. Zhang , C. Xu, *J. Func. Foods,* **119**, 106359 (2024).
14. M.S.M. Firoozabad, M.M. Nasr, *Iranian J. Microbiol.,* **14**, 214 (2022).
15. Y.G. Kim, J.H. Lee, S. Park, S. Kim, J. Lee, J. *Microbial Biotech.,***15**, 590 (2022).
16. C. Zhaohui, F. Jihong, *Zhongchengyao,* **31**, 1727 (2009).
17. A. Hoseinzadeh, Y. Sadeghipour, G. Behbudi, *Advances Appl. Nano-Bio Techn.,* **1**, 10 (2020).
18. M. Perricone, E. Arace, M.R. Corbo, M. Sinigaglia, A. Bevilacqua, *Front. Microbiol.,* **6**, 76 (2015).

Bulgarian Chemical Communications, Volume 58, Issue 3 (pp. 391-395) 2026 *DOI: 10.34049/bcc.58.3.D027*

Reactivity and ecotoxicity of the next-generation herbicide flufenauxirim: a density functional theory (DFT) and quantitative structure-activity relationship (QSAR) study with reference to aminocyclopyrachlor

G. Tumtum, K. Demir, S. Kurumoglu, Y. Yalcin Gurkan*

Tekirdag Namik Kemal University, Department of Chemistry, Tekirdag, Türkiye

Accepted: July 28, 2026

Flufenauxirim is a newly developed pyrimidine carboxylic acid herbicide that received provisional approval from ISO in 2025 but lacks any experimental data on its environmental effects, ecotoxicity or chemical reactivity. In this study, density functional theory (DFT) at the B3LYP/6-31G(d) level was employed to compute global and local reactivity descriptors for flufenauxirim and for the structurally related reference herbicide aminocyclopyrachlor, both in gas phase and in water using the CPCM solvation model. A series of 108 substructural variants were generated by systematic removal of functional groups to identify structural alerts. An XGBoost-based QSAR model with leave-one-out cross-validation predicted the maximum electrophilic Fukui index with excellent accuracy. A composite custom risk score was formulated to rank environmental risk. The NH_2 group was identified as a critical structural alert, and flufenauxirim was predicted to have a medium-to-high aquatic toxicity profile, warranting experimental verification.

Keywords: DFT, QSAR, flufenauxirim, aminocyclopyrachlor, *in silico* toxicology

INTRODUCTION

Carboxylic acid herbicides, particularly pyrimidine and pyridine derivatives, are widely used for the selective control of broadleaf weeds because of their auxin-mimicking mode of action. [1, 2] However, their persistence in soil and water raises concerns about adverse ecotoxicological effects on non-target organisms such as fish, daphnia, algae and soil microorganisms. [3, 4]. Aminocyclopyrachlor (6-amino-5-chloro-2-cyclopropylpyrimidine-4-carboxylic acid) has been relatively well characterized experimentally, with reported acute fish LC_{50} >120 mg/L, Daphnia magna EC_{50} 39.7-43 mg/L and soil half-lives ranging from 3 to 112 days depending on environmental conditions [5, 6]. Flufenauxirim (6-amino-2-[2-fluoro-3-methoxy-4-(trifluoromethyl)phenyl] -5-methoxypyrimidine-4-carboxylic acid) is a next-generation herbicide that was provisionally approved by ISO in 2025 [7, 8]. It contains a trifluoromethyl group ($-CF_3$) and two methoxy substituents, which may alter its lipophilicity, electronic structure and toxicological profile compared to Aminocyclopyrachlor. To date, no experimental or computational data exist on the environmental effect or toxicity of flufenauxirim.

Density functional theory (DFT) provides a robust framework for computing molecular properties such as frontier orbital energies, chemical hardness, electrophilicity and Fukui functions, which are directly linked to chemical reactivity and potential toxicity mechanisms [9-12]. When combined with quantitative structure-activity relationship (QSAR) modelling, these descriptors can predict acute and chronic toxicity for data-poor compounds [13, 14]. Advanced machine learning approaches such as XGBoost, together with leave-one-out cross-validation (LOOCV), have been shown to improve prediction accuracy and are increasingly accepted by regulatory agencies for in silico risk assessment [15, 16].

In the present study, we systematically investigated the parent herbicides flufenauxirim and aminocyclopyrachlor together with a large set of substructural variants (108 structures) generated by removing or modifying key functional groups (NH_2, OCH_3, F, CF_3, Cl, COOH, OH, cyclopropyl and the pyrimidine core). The objectives were: first to compute global and local reactivity descriptors at the B3LYP/6-31G(d) level in gas phase and in water (CPCM); second to develop a high-accuracy QSAR model for predicting the maximum electrophilic Fukui index f^{+}_{max}; third to formulate a composite custom risk score for ranking environmental risk; and finally, to identify structural alerts that significantly elevate the predicted risk. The results provide the first *in silico* risk assessment framework for flufenauxirim and guide future experimental testing.

* To whom all correspondence should be sent:
E-mail: *yyalcin@nku.edu.tr*

© 2026 Bulgarian Academy of Sciences, Union of Chemists in Bulgaria

METHODOLOGY

All calculations were carried out using the Gaussian 09W program package (Revision D.01) [17]. The molecular structures of flufenauxirim and aminocyclopyrachlor were drawn with GaussView 6.0.

In addition to the parent molecules, a series of substructural variants was generated by systematically removing or replacing functional groups while preserving the core heterocyclic scaffold. This procedure yielded 80 unique structures for flufenauxirim and 28 for aminocyclopyrachlor, covering a wide range of electronic environments. The three-dimensional starting geometries were pre-optimized with the MMFF94 force field using Avogadro 1.2.0 before the DFT calculations.

Geometry optimizations and electronic property calculations were performed at the B3LYP hybrid functional level [18, 19] with the 6-31G(d) basis set [20]. This level of theory has been shown to provide reliable geometries, vibrational frequencies and frontier orbital energies for organic molecules of herbicide size [21, 22]. Solvent effects (water) were included using the conductor-like polarizable continuum model (CPCM) [23, 24]. Each structure was optimized twice: once in the gas phase ($\varepsilon = 1.0$) and once in water ($\varepsilon = 78.4$). All stationary points were confirmed by vibrational frequency analysis; no imaginary frequencies were found, indicating true local minima.

From the optimized gas-phase geometries, the following global reactivity descriptors were derived using Koopmans' theorem [25]: ionization potential $I \approx -E_{HOMO}$, electron affinity $A \approx -E_{LUMO}$, chemical hardness $\eta = (I - A)/2 = (E_{LUMO} - E_{HOMO})/2$, chemical softness $S = 1/(2\eta)$, electronegativity $\chi = (I + A)/2$ and the electrophilicity index $\omega = \chi^2/(2\eta)$ [26]. The HOMO and LUMO energies (in eV) as well as the dipole moments (in Debye) were taken directly from the Gaussian output files.

Local reactivity was analyzed *via* the Fukui functions using the finite-difference approximation [27, 28]. Single-point energy calculations were performed on the gas-phase optimized geometries for the neutral (charge 0, singlet), anionic (charge -1, doublet) and cationic (charge +1, doublet) species. Mulliken population analysis provided atomic charges $q_k(N)$ for the neutral molecule, $q_k(N+1)$ for the anion and $q_k(N-1)$ for the cation. The Fukui function for electrophilic attack was computed as $f^+_k = q_k(N) - q_k(N+1)$. The maximum value over all atoms, f^+_{max}, was recorded for each structure as a measure of the most electrophilically reactive site. Nucleophilic (f^-) and radical (f^0) indices were also calculated but are not discussed in detail here.

The solvation free energy ΔG_{solv} (in kcal·mol^{-1}) was obtained as the difference between the water-phase and gas-phase single-point energies at the same level of theory. All computed data including total energies (Hartree), dipole moments (Debye), HOMO, LUMO, ΔE, η, χ, ω, f^+_{max}, ΔG_{solv} and molecular descriptors such as molecular weight (MW), logP, topological polar surface area (TPSA) were extracted automatically using Python 3.14 with the CCLIB and PANDAS libraries and compiled into two Excel files which serve as the primary data repository.

A quantitative structure-activity relationship (QSAR) model was developed to predict f^+_{max} from the computed DFT descriptors and derived features. The model was built using the XGBoost algorithm [15] with leave-one-out cross-validation (LOOCV). The feature set included ΔE, η, ω, dipole moments (gas and water), ΔG_{solv}, logP, MW, TPSA, as well as interaction terms: $\log(f^+_{max})$, f^+/f^- ratio, $f^+ \times \Delta E$, $f^+ \times \eta$, $f^+ \times$dipole water and $f^+ \times \Delta G_{solv}$. The cross-validated predictive performance was evaluated using Q^2 (the squared correlation coefficient between predicted and observed values). The model achieved an excellent Q^2 of 0.9849, confirming its high predictive power.

Finally, a composite custom risk score was formulated to integrate multiple reactivity dimensions into a single ranking metric that can be used for environmental risk prioritization. The score is defined as Risk Score = $0.35 \cdot \omega + 0.45 \cdot f^+_{max} - 0.20 \cdot \eta$, where ω and f^+_{max} is positively correlated with electrophilic reactivity and potential toxicity, while η (hardness) is negatively correlated (harder molecules are less reactive). The coefficients were chosen empirically based on sensitivity analysis and on the known importance of electrophilicity and local reactivity in covalent binding to biological macromolecules [29, 30]. Based on the resulting risk scores, the structures were classified into three groups: high risk (score >1.0), medium risk ($0.4 \leq$ score ≤ 1.0) and low risk (score <0.4).

RESULTS AND DISCUSSION

The calculated global and local reactivity descriptors for the parent molecules and selected high-risk, medium-risk, and low-risk substructural variants are summarized in Tables 1 and 2 for aminocyclopyrachlor and flufenauxirim, respectively. Additionally, visual representations of the parent molecules and selected variants are provided in Figures 1 and 2.

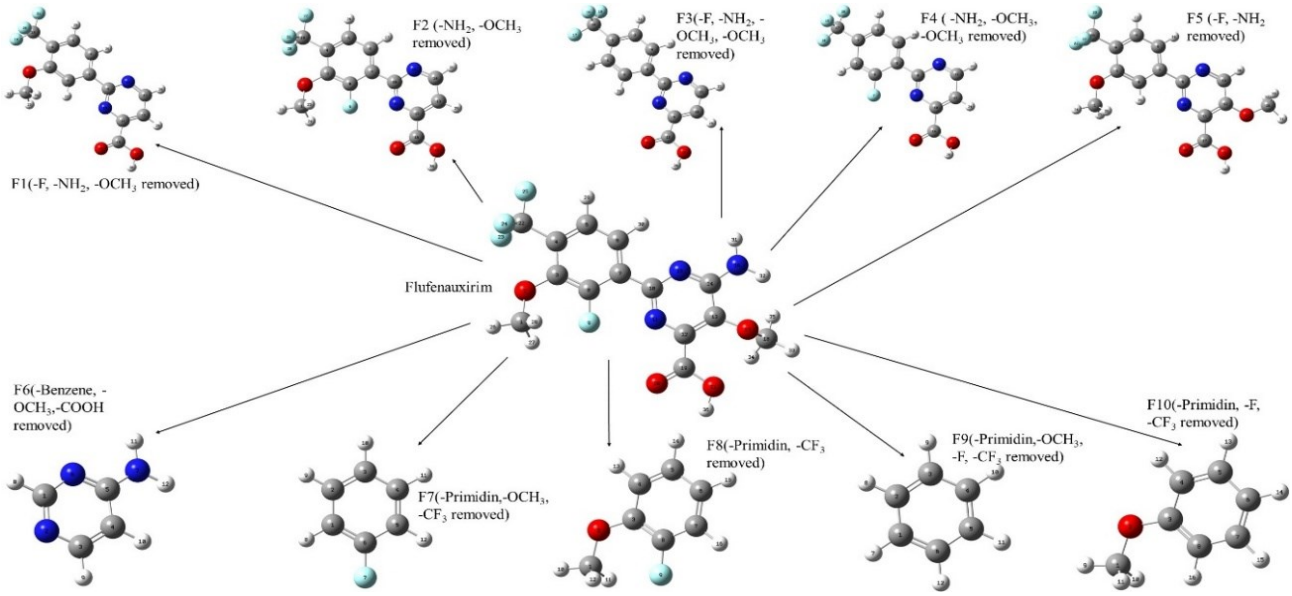

Figure 1. Chemical structures of the flufenauxirim parent molecule and selected substructural variants (A1-A10). (grey, C; white, H; red, O; blue, N; turquoise, F)

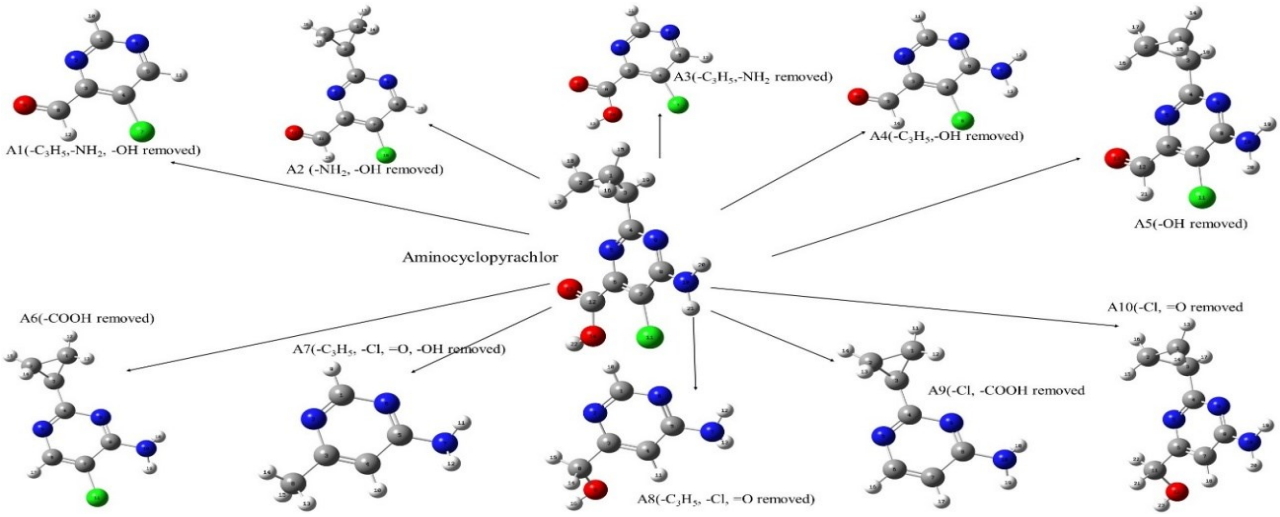

Figure 2. Chemical structures of the aminocyclopyrachlor parent molecule and selected substructural variants (F1-F10). (grey, C; white, H; red, O; blue, N; green, Cl)

Table 1. Computed reactivity descriptors and custom risk scores for flufenauxirim and its substructural variants (B3LYP/6-31G(d) CPCM water).

Molecule	ΔE Energy (eV)	η Hardness (eV)	f^{+}_{max}	ω Electrophilicity index (eV)	Risk score	Risk group
F1	4.116	2.066	0.135	4.716	1.298	High
F2	4.457	2.229	0.143	4.712	1.268	High
F3	4.625	2.312	0.151	4.711	1.255	High
F4	4.647	2.324	0.127	4.723	1.245	High
F5	4.112	2.061	0.145	4.428	1.203	High
Flufenauxirim	4.716	2.356	0.138	3.652	0.869	Medium
F6	5.698	2.849	0.213	1.981	0.219	Low
F7	6.066	3.033	0.170	1.841	0.114	Low
F8	5.749	2.871	0.212	1.497	0.045	Low
F9	6.031	3.021	0.165	1.603	0.031	Low
F10	5.801	2.901	0.191	1.384	-0.010	Low

Table 2. Computed reactivity descriptors and custom risk scores for aminocyclopyrachlor and its substructural variants (B3LYP/6-31G(d) CPCM water).

ID	ΔE Energy (eV)	η Hardness (eV)	f^{+}_{max}	ω Electrophilicity index (eV)	Risk score	Risk group
A1	4.651	2.323	0.168	5.827	1.650	High
A2	4.654	2.324	0.146	5.367	1.479	High
A3	5.031	2.516	0.172	4.949	1.306	High
A4	4.637	2.320	0.169	4.755	1.277	High
A5	4.644	2.321	0.171	4.458	1.173	High
Aminocyclopyrachlor	5.151	2.575	0.159	2.974	0.597	Medium
A6	5.525	2.763	0.155	2.171	0.277	Low
A7	5.752	2.872	0.166	1.890	0.162	Low
A8	5.758	2.881	0.208	1.822	0.155	Low
A9	5.754	2.878	0.181	1.817	0.142	Low
A10	5.736	2.869	0.188	1.630	0.082	Low

In both herbicide families, the removal of the amino ($-NH_2$) group consistently resulted in the highest risk scores, driven by a marked rise in electrophilicity and a decrease in chemical hardness. The parent molecule flufenauxirim exhibits a medium risk classification, yet its score is notably higher than that of aminocyclopyrachlor, indicating that flufenauxirim is intrinsically more reactive and potentially more toxic to aquatic organisms. The presence of the trifluoromethyl group and the two methoxy substituents in flufenauxirim thus appears to enhance its overall electron-accepting capacity. Conversely, variants lacking electron-withdrawing groups such as Cl, COOH or the entire pyrimidine core were assigned to the low-risk category. These structures display larger HOMO-LUMO gaps and higher chemical hardness, which are classic indicators of kinetic stability and reduced toxicity potential.

The XGBoost-based QSAR model demonstrated high predictive accuracy for the maximum electrophilic Fukui index, confirming that the selected DFT descriptors and interaction terms adequately capture the electronic factors governing local electrophilicity. This reliability reinforces the confidence in the resulting risk rankings.

A clear structural alert was identified: the amino ($-NH_2$) group functions as a critical modulator of environmental risk in pyrimidine carboxylic acid herbicides. Its removal renders the molecule more electron-deficient, as evidenced by increased electrophilicity and decreased hardness, making the derivatives more prone to covalent binding with nucleophilic sites in biological macromolecules a key mechanism of aquatic toxicity. The finding aligns with the known electron-donating nature of primary amines, and the presence or absence of this group can serve as a rapid screening criterion for toxicity.

The higher risk profile of flufenauxirim relative to aminocyclopyrachlor can be attributed to the strong electron-withdrawing effect of the $-CF_3$ group and the net electron-withdrawing contribution of the methoxy substituents in this conjugated system. The combined effect yields a molecule that is both more polarizable and more electrophilic than the reference herbicide. Experimental validation of this prediction through acute toxicity assays is strongly encouraged, as no such data currently exist for flufenauxirim.

Low-risk variants, characterized by the absence of key electron-withdrawing substituents or the pyrimidine core, exhibit high stability and low electrophilicity, consistent with the known low toxicity of simple heterocyclic cores. This suggests that the environmental risk of herbicide candidates could be substantially reduced by incorporating fewer electron-withdrawing groups or a less conjugated core, provided that herbicidal activity is maintained.

The excellent performance of the QSAR model indicates that the chosen set of DFT descriptors is sufficient for estimating local electrophilicity in related compounds, enabling application to other pyrimidine carboxylic acid derivatives within the applicability domain of the training set.

From a regulatory perspective, the proposed in silico framework supports early-stage screening of new herbicide candidates, aligning with the recommendations of agencies such as ECHA, EPA and OECD for the use of validated QSAR models in read-across and category approaches. For Flufenauxirim, a substance currently under regulatory review, the predicted medium-to-high risk profile highlights the need to prioritize experimental ecotoxicity testing, particularly for Daphnia magna and fish chronic endpoints.

Several limitations must be acknowledged. The QSAR model was trained solely on computed DFT

descriptors, and calibration against experimental toxicity data would strengthen its predictive power. Only the electrophilic Fukui function was incorporated into the risk score; future work should also consider nucleophilic and radical attack mechanisms. The empirical coefficients of the Custom Risk Score may be refined as experimental data become available. Finally, metabolic activation pathways were not considered, although they can convert a low-reactivity parent into a highly reactive intermediate *in vivo*. Despite these limitations, the integrated DFT-QSAR methodology offers a cost-effective, animal-free approach for preliminary environmental risk assessment of newly synthesized herbicides.

CONCLUSIONS

NH_2 group was identified as the strongest structural alert for high environmental risk, and Flufenauxirim is predicted to be more reactive than Aminocyclopyrachlor. Removal of electron-withdrawing groups yields low-risk variants with increased hardness and larger HOMO-LUMO gaps. The integrated DFT-QSAR approach provides a reliable framework for early-stage risk screening of new herbicide candidates, reduces the need for animal testing, and supports regulatory decision-making. For flufenauxirim, experimental acute and chronic toxicity tests are strongly recommended to validate the present predictions.

Acknowledgement: *The authors greatly appreciate Tekirdag Namik Kemal University Research Foundation for financial support. Project number: NKUBAP.01.GA.25.666*

REFERENCES

1. K. Grossmann, *Pest Manag. Sci.*, **66**, 113 (2010).
2. H. Cai, X. Gan, Z. Jin, G. Hao, *J. Agric. Food Chem.*, **71**, 9973 (2023).
3. J. Fairchild, in: Herbicides and Environment, A. Kortekamp (ed.), IntechOpen, Rijeka, 2011, p. 383.
4. D. Bamal, A. Duhan, A. Pal, R. K. Beniwal, P. Kumawat, S. Dhanda, A. Goyat, V. S. Hooda, R. Yadav, *Environ. Chem. Lett.*, **22**, 2977 (2024)
5. EPA (Environmental Protection Agency), Pesticide Fact Sheet: Aminocyclopyrachlor, Washington, DC, 2010.
6. OECD, Health and environmental safety of aminocyclopyrachlor and related compounds, OECD Environmental Health and Safety Publications, Paris, 2011.
7. ISO, Flufenauxirim provisional classification and regulatory status, ISO Technical Report, 2025a.
8. ISO, Regulatory decisions on new pesticide active substances, ISO Guidelines Document, 2025b.
9. R. G. Parr, W. Yang, Density-Functional Theory of Atoms and Molecules, Oxford Univ. Press, New York, 1989.
10. D. Şakar, E Üstün, *Russian Journal of Inorganic Chemistry*, **68**(9), 1303 (2023).
11. R. G. Pearson, Chemical Hardness: Applications from Molecules to Solids, Wiley-VCH, Weinheim, 1997.
12. M. Sönmez Çelebi, M. Çol Ayvaz, D. Şakar, E. Üsün, Ö. Ertürk, *Inorganica Chimica Acta*, **585**, 122752 (2025).
13. M. T. D. Cronin, J. D. Walker, J. S. Jaworska, M. H. I. Comber, C. D. Watts, A. P. Worth, *Environ. Health Perspect.*, **111**, 1391 (2003).
14. J. C. Dearden, M. T. D. Cronin, K. L. E. Kaiser, *SAR QSAR Environ. Res.*, **20**, 241 (2009).
15. T. Chen, C. Guestrin, Proc. 22nd ACM SIGKDD Int. Conf. Knowl. Discov. Data Min., 785 (2016).
16. OECD, Guidance on Grouping of Chemicals, Second Edition, OECD Series on Testing and Assessment No. 194, Paris, 2014.
17. M. J. Frisch, G. W. Trucks, H. B. Schlegel, Gaussian 09, Revision D.01, Gaussian Inc., Wallingford, CT, 2009.
18. A. D. Becke, *J. Chem. Phys.*, **98**, 5648 (1993).
19. C. Lee, W. Yang, R. G. Parr, *Phys. Rev. B*, **37**, 785 (1988).
20. W. J. Hehre, L. Radom, P. v. R. Schleyer, J. A. Pople, *Ab Initio* Molecular Orbital Theory, Wiley-Interscience, New York, 1986.
21. Z. Heidarnezhad, F. Heidarnezhad, I. Ganiev, Z. Obidov, *Chem. Sci. Trans.*, **2**, 1370 (2013).
22. J. Lorenc, L. Dyminska, Z. Talik, J. Hanuza, M. Mączka, *J. Raman Spectrosc.*, **39**, 1 (2008).
23. V. Barone, M. Cossi, J. Tomasi, *J. Comput. Chem.*, **19**, 404 (1998).
24. M. Cossi, V. Barone, B. Mennucci, J. Tomasi, *Chem. Phys. Lett.*, **286**, 253 (1998).
25. T. Koopmans, *Physica*, **1**, 104 (1934).
26. R. G. Parr, W. Yang, *J. Am. Chem. Soc.*, **106**, 4049 (1984).
27. W. Yang, W. J. Mortier, *J. Am. Chem. Soc.*, **108**, 5708 (1986).
28. R. G. Parr, W. Yang, *J. Am. Chem. Soc.*, **106**, 4049 (1984).
29. S. J. Enoch, M. T. Cronin, *Crit. Rev. Toxicol.*, **40**, 728 (2010).
30. A. P. Worth, M. T. D. Cronin, *Altern. Lab. Anim.*, **31**, 515 (2003).

Bulgarian Chemical Communications, Volume 58, Issue 3 (pp. 396-400) 2026 *DOI: 10.34049/bcc.58.3.D028*

Sustainable and bioactive chitosan/PVA hydrogels incorporating allantoin for wound healing applications

M. Özbakış[1], D. Ismaili Uka[1], P. Terzioğlu[1]*, Y. Sicak[2]

[1]*Bursa Technical University, Faculty of Engineering and Natural Sciences, Department of Polymer Materials Engineering, Bursa, Türkiye*

[2]*Muğla Sıtkı Koçman University, Köyceğiz Vocational School, Department of Herbal and Animal Production, Muğla, Türkiye*

Accepted: July 28, 2026

Conventional wound dressings mainly provide passive protection and are often insufficient to maintain the bioactive conditions necessary for effective healing. Hydrogel-based materials have attracted considerable attention due to their biocompatibility, moisture-retention capacity, and structural similarity to biological tissues. In this study, bioactive PVA/chitosan hydrogel films incorporating allantoin (0.5–1.5 wt.%) were developed using a solution casting method, and evaluated in terms of morphology, tensile properties, and antioxidant activity. Morphological observations revealed that increasing allantoin concentration affected film homogeneity and transparency. The sample containing 1.0 wt.% allantoin exhibited visible particulate aggregation within the polymer matrix. Tensile analysis demonstrated that allantoin incorporation decreased tensile strength and elongation at break while increasing elastic modulus, indicating reduced polymer chain mobility and a transition toward a stiffer structure. Antioxidant activity results exhibited a concentration-dependent behavior. Among the developed samples, the 0.5 wt.% allantoin-loaded hydrogel showed the highest antioxidant activity in both DPPH and β-carotene/linoleic acid assays, whereas higher concentrations resulted in reduced performance. The results indicate that 0.5 wt.% allantoin incorporation provides an effective balance between antioxidant functionality and mechanical performance, highlighting the promising potential of the hydrogel system as a bioactive and mechanically stable material for wound healing and dermatological applications.

Keywords: Allantoin, Chitosan, Polyvinyl alcohol, Hydrogel, Wound healing.

INTRODUCTION

Wound healing is a complex biological process involving overlapping phases of hemostasis, inflammation, proliferation, and tissue remodeling. Successful healing requires a balanced microenvironment that supports tissue regeneration while minimizing microbial contamination and oxidative stress. Conventional wound dressings such as gauze mainly provide passive protection and are often insufficient to maintain the moist and bioactive conditions required for efficient wound repair. In recent years, hydrogel-based wound dressings have attracted considerable attention due to their high-water content, flexibility, oxygen permeability, and extracellular matrix-like structure, making them promising materials for advanced wound care applications [1]. Among hydrogel-forming polymers, poly (vinyl alcohol) (PVA) is widely used because of its excellent film-forming ability, mechanical stability, hydrophilicity, and biocompatibility. However, PVA alone exhibits limited biological functionality. Chitosan, a naturally derived polysaccharide, has been extensively investigated for biomedical applications owing to its biodegradability, hemostatic activity, and intrinsic antimicrobial behavior. The combination of PVA and chitosan enables the development of composite hydrogel systems with balanced mechanical and biological properties through intermolecular hydrogen bonding interactions [2].

To further improve hydrogel functionality, bioactive compounds can be incorporated into the polymer matrix. Allantoin is a bioactive molecule known for its antioxidant, anti-inflammatory, moisturizing, analgesic activity and tissue regenerative properties [3]. In addition, allantoin has been reported to promote epithelial cell proliferation and support wound healing processes in hydrogel and scaffold systems [3]. Moreover, allantoin promotes skin, moisturization, supports the elimination of necrotic tissue, and aids in the prevention of gastric ulcers [4]. However, studies investigating the influence of allantoin concentration on the mechanical and antioxidant properties of PVA/chitosan hydrogel films remain limited.

Therefore, the present study aimed to develop allantoin-loaded PVA/chitosan hydrogel films using a solution casting method and to evaluate the effect of allantoin concentration on the morphology, tensile

* To whom all correspondence should be sent:
E-mail: pinar.terzioglu@btu.edu.tr

© 2026 Bulgarian Academy of Sciences, Union of Chemists in Bulgaria

properties, and antioxidant activity of the prepared hydrogel systems for potential wound dressing applications.

MATERIALS AND METHODS

Materials

Chitosan was obtained from Sigma-Aldrich (Darmstadt, Germany). Poly (vinyl alcohol) was supplied by Zag Kimya (İstanbul, Türkiye). Glycerol was purchased from Merck (Darmstadt, Germany), while glacial acetic acid (100% anhydrous) was obtained from ISOLAB Chemicals (Germany). Allantoin (≥99%) was provided by Sky Pharmaceutical Chemical Food Industry and Trade Ltd. (Türkiye). Butylated hydroxytoluene (BHT), α-tocopherol, β-carotene, 1,1-diphenyl-2-picrylhydrazyl (DPPH), and linoleic acid were acquired from Sigma-Aldrich (Steinheim, Germany).

Preparation of chitosan/PVA/allantoin films

Four different composite films were developed by the casting method. Chitosan was dissolved in aqueous acetic acid solution (2 % v/v) at 50 °C with continuous stirring (600 rpm) for 2 h to obtain chitosan solution (1 % w/v). The PVA solution (5 % w/v) was prepared in distilled water at 75 °C for 12 h with stirring (250 rpm). The solutions of PVA and chitosan were mixed at 2:1 v/v ratio by mechanical stirrer (600 rpm) to obtain a homogeneous solution. Further, a specific amount of the allantoin (0, 0.50, 1.0 or 1.5 wt. % in respect to the total volume of film forming solution (100 mL) was added to the solution and stirred at 50 °C for 1.5 h (250 rpm). As plasticizer glycerol (300 µL) was added to the mixed solution and the resulting mixture was stirred for half an hour at room temperature. This mixture (40 mL) was then cast onto round glass petri dishes (14 × 14 cm) and dried in an oven at 50 °C for 18 h (Fig. 1.). The prepared films were labeled as CP-0A (control, without allantoin) and CPA-x, where x represents the allantoin concentration (0.5, 1.0, and 1.5%, w/w), respectively.

Tensile properties determination

The mechanical properties of the composite films were determined with ASTM D882 standard using an AGS-X Series universal testing machine (Shimadzu, Japan). The crosshead speed and load cell were 15 mm/min and 1 kN, respectively. The data was collected by testing five separate samples.

Antioxidant activity determination

The antioxidant capacities of the samples were evaluated using two complementary assays: the DPPH radical scavenging method [5, 6], and the β-carotene/linoleic acid assay [7].

For the analyses, the films were cut into small fragments and dissolved in the corresponding test solutions. Biological activity measurements were performed at four different concentrations: 25, 12.5, 6.25, and 3.125 µg/mL. Antioxidant performance was expressed as the IC_{50} value, representing the concentration required to achieve 50% inhibition. Butylated hydroxytoluene (BHT) and α-tocopherol (TOC) were used as reference antioxidant compounds for comparison. All measurements were conducted using a 96-well microplate reader (SpectraMax 340PC384, Molecular Devices, USA).

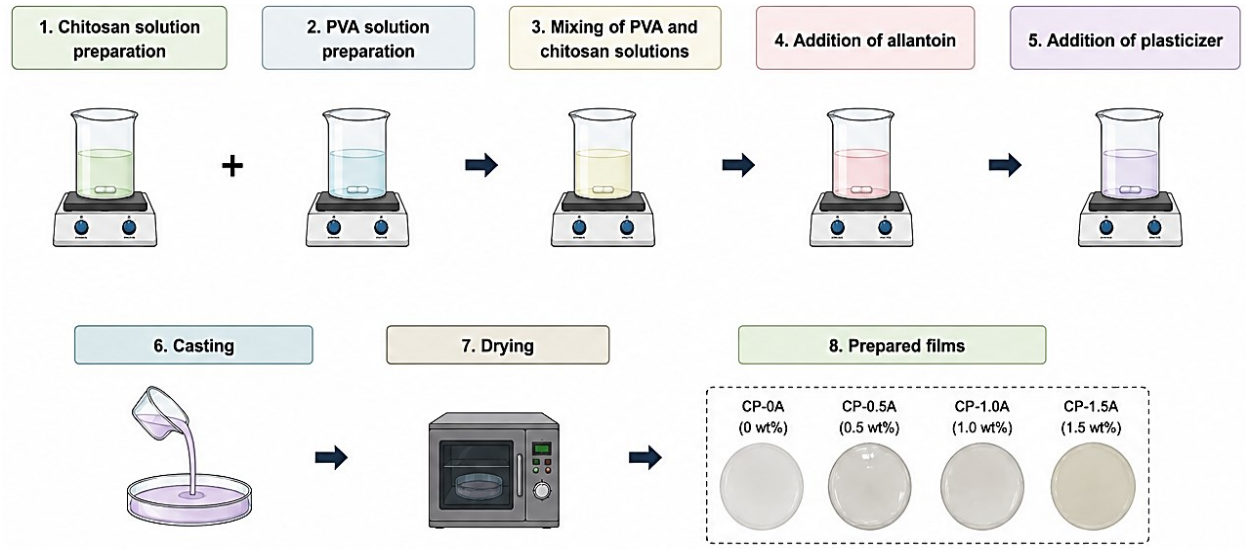

Figure 1. Schematic illustration of allantoin-loaded composite film preparation.

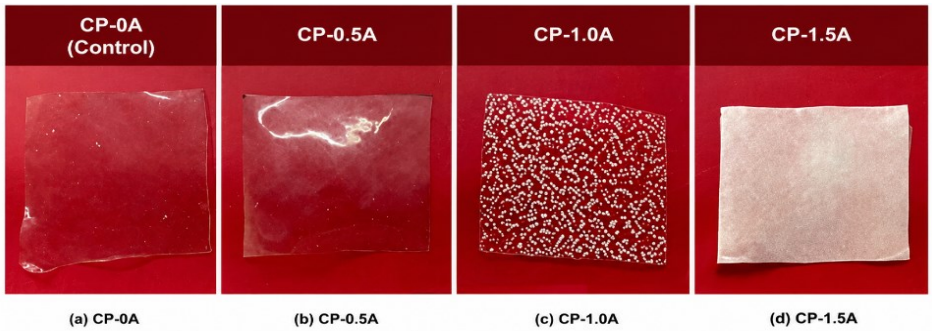

Figure 2. Photographs of chitosan/PVA hydrogel films incorporating different concentrations of allantoin. a) CP-0A (control, without allantoin), b) CP-0.5A (0.5% w/w), c) CP-1.0A (1.0% w/w), and d) CP-1.5A (1.5% w/w).

RESULTS

Morphological evaluation of films

The visual appearance of chitosan/PVA films incorporating different concentrations of allantoin were presented in Figure 2. The images demonstrated the successful formation of chitosan/PVA/allantoin films using the casting method. The control sample (CP-0A) exhibited a relatively smooth and transparent structure, indicating a homogeneous polymeric network. A similar morphology was observed for CP-0.5A, although slight surface irregularities and minor opacity changes became noticeable, suggesting initial interactions between allantoin and the polymer matrix.

In contrast, the CP-1.0A sample showed a distinctly heterogeneous appearance with visible white particulates distributed throughout the film. This observation may indicate aggregation of allantoin within the polymer network, leading to reduced structural uniformity. Such heterogeneity can be associated with limited dispersion of the bioactive compound at higher concentrations.

For the CP-1.5A sample, the film appeared opaquer and more uniform compared to CP-1.0A, although transparency was significantly reduced relative to lower concentrations. This change may reflect a partial redispersion of allantoin, resulting in a more compact but less transparent structure.

The visual observations suggest that allantoin concentration influences the morphological characteristics of the hydrogel films, affecting transparency, homogeneity, and surface structure. These changes may have implications on the functional properties of the materials.

Mechanical properties of the films

The mechanical properties of the chitosan/PVA films are presented in Table 1. The control sample (CP-0A) exhibited the highest tensile strength (40.55 N / mm^2) and elongation at break (325.17 %), indicating a flexible and mechanically robust network.

Table 1. Tensile results of synthesized compounds

Parameter	CP-0A	CP-0.5A	CP-1.5A
Tensile strength at break (N/mm^2)	40.55	30.50	23.25
Elongation at break (%)	325.17	287.50	132.65
Elastic modulus	20.91	70.00	100.26

The incorporation of allantoin (CP-0.5A and CP-1.5A) resulted in a decrease in tensile strength and elongation at break, accompanied by a significant increase in elastic modulus. This behavior can be attributed to the disruption of intermolecular hydrogen bonding between chitosan and PVA chains, as well as the formation of heterogeneous domains that restrict polymer chain mobility. It is well established that the mechanical performance of chitosan/PVA hydrogels is strongly influenced by hydrogen bonding, crystallinity, and network homogeneity [8, 9]. Furthermore, the increase in elastic modulus with higher allantoin content indicates a transition toward a stiffer and less deformable structure, consistent with reduced chain mobility. From an application perspective, an ideal wound dressing material requires a balance between mechanical strength and flexibility. In this context, the CP-0.5A formulation appears to provide a more suitable mechanical profile compared to higher allantoin concentrations.

It should be noted that the CP-1.0A sample was not included in the tensile analysis. As observed in the morphological evaluation (Figure 2), this formulation exhibited pronounced heterogeneity and visible particulate domains, suggesting phase separation and poor dispersion of allantoin within the polymer matrix. Such structural inhomogeneity can compromise film integrity and reproducibility during tensile testing, leading to unreliable mechanical data. Similar limitations have been

reported in hydrogel systems where non-uniform distribution of components adversely affects structural integrity and mechanical performance [10].

Antioxidant activity of the films

Oxidative stress arises from an imbalance between the production of reactive oxygen species (ROS) and the capacity of the biological system's antioxidant defenses to neutralize them [11]. ROS are regulated by a complex antioxidant defense system that maintains their levels within an appropriate range, enabling their normal physiological functions while limiting excessive oxidative damage that may contribute to the development of various diseases [12]. Elevated ROS levels can lead to metabolic disturbances, loss of cellular integrity, altered gene expression, and impaired enzymatic activity [13]. In infected wounds, excessive ROS and free radicals further damage tissues and inflammatory cells, thereby delaying the healing process and contributing to chronic wounds [14]. Compounds exhibiting strong free radical scavenging activity have been reported to enhance and accelerate wound repair [15].

The antioxidant activity results varied by the allantoin concentration (Table 2). The control sample exhibited the highest IC_{50} values, indicating minimal activity that can be attributed to the chitosan containing the amino groups, whereas 0.5 wt.% allantoin significantly enhanced antioxidant performance, suggesting effective radical scavenging at low concentrations. Increasing the concentration of allantoin to 1 wt.% and 1.5 wt.% resulted in decline in antioxidant activity. This reduction may be attributed to concentration-dependent physicochemical changes, such as intermolecular interactions or aggregation, limiting the accessibility of active sites. Similar behavior has been reported in hydrogel-based systems, where antioxidant efficiency depends on network structure and the distribution of functional components [16]. Additionally, studies on allantoin-containing biomaterials indicate that its activity depends on its interaction with the surrounding matrix and effective availability within the system [4].

In conclusion, allantoin exhibits a concentration-dependent dual effect, where lower dose of incorporation enhances antioxidant capacity, whereas higher concentrations may reduce functional efficiency, highlighting the need for optimized formulation.

Table 2. Antioxidant activity results of the synthesized compounds

Compounds antioxidant activity	β-Carotene-linoleic acid (IC_{50} μM/mL)	$DPPH^{\cdot}$ assay (IC_{50} μM/mL)
CP-0A	75.11±0.27	60.44±0.35
CP-0.5A	30.36±0.28	21.19±1.01
CP-1.0A	64.13±1.21	55.07±0.44
CP-1.5A	46.04±0.09	34.31±0.20
α-TOC	4.67±0.20	12.79±0.65
BHT	2.84±0.65	55.22±0.84

CONCLUSION

In this study, chitosan/PVA-based hydrogel films incorporating different concentrations of allantoin were successfully prepared and evaluated in terms of their morphological, mechanical, and antioxidant properties. The results demonstrated that allantoin concentration plays a critical role in determining the overall performance of the hydrogel system.

Morphological observations revealed that increasing allantoin content affects the structural homogeneity of the films, with higher concentrations leading to visible heterogeneity and reduced transparency. These structural changes were found to be closely associated with variations in mechanical behavior. Specifically, the incorporation of allantoin resulted in decreased tensile strength and elongation at break, accompanied by an increase in elastic modulus, indicating a transition toward a stiffer but less flexible network. Antioxidant analysis further indicated a non-linear concentration-dependent behavior, with the 0.5 wt.% allantoin formulation exhibiting the highest antioxidant activity.

The findings highlight that an optimal balance between structural integrity, mechanical performance, and antioxidant activity can be achieved at lowest allantoin concentration. Among the tested formulations, CP-0.5A demonstrated the most favorable combination of properties, suggesting its potential suitability for wound healing applications and skin regeneration. These results emphasize the importance of formulation optimization in the development of bioactive hydrogel systems. Further studies should be realized on the anti-inflammatory, antimicrobial and cytocompatibility properties of the fabricated films.

REFERENCES

1. J. Zhao, P. Qiu, Y. Wang, Y. Wang, J. Zhou, B. Zhang, D. Gou. Int. *J. Biol. Macromol*., **244**, 125250 (2023).
2. S. Liu, D. Li, Y. Wang, G. Zhou, K. Ge, L. Jiang. *Int. J. Biol. Macromol*., **228**, 744 (2023).
3. Y.D. Nokoorani, A. Shamloo, M. Bahadoran, H. Moravvej. *Sci. Rep*., **11**(1), 16164 (2021).

4. M. Koosha, H. Aalipour, M.J. Sarraf Shirazi, A. Jebali, H. Chi, S. Hamedi, N. Wang, T. Li, H. Moravvej. *J. Funct. Biomater*., **12**(4), 61 (2021).
5. P. Terzioglu, F. Güney, F.N. Parın, I. Sen, S. Tuna. *Food Packag. Shelf Life,* **30**, 100742 (2021).
6. M. Oztürk, G. Tel, F.A. Oztürk, M.E. Duru. *J. Nat. Prod.,* **8**(2), 189 (2014).
7. M. Öztürk, F. Aydoğmuş-Öztürk, M.E. Duru, G. Topçu. *Food Chem*. **103**(2), 623 (2007).
8. C. Luo, Y. Zhao, X. Sun, B. Hu. *Mater. Lett*., **280**, 128499 (2020).
9. S. Bi, J. Pang, L. Huang, M. Sun, X. Cheng, X. Chen. *Int. J. Biol. Macromol*., **146**, 99 (2020).
10. D.N. Iqbal, S. Shafiq, S.M. Khan, S.M. Ibrahim, S.A. Abubshait, A. Nazir, M. Iqbal. *Int. J. Biol. Macromol*., **164**, 499 (2020).
11. A. Rauf, A.A. Khalil, S. Awadallah, S. A. Khan, T. Abu-Izneid, M. Kamran, H. Hemeg, M. S. Mubarak, A. Khalid, P. Wilairatana. *Food Science & Nutrition*, **12**, 675 (2024).
12. B. Halliwell. *Nat. Rev. Mol. Cel.l Biol.,* **25**, 13 (2024).
13. K. Khorsandi, R. Hosseinzadeh, H.S. Esfahani, K. Zandsalimi, F. K. Shahidi, H. Abrahamse. *Inflamm. Regener.,* **42**, 40 (2022).
14. K. Ukaegbu, E. Allen, K.K.H. Svoboda. *Int. Wound J.*. **22**, e70330 (2025).
15. N. Sakthiguru, M.A. Sithique. *Int. J. Biol. Macromol*., **152**, 873 (2020).
16. L. Yang, Y. Zeng, H. Wu, C. Zhou, L. Tao. *J. Mater. Chem., B,* **8**(7), 1383 (2020).

Bulgarian Chemical Communications, Volume 58, Issue 3 (pp. 401-410) 2026 *DOI: 10.34049/bcc.58.3.D029*

Comparative evaluation of infrared and microwave drying of berries: kinetics, diffusivity, and modeling approaches

E. Kıpçak*

Department of Chemical Engineering, Faculty of Chemical and Metallurgical Engineering, Davutpasa Campus, Yıldız Technical University, Davutpasa Street, No. 127, 34220, Esenler, İstanbul, Türkiye

Accepted: July 28, 2026

Berries are highly valued fruits which are widely cultivated for their distinctive flavor, rich nutritional composition, and health-promoting properties. However, despite their health benefits and nutritional merit, berries have a perishable nature due to their high moisture contents and delicate structures. Therefore, effective preservation methods are essential to extend their availability and reduce losses associated with microbial spoilage and seasonal production. Drying is a commonly employed preservation method which prolongs the shelf life while helping to retain nutritional quality and bioactive components. Although numerous studies have investigated changes in antioxidant capacity and nutritional composition during drying, research focusing on drying kinetics and mathematical modelling remains relatively limited. Therefore, the present study examines the infrared and microwave drying behavior of two types of berries: blueberries and golden berries. Infrared drying experiments were performed at temperatures of 60, 70, and 80°C, and microwave drying was carried out at power levels of 140, 210, and 350 W. For all experimental conditions, key kinetic parameters, along with effective moisture diffusivity values (D_{eff}) were determined. In addition, drying curves were analyzed using widely recognized mathematical models reported in the literature studies. Experimental results demonstrated that both drying methods are effective for the drying of blueberries and golden berries. The shortest drying times and the highest D_{eff} values were obtained at the highest infrared temperature and microwave power level.

Keywords: Blueberry; golden berry; infrared drying; microwave drying; mathematical modelling

INTRODUCTION

In recent years, berries have attracted increasing attention owing to their desirable taste and numerous health benefits. In addition, berries are rich in bioactive compounds that are associated with their anticarcinogenic and antioxidant properties. Blueberries and golden berries are among the berry fruits that have gained considerable consumer interest. Blueberries (*Vaccinium corymbosum*) are fruits characterized by their distinctive sweet-sour flavor and dark purple color. They are predominantly cultivated in regions of America and Europe. Blueberries are an important source of bioactive compounds, phenolic acids, flavonoids, vitamins, minerals, anthocyanins, and dietary fibers [1]. Furthermore, blueberries have been associated with protective effects against several diseases and health disorders, including Alzheimer's disease, urinary and cardiovascular diseases, muscular degeneration, diabetes, and cancer [2-5].

Golden berry (*Physalis peruviana*), on the other hand, is native to the Andean region of South America, where it has traditionally been cultivated [6, 7]. Also known as cape gooseberry, the fruit has a yellow-colored skin and is enclosed within a dry, parchment-like husk known as the calyx, which provides protection against unfavorable climatic conditions, as well as birds and insects [8-10]. Similar to blueberries, golden berries have received considerable attention because of their nutritional composition and high content of bioactive compounds. They contain considerable amounts of vitamins, particularly vitamins A, B-complex, C, and K, as well as minerals, dietary fibers, ascorbic acid, polyphenols, and carotenoids [7-11]. Golden berries have also been reported to have traditional and potential therapeutic applications in the management of various conditions, including cancer, hypertension, hepatitis, asthma, dermatitis, and rheumatism [12-14]. The relatively high vitamin K content may contribute to health benefits associated with blood clotting and bone metabolism and has been linked to a reduced risk of cancer and cardiovascular diseases. Owing to their fructose content, golden berries have also been suggested as a suitable fruit option for people with diabetes [10, 13]. Despite their nutritional and health-related benefits, both berries have relatively limited seasonal availability. Their delicate structure makes them susceptible to mechanical damage, while their high perishability limits their storage lives [3, 5].

* To whom all correspondence should be sent:
E-mail: eyildir@yildiz.edu.tr

© 2026 Bulgarian Academy of Sciences, Union of Chemists in Bulgaria

Consequently, different food processing and preservation technologies have been employed to improve their shelf lives and maintain their quality during storage. Among these preservation techniques, drying is one of the most effective approaches. It involves the removal of moisture from a material, thereby slowing deterioration processes and helping to maintain product quality. Under regulated drying conditions, moisture can be efficiently removed from food products, reducing microbial growth and moisture-related deterioration, including decay and mold formation [15, 16]. This is particularly advantageous for food products with short harvesting seasons, as drying enables the preservation of large quantities of produce for extended periods. In addition, drying reduces product volume and weight, thereby decreasing packaging, processing, transportation, and storage costs while simultaneously improving the shelf life and increasing the overall value of the product [2, 17]. Nevertheless, traditional drying methods are slow and energy-demanding because they depend on heat and air flow to evaporate water. This creates a major problem for delicate berries, as high temperatures easily destroy their heat-sensitive, beneficial bioactive compounds. Consequently, exploring alternative options like infrared and microwave drying is essential to protect berry quality, while improving the drying performance.

Infrared drying facilitates thermal energy transfer to the product through electromagnetic radiation, enabling efficient and relatively uniform heating. In this technique, thermal energy is delivered directly to the food material in the form of radiant energy [18]. Water strongly absorbs infrared radiation, and the absorbed energy induces vibrational motion of the O-H bonds within water molecules. The rapid internal heating generated by this mechanism elevates the vapor pressure in the food material, promoting the expansion of pores and, consequently, accelerating moisture removal [18, 19]. As a result, infrared drying can achieve rapid and efficient moisture removal. In addition to shortening drying times, infrared drying provides several advantages, including simpler equipment design, more uniform product temperatures, improved product quality, reduced energy consumption, lower operating costs, and broad applicability to different food materials [15, 20-23].

Microwave drying, in contrast, uses electromagnetic radiation within the frequency range between 300 MHz and 300 GHz [21, 24]. This technology offers several important advantages because electromagnetic energy is directly absorbed by water molecules as a result of their dipolar nature and subsequently converted into heat through molecular motion [16, 18, 25]. According to Feng *et al*. [24], the principal advantages of microwave drying are volumetric heating and generation of vapor within the product. Heating within the product promotes the development of internal vapor pressure, which facilitates the migration and removal of moisture from the material. Consequently, microwave drying can provide rapid drying with high energy efficiency, while contributing to better product quality and color retention, as well as safer handling and easier operation [21, 23, 24, 26]. In food drying applications, microwave drying is also frequently combined with conventional techniques, including hot-air and vacuum drying [14, 18]. Previous studies have shown that integrating microwave heating with conventional drying methods as a hybrid process can substantially reduce drying time and energy consumption, while increasing the drying rate and overall process efficiency [16, 21].

To date, research on berry drying has primarily focused on the extraction of bioactive materials and the evaluation of antioxidant activity, whereas comparatively limited attention has been given to the kinetic characteristics of the drying procedure. Considering the information presented above and the limited number of studies addressing drying kinetics, moisture diffusivity, and mathematical modelling, the present study investigated the infrared and microwave drying behavior of blueberries and golden berries. The experiments on infrared drying were performed at 60, 70, and 80°C, whereas microwave drying was performed at powers of 140, 210, and 350 W. For each experimental condition, drying time, moisture content, and drying rate were evaluated. Important kinetic parameters were subsequently calculated, including effective moisture diffusivity. Furthermore, 14 standard mathematical models from existing literature were used to fit the experimental drying curves. The results were then compared with the author's prior research on oven drying and vacuum oven drying of blueberries [27] and golden berries [28].

EXPERIMENTAL

Berry samples

The blueberries employed in this study were cultivated in Chile, while the golden berries were cultivated in Columbia. Both types of berries were purchased from a market in İstanbul. For each experimental run, 10 ± 0.1 g of berries with comparable dimensions were selected. The blueberries had an approximately 1.1 cm diameter, whereas the golden berries had an approximately 2.1

cm diameter. The berries were horizontally sectioned into two equal halves prior to the drying experiments to facilitate the investigation of thin layer moisture diffusion.

The initial moisture content of the berry samples were determined with respect to the AOAC method [29]. For this purpose, the berry samples were dried at 105°C in a hot-air oven for 4 h (KH - 45, Kenton, Guangzhou, China). Accordingly, the initial moisture content of the blueberries and golden berries was determined as 84.33% and 74.93% on wet basis, corresponding to 5.38 and 2.99 kg water/kg dry matter, respectively.

Experimental procedure

In the infrared drying experiments, a Radwag MA 50. R infrared dryer was employed, operating at 50 MHz and with 230 V (Radwag Balances and Scales, Radom, Poland). The drying experiments were performed at temperatures of 60, 70, and 80°C. Microwave drying experiments were conducted using an HMT72G420 model Bosch microwave oven, with dimensions of 530 × 500 × 322 mm (Robert Bosch Hausgeräte GmbH, Munich, Germany). The microwave oven operated at 2450 MHz and had a maximum power of 800 W. Drying experiments were performed at microwave powers of 140, 210, and 350 W.

During infrared drying, the sample weights were monitored at 15-min intervals throughout the process to calculate the moisture loss and corresponding drying rate. Owing to the considerably faster moisture removal observed during microwave drying, shorter weighing intervals were employed. Accordingly, the blueberry samples were weighed every 6 min, while the golden berry samples were weighed every 30 s, 20 s, and 10 s at microwave powers of 140, 210, and 350 W, respectively. The mean values obtained for three independent replicates at each experimental condition were used in the calculations. Drying was conducted across all experimental runs, until a final moisture content of 7% was attained.

Kinetic calculations

For each experimental condition the moisture content, M, the drying rate, DR, and the moisture ratio, MR were determined by using Equations (1), (2), and (3), respectively [15, 27, 28]:

$$M = \frac{m_w}{m_d} \quad (1)$$

$$DR = \frac{M_{t+dt} - M_t}{dt} \quad (2)$$

$$MR = \frac{M_t - M_e}{M_0 - M_e} \quad (3)$$

In Equation (1), m_w and m_d are the water content of the berry samples and their dry matter content (kg), respectively. In Equation (2), t is the drying time in min, M_{t+dt} denotes the moisture content at the time t+dt, and M_t represents the moisture content at the time t (kg water/kg dry matter). In Equation (3), M_t, M_e, M_0 correspond to the moisture content at time t, the moisture content at equilibrium, and the initial moisture content, respectively, expressed as kg water/kg dry matter. Since M_e had a relatively low value, it was assumed to be negligible in the calculations [1, 30].

Moisture diffusion during drying was analyzed by Fick's 2nd law of diffusion. Application of this model was based on the assumptions of negligible sample shrinkage, symmetrical moisture diffusion with respect to the sample's center, and constant effective moisture diffusivity. With these assumptions, Fick's 2nd law of diffusion for moisture through a thin layer with a 2L thickness is given by Equation (4) [1, 19, 30]:

$$\mathrm{MR} = \frac{8}{\pi^2} \sum_{n=1}^{\infty} \frac{1}{(2n+1)^2} \exp\left(-\frac{(2n+1)^2 \pi^2 D_{eff} \times t}{4L^2}\right) \quad (4)$$

Here, n is positive and can be approximated as 1 for sufficient drying times. L corresponds to half of the sample thickness (m), D_{eff} is the effective moisture diffusivity (m^2/s), and t is the drying time (s). By considering n = 1, Equation (4) can be expressed in its linearized form as Equation (5) [1, 19, 30]. Accordingly, D_{eff} can be calculated through the slope of the linear relation between ln(MR) and drying time.

$$\ln(\mathrm{MR}) = \ln\left(\frac{8}{\pi^2}\right) - \left(\pi^2 \frac{D_{eff} \times t}{4L^2}\right) \quad (5)$$

Mathematical modelling

To model the infrared and microwave drying behavior of blueberries and golden berries, experimental data were fitted to 14 standard mathematical models from existing literature. The 14 models considered in the analysis were given in the author's previous work [27, 28]. The model parameters were estimated *via* non-linear regression, through the Levenberg-Marquardt algorithm implemented in Statistica 8 program. The adequacy of each mathematical model was assessed using the coefficient of determination, root mean square error, and reduced chi-square, denoted by R^2, RMSE, and χ^2, respectively, which were determined through Equations (6), (7), and (8) [27, 31].

$$R^2 = 1 - \frac{\sum_{i=1}^{N}\left(MR_{exp,i} - MR_{pre,i}\right)^2}{\sum_{i=1}^{N}\left(MR_{exp,i} - \left(\frac{1}{n}\right)MR_{exp,i}\right)^2} \quad (6)$$

$$RMSE = \left(\frac{1}{N}\sum_{i=1}^{N}\left(MR_{exp,i} - MR_{pre,i}\right)^2\right)^{\frac{1}{2}} \quad (7)$$

$$\chi^2 = \frac{\sum_{i=1}^{N}\left(MR_{exp,i} - MR_{pre,i}\right)^2}{N-z} \quad (8)$$

In the above-mentioned equations, MR_{exp} and MR_{pre} represent the moisture ratios, which were determined experimentally and model-predicted, respectively. z represents the number of the constants that were employed in the corresponding model equations, whereas N denotes the number of the experiments considered. The mathematical model which provided the highest R^2 value, together with the lowest χ^2 and RMSE values was considered as the most suitable one for describing the drying behavior of the blueberries and golden berries.

RESULTS AND DISCUSSION

Infrared drying of blueberries and golden berries

Figs. 1 and 2 display the moisture content curves (left) and drying rate curves (right) for blueberries and golden berries, respectively, during infrared drying at 60, 70, and 80°C. The initial moisture content of blueberries, 5.3800 kg water/kg dry matter, decreased to 0.2874, 0.2146, and 0.1813 kg water/kg dry matter at 60, 70, and 80°C, respectively, as shown in Fig. 1. Reaching the 7% final moisture content target required 240 min at 60°C, 180 min at 70°C, and 135 min at 80°C. For the infrared drying of golden berries (Fig. 2), on the other hand, starting from an initial moisture content of 2.9889 kg water/kg dry matter, the final moisture content decreased to 0.2868, 0.1695, and 0.1624 kg water/kg dry matter at 60, 70, and 80°C, respectively. Reaching the target 7% final moisture content took 240 min at 60°C, 165 min at 70°C, and 135 min at 80°C.

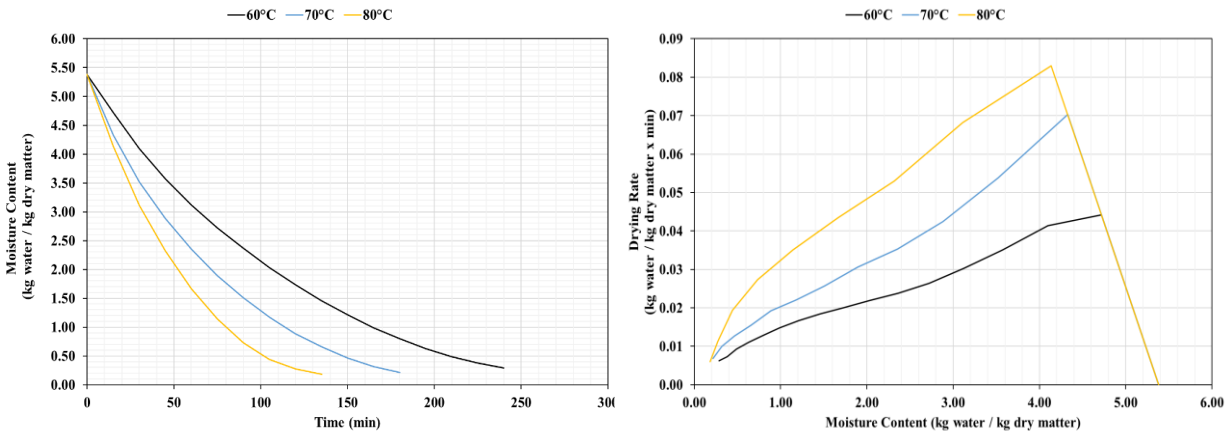

Figure 1. Variation of moisture contents and drying rates for the infrared drying of blueberries at 60, 70, and 80°C.

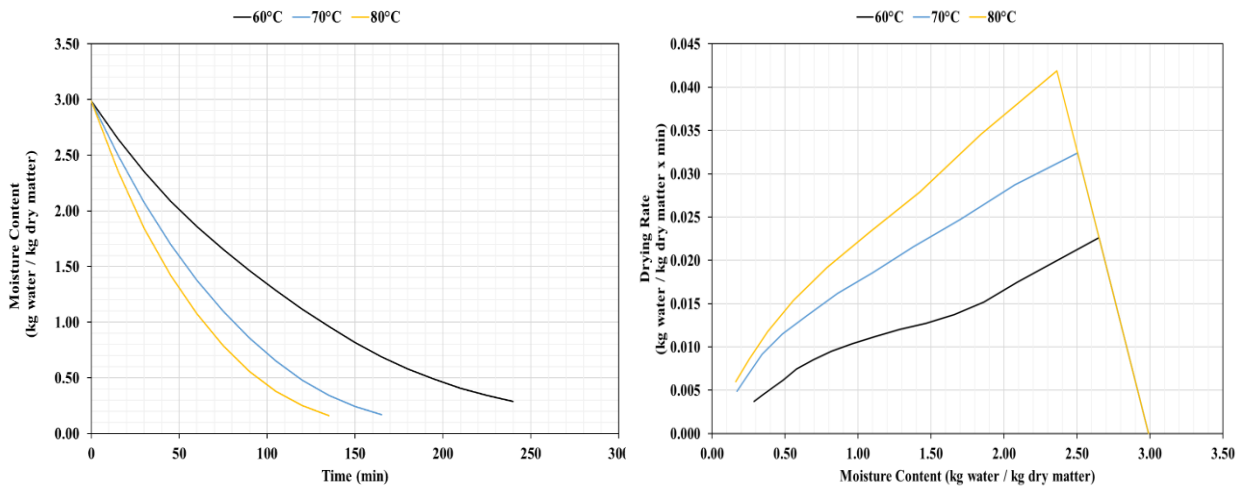

Figure 2. Variation of moisture contents and drying rates for the infrared drying of golden berries at 60, 70, and 80°C.

The results demonstrate that the berry type did not have a notable effect on the time required to reach the target final moisture content under infrared drying conditions. However, the drying temperature had a pronounced effect on the drying time for both berry types. The reduction in drying time with increasing temperature is consistent with findings reported in previous literature studies. For instance, Lopez *et al.*, investigated the influence of air-drying temperatures ranging from 50 to 90°C on the drying behavior of golden berries [9]. Accordingly, the time for reaching a moisture ratio of 0.1 decreased from approximately 800 min at 50°C to 180 min at 90°C. Similarly, Ozyalcin and Kipcak [31] investigated the infrared drying of squid and reported drying times of 277, 240, and 150 min at 60, 70, and 80°C, respectively. In another study, convective, infrared and freeze-drying of golden berry pulp were comparatively investigated [11]. Accordingly, increasing the temperature from 60°C to 80°C reduced the infrared drying time to reach below 0.078 g water/g dry matter from 630 to 450 min. Likewise, Zhang *et al*. [33] investigated ultrasonic-assisted infrared drying of ginger slices at 50, 60, and 70°C. When the temperature for drying increased from 50 to 70°C, the drying time decreased from 225 min to 105 min. The authors attributed this behavior to the increased energy absorbed by the samples at higher temperatures, thereby enhancing moisture removal and consequently accelerating the drying process.

When the drying rate curves are investigated, it is seen that higher drying temperatures resulted in faster drying rates. For both berries, the drying curves consisted primarily of rising-rate and falling-rate periods with no distinct constant-rate period. Puente *et al*. [11] attributed the absence of a constant-rate period to the waxy layer covering of the fruit surface which may hinder moisture transfer from the fruit's interior to its surface. Similar behavior was reported by Doymaz during the infrared drying of red kidney bean seeds at various infrared power levels [15]. The drying rate was found to increase with increasing infrared power, no constant-rate period being observed. Kipcak and Doymaz [19] reported comparable results for the infrared drying of cherry tomatoes, where a distinct constant-rate period was absent. Likewise, in another study regarding the infrared drying of squid, it was reported that a falling-rate period was seen in the drying rate curves only, with drying rates increasing with respect to the drying temperature [31]. More recently, Uribe *et al*. [32] investigated the infrared, vacuum, hot air, and freeze-drying of blueberries, and reported that no constant-rate period was observed during infrared drying at 70°C. The authors suggested that the fast removal of the unbound water from the surface of the fruit may have resulted in a negligible constant-rate period.

Overall, the performance of infrared drying can also be evaluated by comparing the results obtained in this study with those reported in the author's previous studies on oven drying and vacuum oven drying of blueberries [27] and golden berries [28] under the same drying temperatures. Infrared drying resulted in considerably shorter drying times than both conventional oven and vacuum oven drying. The drying times were 420, 390, and 210 min for the oven drying and 240, 210, and 150 min for the vacuum oven drying at 60, 70, and 80°C, respectively for blueberries [27]. Similarly, for golden berries, drying times of 480, 300, and 285 min were obtained using oven drying, whereas vacuum oven drying required 435, 285, and 195 min at 60, 70, and 80°C, respectively [28]. These comparisons indicate that infrared drying can substantially accelerate the drying rate and reduce the overall processing time of both berry types.

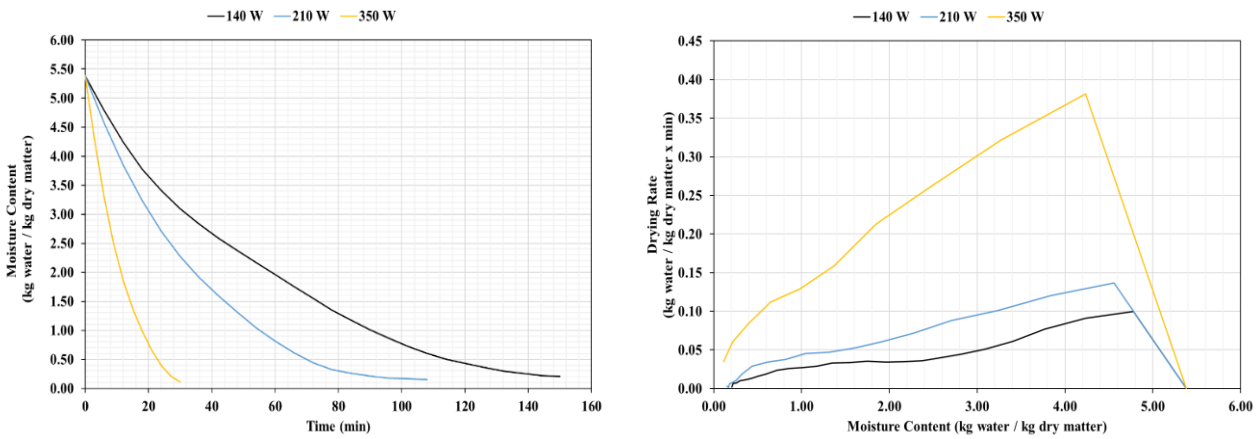

Figure 3. Variation of moisture content and drying rate for the microwave drying of blueberries at 140 W, 210 W, and 350 W.

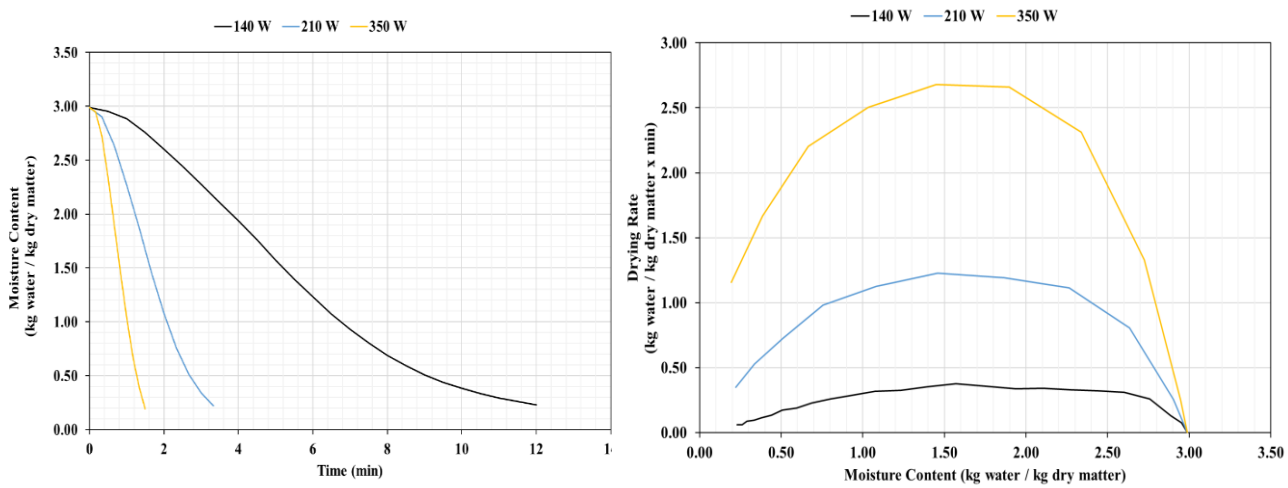

Figure 4. Variation of moisture content and drying rate for the microwave drying of golden berries at 140 W, 210 W, and 350 W.

Microwave drying of blueberries and golden berries

Figs. 3 and 4 display the moisture content curves (left) and drying rate curves (right) for blueberries and golden berries, respectively, during microwave drying across power levels of 140 W, 210 W, and 350 W.

As presented in Fig. 3 for the blueberry microwave drying, the initial moisture content of 5.3800 kg water/kg dry matter decreased to 0.2078, 0.1491, and 0.1104 kg water/kg dry matter at microwave powers of 140, 210, and 350 W, respectively. The corresponding drying times required to reach the 7% final moisture content were 150, 108, and 30 min. For the microwave drying of golden berries (Fig. 4) on the other hand, the initial moisture content of 2.9889 kg water/kg dry matter decreased to 0.2311, 0.2210, and 0.1941 kg water/kg dry matter at 140, 210, and 350 W, respectively. Attaining the target 7% final moisture content required drying times of 12 min (at 140 W), 3.3 min (at 210 W), and 1.5 min (at 350 W). A pronounced decrease in drying time was therefore observed for the microwave drying of golden berries. However, an important limitation was also observed at higher microwave power levels. At 210 W and 350 W, the golden berry samples burst and ruptured in all experimental replicates and were unable to retain their original shape. Such behavior was not observed during the microwave drying of blueberries. Examination of the drying rate curves showed that the drying rate increased with increasing microwave power. Similar to infrared drying, the drying curves of blueberries exhibited rising-rate and falling-rate periods, whereas a distinct constant-rate period was not observed.

The enhancement in drying rate with increasing microwave power is consistent with previous studies on various food products. For instance, Beaudry *et al.* [25] investigated hot air, vacuum, microwave-assisted hot air, and freeze-drying of osmotically dehydrated cranberries. Among the aforementioned methods investigated, microwave-assisted drying produced the shortest drying times. In a study on microwave-dried tomato slices, Horuz *et al.* [34] reported that raising the microwave power from 120 W to 180 W reduced the time needed to reach a 17% moisture content from 636 min to 341 min. The authors attributed this reduction to an increase in the diffusivity of water within the tomato samples as microwave power increased. Moreover, no constant-rate period was encountered during drying. The high drying rates achieved under microwave heating were attributed to heat generation inside the sample, which produced a substantial vapor pressure gradient between the interior and surface of the tomatoes and thereby facilitated water removal from the tissue. Kipcak and Doymaz [19] investigated the microwave drying of cherry tomatoes at microwave powers of 90, 180, 270, and 360 W. The required drying times to reach the final moisture content were 68, 34, 12, and 7 min, respectively. These drying times were considerably shorter than the drying times obtained during infrared drying, for which the corresponding drying times were 510, 390, and 330 min at infrared powers of 74, 88, and 104 W, respectively. In another study, in which the microwave drying of squid was examined, the drying times were reported as 18, 7, and 4.5 min for the microwave powers of 140, 210, and 350 W, respectively [31]. The authors also reported that only the falling-rate period could be identified in the corresponding drying curves.

The rupture observed in the golden berry samples during microwave drying may be associated with the highly waxy nature of their outer skin. This waxy layer can restrict migration of moisture from the

interior toward the surface, resulting in the accumulation of internal pressure within the fruit. Chen *et al.* [4] reported that when the internal pressure exceeds the mechanical strength of the epidermis, the fruit skin may crack or burst as a means of pressure release. Such behavior can subsequently result in structural collapse and deformation, adversely affecting the appearance of the dried product, as observed in the present study.

In addition to structural damage, other limitations associated with microwave drying have been reported. Belwal *et al.* identified scorching, particularly toward the end of drying with low moisture contents, as one of the major drawbacks of microwave drying [21]. Carranza-Conca *et al.* also reported cell disruption and rupture in microwave dried grapes, which was attributed to the elevated temperatures attained within the fruit [26]. Zhang *et al.* [33] noted that although microwave drying is a fast and potentially energy-efficient process, localized overheating may occur, resulting in burning or charring, particularly at the corners and edges of the material. Furthermore, microwave energy may damage the structure of the food materials, consequently impairing the rehydration characteristics of the dried product. Karam *et al.* similarly reported textural damage and subsequent scorching as potential disadvantages associated with microwave drying [16].

Drying kinetics

Understanding the drying kinetics of berries is significant for the effective design, operation, and optimization of drying processes, particularly when the preservation of product quality is considered. As described in the Experimental section, the effective moisture diffusivity (D_{eff}) was calculated by using Equation (5) for all experimental conditions summarized in Table 1. As presented in Table 1, the values of D_{eff} increased with increasing drying temperature. A similar increase was observed with increasing microwave power. For both berry types, microwave drying resulted in considerably higher D_{eff} values than infrared drying. For blueberries, the D_{eff} values obtained by infrared drying ranged from $2.02\cdot10^{-9}$ to $4.32\cdot10^{-9}$ m^2/s, whereas microwave drying resulted in values ranging from $3.74\cdot10^{-9}$ to $2.02\cdot10^{-8}$ m^2/s. A similar trend was observed for golden berries. D_{eff} values ranged from $1.64\cdot10^{-9}$ to $3.61\cdot10^{-8}$ m^2/s during infrared drying and increased to $3.89\cdot10^{-8}$ - $2.99\cdot10^{-7}$ m^2/s during microwave drying. Comparison with the author's previous studies on the conventional oven drying and vacuum oven drying of blueberries and golden berries [27, 28] revealed different rankings of the drying methods regarding moisture diffusivity. For blueberries, the highest D_{eff} values were obtained during microwave drying, followed by vacuum oven, infrared, and oven drying. For golden berries, microwave drying also yielded the highest D_{eff} values, followed by infrared, vacuum oven, and oven drying. These results indicate that microwave heating substantially enhances internal moisture transport in both berry types.

Although relatively few studies have focused specifically on the kinetic evaluation of berry drying, the observed trends are consistent with findings reported for other food materials. For the infrared drying of squid at 60, 70 and 80°C, the corresponding D_{eff} values were found as $6.57\cdot10^{-10}$, $7.95\cdot10^{-10}$, and $1.35\cdot10^{-9}$ m^2/s, respectively [31]. Thus, D_{eff} increased with respect to infrared temperature. The same authors also investigated the microwave drying of squid at microwave powers of 140 W, 210 W, and 350 W, obtaining D_{eff} values of $1.25\cdot10^{-8}$, $3.52\cdot10^{-8}$, and $5.62\cdot10^{-8}$ m^2/s, respectively.

Table 1. Drying time and D_{eff} values for the infrared and microwave drying

Berry investigated	Drying method	Drying temperature/Power	Drying time (min)	D_{eff} (m^2/s)
Blueberry	Infrared drying	60°C	240	$2.02\cdot10^{-9}$
		70°C	180	$2.93\cdot10^{-9}$
		80°C	135	$4.32\cdot10^{-9}$
	Microwave drying	140 W	150	$3.74\cdot10^{-9}$
		210 W	108	$5.84\cdot10^{-9}$
		350 W	30	$2.02\cdot10^{-8}$
Golden berry	Infrared drying	60°C	240	$1.64\cdot10^{-9}$
		70°C	165	$2.80\cdot10^{-9}$
		80°C	135	$3.61\cdot10^{-8}$
	Microwave drying	140 W	12	$3.89\cdot10^{-8}$
		210 W	3.3	$1.35\cdot10^{-7}$
		350 W	1.5	$2.99\cdot10^{-7}$

For the drying of blueberries at 70°C, Uribe *et al.* [32] reported a higher D_{eff} for infrared drying ($1.61 \cdot 10^{-10}$ m^2/s) than for hot air drying ($1.40 \cdot 10^{-10}$ m^2/s). Similarly, Kipcak and Doymaz [19] reported a substantial increase in D_{eff} with microwave power during the microwave drying of cherry tomatoes. This behavior was attributed to the rapid increase in the sample temperatures under microwave heating, which increased the internal vapor pressure and consequently promoted faster moisture migration.

Mathematical modelling

Table 2 summarizes the mathematical modelling results for the infrared and microwave drying of blueberries and golden berries, highlighting the optimal fit among the 14 tested models for each condition. Model performance was evaluated using R^2, RMSE, and χ^2 values, with the best model selected based on the highest R^2, paired with the lowest RMSE and χ^2 values.

Table 2. Best-fitted mathematical models for the infrared drying and microwave drying of blueberries and golden berries

Infrared drying of blueberries		
60°C	70°C	80°C
Alibas a = 2.46918 k = 0.00536 n = 0.94538 b = 0.00236 g = -1.46791 R^2 = 0.99992 χ^2 = 0.00001 RMSE = 0.00258	Logarithmic a = 1.07179 k = 0.01228 c = -0.07962 R^2 = 0.99975 χ^2 = 0.00003 RMSE = 0.00462	Alibas a = 4.19485 k = 0.00684 n = 0.97824 b = 0.01036 g = -3.19510 R^2 = 0.99996 χ^2 = 0.00001 RMSE = 0.00204
Microwave drying of blueberries		
140 W	210 W	350 W
Midilli & Kucuk a = 0.99019 k = 0.01887 n = 0.95409 b = -0.00059 R^2 = 0.99854 χ^2 = 0.00014 RMSE = 0.01068	Aghbashlo *et al.* k_1 = 0.02618 k_2 = -0.00276 R^2 = 0.99893 χ^2 = 0.00010 RMSE = 0.00956	Aghbashlo *et al.* k_1 = 0.07478 k_2 = -0.01263 R^2 = 0.99966 χ^2 = 0.00004 RMSE = 0.00570
Infrared drying of golden berries		
60°C	70°C	80°C
Alibas a = 2.80443 k = 0.00408 n = 0.96600 b = 0.00272 g = -1.80632 R^2 = 0.99985 χ^2 = 0.00002 RMSE = 0.00333	Alibas a = 3.02096 k = 0.00553 n = 0.99982 b = 0.00523 g = -2.02131 R^2 = 0.99998 χ^2 = 0.00002 RMSE = 0.00114	Alibas a = 3.19274 k = 0.00738 n = 0.97526 b = 0.00685 g = -2.19265 R^2 = 0.99999 χ^2 = 0.00001 RMSE = 0.00073
Microwave drying of golden berries		
140 W	210 W	350 W
Alibas a = 50.81750 k = 0.01950 n = 1.07660 b = 0.97020 g = -49.83200 R^2 = 0.99955 χ^2 = 0.00006 RMSE = 0.00676	Page k = 0.27400 n = 1.89164 R^2 = 0.99994 χ^2 = 0.00001 RMSE = 0.00266	Page k = 1.08259 n = 2.18701 R^2 = 0.99978 χ^2 = 0.00003 RMSE = 0.00503

CONCLUSION

In the present study, the drying behavior and kinetics of blueberries and golden berries using infrared and microwave drying methods under different operating conditions was investigated. The results demonstrated that both drying temperature and microwave power substantially affected moisture removal, drying rate, and effective moisture diffusivity. For infrared drying, increasing the drying temperature from 60°C to 80°C progressively accelerated moisture removal and reduced the time required to reach the final moisture content of 7%. The required drying times decreased from 240 min to 135 min for both blueberries and for golden berries. In addition, the drying curves of both berries were characterized mainly by rising-rate and falling-rate periods, with no distinct constant-rate period.

Microwave drying provided a considerably greater enhancement in drying performance. Increasing the power of the microwave from 140 to 350 W reduced the time required for the drying of blueberries from 150 to 30 min, while the corresponding drying time for golden berries decreased from 12 min to only 1.5 min. D_{eff} increased with increasing drying temperature during infrared drying and with increasing microwave power during microwave drying. Moreover, microwave drying resulted in substantially higher effective moisture diffusivity values than infrared drying for both berry types, indicating that volumetric microwave heating markedly enhanced internal moisture transport. Comparison with the conventional oven and vacuum oven drying results from the authors' previous studies further demonstrated the superior drying efficiency of infrared and, particularly, microwave drying.

Despite its remarkable drying rate, microwave drying presented an important limitation for golden berries. At 210 W and 350 W, the samples consistently ruptured and lost their original shape, whereas no comparable structural damage was observed in blueberries. This behavior may be associated with the waxy outer skin of golden berries, which can restrict moisture migration and promote internal pressure buildup during rapid microwave heating. Therefore, although higher microwave powers substantially improve drying efficiency, excessively intense microwave treatment may adversely affect the physical integrity and appearance of the product.

The results obtained for mathematical modeling showed that the drying behavior of both berry types could be described accurately using appropriate empirical models. Among the 14 models evaluated, Alibas model provided the best-fit for most infrared drying conditions, whereas different models, including the Midilli & Kucuk, Aghbashlo *et al.*, Alibas, and Page models, provided the best representation under the microwave drying conditions. The selected models exhibited very high coefficients of determination and low χ^2 and RMSE values, demonstrating their suitability for describing the drying kinetics under the investigated conditions.

Overall, the findings indicate that microwave drying offers a substantial advantage in terms of moisture diffusivity and drying time, while infrared drying provides an effective alternative with considerably shorter processing times than conventional oven and vacuum oven drying. However, the optimum condition for drying should not be selected solely regarding the drying rate. In particular, the structural damage observed in golden berries at high microwave powers highlights the need to balance drying efficiency with product integrity. The results obtained in this study provide useful kinetic data and predictive models for the design, optimization, and potential scale-up of infrared and microwave drying processes for blueberries and golden berries.

REFERENCES

1. B. Gök, E. Kıpçak, *Bulg. Chem. Commun.*, **56** (3), 233 (2024).
2. A. Akcicek, E. Avci, Z. H. Tekin-Cakmak, M. Z. Kasapoglu, O. Sagdic, S. Karasu, *ACS Omega*, **8** (44), 41603 (2023).
3. K. An, M. Fu, H. Zhang, D. Tang, Y. Xu, G. Xiao, *J. Food Sci. Technol.*, **56** (2), 783 (2019).
4. F. Chen, M. Zhang, S. Devahastin, D. Yu, *Food Bioprocess. Technol.*, **14** (10), 1805 (2021).
5. M. Zielinska, A. Michalska, *Food Chem.*, **212**, 671 (2016).
6. L. Etzbach, M. Meinert, T. Faber, C. Klein, A. Schieber, F. Weber, *Curr. Res. Food Sci.*, **3**, 73 (2020).
7. J. R. de J. Junqueira, J. L. G. Corrêa, H. M. de Oliveira, R. Ivo Soares Avelar, L. A. Salles Pio, *LWT – Food Sci. Technol.*, **82**, 404 (2017).
8. K. Bravo, E. Osorio, *Food Chem.*, **197**, 185 (2016).
9. J. Lopez, A. Vega-Gálvez, M. J. Torres, R. Lemus Mondaca, I. Quispe-Fuentes, K. Di Scala, *Chil. J. Agric. Res.*, **73** (3), 293 (2013).
10. A. Nawirska-Olszańska, B. Stępień, A. Biesiada, J. Kolniak-Ostek, M. Oziembłowski, *Foods*, **6** (8), 60 (2017).
11. L. Puente, A. Vega-Gálvez, I. Fuentes, K. Stucken, A. Rodríguez, A. Pastén, *J. Food Sci. Technol.*, **58** (4), 1470 (2021).
12. E. Karacabey, *Braz. Arch. Biol. Technol.*, **59**, e16160470 (2016).
13. M. F. Ramadan, *Food Res. Int.*, **44** (7), 1830 (2011).
14. N. İzli, G. Yıldız, H. Ünal, E. Işık, V. Uylaşer, *Int. J. Food Sci. Technol.*, **49** (1), 9 (2014).

15. I. Doymaz, *J. Food Process. Preserv.*, **39** (6), 933 (2015).
16. M. C. Karam, J. Petit, D. Zimmer, E. B. Djantou, J. Scher, *J. Food Eng.*, **188**, 32 (2016).
17. S. H. Miraei Ashtiani, M. Rafiee, M. Mohebi Morad, A. Martynenko, *Drying Technol.*, **40** (8), 1639 (2022).
18. T. Skåra, T. Løvdal, D. Skipnes, N. N. Mehlomakulu, C. R. Mapengo, R. O. Baah, M. N. Emmambux, *Food Rev. Int.*, **39** (9), 7197 (2023).
19. A. S. Kipcak, I. Doymaz, *Chem. Ind. Chem. Eng. Q.*, **26** (2), 203 (2020).
20. M. Pateiro, M. Vargas-Ramella, D. Franco, A. G. da Cruz, G. Zengin, M. Kumar, K. Dhama, J. M. Lorenzo, *Food Chem.: X*, **16**, 100465 (2022).
21. T. Belwal, C. Cravotto, M. A. Prieto, P. R. Venskutonis, M. Daglia, H. P. Devkota, A. Baldi, S. M. Ezzat, L. Gómez-Gómez, M. M. Salama, L. Campone, L. Rastrelli, J. Echave, S. M. Jafari, G. Cravotto, *Drying Technol.*, **40** (8), 1539 (2022).
22. Y. Sun, M. Zhang, A. Mujumdar, *Food Eng. Rev.*, **11** (1), 61 (2019).
23. C. Cui, D. Zhao, J. Huang, J. Hao, *Int. J. Food Prop.*, **25** (1), 435 (2022).
24. H. Feng, Y. Yin, J. Tang, *Food Eng. Rev.*, **4** (2), 89 (2012).
25. C. Beaudry, G. S. V. Raghavan, C. Ratti, T. J. Rennie, *Drying Technol.*, **22** (3), 521 (2004).
26. J. Carranza-Concha, M. Benlloch, M. M. Camacho, N. Martínez-Navarrete, *Food Bioprod. Process.*, **90** (2), 243 (2012).
27. E. Kıpçak, *Sigma J. Eng. Nat. Sci.*, **42** (3), 739 (2024).
28. E. Kıpçak, *J. Turk. Chem. Soc. Sect. B Chem. Eng.*, **6** (1), 1 (2023).
29. AOAC, *Official Methods of Analysis of AOAC International*, 16th edn., AOAC International, Rockville, MD, 1995.
30. B. Salık, A. Tan, E. Kıpçak, *Bulg. Chem. Commun.*, **57** (3), 235 (2025).
31. Z. O. Ozyalcin, A. S. Kipcak, *Turk. J. Fish. Aquat. Sci.*, **21** (3), 135 (2021).
32. E. Uribe, A. Vega-Galvez, A. Pasten, K. S. Ah-Hen, N. Mejias, L. Sepúlveda, J. Poblete, L. S. Gomez-Perez, *Antioxidants*, **13** (12), 1554 (2024).
33. D. Zhang, D. Huang, Y. Zhang, Y. Lu, S. Huang, G. Gong, L. Li, *Ultrason. Sonochem.*, **92**, 106287 (2023).
34. E. Horuz, H. J. Jaafar, M. Maskan, *Drying Technol.*, **35** (7), 849 (2017).

Instructions about Preparation of Manuscripts

General remarks: Manuscripts are submitted in English by e-mail. The text must be prepared in A4 format sheets using Times New Roman font size 11, normal character spacing. The manuscript should not exceed 15 pages (about 3500 words), including photographs, tables, drawings, formulae, etc. Authors are requested to use margins of 2 cm on all sides.

Manuscripts should be subdivided into labelled sections, e.g. INTRODUCTION, EXPERIMENTAL, RESULTS AND DISCUSSION, etc. **The title page** comprises headline, author(s)' names and affiliations, abstract and key words. Attention is drawn to the following:

a) **The title** of the manuscript should reflect concisely the purpose and findings of the work. Abbreviations, symbols, chemical formulae, references and footnotes should be avoided. If indispensable, abbreviations and formulae should be given in parentheses immediately after the respective full form.

b) **The author(s)'** first and middle name initials and family name in full should be given, followed by the address (or addresses) of the contributing laboratory (laboratories). **The affiliation** of the author(s) should be listed in detail (no abbreviations!). The author to whom correspondence and/or inquiries should be sent should be indicated by an asterisk (*) with e-mail address.

The abstract should be self-explanatory and intelligible without any references to the text and containing up to 250 words. It should be followed by keywords (up to six).

References should be numbered sequentially in the order, in which they are cited in the text. The numbers in the text should be enclosed in brackets [2], [5, 6], [9−12], etc., set on the text line. References are to be listed in numerical order on a separate sheet. All references are to be given in Latin letters. The names of the authors are given without inversion. Titles of journals must be abbreviated according to Chemical Abstracts and given in italics, the volume is typed in bold, the initial page is given and the year in parentheses. Attention is drawn to the following conventions: a) The names of all authors of a certain publications should be given. The use of "et al." in the list of references is not acceptable; b) Only the initials of the first and middle names should be given. In the manuscripts, the reference to author(s) of cited works should be made without giving initials, e.g. "Bush and Smith [7] pioneered...". If the reference carries the names of three or more authors it should be quoted as "Bush et al. [7]", if Bush is the first author, or as "Bush and co-workers [7]", if Bush is the senior author.

Footnotes should be reduced to a minimum. Each footnote should be typed double-spaced at the bottom of the page, on which its subject is first mentioned. **Tables** are numbered with Arabic numerals on the left-hand top. Each table should be referred to in the text. Column headings should be as short as possible but they must define units unambiguously. The units are to be separated from the preceding symbols by a comma or brackets. Note: The following format should be used when figures, equations, etc. are referred to the text (followed by the respective numbers): Fig., Eqns., Table, Scheme.

Schemes and figures. Each manuscript should contain or be accompanied by the respective illustrative material, as well as by the respective figure captions in a separate file. As far as presentation of units is concerned, SI units are to be used. However, some non-SI units are also acceptable, such as °C, ml, l, etc. Avoid using more than 6 (12 for review articles) figures in the manuscript. Since most of the illustrative materials are to be presented as 8-cm wide pictures, attention should be paid that all axis titles, numerals, legend(s) and texts are legible.

The authors are required to submit the text with a list of three individuals and their e-mail addresses that can be considered by the Editors as potential reviewers. Please note that the reviewers should be outside the authors' own institution or organization. The Editorial Board of the journal is not obliged to accept these proposals.

The authors are asked to submit **the** final text (after the manuscript has been accepted for publication) in electronic form by e-mail. The main text, list of references, tables and figure captions should be saved in separate files (as *.rtf or *.doc) with clearly identifiable file names. It is essential that the name and version of the word-processing program and the format of the text files is clearly indicated. It is recommended that the pictures are presented in *.tif, *.jpg, *.cdr or *.bmp format. The equations are written using "Equation Editor" and chemical reaction schemes are written using ISIS Draw or ChemDraw programme.

EXAMPLES FOR PRESENTATION OF REFERENCES

REFERENCES

1. D. S. Newsome, Catal. Rev.–Sci. Eng., 21, 275 (1980).
2. C.-H. Lin, C.-Y. Hsu, J. Chem. Soc. Chem. Commun., 1479 (1992).
3. R. G. Parr, W. Yang, Density Functional Theory of Atoms and Molecules, Oxford Univ. Press, New York, 1989.
4. V. Ponec, G. C. Bond, Catalysis by Metals and Alloys (Stud. Surf. Sci. Catal., vol. 95), Elsevier, Amsterdam, 1995.
5. G. Kadinov, S. Todorova, A. Palazov, in: New Frontiers in Catalysis (Proc. 10th Int. Congr. Catal., Budapest (1992), L. Guczi, F. Solymosi, P. Tetenyi (eds.), Akademiai Kiado, Budapest, 1993, Part C, p. 2817.
6. G. L. C. Maire, F. Garin, in: Catalysis. Science and Technology, J. R. Anderson, M. Boudart (eds.), vol. 6, Springer Verlag, Berlin, 1984, p. 161.
7. D. Pocknell, GB Patent 2 207 355 (1949).
8. G. Angelov, PhD Thesis, UCTM, Sofia, 2001, pp. 121-126.
9. JCPDS International Center for Diffraction Data, Power Diffraction File, Swarthmore, PA, 1991.
10. CA 127, 184 762q (1998).
11. P. Hou, H. Wise, J. Catal., in press.
12. M. Sinev, private communication.
13. http://www.chemweb.com/alchem/articles/1051611477211.html.

Texts with references which do not match these requirements will not be considered for publication!!!

CONTENTS

Papers presented at the 12th International Conference on New Trends in Chemistry, 10-12 April 2026, Barcelona, Spain

A. Katirci, F. U. Nigiz, Production of desalination membranes from recycled PVDF polymers…… 241
Y. Cagliyan, Z. O. Ozyalcin, A. S. Kipcak, Freeze drying of manila clam: drying kinetics and mathematical modelling……..……... 247
O. Ercan, Z. O. Ozyalcin, A. S. Kipcak, Rehydration characteristics of freeze-dried mussel, shrimp and squid……..… 254
B. Eren, A. H. Dökmeci, Degradation mechanisms of selected aminopolycarboxylic acid molecules by DFT method…… 261
A. Menekse, B. K. Isik, N. Tugrul, Utilization of sugar beet pulp as an agricultural by-product in vegan leather production…….. 269
D. S. İşlek, E. Kiriş, A. Şen Yılmaz, E. Köse, Forensic identification of pen ink pigments using dual-wavelength Raman spectroscopy combined with chemometrics…… 276
D. Şakar, H. K. Gürakin, Removing disperse orange 30 dye from simulated wastewater using formaldehyde-stabilized quince leaf powder bioadsorbent….……..… 281
A. B. Demir, D. Bahçeci, S. Özer, Ö. Y. Şahin, D. Şakar, Preparation and analysis of an herbal extract solution having potential restorative effects against radiation dermatitis…….. 286
E. Çolak, B. Çetin, H. C. Kurçin, S. K. Aslan, D. Ünlü, F. U. Nigiz, Synthesis and characterization of polydopamine-modified MOFs for polymer electrolyte membranes… 291
D. Uygunoz, I. Sengor, E. M. Derun, Natural pigments doped polymer films synthesis by solution casting method and characterization…….. 297
D. Uygunoz, I. Sengor, E. M. Derun, Biomass energy production from sunflower plant……. 303
S. Simsek, O. Y. Usoğlu, E. Akyol, Evaluation of the inhibitory effects of phenolic compounds on calcium oxalate crystallization……. 310
N. A. Saleha, E. Akyol, Sustainable heavy metal ion detection of waste-based carbon quantum dots…… 315
H. İ. Özgündüz, B. D. Çorbacıoğlu, S. Keyf, Modıfıcatıon of bıtumen by addıng reactıve terpolymer, polyolefın elastomer and thermoplastic…… 320
O. Tavlıbıyık, İ. Küçük, Effect of hemp filler on the mechanical and physical properties of PLA/PBAT composite films……. 325
K. Akdemir, H. Gonultas, B. K. Isik, N. Tugrul, Synthesis and characterization of eco-friendly edible films based on pistachio shell…….… 331
Ö. İpsalalı, B. Okyay, F. U. Nigiz, From orange peel to sustainable biocomposite: production and characterization of pectin/CMC films with matcha tea extract…….…. 336
N. İşman, Ö. Işık, P. Terzioğlu, M. Orhan, Effect of tannic acid concentration on structural, mechanical, and antibacterial properties of polyvinyl alcohol/chitosan/pomegranate peel-based biocomposite films…….. 341
R. Ozdemir, D. Unlu, Synthesis and characterization of boron-containing benzoxazine resins for advanced thermal protection systems…….. 347
M. Kocaoğlu, S. N. Karabekiroğlu, Activated carbon from gypsophila roots: a sustainable adsorbent for dye removal……. 351
S. Kahraman, E. Özbey, S. Uzun, F. U. Nigiz, Production and characterization of a double-layered wound dressing containing electrospun polylactic acid and hypericum-infused alginate hydrogel…….…… 358
S. Yiğit, T. E. Bektaş, S. Kahraman, F. Uğur Nigiz, Synthesis and in vitro characterization of quercetin-loaded alginate-keratin composite hydrogels for enhanced wound healing applications……... 364

B. Kemanci, S. Kurumoglu, B. Gurkan, Investigation of the correlation between skin permeation and global reactivity descriptors in phenolic antioxidants: a comparative DFT and ADMET study…… 370
C. Ergul, S. Kurumoglu, Y. Yalcin Gurkan, Brain penetration in CNS and non-CNS drugs using molecular electronic parameters……. 377
S. Simsek, E. Akyol, İ. Kucuk, Comparison of the effects of cellulase, pectinase, and xylenase enzymes on the total flavonoid content of *Helichrysum arenarium* extract obtained by enzymatically pre-treated Soxhlet extraction…… 382
T. Sabudak, B. Eren, C. Ozcelik, Determination of the chemical composition of the essential oil of the Rubia tinctorum plant …… 386
G. Tumtum, K. Demir, S. Kurumoglu, Y. Yalcin Gurkan, Reactivity and ecotoxicity of the next-generation herbicide flufenauxirim: a density functional theory (DFT) and quantitative structure-activity relationship (QSAR) study with reference to aminocyclopyrachlor……...…… 391
M. Özbakiş, D. Ismaili Uka, P. Terzioğlu, Y. Sicak, Sustainable and bioactive chitosan/PVA hydrogels incorporating allantoin for wound healing applications…… 396
E. Kıpçak,Comparative evaluation of infrared and microwave drying of berries: kinetics, diffusivity, and modeling approaches…….. 401
INSTRUCTIONS TO AUTHORS…….... 411